The Immiscibles

Capillarity Effects in Porous Media

Pore-Network Modelling

VAHID JOEKAR-NIASAR

Capillarity Effects in Porous Media
Pore-Network Modelling

Capillaire Verschijnselen in Poreuze Media;
Porienetwerk Modellering

(met een samenvatting in het Nederlands)

PROEFSCHRIFT

ter verkrijging van de graad van doctor aan de Universiteit Utrecht op gezag van de rector magnificus, prof.dr. J.C. Stoof, ingevolge het besluit van het college voor promoties in het openbaar te verdedigen op maandag 29 maart 2010 des ochtends te 10.30 uur
door

VAHID JOEKAR-NIASAR
geboren in 1978 te Teheran, Iran

Promoter: Prof. dr. ir. S.M. Hassanizadeh

The Reading Committee

Prof. M. CELIA	Princeton University, USA
Prof. H.K. DAHLE	University of Bergen, Norway
Prof. R. HELMIG	Stuttgart University, Germany
Prof. B. LINDQUIST	Stony Brook University, USA
Prof. R. SCHOTTING	Utrecht University, the Netherlands
Dr. O. VIZIKA	Institute Francais du Petrol, France

ISBN/EAN:	978-90-5744-179-0
Title:	The Immiscibles: Capillarity Effects in Porous Media - Pore-Network Modelling
Author:	Joekar-Niasar, V.
Publisher:	Utrecht University, Geosciences Faculty, Earth sciences department
Printing:	Proefschriftmaken.nl —— Printyourthesis.com
NUR-code:	933
NUR-description:	Geologie
Series:	Geologica Ultraiectina
Series Number:	318
Number of pages:	300

- Cover photo: Leonardo Garcia Alarcon Estrada, Architectural Association
- Cover design: Kourosh Jafari
- This research was supported financially by the Utrecht Centre of Geosciences and NUPUS international research training group.

Acknowledgments

Knowledge is in the end based on acknowledgement.

Ludwig Wittgenstein, philosopher

I would like to acknowledge a number of people, whose supports facilitated fulfillment of my research in the past four years.

I am heartily grateful to my supervisor, Majid Hassanizadeh, who supported me in all aspects during the past four years. Majid introduced the fascinating world of multiphase flow in porous media to me. His encouragement, guidance and support from the initial to the final level of my PhD study enabled me to develop my understanding of the subject and explore the scientific community by attending several conferences and workshops. His careful editing contributed enormously to the production of this book. Majid, thank you for your invaluable support!

I would like to thank Ruud Schotting for his supports. I am sure I will enjoy my postdoc research, which is in direct collaboration with him. I am grateful to Toon Leijnse from *Wageningen University* for his advices on numerical simulations. A sincere gratitude to Helge Dahle from *University of Bergen*, who helped me to develop my knowledge about dynamic pore-network modelling, which led to the production of Chapter 6. His wonderful hospitality made my visit from Bergen and his group unforgettable. I would like to show my gratitude to Laura Pyrak-Nolte from *Purdue University*, who provided me the possibility to visit her group in Purdue and made me familiar with micro-models. I would like to thank Mike Celia from *Princeton University* for very fruitful discussions we had during meetings and conferences. I enjoyed being involved in NUPUS international research training group, since I had very fruitful discussions with Rainer Helmig, Jennifer Niessner and other colleagues from *University of Stuttgart* during my visit from Stuttgart as well as the meetings. Thanks to Dorthe Wildenschild from the *Oregon State University* and Maša Prodanović from the *University of Texas* at *Austin* for the very effective collaboration, which led to the production of Chapter 5. I would like to thank Leonardo Garcia and Kourosh Jafari for designing the cover of my book.

In my daily work I have been blessed with a friendly and cheerful group of colleagues. First of all I should thank Margreet, for her help in administrative tasks, in learning Dutch language, and in organizing the summer school and Marie-Curie workshop. I would like to thank my former office mate, Cas Berentsen, for his comments and feedbacks in my early stage of my research as well as his beautiful nature photographs. After moving of Cas to *TU Delft*, I was lucky to have another nice office mate, Eric Morales-Casique. He and his wife, Elizabeth, made me more familiar with Spanish language, Mexican culture, movies, and cuisine. Thanks to Thomas Geenen for parallelization of the quasi-static code in Chapter 3. I would like to thank my other friends and colleagues Amir, Pasha and Akvile, Reza, Hans, Marzieh, Nikos, David, Li Pei, Marian, Simona, Mariene, Saskia, Hamid, Babak, Brijesh, Imran, and Qiu.

The Earth Sciences Department, Utrecht Centre of Geosciences, and NUPUS international research training group have provided me the supports I have needed to produce and complete this book.

My heartfelt thanks to my parents for supporting me throughout all the days of my life. Finally, my loving thanks to my sweet wife, Sheida, who has endlessly and patiently supported me in finishing my PhD and writing this book. While being busy with her own PhD research, for the past few months she helped me to correct and edit the texts. Without her encouragement and understanding, fulfillment of this work would have been too difficult.

Vahid Joekar-Niasar
Utrecht
March 14, 2010

Contents

Chapter 1

The Immiscibles

If we knew what it was we were doing, it would not be called research, would it?

Albert Einstein, physicist

1.1 Theories of two-phase flow including interfacial area

Darcy's law for multiphase flow assumes that the only driving forces for flow of each fluid are the gravity and the gradient in fluid pressure. The resisting force is assumed to be linearly proportional to the relative fluid velocity with respect to the solid. This results in a linear relationship between the flow velocity and driving forces. While these assumptions are reasonable for single-phase flow, one may expect many other factors to affect the balance of forces in the case of multiphase flow. Among these are interfacial forces that influence the movement of phases and the distribution of interfaces in the porous medium. In fact, through the application of rational thermodynamics, *Hassanizadeh and Gray* (1990, 1993a) developed a theory of two-phase flow in which interfacial areas were introduced as separate thermodynamic entities, possessing mass, momentum, and energy. They derived momentum balance equations not only for phases, but also for interfaces, and macroscale effects of interfacial forces were explicitly included. They found that the driving forces for the flow of a phase were the gradients of Gibbs free energy of the phase, plus gravity. They showed that for the case of single-phase flow, the gradient of Gibbs free energy reduces to the gradient of pressure. But, for the case of two-phase flow, because Gibbs free energy of a phase is a function of saturation and specific interfacial area, as well as mass density, its gradient will lead to terms in addition to the pressure gradient. They derived the following extended form of Darcy's law in which gradients of pressures, saturations and specific interfacial area appeared as driving forces:

$$\mathbf{v}^\alpha = -\frac{\mathbf{K}^\alpha}{\mu^\alpha} \cdot \left(\nabla P^\alpha - \rho^\alpha \mathbf{g} - \Psi^{\alpha a} \nabla a^{nw} - \Psi^{\alpha S} \nabla S^\alpha\right), \quad \alpha = w, n \tag{1.1}$$

where $\mathbf{v}^\alpha$ denotes the relative velocity of fluid phase α with respect to the solid. In the rest of this work, without loss of generality, we assume that the solid phase is rigid. $\mathbf{K}^\alpha$ is α-phase permeability tensor, $\Psi^{\alpha a}$ and $\Psi^{\alpha S}$ represent material properties, $\mathbf{g}$ is the gravity vector, a^{nw} is the specific area of fluid-fluid interfaces (amount of interfacial area per unit volume of the porous medium), P^α, ρ^α, S^α, and μ^α are pressure, mass density, saturation, and viscosity of the α-phase. Superscripts w and n designate wetting and nonwetting phases, respectively. Note that $\mathbf{K}^\alpha$ is the product of relative permeability coefficient and absolute permeability tensor. Thus, it is considered to be a function of average saturation.

Hassanizadeh and Gray (1990, 1993a) also showed that the average motion of fluid-fluid interfaces is due to a gradient in their Gibbs free energy, plus gravity. Again, as Gibbs free energy of interfaces is a function of saturation and specific interfacial area, the following equation for the average velocity of fluid-fluid interfaces was obtained:

$$\mathbf{w}^{nw} = -\mathbf{K}^{nw} \cdot \left[\nabla \left(a^{nw}\sigma^{nw}\right) + \Psi^{nw}\nabla S^w\right] \tag{1.2}$$

where the gravity term is neglected. In this equation, $\mathbf{w}^{nw}$ denotes the relative macroscopic velocity of fluid-fluid interfaces with respect to the solid, $\mathbf{K}^{nw}$ is permeability tensor for nw-interfaces, Ψ^{nw} represents a material property, and σ^{nw} is the macro-scale interfacial tension. These equations may be seen as the truly extended forms of Darcy's law, not only for a fluid phase but also for an interface. They must be supplemented with the following equations of balance of volume for phase saturations and specific interfacial area (assuming incompressible phases and constant mass density for interfaces):

$$\varphi\frac{\partial S^\alpha}{\partial t} + \nabla \cdot \mathbf{v}^\alpha = 0, \quad \alpha = w, n \tag{1.3}$$

$$\frac{\partial a^{nw}}{\partial t} + \nabla \cdot \left(a^{nw}\mathbf{w}^{nw}\right) = E^{nw} \tag{1.4}$$

where φ is porosity, $\mathbf{v}^\alpha$ and $\mathbf{w}^{nw}$ denote average velocities of α-phase and nw-interfaces, respectively, and E^{nw} is the net rate of production of nw-interfaces. It is proposed that E^{nw} should depend on saturation and its time rate of change (*Niessner and Hassanizadeh*, 2008, *Pop et al.*, 2009). *Joekar-Niasar et al.* (2010a) studied dependence of E^{nw} on dynamic parameters (viscosity ratio and different global pressure difference) using a dynamic pore-network model. But, the size of the network was almost one REV and they assumed that the advective flux of specific interfacial area was negligible. Here, the full equation in a long domain is analyzed.

Another central equation in theories of two-phase flow is the so-called capillary pressure-saturation relationship, which is commonly written as:

$$P^n - P^w = P^c(S^w) \tag{1.5}$$

In fact, there are two major assumptions in this equation: capillary pressure is a function of wetting phase saturation only, and fluids pressure difference is equal to capillary pressure (at all times and under all conditions). Regarding the first assumption, it is known that capillary pressure-saturation relationship is not unique and but a function of the history of fluids movements, even though it is obtained under equilibrium conditions. This is probably because P^c-S^w relationship depends not only on the volume fraction of phases, but also on their microscale distribution (*Entov*, 1980). In fact, one would expect capillary pressure to depend also on the interfacial curvature and/or specific interfacial area. *Hassanizadeh and Gray* (1993b) have suggested that the non-uniqueness in the capillary pressure-saturation relationship is indeed due to the absence of specific interfacial area in the capillarity theory and they proposed the following equation for the macroscopic capillary pressure:

$$P^c(S^w) = P^c(S^w, a^{nw}) \tag{1.6}$$

A number of computational and experimental works have shown that under a wide range of drainage and imbibition histories, P^c-S^w-a^{nw} surfaces more or less coincide. This means that the inclusion of a^{nw} leads to the removal or significant reduction of hysteresis in capillary pressure-saturation relationship. In other words, a unique P^c-S^w-a^{nw} surface may exist for all imbibition and drainage process (e.g. *Cheng et al.*, 2004, *Joekar-Niasar et al.*, 2008, 2010b, *Porter et al.*, 2009, *Reeves and Celia*, 1996).

Regarding the second assumption underlying Equation 1.5, it is now an established fact that $P^n - P^w$ is equal to capillary pressure but only under equilibrium conditions (see *Hassanizadeh et al.*, 2002, for an extended review of experimental evidences). For non-equilibrium situations, the following equation for the difference in fluid pressures has been suggested (*Entov*, 1980, *Hassanizadeh and Gray*, 1990, *Kalaydjian and Marle*, 1987, *Stauffer*, 1978):

$$P^n - P^w = P^c - \tau \frac{\partial S^w}{\partial t} \tag{1.7}$$

where τ, the non-equilibrium capillarity coefficient, is a material property that may still be a function of saturation and specific interfacial area.

In particular the behaviour of Equations 1.1, 1.2, and 1.4 has not been investigated in laboratorial works due to the technical limitations. Furthermore, continuum models are not capable to give insights into the involved parameters and their dependencies. Among different pore-scale simulators, we have chosen dynamic pore-network modelling due to its rather cheap computational costs that allows us to simulate large domains. We will investigate Equation 1.6 extensively using quasi-static pore-network models presented in Chapters 3, 4 and 5 for various porous media.

1.2 Pore-network models for two-phase flow

Pore-network models can be divided into quasi-static and dynamic ones.

Quasi-static pore-network models Quasi-static pore-network models have been developed extensively since *Fatt* (1956) introduced them for modelling capillary pressure-saturation (P^c-S^w) curve. They have been used not only for theoretical studies (see e.g. *Dias and Payatakes*, 1986a, *Held and Celia*, 2001, *Reeves and Celia*, 1996), but also for practical purposes for estimating or predicting characteristics of soils and rocks (see e.g. *Blunt et al.*, 2002, *Piri and Blunt*, 2005a,b, *Valvatne and Blunt*, 2004). For example *Blunt et al.* (2002) have suggested that using appropriate pore-scale physics combined with a geologically representative description of the pore space, one can produce capillary pressure and relative permeability curves for a given rock without actual measurements. *Vogel* (1997, 2000) and *Vogel and Roth* (1998) have stated that, to have a predictive representative pore-network model, an accurate translation of topology from the pore space geometry to a pore network is essential. Information on topology of porous samples can be obtained from imaging techniques such as X-ray tomography and micro-tomography (see e.g. *Al-Raoush and Willson*, 2005a,b, *Coles et al.*, 1998, *Culligan et al.*, 2004, 2006, *Knackstedt et al.*, 2004, *Lindquist*, 2002, *Lindquist et al.*, 2000, *Montemagno and Pyrak-Nolte*, 1995, *Wildenschild et al.*, 2002), laser confocal microscopy (*Fredrich et al.*, 1993, 1995, *Montoto et al.*, 1995), and serial sectioning imaging (*Vogel*, 1997). Translation of information from such techniques to a pore-network model can be done in two different ways; statistically representative models and topologically representative models. Statistically representative models capture the statistical distribution of pore size and connectivity and not the exact topology of the pores. They are usually in a structured lattice, and pore-bodies and pore throat distributions are determined so that on a REV scale they represent a real porous medium. In these statistically representative models, information acquired from imaging techniques is used to construct a network of pore bodies connected by pore throats. Pore bodies and pore throats are assigned regular geometrical shapes amenable to simple flow analysis. This translation of information, however, is not straight forward. Often many idealizations of the pore size, shape, and orientation are used. Topologically representative models are also based on detailed data provided by imaging techniques that include connectivity, position and orientation of pore bodies and pore throats. Thus more detailed simulations are possible using these topologically representative models. Therefore, it is desirable to come up with an approach that transforms the real geometry of the porous medium to a pore network with minimum loss of information, yet allows the computation of distribution of fluids within the network in a fairly simple way.

Dynamic pore-network models Among different computational methods for simulating transient behaviour of two-phase flow in porous media, dynamic pore-network modelling has been used extensively as an upscaling tool as it is relatively simple and computationally less demanding than the other computational methods. For example, Lattice Boltzmann (LB) method, which solves *Navier-Stokes* equation, is computationally too expensive and memory demanding compared with dynamic pore-network models, which usually solve a simplified form of the momentum equation such as *Stokes* equation. For instance, *Porter et al.* (2009) have recently used LB method to simulate air-water flow in glass beads with physical domain size of less than 500 pores, which was discretized into 207 × 207 × 166 voxels. At a flux of 0.00008 $muts^{-1}$ (mass unit per time step), approximately 50,000 ts were required to obtain only a 5% change in saturation, which took about 1.25 days to run on four amd64 CPU (2.8 GHz) machines in parallel. Roughly speaking, for their given specifications of domain and fluids, a full drainage simulation would take more than 100 days with a single processor. In another study, *Pan et al.* (2004) have stated that computational limitations are of great concern when applying LB simulations for multiphase porous medium systems, even using large-scale parallel computing. They could not afford to simulate domains with sizes close to an REV. The advantage of Lattice Boltzmann method, however, is that it can solve equations in an arbitrary pore space geometry and topology without simplification. Whereas, in pore-network modelling, the porous medium should be idealized to some simple geometries, such that essential features are adequately represented (*Celia et al.*, 1995). This idealization can lead to loss of geometrical and topological information. Also, information on temporal changes within a single pore in pore-network models is not as detailed as in Lattice Boltzmann simulations. Nevertheless, simplifications in pore-network modelling allow us to simulate much larger domains and with much less computational effort; this is a major advantage.

The first dynamic pore-network model reported in the literature was developed by *Koplik and Lasseter* (1985) who simulated dynamics of two-phase imbibition process in a two-dimensional unstructured pore-network model with circular cross sections. Later, several dynamic pore-network models were developed for various applications, such as simulating two-phase drainage (see e.g. *Aker et al.*, 1998a, *Al-Gharbi and Blunt*, 2005, *Dahle and Celia*, 1999, *Gielen et al.*, 2005, *Nordhaug et al.*, 2003), imbibition (see e.g. *Hughes and Blunt*, 2000, *Koplik and Lasseter*, 1985, *Nguyen et al.*, 2006, *Thompson*, 2002), evaporation (e.g. *Prat*, 2002), three-phase flow (see e.g. *Pereira et al.*, 1996) and ganglia movement (see e.g. *Constantinides and Payatakes*, 1996, *Dias and Payatakes*, 1986a,b). Of notable significance have been the models developed by *Payatakes* and co-workers (see e.g. *Constantinides and Payatakes*, 1996, *Dias and Payatakes*, 1986a,b), which can simulate ganglia displacement.

Dynamics of two-phase flow during drainage has been studied in several works. *Aker et al.* (1998a,b) and *Van der Marck et al.* (1997) studied pressure field evolution with time for a range of viscosity ratios and capillary numbers during drainage. Capillary number (C_a) is traditionally defined as the ratio of viscous forces of the invading phase to capillary forces ($\frac{\mu_{inv} q_{inv}}{\sigma^{nw}}$) and the viscosity ratio is the ratio of viscosity of invading fluid to that of the receding fluid. *Dahle and Celia* (1999) developed an IMPES-type algorithm to explicitly model the dynamics of fluid-fluid interfaces and also pressure field evolution with time for favorable viscosity ratios. *Singh and Mohanty* (2003) as well as *Al-Gharbi and Blunt* (2005) studied effect of capillary number on residual water saturation during drainage for constant injection rate at the boundaries. They also investigated the fractional flow behaviour for different flow rates as did *Knudsen and Hansen* (2002) and *Knudsen et al.* (2002). *Mogensen and Stenby* (1998) developed an angular-shape pore-network model to study dynamics of imbibition under the effect of flow rate, viscosity ratio, aspect ratio, and coordination number.

Thompson (2002) developed a dynamic pore network model to investigate imbibition process in fibrous material for water-air system (favorable viscosity ratio). He solved pressure fields for each phase separately, including local capillary pressure. However, his model failed to simulate capillary-dominated conditions. *Payatakes* and co-workers studied dynamics of oil ganglia as well as dependency of relative permeabilities curves on the capillary number and viscosity ratio in several publications (*Constantinides and Payatakes*, 1991, 1996, *Dias and Payatakes*, 1986a,b, *Payatakes*, 1982).

1.3 Book outline

This book can be considered in three parts:

- Review of dynamic pore-network models (Chapter 2).
- Development and application of various quasi-static pore-network models to analyze Equation 1.6 (Chapters 3,4,5).

- Development and application of a dynamic pore-network model with different geometries to analyze Equations 1.1-1.4 and 1.7(Chapters 6,7,8).

In Chapter 2 a comprehensive review of dynamic pore-network models for two-phase flow is presented. This review surveys different aspects of the models such as structure and geometry, computational algorithm, and applications. Dynamic pore-network models have been employed for many applications, mostly to gain insights into the physics of two-phase flow. They have been used for investigation of the effect of dynamic conditions on trapping, saturation profile, capillary pressure curve, relative permeability curve, disconnected phase displacement, dynamics of fluid-fluid interfacial area, etc.

In Chapter 3, a hypothetical structured regular pore-network model is developed to investigate Equation 1.6. In this regard, primary drainage and imbibition curves with many scanning drainage and imbibition curves are generated. The results are used to produce two surfaces as $a^{nw} = f(P^c, S^w)$ for drainage and imbibition, separately. The hysteresis between these surfaces can show the validity of Equation 1.6. This conjecture has been further investigated in Chapters 4 and 5.

In Chapter 4 a pore-network model for a high-porosity two-dimensional micromodel is developed. For development of the model, a pixel-based distance transform is employed to extract the medial pixels of the domain. Then P^c-S^w curves for primary drainage, scanning imbibition are produced to generate a^{nw}-P^c-S^w surfaces.

Chapter 5 presents a new approach for generating a pore-network model for granular media. This approach is based on the full recovery of shape-factor distribution for a given medium. The cross sections are developed based on irregular hyperbolic triangles or regular hyperbolic polygons. The curvature of cross section boundary facilitates a continuous recovery of shape factor, which provides very accurate representative pore network. The model has been validated against glass-bead experiments. There is a very good agreement between P^c-S^w and a^{nw}-S^w curves resulted from simulations and the experiments for drainage and imbibition processes. Finally, a^{nw}-P^c-S^w surfaces resulted from drainage and imbibition simulations are used to test the validity of Equation 1.6.

In Chapter 6 nonequilibrium effects in phase pressures difference (Equation 1.7), interfacial area (Equation 1.6) and its production rate (Equation 1.4 excluding the second term) have been analyzed. In this regard, a DYynamic POre-network SImulator for Two-phase flow (DYPOSIT) with cubic pore bodies and parallelepiped pore throats is developed. Numerical schemes employed in the model provide numerical stability of the model for unfavorable and favorable viscosity ratios as well as very small and large capillary numbers. This is a new issues, which has not been reported in the literature before.

To increase the consistency between the geometry of the pore bodies in the DYPOSIT model and a real porous medium, geometry of pore bodies has been changed to a truncated octahedron in Chapter 7. In this chapter, extensive simulations are implemented to study dependence of nonequilibrium capillarity coefficients (τ in Equation 1.7) on fluid viscosities (viscosity ratio and effective viscosity) as well as flow process (i.e drainage, imbibition).

Chapter 8 is a long-domain drainage simulation using DYPOSIT with cubic pore bodies. In this chapter we average the local information with a moving averaging window in time and space to analyze the behaviour of coefficients given in Equations 1.1 and 1.2. This is the first attempt to study the behaviour of these coefficients. Since the simulation domain is long enough, Equation 1.4 including its second term has been studied. The upscaled information have been compared along the previous studies or experiments.

Finally, Chapter 9 gives a short overview of the outcomes of each chapter.

Part I

Literature Review

Submitted as: Joekar-Niasar, V., Hassanizadeh – *"Dynamics of Two-Phase Flow in Porous Media; From Pore Scale to Darcy Scale"* journal of Critical Reviews in Environmental Science and Technology, 2010.

Chapter 2

Dynamics of Two-Phase Flow

> *One faces the future with one's past.*
>
> Pearl S. Buck, Writer

Abstract

In this literature survey, different aspects of dynamics of two-phase flow in porous media are discussed. This review is based on the results of developed dynamic pore-network models and their applications. Thus, those concepts of dynamics of two-phase systems are addressed that have been already discussed in the previous studies. Since it is not always possible to study different aspects of laboratory experiments, dynamic pore-network models developed to gain some insights into the process. This characteristic is the major advantage of pore-network models, which gives a better understanding of the physics of a process at pore scale as well as at the scale of representative elementary volume (REV). Dynamic pore-network models have been reviewed under different classifications; structure, computational algorithm and local rules and applications.

2.1 Introduction

To gain a better insight into multiphase flow processes in porous media, various theoretical, computational and experimental methodologies can be applied. Despite the enormous value of experimental work, often it cannot be used to its full potential due to several limitations such as complexity of processes, difficulty of measuring certain quantities, uncertainty in results of measurements, etc. Moreover, experiments are commonly expensive and time-consuming. Thus, theoretical and computational approaches can be used as complementary, and sometimes as a substitute, to gain a more detailed understanding of processes. They can also be used to aid with a more effective design of experiments (see e.g. *Joekar-Niasar et al.*, 2009).

In general, computational methods applied for studying two-phase flow systems can be classified into conventional continuum-scale numerical models and pore-scale models. In the latter approach, one attempts to represent pore-scale geometry and topology of the medium and to model pore-scale processes. Main advantage of pore-scale models is the possibility to define local variables and simulate local processes that lie at the base of continuum-scale observations and descriptions.

Pore-network modelling has been used extensively in a large variety of fields such as hydrology, petroleum engineering, chemical engineering, mechanical engineering, reservoir engineering, and physics, as an investigative tool to study macro-scale and micro-scale processes in porous media (see reviews by *Blunt*, 2001, *Celia et al.*, 1995, *Dullien*, 1992).

Pore-scale models may be subdivided into five different groups: pore-network models (e.g. *Blunt et al.*, 2002, *Fatt*, 1956, *Held and Celia*, 2001, *Joekar-Niasar et al.*, 2008, 2009, *Nordhaug et al.*, 2003, *Payatakes*, 1982, *Payatakes et al.*, 1980, *Reeves and Celia*, 1996, *Valvatne and Blunt*, 2004), lattice- Boltzmann models (e.g. *Knutson et al.*, 2001, *Martys and Hagedorn*, 2002), smoothed particle hydrodynamics approach (e.g. *Liu et al.*, 2006, *Tartakovsky and Meakin*, 2005), level-set models (e.g. *Prodanović and Bryant*, 2006), and percolation models (e.g. *Wilkinson*, 1984). In this review, we focus on pore-network models.

From the physical point of view, pore-network models can be divided into two major classes: quasi-static pore-network models and dynamic pore-network models. Quasi-static pore-network models are used for studying systems under no-flow conditions in multi-phase porous media. Dynamic pore-network models, which are more complex, are used for studying transient phenomena in multi-phase flow systems. Despite the fact that numerous dynamic pore-network models have been proposed over the years, the quasi-static models have remained dominant, largely because of computational tractability. In particular, the extreme nonlinearity at the pore-scale causes severe problems of stability in dynamic pore-network models. In spite of this fact, these models can be very efficient in investigation of dynamics of multi-phase flow at pore-scale.

Dynamic pore-network models have been mostly developed for studying general issues in dynamics of two-phase flow in porous media. But, they have been used for specific applications too. For instance, *Figus et al.* (1999) and *Prat* (2007) studied drying process in porous media using pore-network models. Also very few studies of dynamics of three-phase flow in porous media exist (e.g. *Pereira et al.*, 1996) .

In this review, we introduce and discuss main aspects of dynamic pore-network modelling, including computational formulations for two-phase flow simulations, their advantages and disadvantages, network structures, geometrical and topological properties. Furthermore, various applications of these models, which give new insights into the physics of two-phase flow are discussed. These applications include effect of dynamic parameters on trapping, saturation profile, relative permeability curves, pressure field evolution, disconnected flow, etc.

2.2 Quasi-static vs. dynamic pore-network models

Under dynamic conditions in multi-phase flow, there is a competition between viscous forces and capillary forces. To quantify this competition, a dimensionless number, called capillary number (C_a), is introduced. Capillary number is commonly defined as the ratio of dynamic forces to capillary forces. This is, however, not a suitable definition as such a number would decrease for increasing capillary effects! This would be clearly counter intuitive as we should expect capillary effect to be more important when capillary number is large. A more logical definition is to take the ratio of capillary forces to viscous forces (see e.g. *Manthey et al.*, 2008). Nevertheless, in order to keep the link to the previous works, we follow the traditional definition, namely the ratio of viscous forces to capillary forces:

$$C_a = \frac{\mu_{inv.} q_{inv.}}{\sigma^{nw}} \tag{2.1}$$

Here, $\mu_{inv.}$ $[ML^{-1}T^{-1}]$ is viscosity of the invading phase, $q_{inv.}[LT^{-1}]$ is total Darcy velocity (volume flowing per unit area per unit time) of the invading phase and σ^{nw} is the interfacial tension $[MT^{-2}]$. If C_a is zero or very small, capillary forces dominate. For studying capillary-dominated flow, invasion-percolation models and quasi-static pore-network models have been used extensively. These models are based on the fact that the displacement of fluids is controlled by entry capillary pressure of individual pores. Quasi-static pore-network models can simulate equilibrium states of drainage and imbibition processes only. Flow conditions between equilibrium states are not modelled. For these models to be applicable, it is essential to remain close to equilibrium. Therefore, incremental changes in global pressure differences should be applied to go from one equilibrium to another equilibrium state. The comparison between quasi-static pore-network models and experiments show that these models can be used successfully for predictive purposes (e.g. *Blunt et al.*, 2002, *Joekar-Niasar et al.*, 2009, *Lerdahl et al.*, 2000, *Øren et al.*, 1998).

Under dynamic conditions, both viscous and capillary forces have to be included at the pore scale. Invasion at the pore-scale is determined by the entry capillary pressure of network elements (e.g. pore throats) and time-rate of invasion is determined by local viscous and capillary forces. As a result, dynamic models require much more complicated coding, robust solutions methods, and efficient algorithms. Problems of numerical convergence and instabilities may cause major difficulties. Also, due to the highly non-linear nature of the coupling between viscous forces and capillary forces, simulations are much more time-consuming and memory-demanding (*Al-Gharbi and Blunt*, 2005).

2.3 Model structure

Interstitial spaces in granular porous media are typically very irregular in shape and size. At the pore-scale, there are larger void spaces as well as bottlenecks. To mimic the geometrical features of these interstitial spaces, pore-network models typically consist of pore bodies (larger voids) connected to each other by pore throats (narrow voids). However, the geometry of void spaces is not the only important factor to be considered in a representing a porous medium. Topology of soil (i.e. how voids are connected to each other) is another important parameter that should be considered in the generation of networks.

2.3.1 Network topology

The simplest network structure is a two-dimensional or three-dimensional lattice with uniform spacing; we refer to this as a *uniform lattice network*. In such a network, pore bodies are located at the lattice nodes, which are all equally spaced, and pore throats are lined up along the lattice coordinates. The number of pore throats connected to a pore body is called *coordination number*. In a uniform lattice network, the coordination number is equal to four, for a two-dimensional network, and six, for a three-dimensional network. In a real porous medium, the centers of large pore spaces are not located on lattice points. Also, the number of pore throats connected to large pores is not the same for all pores. Therefore, unstructured pore-network models have been developed to mimic this feature of a real porous medium.

Based on these two characteristics of topology (i.e. center of void spaces and coordination number), pore-network models can be classified into four groups: lattice isotropic, lattice anisotropic, unstructured isotropic, and unstructured anisotropic networks. Up to now, most dynamic pore-network models have had lattice isotropic structures with a uniform coordination number. Also, almost all dynamic pore-network models, except those developed by *King* (1987), *Blunt and King* (1991) and *Koplik and Lasseter* (1985), have had lattice structures, i.e centers of the pore bodies are located in a lattice frame work. *King* (1987) and *Blunt and King* (1991) developed unstructured isotropic networks, and only in models developed by *Koplik and Lasseter* (1985), and *Mogensen and Stenby* (1998) coordination number was variable. *Mogensen and Stenby* (1998) developed a model with a variable coordination number up to a maximum of 26. Geostatistically equivalent networks, which are developed based on topological and geometrical data can be structured anisotropic (e.g. *Raoof*

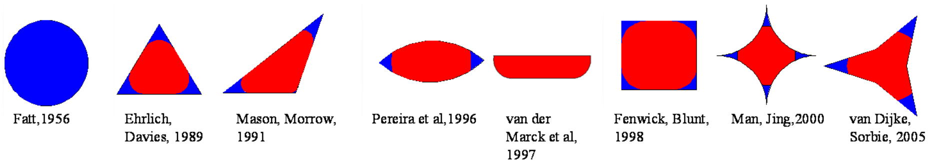

Figure 2.1: *Various cross-sectional shapes used for pore throats in pore-network models*

and Hassanizadeh, 2009) or unstructured and anisotropic. However, they have not be used for dynamic simulation of two-phase flow.

2.3.2 Network geometry

Network geometry is related to the geometrical shape of pore bodies and also cross sections of pore throats. Commonly, pore bodies are assumed to be cubic or spherical in shape. Exceptionally *Joekar-Niasar and Hassanizadeh* (2010) presented the pore bodies as truncated octahedrons. For pore throats, however, a variety of geometrical shapes for the cross sections have been considered, as shown in Figure 2.1. Using such a variety of cross sections for pore throats is because of two facts. First, some pore-network models have been developed for simulating specific experiments, generally micro-model experiments (e.g. *Van der Marck et al.*, 1997). Second, an angular cross section allows for the existence of corner flow along the edges. This feature can allow simulating simultaneous flow of two phases within a pore throat. Obviously, corner flow in a circular cross section is not possible. In a real porous medium, the wetting phase usually fills the corners and grooves, and the corner flow has a significant effect on flow mechanism at pore-scale especially during imbibition. Existence of corner flow will allow phase continuity for the two fluids in a pore throat. Thus, the governing equation for the pressure field will be different from that for circular cross sections.

Many of dynamic pore-network models have pore throats with circular cross sections (e.g. *Dias and Payatakes*, 1986a,b, *Koplik and Lasseter*, 1985), but there are few models with angular cross sections such as *Al-Gharbi and Blunt* (2005) who have assumed triangular cross sections. Also, *Hughes and Blunt* (2000), *Joekar-Niasar et al.* (2010a), *Mogensen and Stenby* (1998), *Singh and Mohanty* (2003) have used cubic pore bodies, and parallelepiped pore throats.

There are some other pore-network models, which do not explicitly consider pore bodies and pore throats. In these models, it is assumed that pore elements have varying cross sections; the narrowest part is located in the middle and it diverges towards both ends, which may be considered to play the role of a pore body (e.g.

Aker et al., 1998a,b, *Al-Gharbi and Blunt*, 2005, *Knudsen and Hansen*, 2002, *Knudsen et al.*, 2002, *Valvanides et al.*, 1998). But, no specific geometry or configuration has been assumed at the connection point of these pore elements. In this paper, these pore elements are referred to as "*composite pores*". Another important geometrical parameter is the ratio of pore body diameter to pore throat diameter, referred to as "aspect ratio". This parameter plays an important role in snap-off, which can influence trapping during imbibition.

2.4 Computational algorithms

Continuum-scale equations of two-phase flow in porous media are usually solved for the pressure and the saturation of wetting or nonwetting phases. Ignoring gravity effect, the following system of equations for a rigid porous medium and incompressible immiscible nonreactive fluids should be solved:

$$\begin{aligned} \phi\frac{\partial S^\alpha}{\partial t} &= -\nabla\cdot\mathbf{u}^\alpha, \quad \alpha=n,w \\ \mathbf{u}^\alpha &= -\frac{1}{\mu^\alpha}k^\alpha\mathbf{K}\nabla P^\alpha, \quad \alpha=n,w \\ S^w+S^n &= 1 \\ P^c &= P^n-P^w=f(S^w) \end{aligned} \tag{2.2}$$

where, superscripts *n* and *w* denote nonwetting and wetting phases, respectively. ϕ is the porosity, μ^α is the viscosity of phase α, S^α is saturation of phase α, $\mathbf{u}^\alpha$ is the velocity of phase α, **K** is the intrinsic permeability tensor, k^α is the relative permeability of phase α, P^α is the pressure of phase α, P^c is the capillary pressure, and superscripts w and n refer to the wetting and nonwetting phases, respectively. Obviously, these equations do not apply at the pore scale. A different, but somewhat similar, set of equations need to be formulated at the pore scale. The form of these equations depends on how the fluid pressure fields are handled. Two general approaches exist: single-pressure and two-pressure algorithms, which are described in detail below.

2.4.1 Single-pressure algorithm

In this algorithm, regardless of the occupancy of pore bodies by the two fluids, a single fluid pressure is assigned to each pore body. This single-pressure algorithm is generally based on one of following three assumptions:

i) It is assumed that each pore body or pore throat can be occupied by only one fluid at any given time. This is generally applied to networks with circular cross sections (e.g. *Aker et al.*, 1998a,b, *Van der Marck et al.*, 1997).

ii) It is assumed that both fluids can be present within a pore body but not within a pore throat. Also, a major assumption is made that the local capillary pressure in pore bodies is negligible. Therefore, to each pore a single pressure is assigned (e.g. *Gielen et al.*, 2005).

iii) It is assumed that pore bodies and pore throats may be occupied by the both fluids. But then, an equivalent fluid is defined; with an equivalent single pressure assigned to each pore body and an equivalent conductivity assigned to each pore throat (e.g. *Al-Gharbi and Blunt*, 2005, *Mogensen and Stenby*, 1998).

In all three cases, the volumetric fluxes through pore throats is calculated by means of *Washburn* equation. The complete system of the equations using single-pressure algorithm may be written as follows for a pore body i connected to an other pore body j by a pore throat ij:

$$
\begin{aligned}
V_i \frac{\partial S_i^w}{\partial t} + \sum_{j=1}^{N_i} Q_{ij} S_{ij}^w &= 0 \\
Q_{ij} &= K_{ij} \Delta_{ij} && (2.3) \\
S_{ij}^w + S_{ij}^n &= 1 \\
S_i^w + S_i^n &= 1 \\
\Delta_{ij} &= f(P_i, P_j, P_{ij}^c, \text{fluids configurations in pore throat } ij) \\
P_{ij}^c &= f(r_{ij}) && (2.4)
\end{aligned}
$$

where, Q_{ij}^w is the wetting volumetric flux from pore body *i* to pore body *j*, P_{ij}^c $\left[ML^{-1}T^{-2}\right]$ is the entry capillary pressure of pore throat *ij*, r_{ij} is the radius of pore throat *ij*, K_{ij} $\left[M^{-1}L^4T\right]$ is the equivalent hydraulic conductivity as a function of the pore throat radius, pore throat length and fluid viscosities. An important issue in this algorithm is how the equivalent pressure drop, Δ_{ij}, is related to the capillary forces in pore throat *ij*. Two different formulations are proposed by *Koplik and Lasseter* (1985) and *Van der Marck et al.* (1997), discussed here.

Koplik and Lasseter (1985) considered various combinations of fluid occupancies in pore bodies i and j, as shown in Table 2.1. They assumed that up to two interfaces may exist in a pore throat ij. Based on the 8 possibilities considered in Table 2.1, a general form is proposed, which covers all the options using saturations at pore bodies.

Koplik and Lasseter (1985) have suggested the following expression for Δ_{ij} and

Table 2.1: *Defining Δ_{ij} (Equation 2.4) based on fluid configurations in two neighboring pore bodies and a pore throat (Koplik and Lasseter, 1985)*

Case	Fluid occupancy in pore body *i*	Fluid occupancy in pore body *j*	Δ_{ij}
1	nonwetting	nonwetting	$P_i^n - P_j^n$
2	wetting	wetting	$P_i^w - P_j^w$ $=P_i^n - P_j^n - P_i^c + P_j^c$
3	nonwetting	wetting	$P_i^n - P_j^w - P_{ij}^c$ $=P_i^n - P_j^n + P_j^c - P_{ij}^c$
4	wetting	nonwetting	$P_i^w - P_j^n + P_{ij}^c$ $=P_i^n - P_j^n - P_i^c + P_{ij}^c$
5	meniscus at pore, nonwetting	nonwetting	$P_i^n - P_j^n$
6	meniscus at pore, wetting	nonwetting	$P_i^w - P_j^n + P_i^c$ $=P_i^n - P_j^n$
7	wetting	meniscus at pore, nonwetting	$P_i^w - P_j^n + P_j^c$ $=P_i^n - P_j^n - P_i^c + P_j^c$
8	wetting	meniscus at pore, wetting	$P_i^w - P_j^w$ $=P_i^n - P_j^n - P_i^c + P_j^c$
	General form	$\Delta_{ij}=P_i^n - P_j^n + S_i^w(P_{ij}^c - P_i^c) - S_j^w(P_{ij}^c - P_j^c)$	

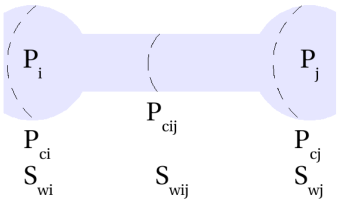

Figure 2.2: *Schematic presentation of pore bodies i and j and pore throat ij and corresponding capillary pressures and saturations. Based on the occupancy of the pore bodies and interface location, pressure drop rules have been defined in Table 2.1.*

have solved the system of Equations 2.4.

$$\Delta_{ij} = P_i^n - P_j^n + S_i^w(P_{ij}^c - P_i^c) - S_j^w(P_{ij}^c - P_j^c), \tag{2.5}$$

in which S_i^w and S_j^w are the wetting saturations in pore bodies *i* and *j*.

Van der Marck et al. (1997) modelled a system similar to what *Koplik and Lasseter* (1985) used but for drainage simulations. They assumed pore throats to have a negligible volume compared with pore bodies. Therefore, the interface was not tracked within the pore throat (i.e. spontaneous filling of a pore throat at the moment of invasion was assumed). *Van der Marck et al.* (1997) also assumed that up to two interfaces can exist in a single pore throat, one at each end. They included the gravity effects in the pore-network model. For a pore throat connecting pore body *i* to pore body *j*, and filled with fluid density ρ_{ij} $[ML^{-3}]$, a variable χ_{ij} was defined as follows:

$$\chi_{ij} = P_i - P_j - \rho_{ij}\mathbf{g}\left(\mathbf{x}_i - \mathbf{x}_j\right) \tag{2.6}$$

One should note that since each pore throat can be filled simultaneously with only one fluid, ρ_{ij} is the density of the fluid filling pore throat ij. Assuming a dummy variable x, *Van der Marck et al.* (1997) also defined a step-wise function, $\theta[x]$, as follows.

$$\theta[x] = \begin{cases} 1 & \text{if } x > 0 \\ 0 & \text{otherwise} \end{cases} \tag{2.7}$$

Considering definitions of χ_{ij} and $\theta[x]$, Δ_{ij} in Equation 2.4 has been defined for different cases as shown in Table 2.2. The entry capillary pressure for pore throat *ij* has been denoted by $P^c_{e_{ij}}$.

Table 2.2: *Defining Δ_{ij} based on fluid configurations in two neighboring pore bodies and a pore throat (Van der Marck et al., 1997)*

Fluid occupancy in pore body *i*	Fluid occupancy in pore body *j*	Δ_{ij}
nonwetting	nonwetting	χ_{ij}
wetting	wetting	χ_{ij}
nonwetting	wetting	$\theta\left[\chi_{ij} - P^e_{ij}\right]\left(\chi_{ij} - P^c_{e_{ij}}\right) + \theta\left[\chi_{ij}\right]\chi_{ij}$
wetting	nonwetting	$\theta\left[\chi_{ji} - P^c_{e_{ij}}\right]\left(\chi_{ij} + P^c_{e_{ij}}\right) + \theta\left[\chi_{ij}\right]\chi_{ij}$
meniscus at pore, nonwetting	meniscus at pore nonwetting	$\theta\left[\chi_{ij} - P^c_{e_{ij}}\right]\left(\chi_{ij} - P^c_{e_{ij}}\right) + \theta\left[\chi_{ji} - P^c_{e_{ij}}\right]\left(\chi_{ij} + P^c_{e_{ij}}\right)$

A similar formulation was also used by *Dias and Payatakes* (1986a,b), *Vizika et al.* (1994) and *Knudsen et al.* (2002) with some modifications. Application of Δ_{ij} formulations in Equation 2.4 results in a nonlinear system of equations that has been solved with a combination of an over-relaxation and a dampened Newton-Raphson methods.

Obviously, corner flow is not included in the original Washburn equation (single-pressure approach). Nevertheless, this equation has been modified and used for angular cross sections, using the concept of equivalent phase described in situation (iii) (page 17) above. The equivalent conductivity of a pore throat K^{eq}_{ij} is defined as the average of conductivities of phases using the rule of equivalent resistor for electrical resistor circuits. Thus, instead of solving for two pressure fields, one can solve for a single pressure field (see e.g. *Al-Gharbi and Blunt*, 2005, *Bravo et al.*, 2007, *Mogensen and Stenby*, 1998).

The advantage of single-pressure approach is that it simplifies the problem significantly, and it can reduce computational effort. But, it has the limitation that it can not be used for angular cross sections properly. *Al-Gharbi and Blunt* (2005) have shown that single-pressure approach in angular cross sections can lead to inconsistent results in fluids occupancy in the network. If we use the same contact angle in static and dynamic simulations, one would expect that during drainage the same equilibrium fluid occupancy to be obtained from a quasi-static pore-network model as well as a dynamic pore-network model for the same boundary conditions. However, *Al-Gharbi and Blunt* (2005) have shown that when employing the concept of equivalent phase pressure, snapshots of fluid occupancy obtained from quasi-static and dynamic pore-network models with the same boundary conditions are not the same.

2.4.2 Two-pressure algorithm

In this algorithm, when a pore body is filled with two fluids, each fluid is assumed to have its own pressure. Therefore, a local capillary pressure exists in a pore body. The complete system of the equations for the two-pressure algorithm may be written as follows:

$$
\begin{aligned}
V_i \frac{\partial S_i^\alpha}{\partial t} + \sum_{j=1}^{N_i} Q_{ij}^\alpha &= 0, \quad \alpha = n, w \\
Q_{ij}^\alpha &= K_{ij}^\alpha \left(P_i^\alpha - P_j^\alpha \right) \qquad (2.8) \\
S_i^w + S_i^n &= 1 \\
P_i^c &= P_i^n - P_i^w = f(S_i^w) \\
K_{ij}^\alpha &= f(P_{ij}^c), \quad \alpha = n, w \qquad (2.9)
\end{aligned}
$$

where K_{ij}^α is the hydraulic conductivity for phase α, and V_i is the volume of pore body i. This formulation has been used initially by *Thompson* (2002) to investigate imbibition process in fibrous materials for water-air system (favorable viscosity ratio). He solved pressure fields for each phase separately, including local capillary pressure. The local capillary pressure in each pore body was defined through the local interface curvature, corresponding to a given local saturation. This formulation provides the possibility to include mechanisms related to the variations of local capillary pressure (such as snap-off, counter-current flow) in simulations. In addition, numerical formulation of this approach is easier to implement compared with the single-pressure approach. However, similar to Equations set 2.4, in capillary-dominated regimes, this equation shows a highly nonlinear behavior that should be treated carefully. *Thompson* (2002) stated that he could not find a good agreement between results of a slow dynamic simulation and a quasi-static simulation. Also, the model could not be used for very small capillary numbers. Later on, *Joekar-Niasar and Hassanizadeh* (2010), *Joekar-Niasar et al.* (2010a) used two-pressure algorithm with some numerical improvements in pressure solver. They investigated non-equilibrium effects in capillary pressure and fluid-fluid interfacial area.

2.4.3 Numerical difficulties

When capillary forces are comparable with viscous forces, there is a competition between them that creates high nonlinearities in pressure field at pore scale. Handling these nonlinearities in simulations is not trivial and equations should be treated carefully, especially in capillary-dominated flow.

The numerical problem in dynamic pore-network modelling was reported for the first time by *Koplik and Lasseter* (1985) who observed that saturations in two neighboring pore bodies were oscillating between 1 and 0 continuously. They referred to this as "capillary pinning" problem. From Equations set 2.4, the volume conservation equation for pore body i can be written as follows:

$$\sum_{j=1}^{N_i}[K_{ij}\Delta_{ij}] = 0$$
$$\Delta_{ij} = P_i^n - P_j^n + S_i^w(P_{ij}^c - P_i^c) - S_j^w(P_{ij}^c - P_j^c) \tag{2.10}$$

Writing this equations for all pore bodies results in a system of nonlinear equations as follows:

$$\begin{aligned} A(S_i^w, S_j^w)\mathbf{P}^n &= \mathbf{B}(S_i^w, S_j^w, P_i^c, P_j^c, P_{ij}^c) \\ A(S_i^w, S_j^w) &= f(K_{ij}(S_i^w, S_j^w)) \end{aligned} \tag{2.11}$$

in which, A is a banded matrix whose elements are functions of the pore throats conductivities. In the above equation, $\mathbf{P}^n$ represent vectors of pressure at pore bodies and $\mathbf{B}$ is a function of capillary pressure and saturation at pore bodies. As it can be observed, $\mathbf{P}^n$ and $\mathbf{B}$ are both functions of local fluid configurations. A similar linear system of equations is resulted from Equations set 2.8. If a decoupled scheme is used to solve the equations system (Equations set 2.4 or 2.8) first $\mathbf{B}$ should be calculated for a given fluid configuration. Then, the pressure field should be solved. Knowing the pressure field (**P**), fluxes at each pore body will be calculated. Finally, saturation can be updated explicitly.

The decoupled scheme does not lead to a serious problem for viscous-dominated flow (i.e. large capillary numbers). At low flow rates, local capillary forces are comparable with viscous forces in which case A, **B** and consequently $\mathbf{P}^n$ will be highly dependent on local fluid configurations. The decoupling procedure will cause oscillation of saturations between two neighboring pores, which was refered to as "capillary pinning" earlier.

To overcome this problem, *Koplik and Lasseter* (1985) linearized the system using a constrained set of equations. For linearization, they defined a criterion to check whether local saturation in a pore body oscillated from 1 to 0 in three successive iterations. If this condition occurred, a no-flow condition was assigned to that pore body (dead-end pore body). Then, the pressure field was solved again. At each time step, validity of the local no-flow pore body (and pore throat) was also checked. They defined the validity criterion using the Δ_{ij} function defined in Table 2.4.1. Assigning a no-flow restriction to a pore throat forces Δ_{ij} to be equal to zero. Thus, saturation of the no-flow pore body (S_j^w) can be calculated in terms of the other variables and parameters as follows: $S_j^w = \frac{P_i^n - P_j^n + S_i^w(P_{ij}^c - P_i^c)}{P_{ij}^c - P_j^c}$. If S_j^w is not between 0 and 1 (> 1 or < 0), the no-flow criterion is violated and it will be removed. Obviously, this approach for the linearization of the system is too complicated and time-consuming, since in many iterations a linear equation should be solved to calculate the pressure to check validity or invalidity of the no-flow criterion.

"Capillary pinning" problem was also observed in other pore-network models, where no geometry was assigned to the connections of pore throats (i.e. no pore bodies were defined) as in *Dias and Payatakes* (1986a), *Aker et al.* (1998a), *Aker et al.* (1998b), and *Knudsen et al.* (2002). When an interface moving in a pore throat reaches a connection point, new interfaces should be created in the connecting pore throats (see Figure 2.3). So, when a meniscus reaches the end of a pore throat (position 1), it is removed and three new menisci are created at position (δ) in the neighboring pore throats (position 2). When a new interface is created, a capillary pressure is assigned to it. If capillary forces are comparable with viscous forces, they can cause the interface to move back and forth in successive time steps. To overcome this problem, a part of all pore throat denoted by δ in Figure 2.3) is defined as the "pore body region". They forced the capillary pressure in a pore throat to change from P_{ij}^c to zero in the connection points of pore throat. This change of capillary pressure occurs in the range shown by δ. This region prevents immediate disappearing of menisci at position 2 and moving back to the initial position 1 in tubes (Figure 2.3). *Dias and Payatakes* (1986a,b) have assumed to have a $delta_{ij}$ equal to 15% of the total length of pore throat ij. *Aker et al.* (1998a,b) and *Løvoll et al.* (2005) assumed that δ_{ij}

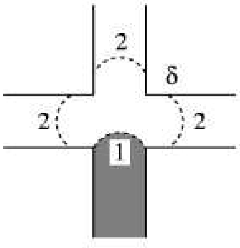

Figure 2.3: *The motion of the menisci at a node. The non-wetting fluid (shaded) reaches the end of the tube (position 1) and moves a distance δ into the neighboring tubes (position 2). A proper time is recorded due to the small movement(Aker et al., 1998a)*

has a length equal to 1-5% of the length of pore throat ij.

In two-pressure algorithm, *Joekar-Niasar and Hassanizadeh* (2010), *Joekar-Niasar et al.* (2010a) proposed a semi-implicit saturation update, instead of explicit saturation update.

$$V_i \frac{(S_i^w)^{k+1} - (S_i^w)^k}{\Delta t} - \sum_{j=1}^{N_i} \left(\frac{K_{ij}^n}{K_{ij}^{tot}} Q_{ij}^{tot} + \frac{K_{ij}^w K_{ij}^n}{K_{ij}^{tot}} \frac{\partial P_{ij}^c}{\partial S_{ij}^w} \left((S_i^w)^{k+1} - (S_j^w)^{k+1} \right) \right) = 0 \qquad (2.12)$$

This formulation includes a term related to viscous forces and another term related to capillary forces. They showed that it worked successfully for both unfavorable and favorable viscosity ratios for very small and large capillary numbers. Based on this formulation they could model very small capillary numbers for drainage and they found a precise agreement between quasi-static and dynamic simulations.

2.4.4 Boundary conditions

Boundary conditions commonly considered in dynamic pore-network models are either constant pressure (*Dirichlet*) or constant flux. Implementing constant pressures at boundaries is numerically quite straight forward. However, since pore-network models have been mostly used to study two-phase flow for prescribed capillary numbers, constant flux boundary conditions have been applied more frequently. Applying constant flow rate in pore-network modelling is not trivial. At pore-scale, pressure field is sensitive to the local capillary pressure and this causes small fluctuations in flow rate in successive time steps. The constant flux boundary conditions has been implemented in various ways. A common approach is what

Al-Gharbi and Blunt (2005) have used. They specified a constant injection rate at the upstream boundary and a constant pressure at the downstream boundary. Although at each time step, fluid configuration and consequently pressure field might change, they assumed that the change in pressure drop required to maintain a constant injection rate between two consecutive time steps is small. But, it seems that this assumption can not be valid for their network where the lattice size is only 9×9 nodes. They selected a small time step to calculate the next pressure step and finally the discharge rate. *Vizika et al.* (1994) considered very narrow (high-resistivity) pore throats at the downstream boundary, and applied a constant flux at the upstream boundary. Applying narrow pore throats at downstream boundary can regulate the flux only during drainage. During imbibition, applying very fine pore throats at downstream can increase probability of the snap-off at the boundary that will result in large amount of trapped nonwetting fluid.

Aker et al. (1998b) implemented constant flux at boundaries, differently. Considering Washburn equation, they suggested that for two-phase flow, total flux (Q) over the whole domain may be written in terms of the global pressure difference and capillary pressure:

$$Q = f_1(\Delta P) + f_2(P^c) \tag{2.13}$$

where ΔP is the difference between the pressures at upstream and downstream boundaries. Assuming a linear relationship, *Aker et al.* (1998b) suggested the following equation:

$$Q(S^w) = A(S^w)\Delta P + B(S^w, P^c) \tag{2.14}$$

Clearly, $A(S^w)$ and $B(S^w, P^c)$ depend on two-phase fluid configurations. Thus, to calculate $A(S^w)$ and $B(S^w, P^c)$ for a given fluid saturation (S^w), two equations are required. For a given fluid configuration, two different pressure drops can be imposed at the boundaries. Thus, two different flux rates can be calculated, which both should be consistent with Equation 2.14. So, two equations are resulted. By solving these two equations, $A(S^w)$ and $B(S^w, P^c)$ can be calculated. Knowing parameters $A(S^w)$ and $B(S^w, P^c)$, and knowing the desired injection rate (Q), proper pressure drop can be estimated. Since, $A(S^w)$ and $B(S^w, P^c)$ are dependent on the fluid configuration, they should be calculated at each time step, with the change of fluid configuration. This makes the problem computationally too expensive.

To investigate steady-state flow conditions, *Constantinides and Payatakes* (1996) and later *Knudsen and Hansen* (2002), *Knudsen et al.* (2002) defined periodic boundary conditions for saturation at inlet and outlet. It means that the amount of $\alpha-$phase that exit the domain, is introduced from the corresponding pore throat at inlet. Side boundaries were assumed to be periodic in saturation and pressure field as well. Thus, saturation of the whole domain does not change with time, and it is possible to simulate the steady-state conditions. However, to prevent simulation results biased by initial conditions, simulations should be continued so that the average values of pressure becomes constant.

2.4.5 Geometry and conductivity assumptions

Assumptions made on the pore-network structure can change complexity of computations. In particular, assumptions are made regarding the volume as well as resistance of pore elements. It is computationally very expensive to track the interfaces within pore throats and pore bodies. In many models (see e.g. *Blunt and King*, 1991, *Blunt et al.*, 1992, *Bravo et al.*, 2007, *Gielen et al.*, 2004, 2005, *Koplik and Lasseter*, 1985, *Touboul et al.*, 1987, *Van der Marck et al.*, 1997), it is assumed that the volume of pore throats is negligible compared to the volume of pore bodies. At the same time, resistance of pore bodies has been considered to be negligible compared to that of pore throats. In some models, since no specific geometry was assigned to the connections (no pore body), volume and resistance were both assigned to the pore throats (e.g. *Aker et al.*, 1998a,b, *Dahle and Celia*, 1999, *Knudsen and Hansen*, 2002, *Knudsen et al.*, 2002, *Løvoll et al.*, 2005). If a pore (body or throat) is considered to have resistance and volume at the same time, the fluid-fluid interfaces should be tracked inside that pore (body or throat), which is computationally expensive. The only case, where volume and resistance were assigned to both pore bodies and pore throats is the work of *Mogensen and Stenby* (1998). Using the harmonic averaging they calculated the effective resistance of a pore throat and connected pore bodies. However, the advantages of this model compared to the other ones have not been discussed.

2.4.6 Local rules

In addition to the general equations required for simulating two-phase flow in a pore-network model, some local rules should be defined too. General local rules usually needed for the development of a pore-network model are as follows:

- *Entry capillary pressure*: Nowetting phase can invade a pore-throat only when the local capillary pressure is larger than the entry capillary pressure of that pore throat. Entry capillary pressure can be calculated by writing balance of forces for a specific cross section (geometry) and based on contact angle and viscosity ratio. The most common approach for calculating entry capillary pressure is the MS-P (*Mayer-Stowe-Princen*) method suggested by *Ma et al.* (1996), *Mayer and Stowe* (1965), *Princen* (1969a,b, 1970), which is based on balance of forces for contact lines. Using this method, entry capillary pressures for different cross sections such as irregular triangular (*Mason and Morrow*, 1991), square (*Fenwick and Blunt*, 1998, *Joekar-Niasar et al.*, 2009, 2010a), start-shape (*van Dijke and Sorbie*, 2006), and hyperbolic polygonal (*Joekar-Niasar et al.*, 2010b) have been calculated.

- *Local conductivities*: Assuming Poiseuille equation to be valid in a pore element, its conductivity can be determined in terms of its geometry (cross section, length) and fluid property. In the case of pores with angular cross section, the conductivity for each phase will be a function of local saturation and thus local capillary pressure. Solving Navier-Stokes equation in pore throats with triangular and square cross sections, some algebraic equations for conductivities have been suggested (*Patzek and Silin*, 2001, *Ransohoff and Radke*, 1988, *Zhou et al.*, 1997). As mentioned earlier, these equations are a function of local capillary pressure, saturation, and pore geometry.

- *Snap-off*: The snap-off phenomenon occurs when the wetting phase pinches off the nonwetting phase (Figure 2.5 and 2.6). This mechanism was introduced by *Roof* (1970) and similar to entry capillary pressure, it is a function of pore geometry, contact angle, and interfacial tension. More detailed explanations are given in the next section.

- *Trapping*: If the receding phase forms clusters that are disconnected from the moving part (which is commonly connected to its boundary reservoir), it is considered to be trapped. In a water-wet porous medium, trapping of the nonwetting phase during imbibition is more important than during drainage process, since the wetting phase can be connected to its boundary through the corners. To find whether local disconnection affect larger groups of pores to get disconnected from the boundary, a search algorithm should be formulated (*Al-Futaisi and Patzek*, 2003).

2.5 Effective fluid and structural parameters

System parameters in two-phase flow are related to topology and geometry of pore-network as well as fluid properties. These parameters include capillary number (C_a), aspect ratio (pore body diameter/pore throat diameter), viscosity ratio (M defined as a ratio of viscosity of invading fluid to receding one) and coordination number. A viscosity ratio is referred to as "favorable" if it is larger than one and as "unfavorable" if it is smaller than one.

As defined by Equation 2.1, capillary number is the ratio of viscous forces to capillary forces. In addition to capillary number, viscosity ratio is another important

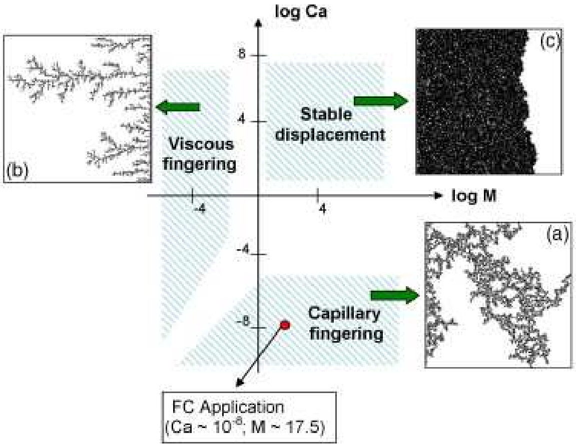

Figure 2.4: *Schematic presentation of flow pattern under different capillary numbers (C_a) and viscosity ratios (M) based on Lenormand (1990), Lenormand et al. (1988), courtesy of Sinha and Wang (2007)*

system parameter, which controls flow pattern and trapping of fluids. *Lenormand et al.* (1988) defined a phase diagram, which shows flow pattern under different capillary numbers and viscosity ratios, as shown in Figure 2.4. For favorable viscosity ratios, two flow patterns are possible depending on capillary number. If capillary number is very small (Figure 2.4a) capillary fingering is observed; and if capillary number is large enough (Figure 2.4c) a stable displacement front occurs. Generally, if the capillary number is less than 10^{-6}, the viscous pressure drop in a phase is negligible and fluids movement is controlled by capillary forces. It means that, for this regime, intrinsic properties of the medium (pore size distribution) control the invasion. However, for unfavorable viscosity ratios, independent of how large the viscous forces are, viscous fingering (Figure 2.4b) occurs and larger pressure gradient can not stabilize the invasion front.

Dynamic pore-network models have been employed to gain insight into the effects of system parameters on different aspects of two-phase flow dynamics at pore scale and REV scale. In particular, the following issues have been studied: trapping mechanisms, piston-like and snap-off displacement, capillarity effects under non-equilibrium conditions, macroscopic front topology (invasion pattern), dynamics of interfacial area, dependencies of relative permeability, and ganglia movement.

2.6 Trapping mechanism

As shown in several studies (e.g. *Dias and Payatakes*, 1986a,b, *Hughes and Blunt*, 2000, *Mogensen and Stenby*, 1998, *Vizika et al.*, 1994) capillary number, viscosity ratio, aspect ratio, and contact angle have significant impact on displacement mechanism and consequently on residual (trapped) saturation of the receding phase.

2.6.1 Piston-like movement vs. snap-off

Generally, there are two mechanisms that regulate fluids displacement; snap-off and piston-like displacement. The phenomenon in which wetting phase in the corners causes the nonwetting phase in the middle of pore throat to become locally disconnected, is referred to as snap-off. Snap-off can occur during both drainage and imbibition.

During drainage, when the nonwetting phase saturation in a pore body increases, the local capillary pressure in that pore body builds up. It continues until it can invade a pore throat (Figure 2.5a). When invasion occurs, if the nonwetting phase can not fill the next pore body (Figure 2.5b), it will be snapped-off by the wetting phase, which remains in the pore throat. After snap-off, there will be a disconnected blob of non-wetting phase in the second pore body (Figure 2.5c). Then, after capillary pressure builds up further in the first pore body, the nonwetting phase will invade the pore throat again. If the nonwetting phase does not fill up the second pore body, it will get disconnected again. This process continues intermittently until the second pore body is filled up and the nonwetting phase in both pore bodies can stay connected without snap-off.

During imbibition, the wetting phase will first fill small pores, crevices, and grooves. If there is already wetting fluid in the porous medium, the wetting phase tends to flow through the films already present in the corners. Thus, a swelling of the wetting film during imbibition will happen (Figure 2.6b). As the injection of the wetting fluid continues, the filling grows so that eventually the wetting fluid is able to fill the pore. This “snap-off ”or “choke-off” mechanism was proposed for the first time by *Roof* (1970).

If the invading fluid can completely sweep the receding fluid in a pore element, the displacement is referred to as piston-like movement. However as snap-off is related to the ability of wetting phase to chock off the non-wetting phase, it is more important during imbibition compared to drainage. In general, the larger the aspect ratio is, the higher the possibility of snap-off is. As explained before, snap-off effect is significant during imbibition, which causes trapping of a part of the nonwetting phase. If the capillary number is very small, snap-off is dominant and with

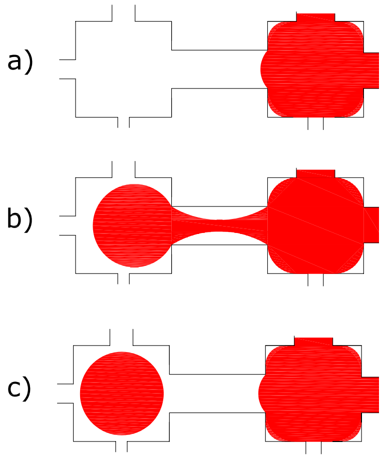

Figure 2.5: *Schematic presentation of snap-off sequence during drainage.*

the increase of capillary number, the possibility of occurrence decreases. Using a pore-network model *Mogensen and Stenby* (1998) found that for capillary numbers between 10^{-8} to 10^{-7}, there was a transition from snap-off movement to piston-like movement. As *Blunt et al.* (1992) have stated, snap-off can happen only when a piston-like movement is topologically impossible. For instance, *Joekar-Niasar et al.* (2009) did not observe any snap-off in a micro-model experiment even for very small capillary numbers due to small aspect ratio (relatively large pore throats) and high porosity of the domain.

2.6.2 Effect of contact angle on trapping

Contact angle can influence the possibility of snap-off especially during imbibition. *Hughes and Blunt* (2000) simulated the effect of flow rate and contact angle on snap-off and piston-like movement using a pore-network model. They showed that with the decrease of contact angle, possibility of snap-off increases. Thus, more disconnection of nonwetting phase would happen and consequently more trapping of nonwetting phase could be resulted (Figure 2.7). As they have shown, snap-off can increase trapped oil saturation significantly; more than 50% of pore throats in their simulation were affected by snap-off when the flow rate was very low and contact angle was zero.

Constantinides and Payatakes (2000) modelled the effect of wetting films on snap-off during imbibition using a pore-network model. Their simulations showed that

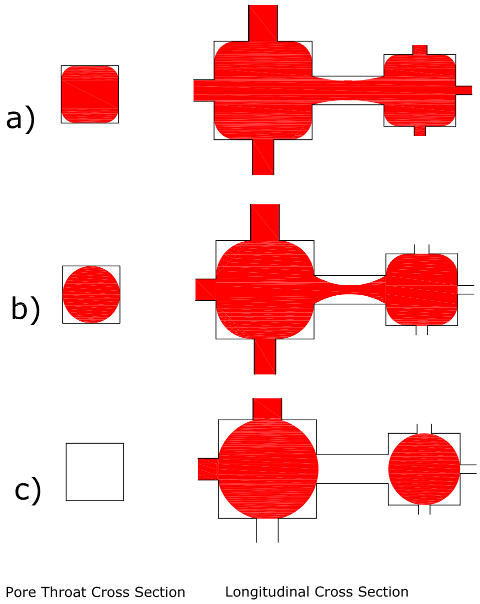

Figure 2.6: *Schematic presentation of snap-off sequence during imbibition. With the decrease of local capillary pressure, the wetting phase in the corners of a pore throat swell till snap-off occurs*

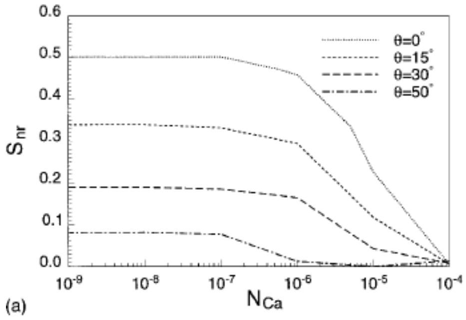

Figure 2.7: *Effect of capillary number and contact angle on residual nonwetting saturation (Hughes and Blunt, 2000)*

the wetting film could cause significant disconnection and entrapment of nonwetting phase during imbibition. This was specially so when contact angle as well as capillary number were small for unfavorable viscosity ratios.

2.6.3 Effect of topology on trapping

As explained earlier, capillary number and viscosity ratio are the main parameters that control the invasion mechanism and trapping. However, under some conditions, porous media topology and geometry can be so important that could suppress effect of dynamic parameters. For instance, in micromodel experiments, *Joekar-Niasar et al.* (2009) observed zero snap-off and consequently zero residual nonwetting phase during imbibition. They did experiments with nitrogen and decane in a two-dimensional micro-model with 68-72% porosity and very small aspect ratio.

As mentioned earlier, the main characteristics of porous media are coordination number and aspect ratio. Some researchers have looked into the effect of structural simplification of porous media on the qualitative results from pore-network models. *Mogensen and Stenby* (1998) investigated the effect of coordination number and aspect ratio on the residual nonwetting saturation (imbibition), using a pore-network model, which had variable coordination numbers up to 26. They found that, for high capillary numbers, effect of coordination number on residual nonwetting saturation is minor compared to the aspect ratio, contact angle, and capillary number. However, for small capillary numbers, where snap-off movement may be more dominant than piston-like movement, effect of coordination number is significant. For example, for $C_a = 10^{-6}$, with the decrease of coordination number from 4 to 3 in a 40×40 two-dimensional network, residual nonwetting saturation increased from 13.3% to 29.4%. However, in general, effect of contact angle, aspect ratio and capillary number on residual nonwetting saturation compared with coordination number is more significant. Aspect ratio, which illustrates contrast between pore body and pore throat size distributions, can magnify the response of the system to the dynamic parameters under different conditions. For instance, there is a transition zone between snap-off-dominated and piston-dominated flow, as shown in Figure 2.8. For large aspect ratios, the change of behavior from snap-off-dominated to piston-like dominated zone is more abrupt than small aspect ratios.

In another study, *Chaouche et al.* (1994) studied the effect of heterogeneity (by increasing the variance of pore sizes) on saturation distribution during drainage. They compared results of continuum model and pore-network model with their experiments. They did not find a good agreement between continuum and pore-network model results, which might be due to the small size of their pore-network model. Their model was based on the algorithm by *Blunt and King* (1991) for a two-dimensional network. Capillary number in the pore-network model varied between 1.5×10^{-6} and 1.5×10^{-3}, and three viscosity ratios were selected equal to 0.1, 1, and 10. The nonwetting saturation rose as the low permeable region was approached. The nonwetting fluid saturation decreased substantially as the low permeable re-

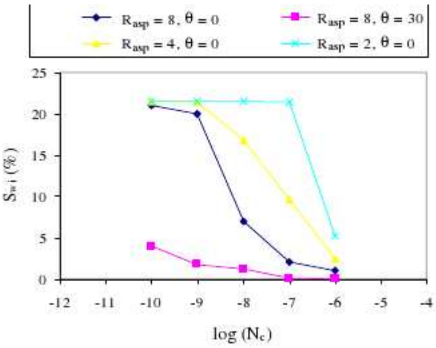

Figure 2.8: *Effect of aspect ratio, contact angle, and capillary number on the amount of wetting fluid accumulating in the corners, Z = 6 (Mogensen and Stenby, 1998).*

gion was entered. Under favorable viscosity ratios during drainage, homogeneous displacement was compact in all regions (low and hight permeability). Thus, high saturation values and high sweeping efficiency was resulted. Variation of saturation in highly permeable region (with small capillarity effect) was insignificant. In contrast, for unfavorable viscosity ratio, displacement was much less efficient and heterogeneity effects were quite pronounced in the saturation profile.

2.6.4 Effect of C_a and M on trapping

Many researchers have focused on the effect of dynamic parameters - capillary number and viscosity ratio - on residual oil saturation during imbibition. *Koplik and Lasseter* (1985) simulated the imbibition process with viscosity ratio equal to one. They showed that capillary number and viscosity ratio significantly influence the fluids distribution during imbibition. They studied the distribution of blob sizes remained in the pore network at the end of the imbibition experiment for different capillary numbers. They investigated two different aspects of the trapped blobs in their simulations. With the increase of capillary number, the size of trapped blobs decreased, but the number of trapped blobs increased. This is because viscous forces tends to fragment residual oil into small parts. Under low capillary number conditions, the size of trapped blobs got larger, but number of trapped blobs decreased compared to high capillary number conditions.

Blunt and King (1991) studied distribution of nonwetting phase-filled pores at breakthrough during drainage for different viscosity ratios. They showed that when capillary number was high, a uniform distribution of filled pores was resulted. But at low capillary numbers, only large pores were invaded. This effect has been illustrated in Figure 2.9 by showing number of pore throats filled with the nonwetting

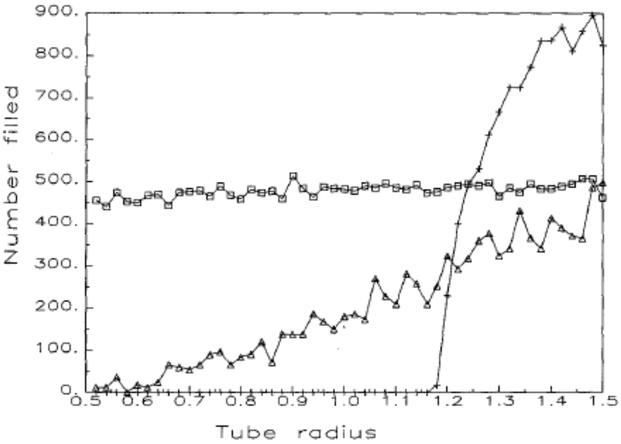

Figure 2.9: *Number of pore throats filled with the nonwetting fluid versus the radii of pore throats for* $M = 0.1$. *Crosses* $C_a = 0$; *triangles* $C_a = 0.5$, *squares* $C_a = \infty$ *(zero entry capillary pressure). Notice that for* $C_a = 0$, *none of the pore throats with entry capillary pressure larger than the percolation threshold are filled (Blunt and King, 1991).*

fluid versus radius of pore throats. The horizonal curve with square symbol shows that at very large capillary number (where only viscous forces are important), pore throat occupancy for different pore throat radii is constant. But, if only capillary forces are dominant ($C_a = 0$), large pore throats are filled (curve with cross symbols). For an intermediate capillary number (triangle symbols), large pore throats are more probable to be filled by the nonwetting fluid and this probability decreases with decrease of pore throat radii. This is similar to the conclusion by *Koplik and Lasseter* (1985); at low capillary number, there is more possibility for trapping and larger blobs are expected.

Dias and Payatakes (1986a), *Vizika et al.* (1994), *Blunt and Scher* (1995), *Mogensen and Stenby* (1998), *Hughes and Blunt* (2000), and *DiCarlo* (2006) have also shown that during imbibition, with the increase of capillary number and viscosity ratio, less trapping of the non-wetting phase (oil) during imbibition would happen. It is due to the suppression of snap-off in high flow rates. *Dias and Payatakes* (1986a) showed the effect of capillary number on residual oil saturation for different viscosity ratios (Figure 2.10). It should be noted that κ in Figure 2.10 is the inverse of M. Thus, with increase of κ, M will decrease. As it can be seen, during imbibition, residual oil saturation remains virtually constant (around 50%) for smaller capillary numbers. From $C_a \approx 10^{-5}$, it starts to decrease drastically with increasing C_a. For viscosity ratios smaller than 1 (unfavorable conditions), residual oil saturation remains constant up to $C_a \leq 10^{-7}$ and in range of $10^{-7} \leq C_a \leq 5 \times 10^{-5}$ it increases slightly. Then, it

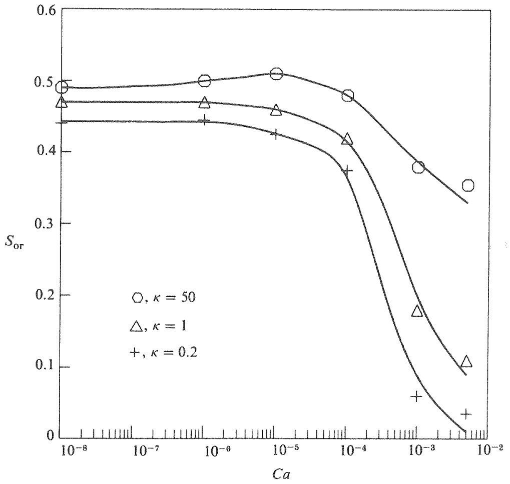

Figure 2.10: *Residual oil saturation (S_{or}) versus the capillary number, C_a, for imbibition simulation on a 15×30 network for various values of inverse viscosity ratio ($\kappa = 1/M$)(Dias and Payatakes, 1986a).*

decreases rapidly for $C_a \geq 10^{-4}$. This figure shows that the effect of capillary number on residual saturation decreases with decrease of viscosity ratio (M). *Hashemi et al.* (1999) and *Hughes and Blunt* (2000) presented a curve qualitatively similar to Figure 2.10.

Vizika et al. (1994) investigated the effect of viscosity ratio in more details for different capillary numbers using three-dimensional pore-network models and also micro-model experiments. They concluded that the viscosity ratio affects the residual oil saturation during imbibition even at low C_a. But when the capillary forces decrease (for example with increase of contact angle), effect of viscosity ratio on residual oil saturation is less pronounced. Their interpretation is that local pressure gradients, which are created by the advance of a single meniscus or a wetting film, may be sufficiently large to make viscous stresses locally important, even if the local overall flow rate is very small. The gradual accumulation of local viscous effects may lead to substantial macroscopic effects.

Although, due to the industrial applications in reservoir engineering, residual nonwetting phase saturation is generally of more interest, some researchers have also investigated the trapped wetting phase during drainage. *Singh and Mohanty* (2003), and *Al-Gharbi and Blunt* (2005) have studied residual water saturation during drainage for constant flow rates. *Singh and Mohanty* (2003) showed that in almost all cases of drainage (including high and low capillary numbers, favorable and un-

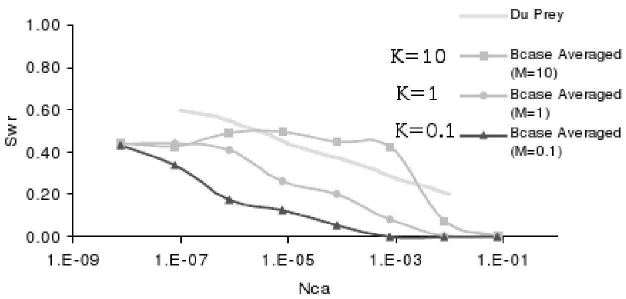

Figure 2.11: *Capillary desaturation curves for different viscosity ratios, due to Singh and Mohanty (2003). Each data point represents an average value over three realizations. Data from Lefebvre du Prey (1973) are also plotted for comparison. It should be noted that* $\kappa = \frac{\mu_{receding}}{\mu_{invading}}$.

favorable viscosity ratios), an increase of viscous forces (large C_a) can lead to a decrease of residual water saturation. However, as it can be observed in Figure 2.11, for unfavorable viscosity ratio, it does not monotonically decrease. They conjecture that the peak values are related to the change of behavior from viscosity fingering to capillary fingering. It should be noted that κ is defined as the ratio of receding phase viscosity to invading phase viscosity.

2.7 Pressure field development

To understand complexities in multi-phase flow, it is essential to investigate pressure field evolution as well as capillarity effects under non-equilibrium conditions. This will help to improve the extended Darcy's law for multiphase flow. *Van der Marck et al.* (1997), *Aker et al.* (1998a,b), *Gielen et al.* (2004, 2005), *Joekar-Niasar et al.* (2010a) studied temporal evolution of pressure field using pore-network models in order to gain a better insight into macroscopic pressure field behavior. They investigated pressure field evolution under the effect of viscosity ratio and capillary number in drainage simulations.

2.7.1 Boundary pressure difference vs. capillary pressure

Van der Marck et al. (1997) have compared pore-network model results with micromodel experiments implemented. These experiments, performed in one-, two- and three-layer micro-models, were designed to investigate the effect of gravity for two different viscosity ratios; equal to one and larger than one. They measured pressures

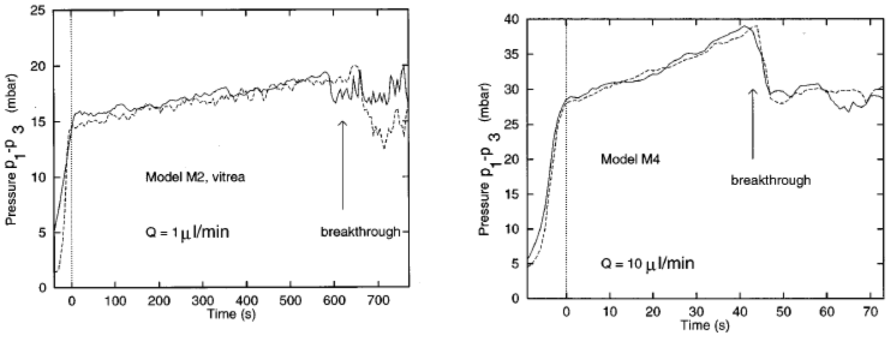

a) b)

Figure 2.12: *An experimental pressure curve for drainage experiment showing pressure drop after breakthrough a) High conductivity network, $M = 12$ b) Low conductivity network $M = 1$ (Van der Marck et al., 1997)*

at the inlet and outlet during drainage experiment under constant flow rate. Agreement between their model results and experimental results decreased for viscosity ratios larger than one and at high capillary numbers.

Obviously, with invasion of nonwetting phase for $M > 1$, the pressure difference between inlet and outlet increased due to increasing viscous energy dissipation, as shown in Figure 2.12. At first, the pressure should increased to reach the entry pressure of the model. After nonwetting phase invaded the model, pressure built up slowly as more and more nonwetting fluid (with higher viscosity) was injected. Capillary blockage of channels and the resulting decrease in the flow conductance of the micro-model were the main reason for the pressure buildup. However, after breakthrough of the nonwetting fluid, pressure build-up changed dramatically, under the influence of the outlet chamber. *Van der Marck et al.* (1997) had chosen a large outlet chamber, which had a negligible influence on flow conductance and capillary pressures. This had a disadvantage, viz., that the nonwetting phase that entered the outlet chamber either remained connected or "snapped off", which is readily influenced by processes occurring outside the micro flow model that are hard to control. They did not include these effects in their pore-network model. Thus, the simulations results after breakthrough deviated from the experimental measurements. The variation of pressure with time is shown in Figure (2.12). *Aker et al.* (1998a) investigated the effect of capillary forces for different viscosity ratios and capillary numbers using a two-dimensional pore-network model. They related the macroscopic flux in two-phase flow to two separate terms related to viscous forces and capillary forces. This formulation was selected in analogy to pore-scale Washburn equation (Equation 2.4, and Table 2.1). In one-phase flow and ignoring the gravity effect, there is a linear relationship between the flux and global pressure drop (between the two boundaries $\Delta P = P_i - P_j$), written as $Q = A\Delta P$. But, in two-phase flow there is a deviation between the flux Q and $A\Delta P$, referred to as B in Equation $Q = A\Delta P + B$. The origin of this different is the capillary pressure acting over the interfaces. They assumed that the total flux (Q) had a linear relationship with the global pressure drop plus the deviation created by the capillary forces; $Q = A\Delta P + B$. This linear relationship can be written as:

$$\Delta P = \frac{Q}{A} - \frac{B}{A} \tag{2.15}$$

During drainage, new interfaces will be created with the invasion of nonwetting phase. The interfaces can be categorized into two groups: "cluster menisci", surrounding the trapped clusters of receding fluid, and the "front menisci" located at the front between the invading and receding fluids. Variation of capillary pressure associated with theses interfaces can be different from each other. So, *Aker et al.* (1998a) introduced two different capillary pressures; global capillary pressure (P_g^c), which contributes to all menisci, and front capillary pressure (P_f^c), which is the averaged capillary pressure associated with the front menisci. Based on the analogy between global pressure drop and pore-scale pressure drop, the second term in Equation 2.15 was assumed to be equal to the global capillary pressure (P_g^c).

$$P_g^c = -\frac{B}{A} \tag{2.16}$$

And, using simple arithmetic averaging, the front capillary pressure was given as:

$$P_f^c = \frac{1}{N}\sum_{i=1}^{N} |P_i^c| \tag{2.17}$$

Based on several drainage simulation they investigated trends of ΔP, A, and B under different capillary numbers, and viscosity ratios.

Unfavorable viscosity ratio: First, they performed drainage simulations with unfavorable viscosity ratio ($M = 0.001$) for different capillary numbers (3.5×10^{-4} to 1.1×10^{-2}) and different sizes of network, so that they could observe capillary fingering as well as viscous fingering. The largest network has 60×80 nodes. They studied the trends of ΔP, global capillary pressure (P_g^c), and average front capillary pressure (P_f^c).

With the invasion of nonwetting fluid (which had a smaller viscosity as $M = 0.001$), ΔP decreased. As Figure 2.13 shows, global capillary pressure (P_g^c) fluctu-

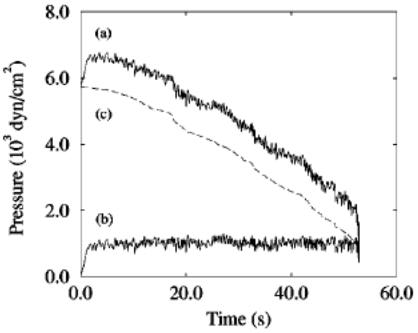

Figure 2.13: *Pressure fluctuations for* $M = 1.0 \times 10^{-3}$ *and* $C_a = 4.6 \times 10^{-3}$ *a)*ΔP *b)*P_g^c *c)* $\Delta P - P_g^c$ *(Aker et al., 1998a).*

ates around a mean value of about 1×10^3 dyn/cm^2, which is about the average threshold capillary pressure of the network, $\frac{2\sigma^{nw}}{<r>}$. Here, $< r >$ is the mean radius of pore throats, equal to 0.4 mm. The fluctuations of ΔP are highly due to fluctuations in P_g^c, as menisci invade into or retreat from tubes. This is clarified by plotting the difference($\Delta P - P_g^c$), which is presented as a smooth curve.

Figure 2.14 shows the variations of P_g^c and P_f^c for different capillary numbers, for $M = 0.001$. The pressures are normalized by the average threshold capillary pressure. Note that, in order to avoid overlap between the two curves at low capillary numbers, the value of threshold capillary pressure (1000 dyn/cm^2) was subtracted from P_g^c before normalization. As it can be observed, for small capillary numbers less than 3.5$\times 10^{-4}$, there is no significant difference between global capillary pressure (P_g^c) and average front capillary pressure (P_f^c). However, this difference increases with the increase of global capillary pressure. This is because the viscous pressure gradient vanishes and capillary pressures of all menisci would become equal to the difference between fluid pressures. Consequently, the global capillary pressure reduces to that describing capillary fluctuations along the front: $P_f^c \approx P_g^c$. Therefore, for $M \ll 1$ or at low injection rates, the effect of the clusters became negligible, and P_g^c reduces to the local capillary of the invading menisci along the front.

Depending on the location of the menisci, their invasion mechanism can be different. The menisci in the uppermost fingertips are more likely to invade the next pore throats compared to the menisci moving behind it. The latter menisci are shielded by the moving fingertips causing their capillary pressures to be less than the entry pressure needed to invade the pore throat. So, they only contribute to P_f^c with a constant value, and their average capillary pressure is almost constant over time. However, those menisci located at the finger tips can vary with time and have

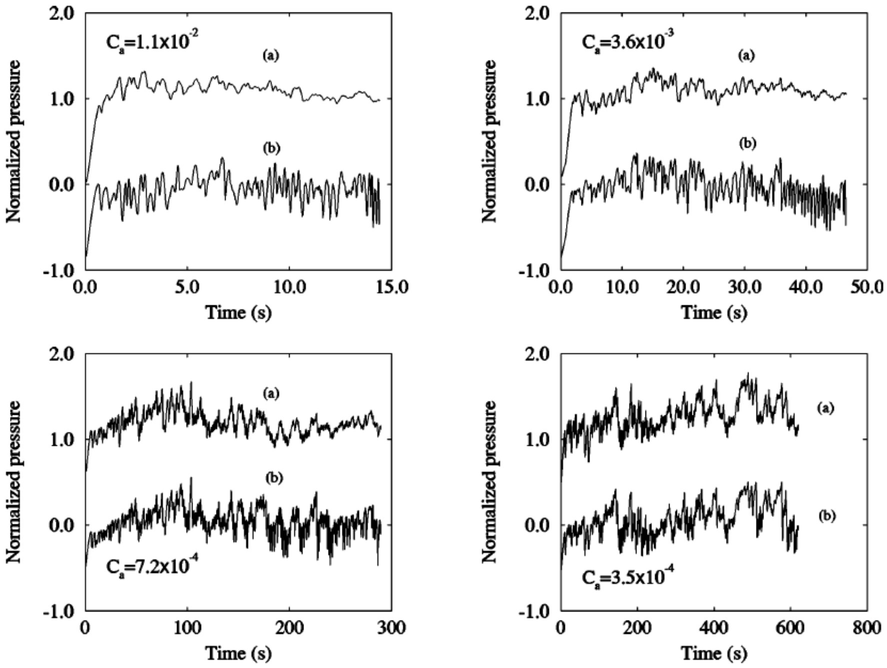

Figure 2.14: *a) P_f^c and b) P_g^c at four different capillary numbers for simulations with $M = 0.001$ and a lattice size of 25 × 35 nodes. The pressures were normalized using the average threshold pressure of the tubes. Note that P_g^c had been subtracted by 1000 dyn/cm^2 before it was normalized, in order to avoid overlap between the two curves at low capillary numbers. The pressures were normalized by $\frac{2\sigma^{nw}}{<r>}$. $< r >$ is the mean radius of pore throats (Aker et al., 1998a).*

a time-dependent contribution to P_f^c. Thus, for sufficiently large systems, the fluctuations in P_f^c will eventually die off when the number of menisci falling behind becomes much larger than the menisci of the moving fingertips. *Aker et al.* (1998a) did not show the evolution of A for unfavorable viscosity ratios.

Favorable viscosity ratio: When viscosity ratio is larger than one, pressure drop increases with the invasion of high viscosity fluid. This pressure drop increases linearly at high flow rates but the linearity of the trend decreases if unstable displacement develops. When the network is fully saturated with the wetting fluid, flux has a linear relationship with pressure gradient. *Aker et al.* (1998a) introduced a pseudo-hydraulic conductivity for the case of single-phase flow such that $Q = A_0\Delta P$. However, for a two-phase problem, used the formula $Q = A\Delta P + B$, where, as explained before, A and B are saturation dependent. They have determined variations of

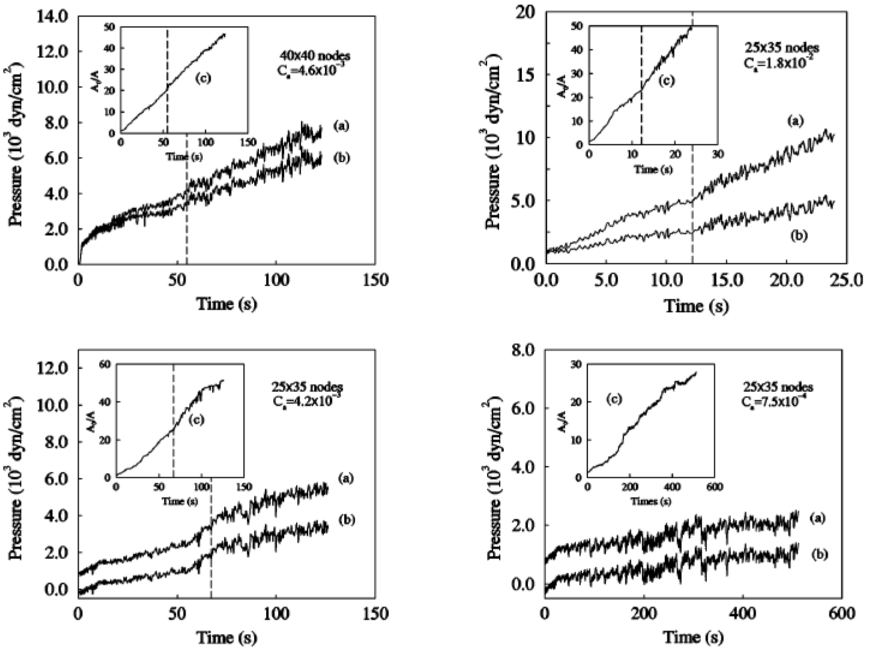

Figure 2.15: *Evolution of pressure evolution at four different capillary numbers. Curves (a) represent* ΔP *and curves (b) show* P_g^c *as functions of time for simulations with* $M = 100$ *at low, intermediate, and high* C_a. *Curves* A_0/A *are shown in the inset. Note that* P_g^c *for* $C_a = 4.2 \times 10^{-3}$ *and* 7.5×10^{-4} *has been reduced by 1000* dyn/cm^2 *to avoid overlap of the curves. Vertical dashed lines indicate time at which front stabilizes, i.e. at that time front width is equal to the saturation width (refer to page 43) (Aker et al., 1998a).*

the ratio A_0/A, ΔP, and P_g^c with time, for four different capillary numbers and $M = 1.0 \times 10^2$. Results, plotted in 2.15, show that with the increase of nonwetting phase saturation, A_0/A increases (starting from 1). For small flow rates, where capillary forces are dominant, the effect of viscous forces disappear and small A values are resulted. Thus, ratio of A_0/A in fast flow is larger than that of slow flow. Initially, P_g^c should be negligible, since the domain is filled by one fluid. With the invasion of the nonwetting phase, the effect of global capillary pressure on the total pressure drop (ΔP) increases.

2.7.2 Non-equilibrium capillarity effects

A central equation in theories of two-phase flow in porous media is the so-called capillary pressure-saturation relationship, which is commonly written as:

$$P^n - P^w = P^c(S^w) \tag{2.18}$$

In fact, there are two major assumptions in this equation: capillary pressure is a function of wetting phase saturation, and fluids pressure difference is equal to capillary pressure (at all times and under all conditions). Regarding the second assumption underlying (2.18), it is now an established fact that $P^n - P^w$ is equal to capillary pressure but only under equilibrium conditions (see *Hassanizadeh et al.*, 2002, for an extended review of experimental evidences). For non-equilibrium situations, the following equation for the difference in fluid pressures has been suggested *Stauffer* (1978), *Kalaydjian and Marle* (1987), and *Hassanizadeh and Gray* (1990):

$$P^n - P^w = P^c - \tau \frac{\partial S^w}{\partial t} \tag{2.19}$$

where τ ($ML^{-1}T^{-1}$) is a material property that may still be a function of saturation. This equation has been the subject of many studies in recent years, both experimentally (*Berentsen and Hassanizadeh*, 2006, *Bottero and Hassanizadeh*, 2006, *Hassanizadeh et al.*, 2004, *O'Carroll et al.*, 2005, *Oung et al.*, 2005) and computationally, using a continuum model (see e.g. *Das et al.*, 2006, *Manthey et al.*, 2005) and pore-network models (see e.g. *Dahle et al.*, 2005, *Gielen et al.*, 2005, *Joekar-Niasar and Hassanizadeh*, 2010, *Joekar-Niasar et al.*, 2010a).

Gielen et al. (2004, 2005), *Gielen* (2007) developed a pore-network model based on the model developed by *Blunt and King* (1991). They assumed that the capillary pressure in pore bodies was negligible. Under Dirichlet boundary conditions, drainage simulations were performed in a three-dimensional network model. They assumed a viscosity ratio of 10; therefore a stable front was dominant in their simulations. A network size of 30×30×40 pore bodies was found to satisfy the requirement of a REV. Imposing different pressures at boundaries resulted in different time rate of saturation change. They determined the intrinsic phase average pressure of each phase (local pressure weighted by local saturation in pore bodies). The difference between $< P^n > - < P^w >$ was denoted by ΔP^c. the resulting curves of ΔP^c vs. $\partial S^w/\partial t$ at a given saturation (obtained for different boundary pressures) are shown in Figure 2.16. As it can be observed, the curves are not parallel, indicating a dependency of τ on wetting fluid saturation. All curves seem to pass through the origin when extrapolated with a linear fit. The dynamic coefficient τ can then be evaluated as the slope of the linearly fitted curves. The relationship between τ and saturation

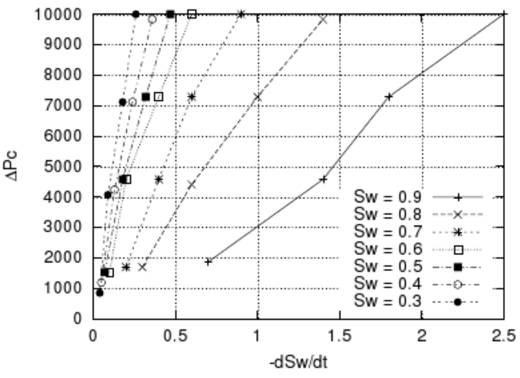

Figure 2.16: *Differences between dynamic and quasi-static capillary pressure vs.* dS^w/dt *for average wetting fluid saturations 0.3 through 0.9 (Gielen et al., 2004).*

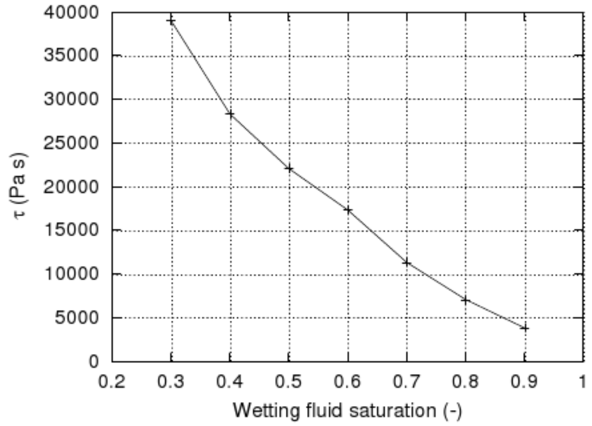

Figure 2.17: τ *as a function of saturation for a 30×30×40 network (Gielen et al., 2004).*

has been shown in Figure 2.17. It is evident that τ increases when fluid saturation decreases.

Since the employed pore-network model had a simplified geometry (circular cross section), many physical processes such as snap-off and capillary diffusion, local counter-current flow could not be observed in simulations. In addition, all simulations were for the case of $M = 1$ and 10, where stable front invasion occurred. *Joekar-Niasar et al.* (2010a) investigated the dynamic effect during drainage in pore-network with a angular cross sections for three different viscosity ratios $M = 10, 1, 0.1$. They used the same procedure as *Gielen et al.* (2004) for the cal-

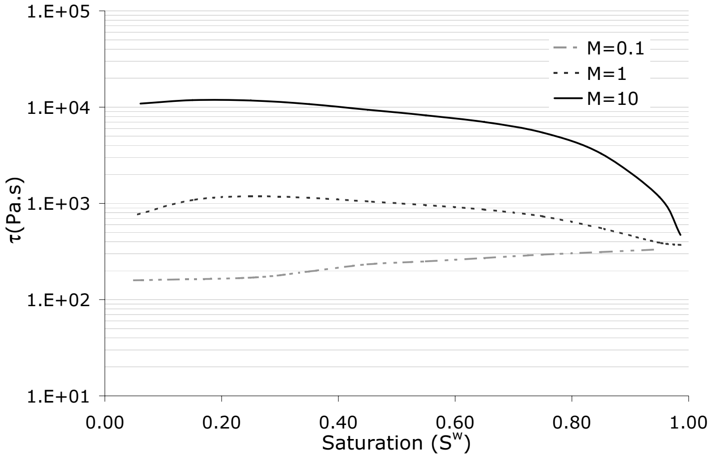

Figure 2.18: *τ as a function of saturation and viscosity ratio for a 35×35×35 network (Joekar-Niasar et al., 2010a).*

culation of the non-equilibrium capillary coefficient used. Figure 2.18 shows relationship between τ and saturation for a 35×35×35 network for different viscosity ratios. As it can be observed, dynamic effect is not only a function of saturation but also viscosity ratios, as found by *Gielen* (2007). Furthermore, it can be found that $\frac{\partial \tau}{\partial S^w}$ is a function of viscosity ratio. For favorable viscosity ratios $\frac{\partial \tau}{\partial S^w} < 0$, while for unfavorable viscosity ratio it is positive. *Joekar-Niasar and Hassanizadeh* (2010) studied the variation of non-equilibrium capillarity coefficient under primary and main drainage as well as main imbibition processes. Their results showed that variation of τ depends on viscosity ratio as well as effective viscosity. In the other word, they found that dynamic effects can be originated from macroscopic invasion mechanism. With shifting the topology of the front from stable front to the fingering, τ value decreases. Although there is no doubt about the dynamic effects on pressure field and its dependency on capillary pressure, magnitude of dynamic coefficient is also a consequence of averaging the pressures. Although there are several averaging methods for phase pressures, the most probable one is still an open question!

2.8 Macroscopic interface dynamics

As shown in Figure 2.4, depending on M and C_a, the invasion front can be classified into three different classes: capillary fingering, viscous fingering, and stable displacement. Due to their versatility and rather inexpensive computational cost, pore-network models have been used to investigate the macroscopic front topology.

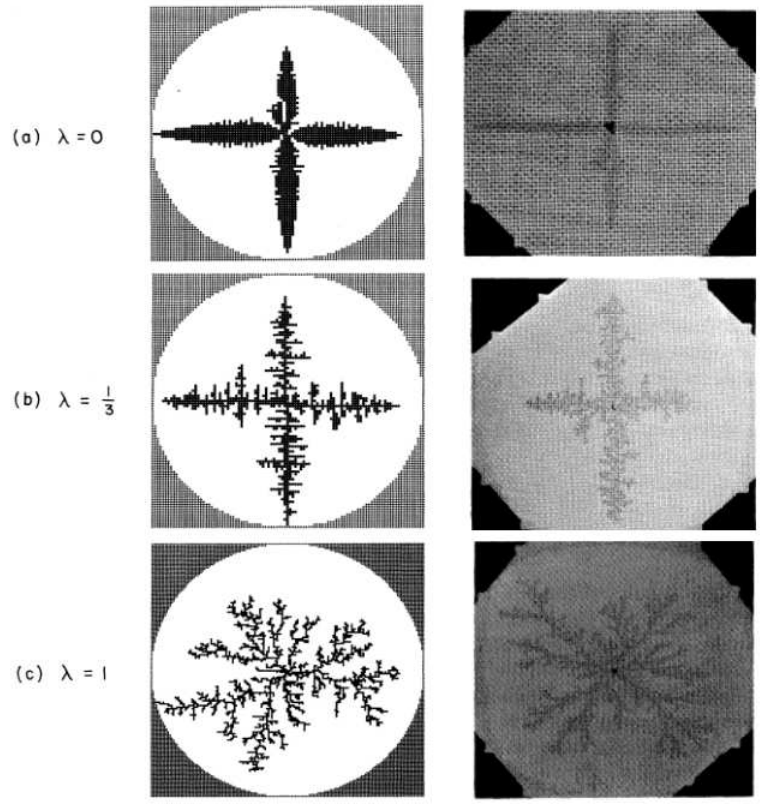

Figure 2.19: *Viscous fingering invasion pattern for different randomness in porous media structure. Left column shows modelling results for different randomness factor (λ) and right column shows the experimental results in a two-dimensional micro-model. These two columns should not be compared with each other quantitatively (Chen and Wilkinson, 1985).*

Chen and Wilkinson (1985) investigated the effect of randomness of the porous medium structure on viscous fingering using experimental and modelling approaches. Using a pore-network model with a single-pressure algorithm, they showed that in a two-dimensional model, size of the fingers would also depend on size distribution of pores. Radii of the pores were generated in interval $[1-\lambda, 1+\lambda]r$, where r is the mean radius and λ is a randomness factor changing from 0 to 1. In the experiments and modelling results, they observed that for a narrow size distribution of the tubes (small λ), fingers formed almost ordered patterns and grew along the injection direction (Figure 2.19a). But, for a wider range of distribution, fingers formed in a chaotic fashion (Figure 2.19c). They compared their results of two-dimensional drainage simulations qualitatively with two-dimensional micro-model experiments.

In those experiments oil was injected into the micro-model initially filled by glycerin ($M = \frac{1}{1200}$). Although there was no quantitative agreement between experiments and model results, the effect of pore size randomness was visible in their results.

One of the interesting features of viscous fingering in multiphase flow is the fractal behavior of the interface. Fractal dimension (D) as the major parameter has been investigated using pore-network models. It is a statistical quantity that gives an indication of how completely a fractal fills the space, as one zooms down to finer and finer scales. The fractal dimension is:

$$D = \frac{\log N(l)}{\log l} \tag{2.20}$$

in which l is the grid size and $N(l)$ is the number of grids filled with the front. *Chen and Wilkinson* (1985) found that fractal dimension in their two-dimensional simulations was about 1.72. Later, *King* (1987) also used a pore-network model to investigate the fractal behavior of fingering in a two-phase flow. He showed that viscous fingering is a fractal phenomenon and the fractal dimension does not depend on the disorder of porous medium structure. Instead, it is highly dependent on the viscosity ratio; fractal dimension decreases with the increase of viscosity ratio. They found the following formula by filling their simulations results:

$$D = 1 + \frac{2}{3}\left(\frac{1-M}{1+M}\right)^2 \tag{2.21}$$

More detailed pore-network simulations have been performed by *Aker et al.* (1998a), *Blunt and King* (1991), *Vizika et al.* (1994),and *Singh and Mohanty* (2003). Using a sigle-pressure dynamic pore-network model with circular cross sections, *Blunt and King* (1990) studied fractal behavior of an invading phase in relation to the structure spacing. Fractal dimension in their network increased from 1.82 in a two-dimensional network to 2.44 in a three-dimensional network.

Results of a pore-network model by *Dias and Payatakes* (1986a) showed that although the effect of capillary number on displacement is essential, but at high and moderate C_a, the effect of viscosity ratio is more important, acting as a pivotal factor. This was also shown by *Touboul et al.* (1987). They showed that at large capillary numbers (when viscous forces dominate the flow), depending on the viscosity ratio, either viscous fingering or stable displacement would occur (Figure 2.4). If the viscosity ratio is larger than one, stable displacement will occur as also shown by *Singh and Mohanty* (2003) and *DiCarlo* (2006). Using a two-dimensional pore-network model, *Aker et al.* (1998b) showed that at $C_a = 4.6 \times 10^{-3}$ for $M = 1.0 \times 10^{-3}$ and 1.0×10^2, two different displacements can be observed. If $M < 1$, at high capillary number, viscous fingering was observed, while for $M > 1$ stable displacement was reported. With decreasing the flow rate, front moved from viscous fingering to capillary fingering. For instance, for $M = 0.1$ at high flow rate, nonwetting front was stable and compact. For very low flow rates, capillary fingering was observed. Thus, one would expect to have less flooding efficiency for $M < 1$ compared with the favorable conditions. *Dias and Payatakes* (1986a) showed that for unfavorable viscosity ratio ($M < 1$), flooding efficiency begins to improve only for capillary numbers larger than 5×10^{-4}, and it is substantially inferior to the achieved values with $M > 1$ with the same C_a.

Vizika et al. (1994) showed that at any flow rate, under unfavorable conditions, micro-fingering can happen and cause macro-fingering. In addition, they found that for favorable displacements ($M > 1$), the extent of micro-fingering decreased with increasing C_a and for unfavorable displacements ($M < 1$), the extent of micro-fingering increased slightly with increasing C_a for $10^{-6} \leq C_a \leq 10^{-5}$.

Another aspect of the macroscopic interface dynamics is related to the macroscopic interface velocity, which was studied by *Nordhaug et al.* (2003) and *Joekar-Niasar et al.* (2010a). *Nordhaug et al.* (2003) studied interface movement in a three-dimensional lattice pore-network model with circular cross sections using a single-pressure algorithm. To save computational time and memory, they did not track the menisci within pore throats (i.e. spontaneous pore throat filling was assumed). They simulated stable and unstable displacement mechanisms during drainage under Dirichlet boundary conditions (during simulation capillary number varied between 10^{-3} to 10^{-2}) for three different viscosity ratios ($M = 0.1, 1, 10$).

They estimated interface velocity for stable displacement as well as viscous fingering regime. Since it was assumed that the pore throats are filled spontaneously, they could not calculate menisci velocity in the pore throats. However, they calculated the magnitude of a local velocity in pore bodies based on time-rate change of local saturation, as follows:

$$\|v_i^{nw}\| = l_{ij}\frac{\Delta S_i^n}{\Delta t}, \quad ij : \text{pore throat including the traveling interface} \tag{2.22}$$

in which, $\|v_i^{nw}\|$ is the menisci velocity in pore body *i*, and l_{ij} denotes the length of pore throat *ij* through which the entering interface travels plus the diameter of the pore body *i*. To define the direction of the velocity, they averaged the directions of total inflow and total outflow in pore body *i*. Equation 2.22 has a shortcoming in definition; if more than one interface enter the pore throats connected to pore body i, different fluxes will flow through the pore throats. Thus, the interface velocity in the pore throats will be different, while Equation 2.22 uses $\frac{\Delta S_i^n}{\Delta t}$ for all pore throats equally.

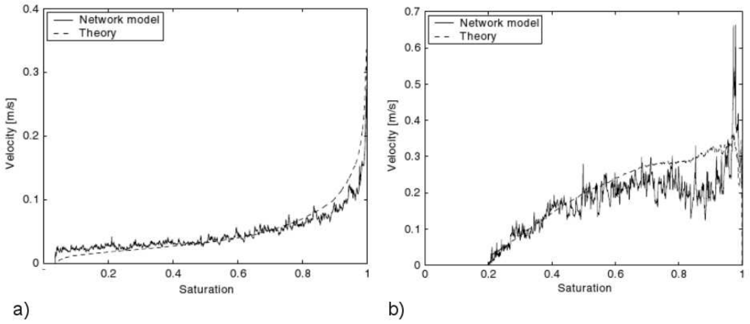

Figure 2.20: *Comparison between velocity of interface resulted from model and theory for a)* $M = 10$ *b)* $M = 0.1$ *(Nordhaug et al., 2003).*

To upscale the velocity from pore body to REV-scale, they averaged local velocities weighted with local interfacial area:

$$v^{nw} = \frac{\sum_{i=1}^{\#pb} a_i^{nw} v_i^{nw}}{\sum_{i=1}^{\#pb} a_i^{nw}} \tag{2.23}$$

In addition, they averaged fluid velocities weighted with local saturation. Since it was not possible to compare their simulation results with experiments, they compared the results with a simplified equation derived from thermodynamic theory developed for multiphase flow in porous media by *Hassanizadeh and Gray* (1990, 1993a). They found that with including the trapped interfaces in the calculation of total interfacial area, results of the simulation will underestimate the menisci velocity compared with the thermodynamic-based equations. As expected, their results were in better agreement with theory for stable displacement ($M = 10$) compared with viscous fingering regime ($M = 0.1$) as shown in Figure 2.20. *Nordhaug et al.* (2003) found that regardless of displacement regime, under constant pressure boundaries, interface velocity decreased nonlinearly with decrease of wetting fluid saturation during drainage; with the major drop in velocity happening in the saturation range from 1.0 to 0.8. Qualitatively a similar behavior for average interface velocity versus saturation was found by *Lam and Horváth* (2000) in pore-network modelling of primary imbibition. Velocity of interfaces in the case of unfavorable viscosity ratio were higher than the case of favorable viscosity ratio. In their model there were some simplifications that might affect results significantly. For instance, capillary diffusion through corner flow, local capillary pressures at pore bodies, tracking of interface in pore throats were not included in the model. In another study, *Joekar-Niasar et al.* (2010a) studied variation of specific interfacial area with saturation under different pressures at the boundaries. Specific interfacial area is

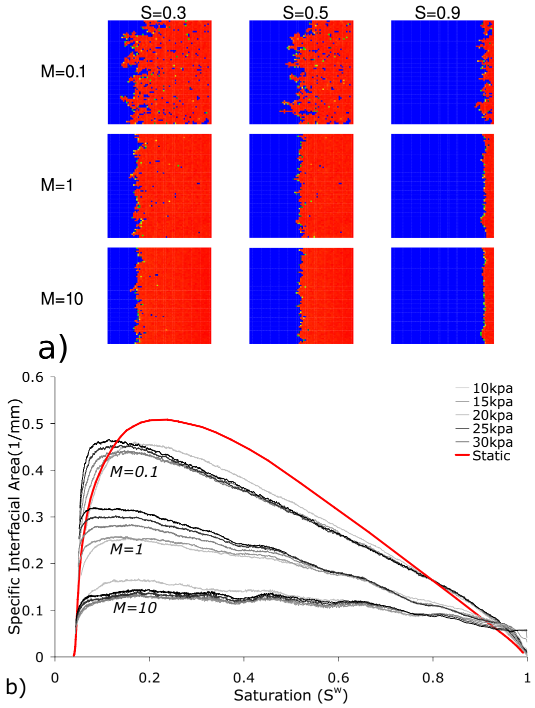

Figure 2.21: *a) Qualitative comparison of macroscopic interface topology for* $M = 0.1, 1$ *and* 10 *in a 2D (70×70) network at three different saturations, b) Quantitative comparison between quasi-static and dynamic specific interfacial area-saturation curves for the same fluid-solid properties as (a) and boundary conditions mentioned.*

defined as the ratio of total fluid-fluid capillary interfaces to the total volume of the sample. They simulated the drainage process under five different global pressure difference and three different viscosity ratios (M =0.1,1, 10). Viscosity of the wetting fluid was kept constant in all simulations. They calculated the specific interfacial area under dynamic conditions and compared it with the quasi-static simulations. It has been shown that with the decrease of invading fingers, the area associated to the main fluid-fluid interfaces will decrease as shown in Figure 2.21. Furthermore, they showed that the production rate of specific interfacial area has a linear function with $\frac{\partial S^w}{\partial t}$ and production rate of interfacial area decreases with decrease of s^w during drainage.

Investigation of width of the invasion front under different conditions is another aspect of interface dynamics, which has been studied by *Aker et al.* (1998a) for applications in reservoir engineering and by *Lam and Horváth* (2000) for application of

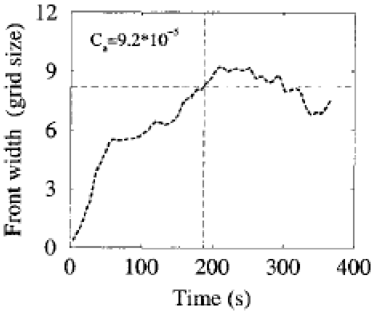

Figure 2.22: *The front width (w) as a function of time for $C_a = 9.2 \times 10^{-5}$. The horizontal dashed line indicates the saturations width (w_s) and the vertical dashed line indicates the saturation time, t_s (Aker et al., 1998a).*

paper wetting process. *Aker et al.* (1998a), *Lam and Horváth* (2000) and *Løvoll et al.* (2005) have studied development of the front width with time using a pore-network model with circular cross sections for pore throats. *Aker et al.* (1998a) used different terminologies:

- Front width: During the invasion of nonwetting phase, there will be some pores on the invasion front, referred to as front pores. Front width (w) is defined as the standard deviation of the distance between all front pores and the centroid of the front.
- Saturation width: Denoted by w_s, it is defined as the standard deviation of the distance between all pores filled with the invading phase and the centroid of part of the domain saturated with the invading phase.
- Saturation time: Denoted by t_s, it is defined as the time in which saturation width (w_s) is equal to the front width.

Aker et al. (1998a) calculated front width for different capillary numbers, including $2.3 \times (10^{-3}, 10^{-4})$, $4.6 \times (10^{-4}, 10^{-5})$ and $9.2 \times (10^{-4}, 10^{-5})$, as shown in Figure 2.22. They used the simulation results to show scaling of the front width for $t < t_s$. They found that data points collapsed onto a more or less single curve when $\log w/w_s$ was plotted against t/t_s (Figure 2.23). For this curve, they assumed the following relationship for $t \ll t_s$:

$$\frac{w}{w_s} = \left(\frac{t}{t_s}\right)^{\beta} \tag{2.24}$$

They found a good agreement between their results and experimental data of *Frette et al.* (1997), who found $\beta = 0.8 \pm 0.3$. Furthermore, they found that saturation front

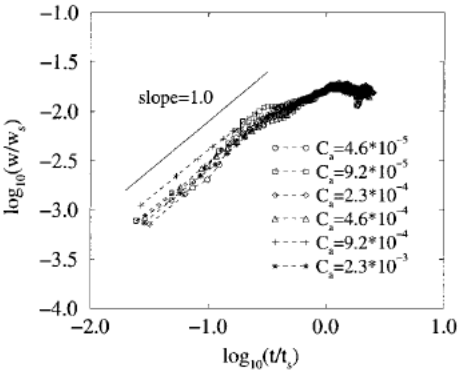

Figure 2.23: *Data collapse for the front width. β is given by the slope when $t/t_s < 1$ and was estimated to $\beta = 1.0 \pm 0.1$ (Aker et al., 1998a).*

width (w_s), and saturation time (t_s) are only functions of capillary number. Results of *Aker et al.* (1998a) related to the drainage process only. *Lam and Horváth* (2000) showed temporal and spatial correlation for fronts during imbibition process. In a series of experiments by *Horváth and Stanley* (1995), a paper sheet was moved continuously downward into a water container at constant speed v. Imbibition front evolution was investigated for various different dynamic conditions (different values of v) and a stationary experiment ($v = 0$). *Lam and Horváth* (2000) simulated imbibition experiments using a pore-network model with circular cross sections. They found $\beta = 0.29 \pm 0.01$. Due to the large viscosity ratio ($M \sim 100$), they solved the pressure field only in the wetting phase (water), and ignored the pressure drop in air phase.

In another study by *Løvoll et al.* (2005), the effect of gravity and viscous forces on front width evolution with time was studied. They performed drainage experiments in a two-dimensional micro-mode of 35×35 cm^2. The nonwetting phase was air and the wetting phase was a mix of glycerol and water. Planer porosity was about 0.63 and permeability was $0.0189 \times 10^{-3} cm^2$. The nonwetting phase viscosity was much smaller than the viscosity of wetting phase. Specifications of their pore network model are presented in Table 2.3. To include gravity forces in the simulations, *Bond* number (Bo), was considered. *Bond* number is defined as the ratio of gravity forces to capillary forces:

$$Bo = \frac{\Delta \rho g a^2}{\sigma^{nw}} \tag{2.25}$$

in which, ρ is the density and a is the length scale (lattice spacing of a pore network). According to *Løvoll et al.* (2005), percolation theory can predict a scaling law for this displacement as follows:

$$w = (Bo - C_a)^{-a} = (Bo - C_a)^{-v/1+v} \tag{2.26}$$

To have a stable width evolution, $(Bo - C_a)$ should be positive. It means that width will increase with time till reaching a steady state. They showed that the width evolution with time reaches a steady state condition with $(Bo - C_a) > 0$. They found that their simulation results were in qualitative agreement with experiments. Front width increased with time, and when $(Bo - C_a) > 0$ a steady-state condition was reached. With increasing $(Bo - C_a)$ values, the required time to reach the steady-state front width decreased.

2.9 Ganglia flow dynamics

As mentioned in Section 2.6, during both drainage and imbibition processes the receding phase can be entrapped in the domain. However, the trapping mechanisms are more significant during imbibition than drainage. In reservoir engineering, at the end of a secondary flooding, a large ratio of oil remains entrapped in the reservoir. The residual oil exists in the form of discrete oil ganglia that can occupy 25 to 50% of the pore space. The size of an individual ganglion is typically ranging from one to fifteen pore volumes (*Payatakes et al.*, 1980). A picture of trapped ganglia in a micromodel is shown in Figure 2.24 (from *Avraam and Payatakes* (1995a)). One of interesting issues - investigated extensively - is the fate of trapped ganglia under different dynamic conditions. Pore-scale investigations, such as pore-network modelling, can be valuable in acquiring a better insight into the physics of the problem. Most pore-network models assume that at any flow rate, disconnected ganglia are immobile. In addition, it has been assumed that the intertwined pathways of the two fluids are nearly independent of the flow rate within a wide range of flow rates. This assumption leads to the result that the superficial velocity is a linear function of macroscopic pressure gradient. However, in reality the superficial velocity is nonlinearly dependent on macroscopic pressure gradient. A number of pore-network models have been developed by *Payatakes* and coworkers for ganglia movement. They have investigated different aspects of ganglia movement and its contribution to the nonlinearity observed in relative permeabilities in several publications. Using pore network modelling for studying ganglia movement has been reported in *Ng and Payatakes* (1980), *Payatakes* (1982), *Payatakes et al.* (1980), *Dias and Payatakes* (1986a,b), *Hinkley et al.* (1987), *Constantinides and Payatakes* (1991, 1996), *Avraam and Payatakes* (1995,a), *Avraam et al.* (1994), *Vizika et al.* (1994), *Valvanides and Payatakes* (2001), *Valvanides et al.* (1998), *Dahle and Celia* (1999), *Al-Gharbi and Blunt* (2005), and

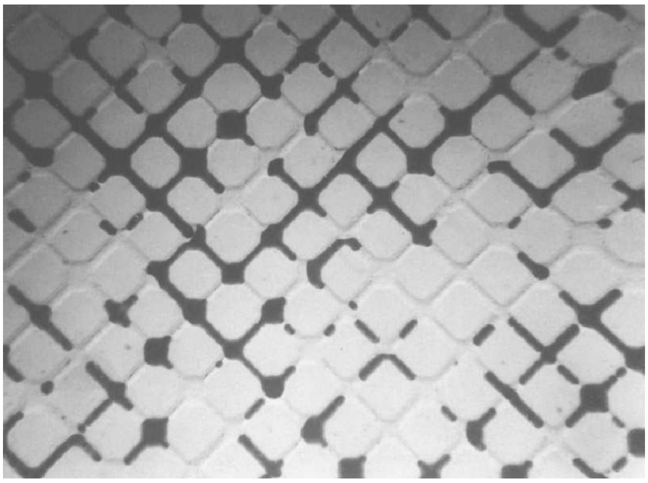

Figure 2.24: *Snap-shot of ganglia trapped in a micro-model under steady-state flow conditions (Avraam and Payatakes, 1995a).*

Bravo et al. (2007).

At pore-scale, various mechanisms can act on ganglia, such as break-up (breaking up a ganglion into two smaller ganglia), mobilization (moving an entrapped ganglion within the pore space), stranding, and coalescence (two or more ganglia join to form a new bigger ganglion). To investigate the effect of these pore-scale phenomena at macro-scale, *Payatakes* and his co-authors adopted the following steps, implemented in several publications from 1980 to 2001:

- Defining system parameters for a single pore, such as geometry, conductivity, entry capillary pressure, etc.

- Simulating ganglia dynamics in a pore-network model at meso-scale ($\sim 10^3$ pores) to calculate system factors. Such as the mean time-averaged ganglion velocity, the stranding and breakup coefficients, the mode of ganglion breakup, the probability of stranding of a newly formed ganglion, and the mean and maximum length of a ganglion for a given volume (*Valvanides et al.*, 1998).

- Development of population-dynamic equations and using the system factors acquired in the previous step in this step to investigate the effect of ganglia dynamics at macro-scale for steady-state conditions.

The whole procedure has been shown schematically in Figure 2.25 and their main findings are described below.

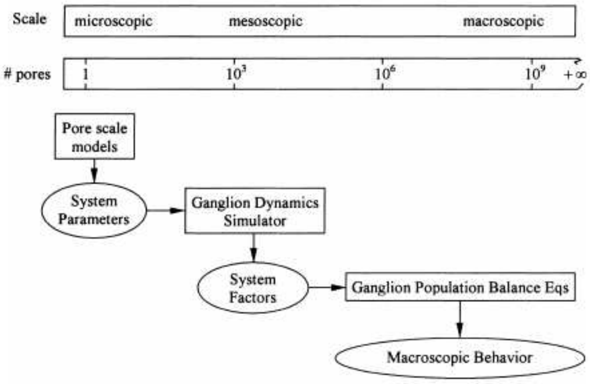

Figure 2.25: *Ranges of number of pores over which the various models are applicable and scale-up of the models (Valvanides et al., 1998)*

2.9.1 Micro-scale phenomenology of ganglia dynamics

Ng and Payatakes (1980) have developed an approach for determining the fate of an immiscible ganglion in a granular porous medium under quasi-static displacement. In other words, ganglia flow phase was not simulated in their model. Since they studied quasi-static displacement of a ganglion, no pressure field was computed. They considered three mechanisms for a solitary ganglion in porous medium including breakup, mobilization and stranding (but not coalescence). *Ng and Payatakes* (1980) calculated at which capillary number the main terminal interfaces of a ganglion might move. Main terminal interfaces are shown in Figure 2.26 by thick curves locating between the blank pore space and the hatched pore space. When ganglia are trapped in a porous medium, under zero pressure gradient ($\nabla P = 0$) and neglecting gravity effects, the curvatures of their menisci should all be equal. Imposing a large pressure gradient in the wetting phase so that it can mobilize the ganglion, and assuming a uniform pressure within the ganglion (P_o), the pressure in the water decreases along the ganglion in the flow direction. Consequently, capillary pressure at downstream interface will be larger than that of the upstream interface, and radius of curvature at the downstream interfaces will be smaller than that of upstream interfaces.

Under this condition, there are backward forces due to capillary pressure and forward forces due to external pressure difference. The two forces may cancel each other so that the ganglion remains in equilibrium. However, with the increase of pressure gradient to a critical value, menisci can move if at least one of its main terminal interfaces can cause drainage and back menisci undergoes imbibition (Figure

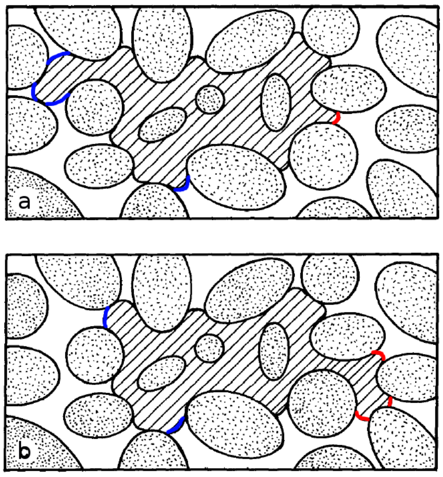

Figure 2.26: *Schematic presentation of a ganglia movement showing drainage menisci and imbibition menisci. Flow direction is from left to right (Payatakes, 1982).*

2.26). Thus, this criterion is met, the ganglion cannot resist mobilization any longer. This displacement is referred to as a "rheon". During the rheon, oil invades one of the downstream chambers and this displacement is referred to as "xeron". Furthermore, the aqueous phase invades one of the upstream chambers that used to be occupied by the oil. This displacement is referred to as "hygron". In porous media with very irregular geometry, it is possible that if the xeron occurs in an unusually large chamber, two (or more) hygrons may be necessary to supply enough oil for the xeron. The reverse may also occur. Finally, if proper conditions for a hygron develop at a site (where the ganglion is one-chamber long), the ganglion may fission in two daughter ganglia.

Thus, to develop displacement criterion for the quasi-static mobilization of oil ganglia, menisci locations should be identified in calculations. Based on the schematic presentation shown in Figure 2.27, *Ng and Payatakes* (1980) assumed that all interfaces were locked in their unit cells, except for two; one downstream with index *I* and one upstream with index *K*. For this particular pair of menisci locations, there is a critical pressure gradient that may cause mobilization. By repeating this calculation for all possible pairs, one can identify the particular pair (i =I, k = K) for which the required pressure gradient is minimum. If the mobilization is to occur, it will proceed through the I^{th} and K^{th} menisci. This analysis is equivalent to identifying the maximum mobility factor (β_{KI}), namely

$$\beta_{KI} = \Delta L_{KI} \cos\theta_{KI} / \left[J_{dr,I}\left(\theta_r^o\right) - J_{im,K}\left(\theta_a^o\right) \right] \tag{2.27}$$

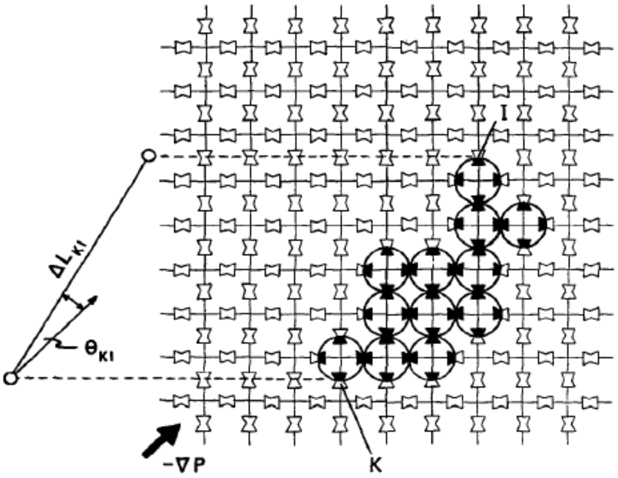

Figure 2.27: *Concepts involved in the quasi-static criterion for mobilization (Payatakes, 1982)*

in which, ΔL_{KI} is the distance between menisci *K* and *I*, θ_{KI} is the angle between the line connecting throats *K* and *I* and the macroscopic flow direction, $J_{dr,I}$ is the drainage curvature in the downstream meniscus *I*, $J_{im,K}$ is imbibition curvature in the upstream meniscus *K*, estimated as $J_{j,i} = \frac{4\cos\theta_j}{d_i}$, in which d_i is diameter of pore *i* with circular cross section.

Finally, *Ng and Payatakes* (1980) defined the following mobilization and stranding criterion:

If $\beta_{KI}|\bigtriangledown P|/\gamma_{ow} \geq 1$, mobilization occurs.

If $\beta_{KI}|\bigtriangledown P|/\gamma_{ow} < 1$, stranding occurs.

To summarize their approach, a ganglion with an arbitrary volume was considered in the network model and the exact geometry of the ganglion was captured. Then, mobilization-breakup criterion was applied to all interfaces to determine advancing/receding interfaces at that capillary number. Simulations would be terminated when stranding or breakup occurred. To understand the mechanisms more clearly, several realizations in each class of capillary number and ganglion volume were implemented. Finally probability functions were produced for the fate of a solitary ganglion based on quasi-static conditions as shown in Figure 2.28. Figure 2.28 shows variations of occurrence probability in a capillary number range of 10^{-4} to 10^{-2}. *Ng and Payatakes* (1980) have shown that the threshold capillary number for moving the stranded ganglia is 10^{-4}. It decreases form 10^{-4} to 10^{-3} from probability of 1 to zero. But probability of two other phenomena, namely breaking up and mobilization, increases. However, mobilization increases to the probability of

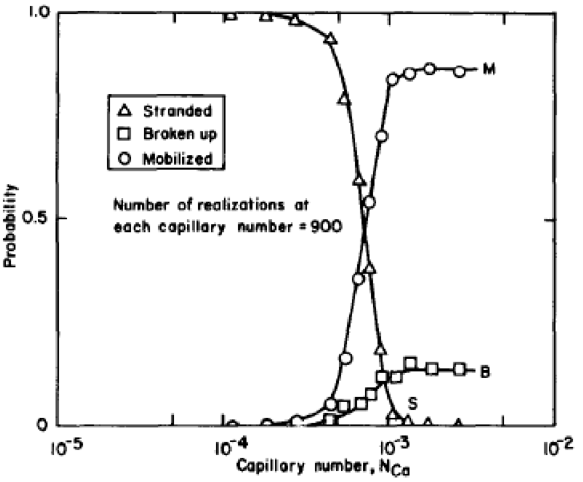

Figure 2.28: *Probability of mobilization (M), breakup (B) and stranding (S) per rheon for a ganglion vs. capillary number (Ng and Payatakes, 1980)*

0.85 and breaking up increases to almost 0.15. When stranding of ganglia begins to decrease, probability of mobilization begins to increase.

These three mechanisms are functions of ganglion volume and capillary number; larger ganglia have higher probability for breakup and less probability for stranding as shown in Figure 2.29. *Ng and Payatakes* (1980) introduced the term CEVS to indicate conceptual element void space, which is assigned to the pore elements surrounded by circles in Figure 2.27. In the simulations, they observed that in the absence of coalescence, the ganglia would be immobile. Thus it was necessary to study the role of coalescence in producing large ganglia.

All results shown above were obtained from a quasi-static pore-network model. However, dynamics of ganglia is more complex. It has been observed in experiments that in viscous-dominated flows, ganglia can move through several pores simultaneously. Due to the lack of this feature in quasi-static models they showed two major shortcomings in such simulations. First, it was observed that tendency for alignment and elongation in experiments was less compared with simulations. Second, if downstream part of a ganglion encounters small pores, it cannot advance into them quickly. Thus, the ganglion may grow a new branch at some appropriate site along its body to bypass the elongation (*Payatakes*, 1982). Since *Payatakes* and co-workers were interested in using the micro-scale results for macro-scale simulations based on population-dynamics formulation, they had to define coefficients representing micro-scale mechanisms, such as stranding (λ), break-up (ϕ), and coa-

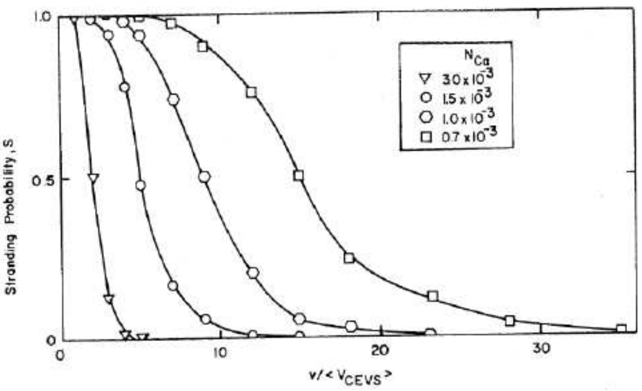

Figure 2.29: *Probability of stranding (S) per rheon for a ganglion vs. volume of ganglion for different capillary number (CEVS:conceptual element void space) (Ng and Payatakes, 1980).*

lescence (Co). The first two ones were defined as follow:

$$\lambda = -\frac{1}{n}\frac{\partial n}{\partial z}|_{\text{due to stranding}} \tag{2.28}$$

$$\phi = -\frac{1}{n}\frac{\partial n}{\partial z}|_{\text{due to break-up}} \tag{2.29}$$

in which, n is the total number of ganglia and $\frac{\partial n}{\partial z}$ is the variation of n in z direction. But, the coalescence factor was not as straight-forward as breakup and stranding factors. Coalescence factor of ganglia was investigated by *Constantinides and Payatakes* (1991). It is related to the merging of menisci when they meet each other. Coalescence at pore scale depends on many factors including pore geometry, physical properties of fluids, interfacial tension, interface velocity, double ionic layer interactions, initial positions of interfaces, pressure difference between oil bodies. *Constantinides and Payatakes* (1991) tried to quantify the coalescence parameter using their pore-network model. The model consisted of two components, simulating bulk motion of ganglia in a pore-network, and simulating drainage of a water film trapped between two colliding menisci at each pore (Figure 2.30). Both parts were coupled together at different time scales. The time scale of the inner component (water film simulator) was much smaller than the outer one. They tried to simulate the film flow using a criterion for critical thickness of film. When the thickness of the film is larger than the critical value, the interfaces are non-interacting. However, in very small thickness (in this work $<\sim 100\text{Å}$), *London-van der Waals* forces are considered using the *Hamaker* constant (*Sheludko*, 1967). *Constantinides and Payatakes* (1991) tried to define a probability rate for coalescence for two ganglia with different sizes and

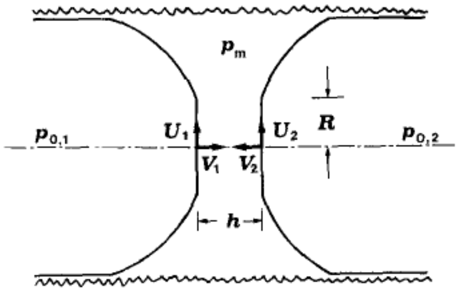

Figure 2.30: *Schematic presentation of two-component model for simulating coalescence (Constantinides and Payatakes, 1991).*

found a range of 0.03 to 0.15. Coalescence probability would increase gradually with the increase of capillary number, but it increased significantly with the decrease of contact angle.

Figure 2.31 shows plots of stranding and break-up coefficients against the ganglia volumes for different wetting-phase saturations resulted from dynamic pore-network modelling, while coalescence probability (Co) was set equal to 0.15 (*Valvanides et al.*, 1998). According to Figure 2.31, with the increase of ganglia volume, breakup coefficient increases while stranding coefficient decreases nonlinearly. Furthermore, with the increase of wetting phase saturation, stranding coefficient increases and break-up coefficient decreases.

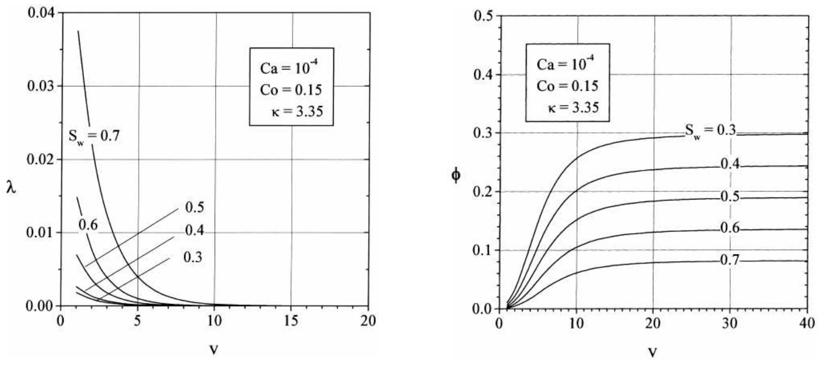

a) b)

Figure 2.31: *Dependency of a) Stranding coefficient, λ and b) Break-up coefficient ϕ on the ganglion volume, v, and the water saturation,S_w, for $C_a = 10^{-4}$, $\kappa = \frac{\mu_n}{\mu_w} = 3.35$, $Co = 0.15$, $\theta_a = 45$, $\theta_r = 35$ (Valvanides et al., 1998).*

Length of ganglia under different dynamic conditions is another system factor that should be determined for macro-scale modelling of ganglia dynamics. For

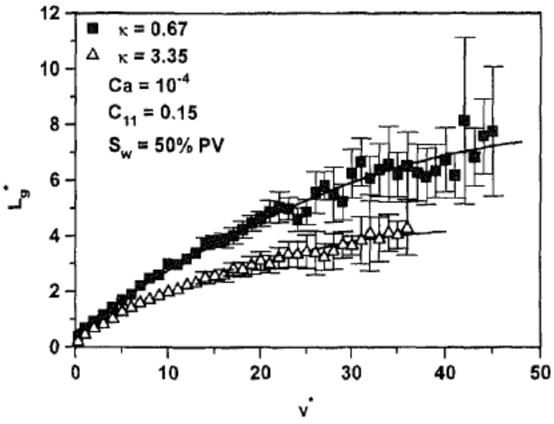

Figure 2.32: *Length of ganglia (normalized by mean lattice spacing length) for different ganglia volume and two viscosity ratios ($\kappa = 1/M$)(Constantinides and Payatakes, 1996).*

$M > 1$ during imbibition, length of ganglia aligned to the direction of macroscopic flow is relatively high (Figure 2.32). But, for $M < 1$ length of ganglia decreases in direction of flow (Figure 2.32), and it prefers to follow a path composed of large pores. With decrease of water saturation, interstitial velocity and local pressure gradient increases, which increases dynamic behavior of ganglion displacement. Thus, with decrease of saturation, tendency of ganglia to become long and aligned with the macroscopic flow direction increases. Thus ganglia displace not only in the direction of the macroscopic flow, but also in other directions due to the population density. As *Valvanides et al.* (1998) have observed, stranding of ganglia decreases as C_a or ganglia size increases and break-up increases. With the increase of viscosity ratio (decrease of κ) during imbibition, time rate of stranding decreases and break-up rate decreases (*Constantinides and Payatakes*, 1996), although the first one is stronger. In addition, with the decrease of M ganglia volume decreases. Effect of viscosity ratio on the size of ganglia is significant at large wetting phase saturations.

Another system factor required for macro-scale modelling is the average velocity of ganglia for different ganglia volumes. To understand the dynamics of ganglion, *Payatakes* (1982) reviewed data from a micro-model experiment done by *Rapin* (1980). *Rapin* (1980) investigated the velocity of ganglia using visualization techniques in experiments. His results are shown in Figure 2.33, where u_z/V_f is the normalized velocity of a ganglion defined as the velocity of the centroid of a ganglion (u_z) divided by the superficial velocity of the flooding (V_f). According to Figure 2.33, for a given volume of ganglia, the normalized velocity is a monotonically-increasing function of capillary number. Near a critical mobilization capillary number, the

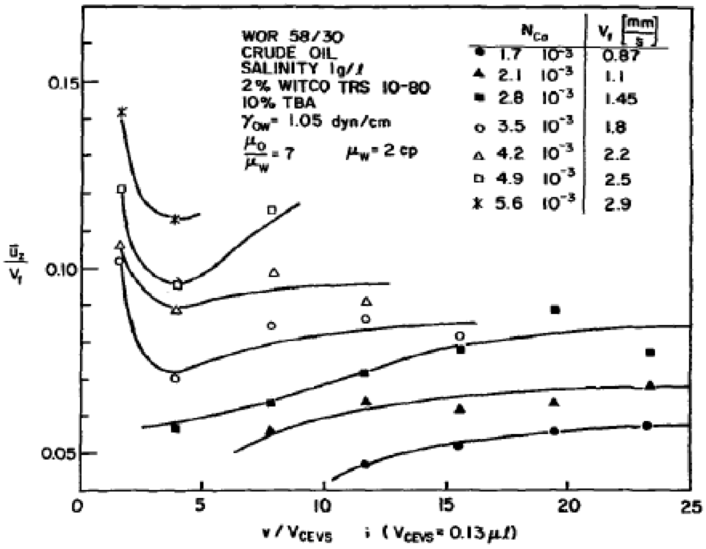

Figure 2.33: *Average ganglion velocity (normalized by superficial fluid velocity) versus ganglion volume (normalized by volume of CEVS) for several typical capillary number values. Here, the viscosity ratio is* μ_n/μ_w*=(Payatakes, 1982). Data are from Rapin (1980).*

normalized velocity increases monotonically with volume, reaching an asymptotic value for volume of ganglia. The asymptotic value of ganglia is about $15 \sim 20$ CEVS volume. However, when the value of capillary number exceeds critical mobilization value, velocity will have a minimum in range of $3 \sim 5$ CEVS volume. Later *Dias and Payatakes* (1986a,b) and *Valvanides et al.* (1998) could develop a dynamic pore-network model to investigate velocity of ganglia and its dependencies on system parameters. Simulation results shown in Figure 2.34 are qualitatively comparable with the experiments. Figure 2.34 shows velocity of a ganglion versus its volume for different viscosity ratios. For viscosity ratio smaller than 1 ($M = 1/\kappa$, $\kappa > 1$), the time-averaged ganglion velocity of oil is smaller than the average velocity of the water. If viscosity ratio is larger than 1 ($\kappa < 1$), this ratio will be larger than 1. obviously, ganglia velocity increases with the increase of C_a.

An interesting result from these simulations is that for a ganglion with a given volume, with the increase of C_a, ganglia velocity can reach an asymptotic value for $M < 1$. However, this is not found to hold for $M > 1$. This means that when the wetting fluid is less viscous than the nowetting fluid, the blobs of the nonwetting phase can move faster and they are less constrained by the invading phase. Based on these simulations, hysteresis in contact angle cannot significantly affect the trend

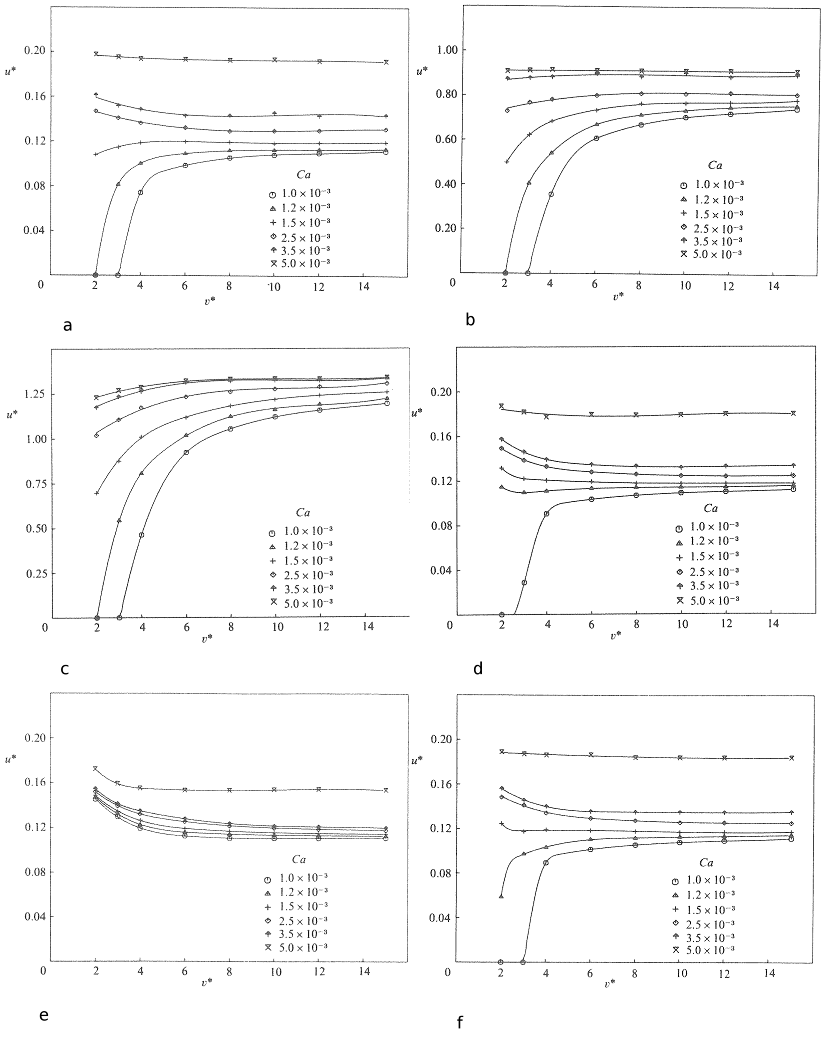

Figure 2.34: *Normalized time-averaged ganglion velocity, $u^* = u_z/V_f$, versus the normalized ganglion volume v^* (ganglia volume divided by the volume of a CEVS), in a 15×30 network for various C_a values, u_z is the velocity of the centroid of a ganglion, and V_f is the superficial velocity of the flooding. a) $\kappa = 7, \theta_e = \theta_a = \theta_r = 0$ b) $\kappa = 1, \theta_e = \theta_a = \theta_r = 0$ c) $\kappa = 0.6, \theta_e = \theta_a = \theta_r = 0$ d) $\kappa = 7, \theta_e = \theta_a = \theta_r = 10$ e) $\kappa = 7, \theta_e = \theta_a = \theta_r = 30$ f) $\kappa = 7, \theta_e = 10\theta_a = 11.4\theta_r = 0$, $\kappa = \frac{\mu_n}{\mu_w}$ (Dias and Payatakes, 1986b).*

of time-average velocity especially for large ganglia and large C_a values.

Hinkley et al. (1987) compared results of the pore-network modelling of *Dias and Payatakes* (1986a) with the micro-model experiments. They performed some two-dimensional micro-model experiments to investigate the velocity of ganglia for different viscosity ratios and capillary numbers. The model was made of one layer of grains sandwiched between two *Plexiglass* sheets. Resulting pores were completely regular and uni-size. Comparison between simulation and experimental results is shown in Figure 2.35. The agreement is very good large capillary numbers, since nonlinearity of the multiphase flow system is not significant. With the decrease of capillary number and increase of viscosity ratio (decrease of κ), the agreement decreases significantly, due to the increase of nonlinearity of the system. The difference can be due to the fact that ganglion motion depends on the initial shape and orientation of the ganglion, the local characteristics of the porous medium, and the distribution of the two phases in the nearby region (*Valvanides et al.*, 1998). In any case, in spite of the quantitative difference, the same behavior for ganglia dynamics which was observed by *Rapin* (1980) was captured by the model.

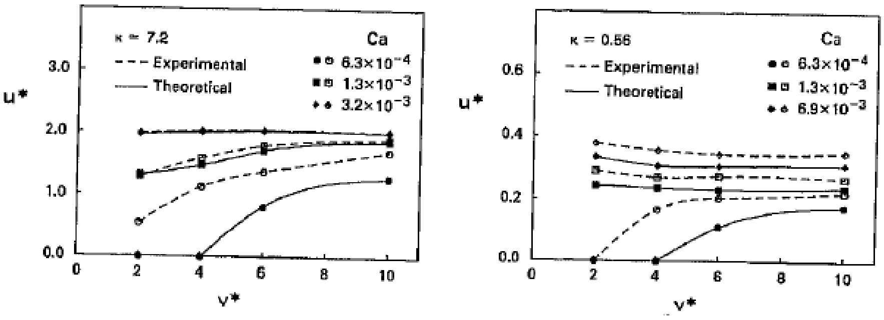

a) b)

Figure 2.35: *Comparison between experimental and theoretical values of the normalized time-averaged ganglion velocity,* $u^* = u_z/V_f$*, vs. the ganglion volume (normalized by the volume of a CEVS),* v^**, for various capillary numbers and viscosity ratios (a)* κ*=7.2 (b)* κ *=0.56,* $\kappa = \frac{\mu_n}{\mu_w}$*,* u_z *is the velocity of the centroid of a ganglion, and* V_f *is the superficial velocity of the flooding (Hinkley et al., 1987).*

2.9.2 Macro-scale ganglia dynamics

Based on the system factors resulted from pore-network modelling and proposing population dynamics balance equations developed for macro scale ganglia dynamics, *Payatakes et al.* (1980), *Constantinides and Payatakes* (1996) and *Valvanides et al.* (1998) studied macro-scale dynamic motion of the ganglia in porous media.

Main assumptions of this model include a) oil is totally disconnected in the form of ganglia of various sizes, b) the macroscopic flow is one-dimensional, c) the longitudinal dispersion of ganglia is neglected, d) gravity is neglected, e) in the integration of the population balance equations, the ganglia are considered as points coinciding with their mass centers. f) specific assumptions are made for the calculation of the dimensionless collision rate.

The resulted populations dynamics equations for moving and stranded ganglia were integro-differential type of equations that were solved numerically. For sake of space the equations and their explanations have not been mentioned in this review. Complete explanation can be found in *Payatakes et al.* (1980) and *Valvanides et al.* (1998). Using the population dynamics equation, *Valvanides et al.* (1998) investigated fate of stranded as well as moving ganglia with space and time for two different types of regime: steady state fully developed (SSFD) and steady state non-fully developed (SSnFD). Under SSFD conditions, number concentrations of moving and stranded ganglia are independent of time and space. However, under SSnFD conditions, number concentrations of moving and stranded ganglia are only independent of time.

Although *Payatakes* and his co-workers investigated ganglia dynamics extensively, there are some major shortcomings in their approach:

1. Topology and geometrical properties of porous medium has not been investigated at all, while they have major effects especially geometrical properties such as shape factor and aspect ratio.

2. The pore-network simulator is based on single-pressure solver. Thus effect of corner flow, which is important in ganglia dynamics has not been explicitly considered.

3. The equations used for population dynamics of ganglia are developed for one dimension only. Thus, there is not a clear picture how this approach can be used for a real three-dimensional case.

4. From practical point of view, it seems that as *Al-Gharbi and Blunt* (2005) have concluded, in reservoir engineering the capillary number values are smaller than those ones used here that and disconnected flow in these conditions is not significant.

2.10 Relative permeability

One of the major applications of pore-network models has been in the investigation of relative permeability curves especially for predictive purposes. However, relative permeability curves have been mostly produced by quasi-static pore-network models. To use quasi-static pore-network models for relative permeability simulation, it is assumed that flow paths of both phases are frozen at a given saturation (or a grain global capillary pressure). Thus, dynamic effects on the flow path are ignored. But, *Hughes and Blunt* (2000) have showed that the contact angle, initial wetting saturation, and flow rate can affect significantly the displacement pattern and consequently the relative permeability curves. Extensive experimental and theoretical investigations have shown that the relative permeabilities are strong functions of a large number of parameters, including S_w, C_a, flow rates ratio r, viscosity ratio M, advancing and receding contact angles θ_a and θ_r, coalescence factor, Bond number (*Bo*), and the flow history (*Avraam and Payatakes*, 1995, *Avraam et al.*, 1994, *Constantinides and Payatakes*, 1996, *Valvanides et al.*, 1998).

$$k_{ro} = k_{ro}(S_w, C_a, r, M, \cos(\theta_r^0), \cos(\theta_a^0), Co, Bo, \text{flow history}) \tag{2.30}$$

Payatakes and co-authors, carried out extensive experimental and numerical studies, using micro-models and pore-network models, to investigate the effect of ganglia movement on relative permeability (*Avraam and Payatakes*, 1995, *Avraam et al.*, 1994).

Constantinides and Payatakes (1996) developed a dynamic pore-network model, including dynamics of ganglia, to investigate relative permeability curves at steady-state flow for different saturations. To calculate relative permeability, they used the following equation:

$$\frac{q^\alpha}{A} = -k_{r\alpha}\frac{k}{\mu^\alpha}\frac{\Delta P^\alpha}{L}, \alpha = w, n \tag{2.31}$$

in which, q^α is the total flux for α phase, A is the cross section of pore-network model normal to the flow direction, $k_{r\alpha}$ is the relative permeability of α-phase, k is the intrinsic permeability of the pore-network, μ^α is the viscosity of phase α, L is the length of the pore network in flow direction, w and n denote wetting and nonwetting phase, respectively, and ΔP^α is the pressure drop of phase α. The approach for defining boundary conditions in pore-network model developed by *Constantinides and Payatakes* (1996) has been explained in Section 2.4.4. To prevent effect of initial condition on simulation results, they continued the simulations so that the time-averaged relative permeability became constant. Results for relative permeability of oil are shown in (Figure 2.36). The same behavior was found for relative permeability of water, and macroscopic pressure drop for nonwetting and wetting phase. Oscillations in relative permeability values of oil are small for large ganglion dynamics. But, they are significant for connected-path flow regime. The wetting phase relative permeability oscillations were minimal for small ganglion dynamics.

Constantinides and Payatakes (1996) calculated relative permeability curves for different viscosity ratios and capillary numbers, including ganglia dynamics effect.

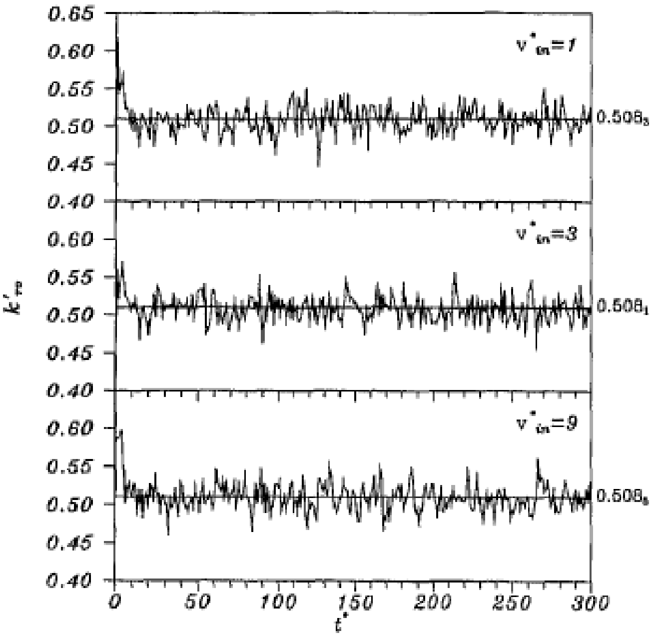

Figure 2.36: *Time series of the instantaneous relative permeability of oil, k'_{ro} for a) Ganglia with 1 CEVS volume b) Ganglia with 3 CEVS volume c) Ganglia with 9 CEVS volume ($\kappa = 3.35, C_a = 10^{-4}, C_{11} = 0.15, S_w = 0.5$pore-volume, $\theta_a^0 = 45°, \theta_r^0 = 35°$) (Constantinides and Payatakes, 1996).*

Figure 2.37(a) shows the effect of viscosity ratio on relative permeability curves. With the increase of viscosity ratio (decrease of $\kappa = \frac{\mu^n}{\mu^w}$), relative permeability decreases. It is clear that relative permeability of nonwetting phase is more sensitive to the viscosity ratio. *Constantinides and Payatakes* (1996) postulated that with the decrease of M ($= \frac{\mu^w}{\mu^n}$), both phases tend to segregate and create their own separate flow paths. Nonwetting phase tends to flow through big pores, which causes an increase of its permeability. This segregation reduces viscous dissipation in the system. However, these results differ from the findings of *Lefebvre du Prey* (1973) and *Fulcher et al.* (1985), who observed experimentally that with the decrease of M, relative permeability of nonwetting phase increased but relative permeability of wetting phase decreased. *Constantinides and Payatakes* (1996) have conjectured that this contradiction may be due to the fact that in those experiments, different fluids and porous medium sample were used, which may indeed affect contact angle and consequently relative permeabilities.

Figure 2.37(b) shows the effect of capillary number on relative permeability. With

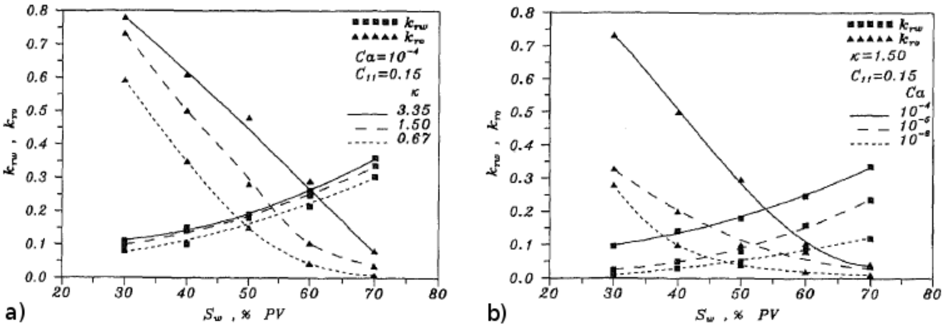

Figure 2.37: *Dependency of steady state relative permeability of both fluids (k_{rw} and k_{ro}) on water saturation a) for different* $\kappa = 1/M$ *(*$\kappa = 0.67, 1.5, 3.35$*,*$C_a = 10^{-4}$*,* $\theta_{advancing} = 45°$*,* $\theta_{receding} = 35°$*) b) for different capillary number values* C_a *(*$C_a = 10^{-4}, 10^{-5}, 10^{-6}$*,* $\theta_{advancing} = 45°$*,* $\theta_{receding} = 35°$*) (Constantinides and Payatakes, 1996).*

the increase of capillary number, relative permeability increases as well. *Constantinides and Payatakes* (1996) have found that at medium and high C_a values, the two fluids tend to become more segregated compared with small capillary number values. This causes an increase of both relative permeabilities.

Avraam et al. (1994) observed the same behavior in two-dimensional and quasi-three-dimensional (consisting of two layers of pores) micro-models under steady-state conditions. They found that relative permeability of oil correlates strongly with the flow regimes and dynamic parameters of the system such as capillary number and viscosity ratio. *Avraam and Payatakes* (1999) showed that the lubrication effect can be significant for strongly wetting systems. They observed experimentally that for small capillary numbers ($C_a \leq 10^{-6}$), flow of oil takes place through the motion of ganglia and/or droplets. For larger capillary numbers ($C_a > 10^{-6}$), connected pathways for the flow of oil can form, but the disconnected flow can also lubricate the flow of ganglia.

Avraam and Payatakes (1995), *Avraam et al.* (1994) also investigated relative permeability curves using micro-model experiments. Their micro-model had a square lattice structure with node-to-node distance of $1221\mu m$. Macroscopic flow direction was parallel to one of the diagonals. The network consisted of 11300 chambers and 22600 throats. Mean diameters of chambers and pore throats were 560 μm and 112 μm, respectively. Maximum depth of pores was almost uniform equal to 140 μm. Cross section of pore throats was almost eye-shaped with a planer porosity of 0.25. To study the effects of different physical parameters such as viscosity ratio and interfacial tension, three different fluid sets were used. In each experiment, simultaneous injection of the two fluids was continued (at a constant rate) until steady

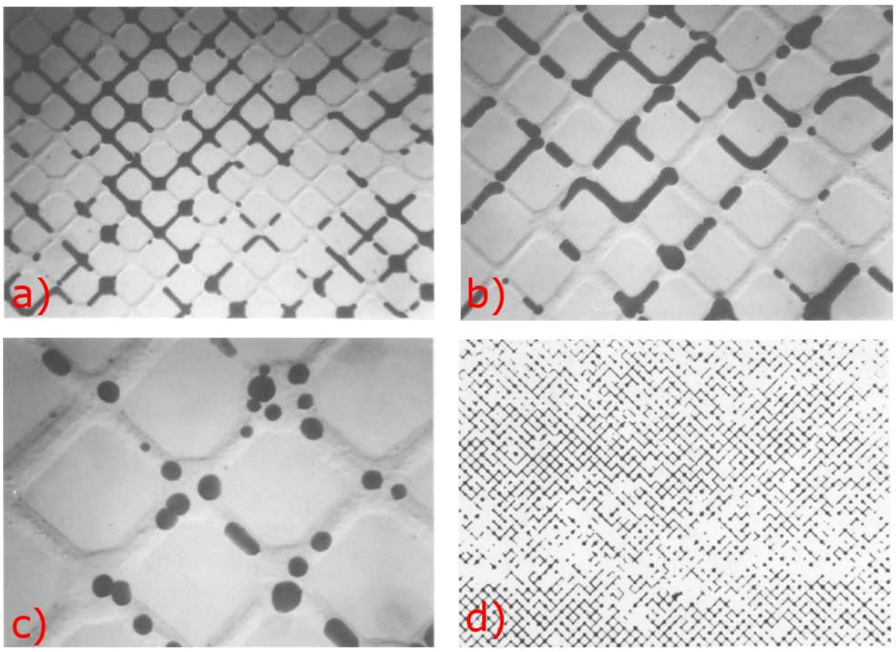

Figure 2.38: *Ganglia flow regimes a) Large ganglia dynamics b) Small ganglia dynamics c) Droplet traffic flow d) Connected-path flow (Avraam and Payatakes, 1995a).*

state conditions was reached. Based on visual observations and flow rate measurements, (*Avraam and Payatakes*, 1995, *Avraam et al.*, 1994) found that the disconnected oil movement contributed substantially to the flow of oil during imbibition.

They stated that over a large range of system parameters (in the range of practical interest) the flow of oil takes place solely through the movement of ganglia and/or droplets. Based on their experiments, two-phase flow behavior can be roughly classified into four flow regimes: large ganglion dynamics (Figure 2.38a), small ganglion dynamics (Figure 2.38b), drop traffic flow (Figure 2.38c) and connected-path flow (Figure 2.38d). In the first three classes, oil flow is due to the motion of disconnected bodies of oil. This is even the case in connected-path flow regime (high values), where many droplets and ganglia move at the fringes of connected pathways. Nonlinearity in the relative permeability depends on the pressure gradient which is related to the creation, motion, fission and coalescence of ganglia/drops or menisci/interfaces.

Observations showed that for a wide range of variables ($10^{-8} \leq C_a \leq 10^{-6}$;$0.6 \leq M \leq 3.4$; $0.2 \leq S_w \leq 0.8$) oil is disconnected in the form of ganglia or droplet. *Avraam and Payatakes* (1995) observed that at the pore scale this mechanism is transient but at meso-scale it is almost stationary, such that it can be identified as steady-state.

Based on the experimental data reported by *Avraam and Payatakes* (1995), *Avraam and Payatakes* (1995a) implemented some optimization calculations to study the behavior of viscous coupling coefficients ($k_{r\alpha\beta}$, $k_{r\beta\alpha}$) introduced in the following extended darcy's law.

$$v_\alpha = -\frac{kk_{r\alpha}}{\mu_\alpha}\frac{\Delta P_\alpha}{L} - \frac{kk_{r\alpha\beta}}{\mu_\beta}\frac{\Delta P_\beta}{L}$$
$$v_\beta = -\frac{kk_{r\beta}}{\mu_\beta}\frac{\Delta P_\beta}{L} - \frac{kk_{r\beta\alpha}}{\mu_\alpha}\frac{\Delta P_\alpha}{L} \tag{2.32}$$

The cross-coupling terms are needed in order to describe the macroscopic flow when a disconnected fluids is present. *Avraam and Payatakes* (1995a) used their pore-network model to study changes of the coefficients with S_w, C_a ,and M. Conventional and generalized relative permeabilities were determined based on B-spline functions combined with standard constrained optimization techniques. They found that the cross coefficients were not equal ($k_{r\alpha\beta}/\mu_\beta \neq k_{r\beta\alpha}/\mu_\alpha$). These coefficients as well as conventional coefficients were found to depend on the flow conditions and the corresponding flow mechanics.

Relative permeabilities $k_{r\alpha}$ and $k_{r\beta}$ are increasing functions of the saturation of the respective fluid. $k_{r\alpha}$ and $k_{r\beta}$ increase as C_a increases. The behavior of $k_{r\alpha}$ is more complicated. In most cases $k_{r\alpha}$ increases as S_α increases, but in certain cases the opposite behaviour has been observed. Roughly speaking, as C_a increases, all the generalized coefficients increase.

Afterwards, *Valvanides and Payatakes* (2001) developed a continuum two-phase flow model, which included the nonlinear dependence of permeability coefficients. Their model was based on the decomposition of a two-phase system into two subdomains; connected-oil path domain and ganglion dynamics domain. The main goal in their model was to save computation time to have a mesoscale predictive model that for practical applications. The model results were compared with experimental results done in a two-dimensional micro-model by *Avraam and Payatakes* (1995a). They founded fairly good to good agreement with experimental results for low capillary numbers ($C_a = 10^{-6}$) at different viscosity ratios. It seems that for high capillary numbers, where ganglia dynamics can be important, the model was not fully successful and there was a need for further improvement before it could be used for predictive purposes.

Bravo et al. (2007) followed the same approach as *Avraam and Payatakes* (1995,a) did, to study coupling coefficients in extended Darcy's law. They used a dynamic pore-network model for simulating disconnected gas and oil flow. What they pre-

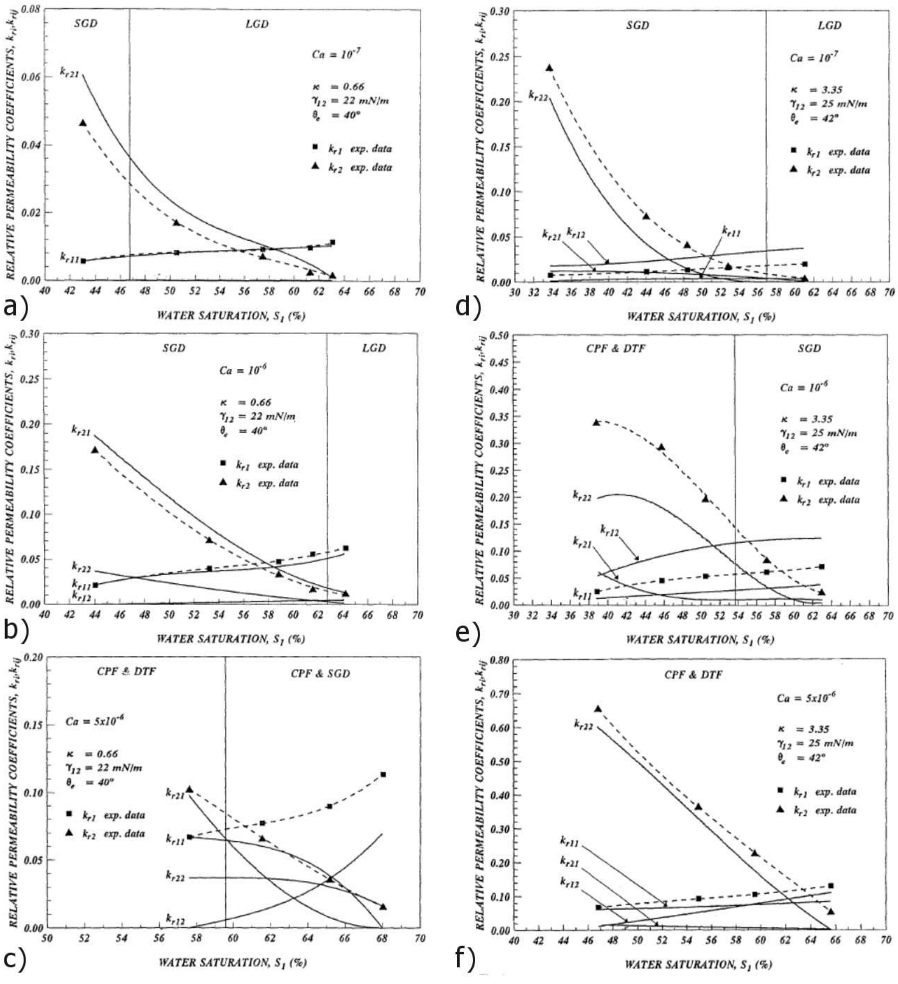

Figure 2.39: *Conventional (broken lines) and generalized (solid lines) relative permeability coefficients for* $\kappa = 0.66$ *(left column) and* $\kappa = 3.35$ *(right column), a,d)* $C_a = 10^{-7}$ *b,e)* $C_a = 10^{-6}$ *c,f)* $C_a = 5 \times 10^{-5}$ *(Avraam and Payatakes, 1995a).*

sented is very similar to the results of *Avraam and Payatakes* (1995a) for very limited cases. They studied the effect of disconnected gas bubbles on relative permeability curves for different bubbles sizes, but only in the viscous-dominated flow regime. They assumed that gas bubbles were incompressible, which is a good approximation when the relative variations of absolute pressures of gas bubbles due to the pressure gradient in water phase and also capillary pressure differences are negligible. However, at least at pore-scale, this assumption is no valid, because absolute pressure is known to fluctuate with time and space as *Constantinides and Payatakes* (1996) have shown.

Bravo et al. (2007) found that when relative permeability of oil increases, when the viscosity of gas bubbles is smaller than that of oil, and even relative permeabilities larger than one can be obtained. In addition, they showed that the effect of gas bubble size at different gas saturations on relative permeability is not monotonic. There is a peak of relative permeability in the intermediate bubble size.

Using a dynamic pore-network model, and assuming a constant injection rate for drainage, *Singh and Mohanty* (2003) showed that for low capillary numbers, flow in the wetting phase flow includes only 1% of the total flow. Based on their results, saturation-relative permeability relationship is a function of capillary number, viscosity ratio and distribution of the pores as shown already by *Blunt and King* (1990) and *Blunt and King* (1991). Their model is based on the pore-network model developed by *King* (1987). However, *King* (1987) did not consider capillary pressure in the setup of equations. Later, *Blunt and King* (1991) added capillary pressure as a function of local pore size and showed that at the same saturation, relative permeability of the receding phase in low capillary numbers is below those with high capillary number as shown in Figure 2.40. But for the invading phase, both cases may occur. They explanation was that at very high rates, flow can proceed through all parts of the network, including the very small tubes. As C_a decreases, flow is blocked in some places due to capillary forces. This will tend to decrease the relative permeability of both injected and displaced fluids. At low rates, the injected fluid moves through only the widest channels, which means an increase of its permeability relative to the displaced fluid. Thus, at a given saturation, $k_{r\alpha}$ must decrease with the decrease of flow rate, while $k_{r\alpha}$ may either increase or decrease. This explanation works for different mobility ratios; so that with the decrease of mobility ratio, relative permeability of the invading phase will decrease. In addition, nonlinearity of relative permeability-saturation curve increases with the increase of interfacial tension.

2.11 Summary

In this review paper we give an overview of various dynamic pore-network models that have been developed for the study of two-phase flow in porous media (Table 2.3). We provide detailed description of various types of network structure, governing equations, and boundary conditions. One of the major computational issues in the dynamic pore-network modelling is related to the pressure field cal-

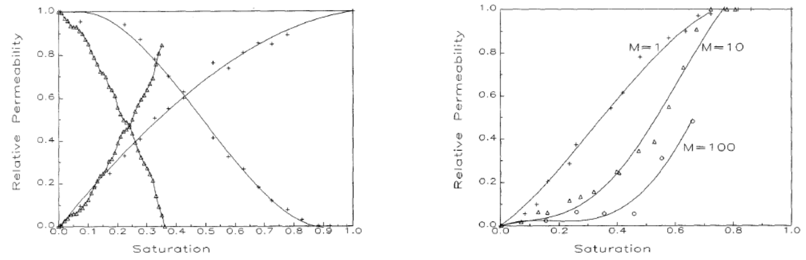

a) b)

Figure 2.40: *Relative permeability-saturation curves for different values of a) C_a number and b) viscosity ratios (Blunt and King, 1991).*

culation. There are two different pressure solver algorithm, namely single-pressure and two-pressure solvers. The latter one has improved physical-based features and computationally is more expernsive than the first one. The second computational issue in the dynamic pore-network modelling is related to the numerical instability problem under capillary-dominated regimes. This problem, referred to as "capillary pinning" has been reported in many studies. Semi-implicit saturation update is one of the solutions that can improve numerical stability of the dynamic pore-network models.

We also give an overview of various applications for which dynamic pore-network models have been used. Different aspects of dynamics of two-phase flow such as pressure field development, macroscopic invasion pattern, effect of capillary number and viscosity ratio on trapping, effect of aspect ratio and coordination number on trapping, nonequilibrium capillarity effects, coupling coefficients for relative permeabilities, ganglia movement, and behavior and dependence of interface velocity have been extensively discussed.

This review shows the capability of pore-network models for giving a better and extensive insight into a larger number of the physical problems related to two-phase flow in porous media. This technique can be very useful not only for investigation of new theories, but also for application in predictive purposes. Although many improvement in dynamic pore-network modelling is achieved, there is still so much room for further development, especially for application for predictive purposes.

Table 2.3: *Summary of the developed dynamic pore-network models and their applications, specifications*

Model Developer	structure	Network elements	Application	Boundary Condition	Dimension Size	Structure	Pressure solver
Aker et al. (1998b)	2-D, S, R	Circular comp.	Drainage, flow regime patterns, front width as a function of C_a	Cons. Flux	60 × 80	A	one-pressure
Aker et al. (1998a)	2-D, S, R	Circular comp.	Drainage, Pressure field evolution with time, effect of trapping on permeabilities	Cons. Flux	60×80 40×40 25×35	A	one-pressure
Al-Gharbi and Blunt (2005)	2-D, S, R	Triangular comp.	Drainage, flow regime patterns, residual saturation vs. C_a	Cons. Flux	9×9	A	one-pressure
Blunt and King (1990)	2-D,3-D, Irr UnS., Iso.	Circular p.th. Spherical p.b.	Drainage, invasion patterns fractional flow vs. C_a and M, relative permeabilities	Cons. Flux	80000 in a sphere	B	one-pressure
Bravo et al. (2007)	2-D, S, R	Square p.th. No p.b.	Disconnected gas flow in oil flow	Cons. Flux	50×50	A	one-pressure
Chaouche et al. (1994)	2-D, S, R	Circular p.th. Spherical p.b.	Drainage, Effect of heterogeneity on saturation distribution	Cons. Flux	100×21 100×60	B	one-pressure
Constantinides and Payatakes (1991)	3-D, S, Dist.R.	Circular comp.	Imbibition, coalescence dependency on topology system dynamics	Cons. Flux	100×7×2	A	one-pressure
Constantinides and Payatakes (1996)	3-D, S, Dist.R.	Circular comp.	Imbibition, steady-state relative permeabilities vs. system dynamics	Cons. Flux	30×20×5	A	one-pressure
Dahle and Celia (1999)	3-D, S, R	Circular p.th. No p.b.	Drainage, P^c-S curve	Cons. Flux	17×17×29	A	one-pressure
Dias and Payatakes (1986a)	2-D, S, R	Circular comp.	Imbibition, effect of C_a and M on residual saturation and interface dynamics	Cons. Flux	15×40	A	one-pressure

S: Structure, UnS:Unstructured, R:Regular, Irr: Irregular, Comp.:composite, p.th.:pore throat, p.b.:pore body, A: No pore body is assumed, resistance and volume are assigned only to pore throats, B: No resistance is assigned to pore bodies and no volume is assigned to pore bodies, C: Volume and resistance are assigned to either pore throats or pore bodies

Model Developer	structure	Network elements	Application	Boundary Condition	Dimension Size	Structure	Pressure Solver
Dias and Payatakes (1986b)	2-D, S, R	Circular comp.	Imbibition, effect of C_a and M on ganglia mobilization, stranding, and breakup	Cons. Flux	15×40	A	one-pressure
Gielen et al. (2004, 2005)	3-D, S,. R	Circular p.th. Spherical p.b.	Drainage, nonequilibrium effects in phase pressures difference	Cons. Pres.	30×30×40 10×10×82	B	one-pressure
Hughes and Blunt (2000)	2-D, 3-D, S, R	Angular p.th. Angular p.b.	Imbibition, effect of C_a, aspect ratio, contact angle, initial saturation on invasion regime and its pattern	Cons. Flux	128×128 20×20×20	B	one-pressure
Joekar-Niasar et al. (2010a)	3-D, S., R	Square p.th. Cubic p.b.	Drainage, Non-equilibrium effects on phase pressures difference and interfacial area	Cons. Pres.	35×35×35	B	two-pressure
Joekar-Niasar and Hassanizadeh (2010)	3-D, S., R	Square p.th. Octahedon p.b.	Drainage & Imbibition, Non-equilibrium effects on phase pressures difference	Cons. Pres.	45×35×35	B	two-pressure
King (1987)	2-D, Uns., Irr	Circular p.th.	Drainage, Fractal nature of invasion front	Cons. Pres.	N.A.	A	one-pressure
Knudsen and Hansen (2002) *Knudsen et al.* (2002)	2-D, R, S	Circular comp.	Countercurrent flow, nonequilibrium relative permeabilities	Closed boundaries	20×40 40×80	A	one-pressure
Koplik and Lasseter (1985)	2-D, UnS., Irr	Circular p.th. Spherical p.b.	Imbibition, Effect of C_a on residual saturation, snap-off and piston-like movement	Cons. Flux	10×10	-	one-pressure
Lam and Horváth (2000)	2-D, S, R	Circular p.th., no p.b.	Imbibition, scaling fronts	Periodic boundaries	1000×200	A	one-pressure
Løvoll et al. (2005)	2-D, S, R	Circular p.th., no p.b.	Drainage, gravity and viscous forces on invasion pattern	Cons. Press. boundaries	N.A.	A	one-pressure

S: Structure, UnS:Unstructured, R:Regular, Irr: Irregular, Comp.:composite, p.th.:pore throat, p.b.:pore body, A: No pore body is assumed, resistance and volume are assigned only to pore throats, B: No resistance is assigned to pore bodies and no volume is assigned to pore bodies, C: Volume and resistance are assigned to either pore throats or pore bodies.

Model Developer	structure	Network elements	Application	Boundary Condition	Dimension Size	Structure	Pressure Solver
Mogensen and Stenby (1998)	3-D, S, Irr	Square p.th., Cubic p.b.	Imbibition, Effect of C_a,M, aspect ratio, coordination no., on snap-off & piston-like movement	Cons. Flux	25×25×25	C	one-pressure
Nguyen et al. (2004, 2006)	3-D, UnS, Irr	Triangular p.th. Cubic p.b.	Imbibition, effect of contact angle, C_a , aspect ratio on relative permeabilities	Cons. Flux.	12349 p.b. 26146 p.th.	C	one-pressure
Nordhaug et al. (2003)	3-D, S, R	Circular p.th. Spherical p.b.	Drainage, interface velocity for different regimes	Cons. Press.	10×10×50	B	one-pressure
Payatakes (1982)	2-D, S, R	Circular comp. Spherical p.b.	Imbibition, ganglia movement	Cons. Flux	15×30	A	one-pressure
Pereira et al. (1996)	2-D, S, R	Eye-shaped p.th. Spherical p.b	Drainage, three-phase flow	Cons. Press.	50×50	B	Three-phase pressure
Singh and Mohanty (2003)	3-D, S, R	Square p.th. Cubic p.b.	Drainage, Effect of C_a on residual saturation	Cons. Flux.	30×8×8	B.	one-pressure
Thompson (2002)	3-D, S, R	Angular. p.th. Cubic p.b	Imbibition, Effect flow rate on water invasion in paper	Cons. Flux.	2000		two-pressure
Touboul et al. (1987)	2-D, S, R	Circular p.th. Spherical p.b.	Drainage, Effect of pressure on fingering and stable movement	Cons. Flux.	100×100	A	one-pressure
Valvanides et al. (1998)	3-D, S, R	Circular comp.	Imbibition, large and small ganglia dynamics	Cons. Flux.	30×20×5	A	one-pressure
Van der Marck et al. (1997)	3-D, S, R	Circular p.th. Spherical p.b.	Drainage, Pressure field evolution vs. saturation	Cons. Flux.	25×25×2	B	one-pressure
Vizika et al. (1994)	3-D, S, R	Circular comp.	Imbibition, Effect of M and C_a on residual saturation	Cons. Flux.	12×5×2	A	one-pressure

S: Structure, UnS:Unstructured, R:Regular, Irr: Irregular, Comp.:composite, p.th.:pore throat, p.b.:pore body, A: No pore body is assumed, resistance and volume are assigned only to pore throats, B: No resistance is assigned to pore bodies and no volume is assigned to pore bodies, C: Volume and resistance are assigned to either pore throats or pore bodies.

Part II

Quasi-Static Simulations

Published as: Joekar-Niasar, V., Hassanizadeh, S.M., Leijnse A. – *"Insights into the relationships among capillary pressure, saturation, interfacial area and relative permeability using pore-network modelling,"* Transport in Porous Media, vol. 74, pp. 201–219, 2008.

Chapter 3

Conceptual Pore-Network Models

The question is not what you look at, but what you see.

Henry David Thoreau, writer

Abstract

To gain insight into relationships among capillary pressure, interfacial area, saturation and relative permeability in two-phase flow in porous media, we have developed two types of pore-network models. The first one, called tube model, has only one element type, namely pore throats. The second one is a sphere-and-tube model with both pore bodies and pore throats. We have shown that the two models produce distinctly different curves for capillary pressure and relative permeability. In particular, we find that the tube model cannot reproduce hysteresis. We have investigated some basic issues such as effect of network size, network dimension, and different trapping assumptions in the two networks. We have also obtained curves of fluid-fluid interfacial area versus saturation. We show that the trend of relationship between interfacial area and saturation is largely influenced by trapping assumptions.

Through simulating primary and scanning drainage and imbibition cycles, we have generated two surfaces fitted to capillary pressure, saturation, and interfacial area (P^c-S^w-a^{nw}) points as well as to relative permeability, saturation and interfacial area (k_r-S^w-a^{nw}) points. The two fitted three-dimensional surfaces show very good correlation with the data points. We have fitted two different surfaces to P^c-S^w-a^{nw} points for drainage and imbibition separately. The two surfaces do not completely coincide. But, their mean absolute difference decreases with increasing overlap in the statistical distributions of pore bodies and pore throats. We have shown that interfacial area can be considered as an essential variable for diminishing or eliminating the hysteresis observed in capillary pressure- saturation (P^c-S^w) and the relative permeability-saturation (k_r-S^w) curves.

3.1 Introduction

In two-phase systems in porous media, the constitutive equation that relates fluid pressures to saturation plays an important role. Equation 3.1 states that the difference in fluid pressures, called capillary pressure, is a function of saturation (*Bear* *et al.*, 1968).

$$P^n - P^w = P^c \equiv f(S^w) \tag{3.1}$$

in which, P^n $[ML^{-1}T^{-2}]$ is the pressure of the nonwetting phase,P^w $[ML^{-1}T^{-2}]$ is the pressure of the wetting phase, $P^c[ML^{-1}T^{-2}]$ is the capillary pressure, and S^w is the saturation of the wetting phase. This relationship is known to be hysteretic. For a given soil, many P^c-S^w curves pertaining to different drainage/imbibition stages and histories are possible. Using a thermodynamically-constrained averaging approach, *Hassanizadeh and Gray* (1990) derived an extended theory of capillarity. According to their results, capillary pressure is not only a function of saturation but also of specific areas of the three interfaces that are present in a two-phase flow system:

$$P^c = f(S^w, a^{\alpha\beta}); \alpha\beta = wn, ws, ns \tag{3.2}$$

where $a^{\alpha\beta}[L^{-1}]$ denotes the specific area of $\alpha\beta$-interface; that is, the area of $\alpha\beta$-interface per unit volume of the porous medium. Here, subscripts w, n, and s denote wetting phase, nonwetting phase, and solid phase, respectively. Later, *Hassanizadeh and Gray* (1993a) suggested that the role of ws-and ns-interfaces are not significant and proposed a simpler relationship:

$$P^c = f(S^w, a^{nw}) \tag{3.3}$$

where a^{nw} denotes the specific area of wn-interface, which we refer to it simply as specific interfacial area in the remainder of this paper. Equation 3.3 prescribes a surface relating capillary pressure, saturation and interfacial area. *Hassanizadeh and Gray* (1993a) conjectured that the resulting surface might be the same for drainage and imbibition; i.e. it might be devoid of hysteresis. This conjecture has been investigated in few studies using computational and experimental approaches (see e.g. *Chen and Kibbey*, 2006, *Held and Celia*, 2001, *Reeves and Celia*, 1996). In experimental studies, many researchers have tried to measure the interfacial area under static conditions. These techniques are mostly categorized under two main groups; tracers or imaging techniques. Aqueous tracers have been used by *Anwar et al.* (2000), *Brusseau et al.* (1997), *Chen and Kibbey* (2006), *Karkare and Fort* (1996), *Kim et al.* (1997), *Saripalli et al.* (1998), *Schaefer et al.* (2000), and gas tracers have been used in some other studies such as *Brusseau et al.* (2006), *Costanza-Robinson and Brusseau* (2002), *Kim et al.* (1999). Imaging techniques have been used by *Al-Raoush and Willson* (2005a,b), *Cheng et al.* (2004), *Culligan et al.* (2004), *Montemagno and Pyrak-Nolte* (1995), *Wildenschild et al.* (2002); and *Schnaar and Brusseau* (2005, 2006).

Computational approaches have been mainly based on pore-network modelling or lattice-Boltzmann models. A valuable tool for the theoretical study of two-phase flow in porous media is pore-network modelling (traditionally called pore-scale network modelling, which is unnecessarily long), introduced for the first time by (*Fatt*, 1956). This tool has been used extensively by many researchers for studying various processes in porous media (e.g. *Blunt et al.*, 2002, *Burganos and Payatakes*, 1992, *Dias and Payatakes*, 1986a, *Gielen*, 2007, *Reeves and Celia*, 1996). In addition to using pore-network models for theoretical studies, some researchers have tried to develop predictive models for various purposes. *Vogel* (1997, 2000), *Vogel and Roth* (1998) used the serial sectioning technique to produce a representative pore-network, and modelled soil relative permeability. *Hui and Blunt* (2000) have also modelled the relative permeability for a three-phase system using a bundle of tubes of different sizes with constant triangular cross sections. *Blunt et al.* (2002) have concluded that by combining an appropriate pore-scale physics with a geologically representative description of the pore space, one can produce capillary pressure and relative permeability curves for a given rock without actual measurements. They produced primary drainage and water-flood relative permeabilities for Berea sandstone using pore-network modelling. *Piri and Blunt* (2005a) developed a pore-scale model, which included all important features of immiscible fluid flow at the pore-scale, such as wetting layers, spreading layers of the intermediate-wetting phase, hysteresis and wettability alteration. The model computes relative permeabilities, saturation paths, and capillary pressure for any displacement sequence. They have reported a good agreement between experiment and simulation results for the relative permeability in a two-phase (water-wet) system.

Despite the wide interest in measuring and /or calculating specific interfacial area and capillary pressure, there are surprisingly very few works on the validity of Equation 3.3. There are some experimental studies where a^{nw}-S^w curves are produced (see e.g. *Chen and Kibbey*, 2006, *Cheng et al.*, 2004). These curves are all found to be hysteretic. In the recent experiments by *Cheng et al.* (2004), a^{nw}-P^c-S^w surfaces are obtained. They find that the drainage and imbibition surfaces have a difference of only 2.77%.

The first theoretical studies of Equation 3.3 were done by *Reeves and Celia* (1996) and later by *Held and Celia* (2001) using pore-network models. They developed a static pore-scale cubic lattice network model that included spheres and bi-conical elements representing pore bodies and pore throats, respectively. They did not consider trapping during drainage in their simulations. They could produce smooth and well-behaved three-dimensional surfaces relating saturation, interfacial area, and capillary pressure, based on successive drainage and imbibition cycles. The drainage and imbibition surfaces obtained by *Reeves and Celia* (1996), however, were distinctly different. So, they concluded that P^c-S^w-a^{nw} surface was still hysteretic. Moreover, they noticed that the surface was not monotonic; for a given a^{nw} and

S^w two different values of P^c were possible. This led to the proposition to replace Equation 3.3 with a relationship for fluid-fluid interfacial area:

$$a^{nw} = F(S^w, P^c) \tag{3.4}$$

Later, *Held and Celia* (2001) showed that the hysteresis in the a^{nw}-S^w-P^c surface could be almost eliminated if a certain choice of fluid displacement parameters is used. For some specific values for snap-off and local coefficients related to the fluid configuration, they found a separation of less than 1.5 % between imbibition and drainage surfaces. Because the required displacement rules were in agreement with commonly observed experimental condition, they argued that the modelling of hysteresis in capillary pressure-saturation curves through inclusion of fluid-fluid interfacial area in the formulation of two-phase flow theories is a real possibility. In a recent work, *Helland and Skjæveland* (2007) have also studied a^{nw}-S^w-P^c relationship using mixed-wet triangular bundle of tubes. They have concluded that very different trends in the specific interfacial area vs. saturation curves can occur during imbibition, depending on the reversal point after primary drainage and the advancing contact angle. In addition, they found that hysteresis can be present between imbibition and secondary drainage if contact angle hysteresis is assumed. They also concluded that a more complex model is required if one is to consider effect of phase entrapment and snap-off events.

It is evident that the effect of interfacial area on P^c-S^w relationship has been studied in very few works. Also, so far no one has studied the role of interfacial area in k_r-S^w relationship. In this study, we focus on understanding the relationships among interfacial area, capillary pressure, saturation, and relative permeability, using pore-network models. We will show that the inclusion of interfacial area in S^w-P^c and k_r-S^w relationships may lead to a very significant decrease in the hysteresis observed in these curves. Two different static pore-networks have been developed, and the aforementioned relationships have been studied. One is based on Fatts model and has only one element type, namely pore throat. The second one is a sphere-and-tube model with both pore bodies and pore throats. We have studied Representative Elementary Volume (REV) size, side boundaries effect, effect of trapping assumptions, and the role of pore size distribution in our models. We investigate the role of interfacial area in qualifying hysteresis observed in P^c-S^w and S^w-k_r relationships. To this end, we have produced surfaces linking capillary pressure and saturation to interfacial area (P^c-S^w-a^{nw} surface) as well as saturation and relative permeability to interfacial area (S^w-a^{nw}-k_r surface).

3.2 Model description

3.2.1 Model structure

We have developed two types of pore-networks. Both of them have a fixed coordination number of six. The first network is based on Fatts model (*Fatt*, 1956). It consists of tubes only and is hereafter called the *tube network*. No volume is assigned to the nodes, where tubes are connected to each other. The second network consists of tubes and spheres, which represent pore throats and pore bodies, respectively. We refer to it as the *sphere-and-tube network*. The cross section of network elements is considered to be circular. Radius distribution of pore bodies in the sphere-and-tube network, and radius distribution of pore throats (tubes) in the tube network have been generated using a truncated random log-normal number generator. In the tube network, after generating the radii of the pore throats, their lengths are determined. We use a relationship between the radius and the length of a pore for sandy soil suggested by *Fatt* (1956):

$$l = Cr^{-1} \tag{3.5}$$

in which, l is the pore length $[L]$, C is an empirical constant$[L^2]$, and r is the radius of pore $[L]$. It is clear that using this relationship, the ends of the tubes do not necessarily fall on lattice points. In fact, we do not specify how the tubes are geometrically connected to each other. In the sphere-and-tube network, the length of a pore throat is equal to the spacing of the lattice points minus the sum of radii of the two neighboring pore bodies. The radius of a pore throat is also determined from the radii of neighboring pore bodies. In real porous media, it has been observed that the pore throat radius is correlated with the radii of neighboring pore bodies (see e.g. *Al-Raoush and Willson*, 2005a,b). Thus, we have formulated a procedure, explained in the Appendix A, to determine the radius of a pore throat based on radii of neighboring pore bodies. The porosity of the network is calculated from the sum of volumes of all pore bodies and pore throats divided by the total volume of the lattice. For fluid displacement simulations, the pore network is considered to be connected at the top to a nonwetting phase reservoir, and at the bottom to a wetting phase reservoir. Side faces are assumed to be no-flow boundaries.

3.2.2 Trapping assumptions

For drainage, we have employed two different algorithms regarding the trapping of the wetting phase. In one case, it is assumed that the wetting phase in a pore can be displaced by the nonwetting phase, only if the former is connected to its

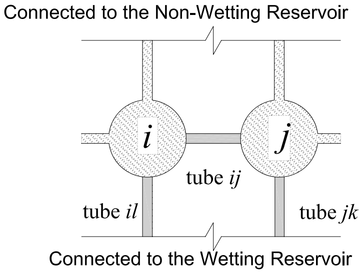

Figure 3.1: *Schematic illustration of the trapping assumptions during drainage*

boundary reservoir. This means when the neighboring pore bodies of a pore throats are filled with the nonwetting phase, that pore throat is considered to be trapped. We refer to this as *tight trapping*. For example in Figure 3.1, if we assume tight trapping, the tube *ij* will be trapped due to the occupation of the neighboring pore bodies by invading phase. However, in real porous media, it is possible for the wetting phase in a trapped pore throat to escape if at least one of the neighboring pore throats is still connected to the wetting phase reservoir. We refer to this as *loose trapping*. So, for example, tube *ij* in Figure 3.1 may be still drained into tubes *il* and *jk*. If, however, tubes *il* and *jk* are also filled with nonwetting phase, the tubes *ij* remains trapped. The trapping assumptions can be seen as a consequence of the real geometrical and topological characteristics of voids. With loose trapping assumption, possibility of occurrence of an individual trapped pore element is less than that of the tight trapping cases. Figure 3.2 schematically shows individual and cluster trapped configurations for loose trapping assumptions.

For imbibition we have applied the tight trapping assumptions, since the wetting phase intends to fill the corners. When the neighboring pore bodies of a pore throats are filled completely with the wetting phase, that pore throat is considered to be trapped. In our simulations of imbibition, no snap-off has been considered. *Mahmud and Nguyen* (2006) have shown in a recent study that the occurrence frequency of piston-like movement of the wetting phase for contact angles larger than 30 degrees in a spatially uncorrelated network is about twice that of snap-off movements. According to their conclusion, if there is no spatial correlation between the pores (similar to our pore-network model), the role of snap-off movements in fluid configuration is not important. Thus we have not considered the snap-off mechanism in our simulations.

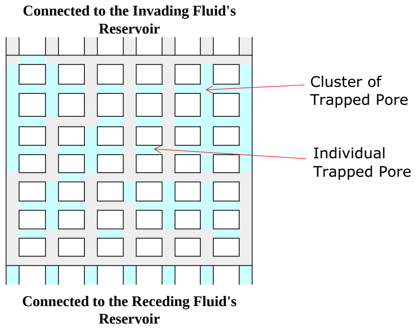

Figure 3.2: *Schematic presentation of individual and cluster trapped pore*

3.3 Numerical experiments

Conventional drainage and imbibition experiments have been simulated with the two pore networks. Primary and/or main drainage and imbibition curves as well as scanning curves are obtained following the procedure described farther below. For an imposed capillary pressure, the occupancy of pore throats and pore bodies, under imbibition or drainage and assuming equilibrium, has to be determined. To do so, we need to have the entry capillary pressure for a pore throat, which is calculated using Young-Laplace equation:

$$P^c = P^n - P^w = \frac{2\sigma cos\theta}{r} \tag{3.6}$$

where σ is the interfacial tension $[MT^{-2}]$, r is the radius of pore $[L]$, and θ is the contact angle between solid surface and fluid-fluid interface. The entry pressure of a pore throat in our network is always larger than that of its neighboring pore bodies, because it has a smaller radius than the connected pore bodies.

At any imposed capillary pressure, saturation of each phase can be easily calculated as we know the occupancy of the network. We can also calculate the interfacial areas as we know the location of fluid-fluid interfaces for any given configuration of fluids. During drainage, interface area is calculated based on the radius of the pore throats where the interface is located. However, during imbibition we may also interface in the pore bodies. The interface area in pore bodies is calculated based on the curvature of interface, which can be obtained from Equation 3.6, for an imposed capillary pressure. As shown in Figure 3.3, we have not considered existence of multiple interfaces in a pore body even if the wetting phase enters a pore body through two or more pore throat. Area of the interface is calculated based on the curvature assigned by the imposed capillary pressure. Thus, at each capillary pressure, corresponding wetting (or nonwetting) saturation and interfacial area will be known. So, our simulations result in a large number of P^c-S^w-a^{nw} data points. Using these data, and producing P^c-S^w-a^{nw} surfaces for drainage and imbibition, we can investigate the role of interfacial area in eliminating the hysteresis observed in P^c-S^w curve.

3.3.1 Drainage steps

Initially, the network is assumed to be saturated with the wetting phase. The pressure of the wetting phase reservoir is assumed to be zero and not changing. Therefore, the pressure of wetting phase in all pores connected to the wetting phase reservoir is also zero until a pore becomes trapped. Initially, the pressure of nonwetting phase reservoir is zero, and thus the imposed capillary pressure is also zero. Primary drainage simulations start by increasing the pressure of nonwetting phase reservoir until it exceeds the entry pressure of the largest pore throat connected to the reservoir. As the radius of a pore body is larger than that of a pore throat, the controlling element is the pore throat. Thus, as soon as the pressure is high enough to enter a pore throat, nonwetting phase will occupy that pore and the connected pore body. When no other pores can be occupied in that pressure step, the nonwetting phase pressure will be increased and more pores will be occupied by the nonwetting phase. Drainage continues, with incrementally increasing nonwetting phase pressure, until the last row of pore throats is filled by the nonwetting phase. Scanning drainage curves are obtained following imbibition simulations by reversing the imbibition process (described below) at various saturations.

3.3.2 Imbibition steps

Imbibition is simulated by decreasing the pressure of nonwetting-phase reservoir (or increasing the pressure of wetting-phase reservoir), causing the nonwetting phase to recede. The replacement of the nonwetting phase by the wetting phase starts from those pore throats that have the highest entry pressure (smallest size). Then, as shown in Figure 3.3, the wetting phase enters the neighboring pore body and stops at a position with a curvature corresponding to the imposed capillary pressure. In each pore body, one interface is permitted, regardless the occupancy of the connected pore throats. As the capillary pressure is decreased, the wetting phase gradually fills the pore body. As soon as the interface radius is equal to the pore body radius, the rest of the pore body and the connected pore throats will be filled up instantaneously by the wetting phase. Hence, the governing element dur-

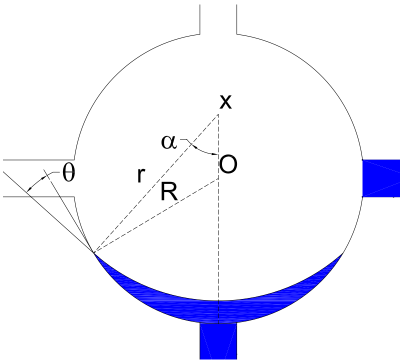

Figure 3.3: *Schematic of interface positioning during imbibition. R is radius of pore body, r is radius of interface dictated by the imposed capillary pressure, and θ is the contact angle. The pore body will be filled up gradually controlled by r. As soon as r is equal to R, the pore body will be filled up instantaneously.*

ing imbibition is the pore body.

3.3.3 Relative permeability

Relative permeability for each phase is commonly determined as a function of average saturation. The relationship is known to be hysteretic. We would like to establish whether wetting-nonwetting interfacial area plays a role in this relationship. In this section, we describe how relative permeability is determined for a succession of different fluids configurations in a network, corresponding to the full range of saturation. As described above, in simulations of drainage and imbibition at any imposed P^c, we obtain a static fluids configuration in the network. For each configuration, we calculate the relative permeabilities for the two phases. This will be done by assigning a pressure difference within each phase across the network, and calculating flow rate and consequently relative permeability for each phase. The flow rate in each pore throat is calculated using the Poiseuilles formula:

$$q_{ij} = \frac{\pi}{8\mu} r_{ij}^4 \frac{P_i - P_j}{l_{ij}} \tag{3.7}$$

in which q_{ij} is the discharge through the tube from pore body *i* to *j*, μ is the viscosity, P_i and P_j are the pressures in pore bodies *i* and *j*, respectively, and l_{ij} is the length of the pore throat. The volume balance for each pore body i would require:

$$\sum_{j=1}^{N_i} q_{ij} = \frac{\pi}{8\mu} \sum_{j=1}^{N_i} r_{ij}^4 \frac{P_i - P_j}{l_{ij}} = 0 \tag{3.8}$$

Writing this equation for each pore body results in a set of linear equations, **A**x =b, which can be solved for the pressure in each fluid phase. In matrix **A**, for a given phase, only those pore bodies are involved that are connected to both upstream and downstream reservoirs, as there is no flow in dead-end or isolated pores. Having determined the pressure field in the network, the total flow rate through the network for each phase can be calculated.

3.4 Results and discussion

3.4.1 REV in a pore-network model

One of the first questions we investigated was the minimum network size for which the results become insensitive to the network size. This representative network size may be considered to correspond to the Representative Elementary Volume (REV) for the porous medium being modelled. The REV size of the network has been determined based on the value of irreducible saturation as well as S^w-a^{nw} relationship. Determination of REV is also essential for testing the validity of results for a given statistical distribution and for saving computer time and memory, as we do not want to work with a too large network. Figure 3.4a shows values of irreducible wetting phase saturation for different sizes of network. It confirms that irreducible saturation does not change significantly for cubic networks larger than 40 nodes in each coordinate direction. Similarly, Figure 3.4b shows that for a specific statistical distribution of pore elements, the slope of S^w-a^{nw} curve is not significantly influenced by the cubic network size larger than 40 nodes. We are also interested to see what the effect of no-flow side boundaries on the results is. This is done by varying the size of the network cross section perpendicular to the flow, and comparing resulting P^c-S^w and S^w-a^{nw} curves of sphere-and-tube network and tube network, given in Figures 3.5a and 3.5b, respectively. As it is illustrated, results of networks with cross sections of 10×40 nodes and 40×40 nodes are almost identical. Thus, we conclude that there is no effect from assuming no-flow side boundaries of the network. However, as expected, there is a significant difference between the results of 2-dimensional (e.g. 1×40×40) networks and 3-dimensional networks (e.g. 2×40×40 or larger). This is mainly due to the differences in the coordination number. Coordination number for internal nodes of the 1×40×40 network is 4, for 2×40×40

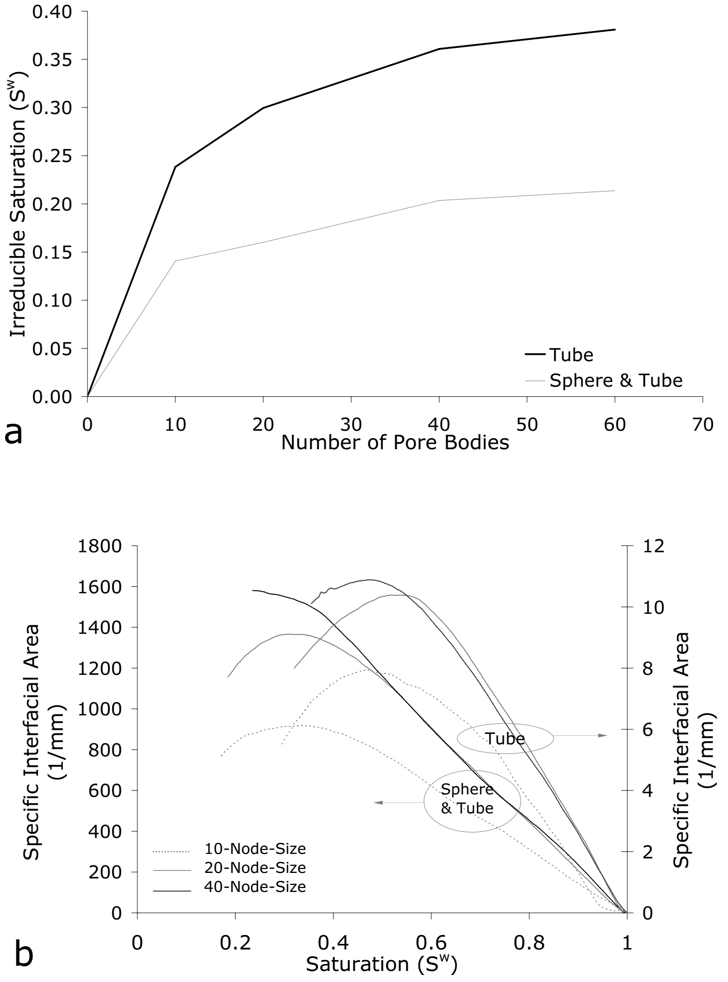

Figure 3.4: *REV definition for networks in terms of irreducible saturation and* a^{nw} *curve. a) Irreducible saturation vs. size of network b) Specific* a^{nw} *vs.* S^w *during drainage for tube and sphere-and-tube networks with different sizes of 40, 20 and 10 nodes.*

network is 5 and, for larger networks is 6. A smaller coordination number means less possibility for escape of the receding phase, and this influences the results significantly.

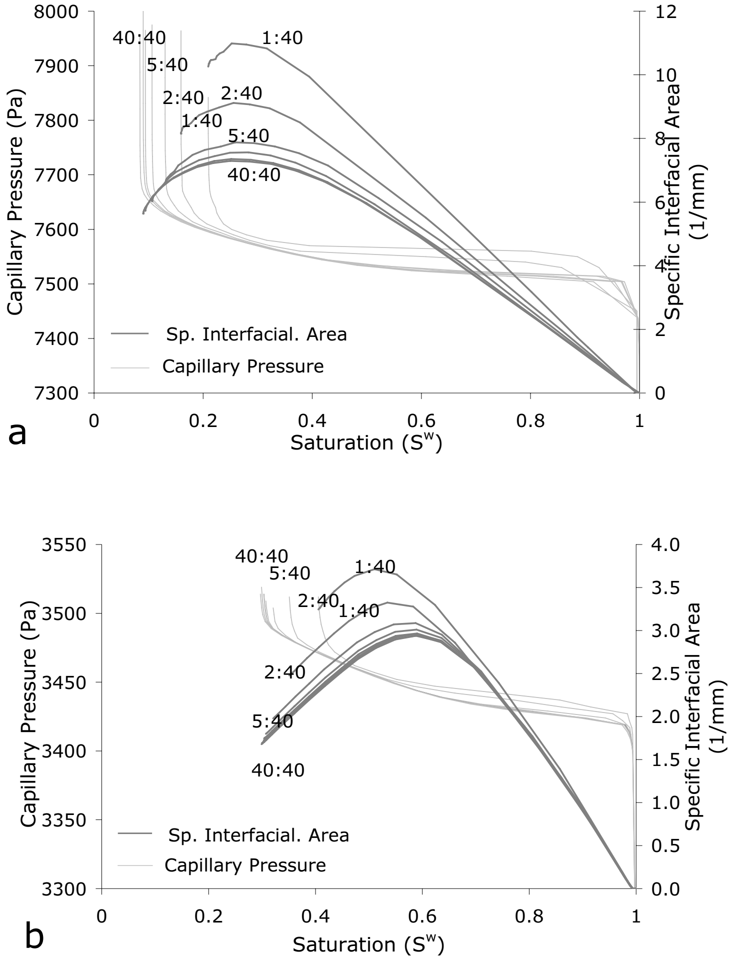

Figure 3.5: *Effect of boundary on P^c-S^w and S^w-a^{nw} curves for drainage. a) Sphere-and-tube network. b) Tube network. Dashed lines show S^w-a^{nw} relationship, and solid lines show P^c-S^w relationship. The full size network is a cubic 40-node network. The curves are shown for different cross section sizes normal to the flow direction.*

3.4.2 Effect of trapping assumptions

As shown in Figure 3.6a, variation of interfacial area with saturation can be influenced by different trapping assumptions we make in the simulations. Figure 3.6a shows the variation of interfacial area with saturation under three different assumptions; no trapping, loose trapping and tight trapping. Drainage simulations with these three assumptions are done up to the irreducible saturation. Under the tight-trapping assumption, interfacial area increases monotonically with decreasing saturation during drainage, while in no-trapping or loose trapping conditions it reaches a maximum value. In the saturation range of 100% to 55-60%, all curves are almost the same. As the invasion of nonwetting fluid into the porous medium occurs, more and more interfacial area is created until the clusters of invading fluid reconnect. At that stage, in some parts of the network, not only no new interfacial area is created, but also interfacial area disappears due to the re-connection of invading clusters. The tight trapping and no-trapping curves show the extremes of a^{nw}-S^w curves for various trapping assumptions. Figure 6a illustrates that the trapping conditions can control the irreducible saturation to be 0%, 15%, or 30% for no-trapping, loose-trapping, or tight-trapping conditions, respectively.

Qualitative comparison between our results and experiments on real porous media (Figure 3.6b) suggests that loose-trapping assumption in modelling seems more in agreement with some real porous media. In addition, the order of magnitude of specific interfacial area in simulations is in agreement with measurements done using imaging techniques in real porous media (see e.g. *Brusseau et al.*, 2006, *Culligan et al.*, 2004, 2006).

3.4.3 P^c-S^w and S^w-a^{nw} relationships

Figures 3.7 and 3.8 show P^c-S^w and S^w-a^{nw} curves, respectively, from a series of networks with different pore size distributions. These curves have been obtained from tube and sphere-and-tube networks with loose-trapping assumption. Log-normal distributions of pore body radii with mean and standard deviation of 0.065 mm and 0.02 mm, respectively, have been employed. In each case, curves for 20 realizations for uncorrelated networks as well as the average curve with cubic size of either 20 or 40 nodes are shown. With increasing network size, band width of variation of P^c-S^w and S^w-a^{nw} curves decreases. This implies that to obtain the average P^c-S^w and S^w-a^{nw} curves of a specific pore-network model, with increase of network size, fewer realizations will be required. Furthermore, our simulations showed (not presented here) that for larger variances more realizations are required to achieve the average behaviour.

As seen in Figure 3.7, the two types of networks produce different P^c-S^w curves. This is partly due to the fact that we assign the same size distribution to pore bodies in the sphere-and-tube network, and to pore throats in the tube network. Thus, the minimum size of the pore throats in the tube network is the same as the minimum pore body size in the sphere-and-tube network. The latter is always larger than the

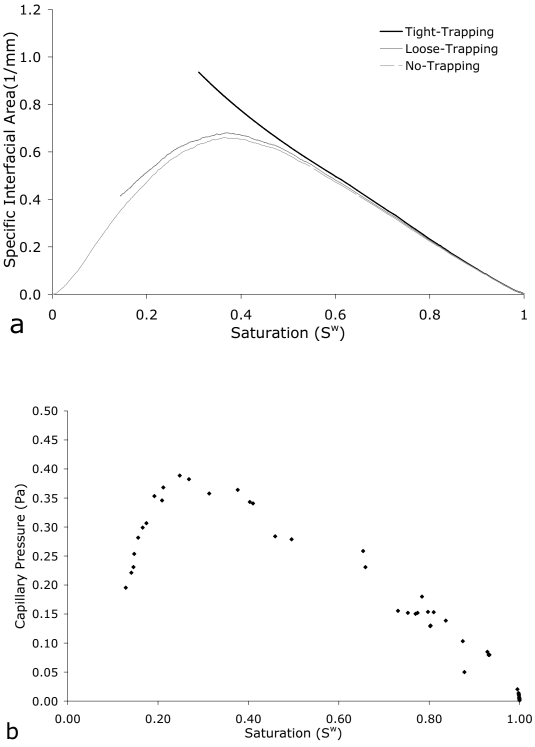

Figure 3.6: *Qualitative comparison between the model results and experiments for a^{nw}-S^w relationship a) Variation of interfacial area with saturation under drainage for three different trapping assumptions. Solid black line shows tight trapping, solid gray line shows loose trapping and dashed gray line shows no trapping. b) Graph of specific interfacial area vs saturation obtained by microtomography of glass beads (Culligan et al., 2006).*

minimum pore throat size in that network. That procedure sometimes results in very small pore throats. As a result, the range of capillary pressure and interfacial area in the two networks are quite different.

Figure 3.9a shows that, as there is only one network element (namely pore throats) in the tube model, it cannot reproduce hysteresis in a P^c-S^w curve. Furthermore, as shown in Figure 3.9b, there is a jump in interfacial area at the beginning of imbibition experiment in the tube network. Since there is no pore body, there is no gradual change of interfacial area during imbibition, contrary to the sphere-and-tube network results. As seen in Figure 3.9a, when the controlling elements during drainage and imbibition are different (as in the sphere-and-tube network), hystere-

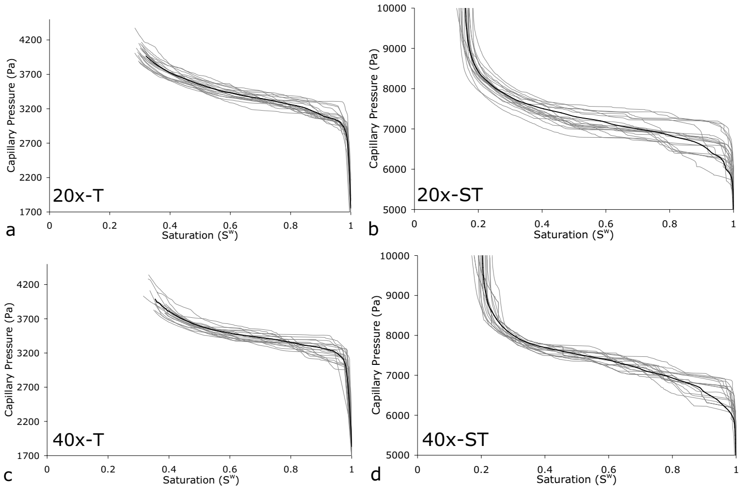

Figure 3.7: *P^c-S^w curves for drainage with loose trapping assumption. Thin and thick solid lines show realizations and the average curve, respectively.*

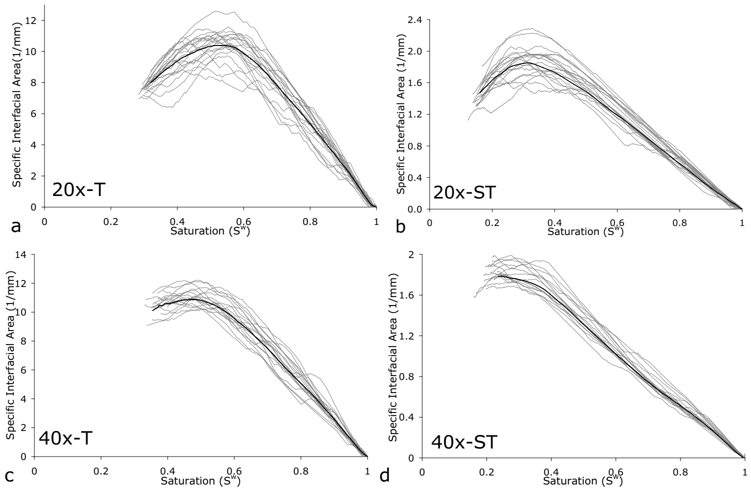

Figure 3.8: *S^w-a^{nw} curves for drainage with loose trapping assumption. Thin solid and thick lines show realizations and the average curve, respectively.*

sis in P^c-S^w curves can be produced. In recent experiments for determining the S^w-a^{nw} relationship (see e.g. *Culligan et al.*, 2004, 2006), it was found that the maximum interfacial area occurs at saturations around 30%. Figures 3.8 and 3.9 show that this maximum value occurs at saturation of 25-30% in the sphere-and-tube and at saturation of 45-55% in the tube network. It is evident that the behaviour of the

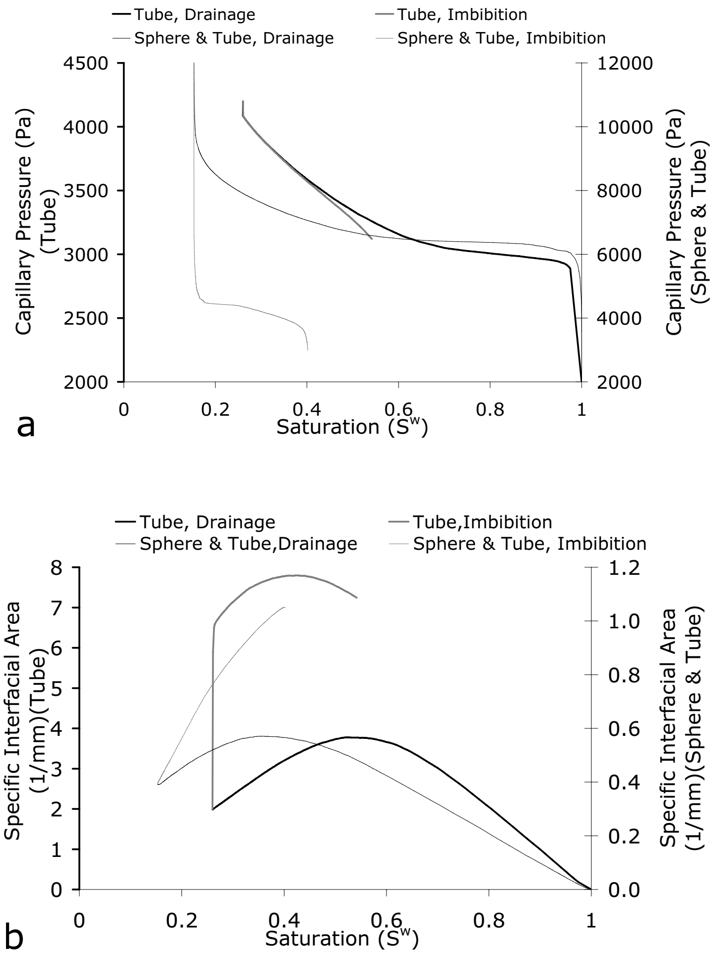

Figure 3.9: *Typical* P^c-S^w *and* S^w-a^{nw} *curves of drainage and imbibition for tube and sphere-and-tube networks. a)* P^c-S^w *relationship b)* S^w-a^{nw} *relationship. Solid lines are related to the tube network and dashed lines show sphere-and-tube network results. Black lines represent drainage, and gray lines represent imbibition.*

sphere-and-tube model is more realistic in representing the soil characteristics than the tube model. Although this result may have been expected, it is important to have it established with the aid of model simulation.

3.4.4 P^c-S^w-a^{nw} surface

Using data points from primary and scanning curves of drainage and imbibition simulations in sphere-and-tube network, we can produce a surface relating capillary pressure, saturation and interfacial area. The full set of drainage and imbibition curves are shown in Figures 3.10a and 3.10b, respectively. The corresponding interfacial area points are plotted in Figure 3.10c. We were able to fit a second-order polynomial surface to the data points. As shown in Table 3.1, there is a very good correlation coefficient (0.956) for the fitted surface. We have also fitted two separate surfaces to P^c-S^w-a^{nw} drainage and imbibition data points as shown in Figure 3.11. The mean absolute difference between these two surfaces is 8.5%. We also produced such surfaces for a pore network with disconnected statistical distributions for pore bodies and pore throats. As usual, the pore throats are smaller than pore bodies and their distributions have no overlap. In this case (results are not presented here), the mean absolute difference between the two surfaces was much larger (about 18%). These results show that if the size distributions of pore bodies and pore throat are correlated and show overlap, one may expect less difference between imbibition and drainage surfaces. As *Al-Raoush and Willson* (2005a,b) have shown in their experimental measurements, the size distributions of pore bodies and pore throats do have a large overlap and it is hard to distinguish pore bodies from pore throats in real porous media. Thus we expect less difference between imbibition and drainage surfaces in correlated pore-network models mimicking the reality, as compared to uncorrelated pore-network models.

3.4.5 k_r^w-S^w-a^{nw} surface

After calculating relative permeability at various average saturations in the sphere-and-tube network, we can construct k_{rw}-S^w-a^{nw} surface similar to work done by *Reeves* (1997). Figure 3.12a shows relative permeability-saturation curves for the two phases during drainage and imbibition. It shows that the hysteresis observed in the krw-Sw relationship is not as strong as the hysteresis observed in P^c-S^w relationship. Figure 3.12b shows a typical kr-anw relationship for the two phases. It can be observed that at a given interfacial area, two different values for the relative permeability are possible, and hysteresis observed in k_r-a^{nw} relationship is more significant than that of k_r-S^w relationship. Finally, a three-dimensional representation of the k_{rw}-S^w-a^{nw} surface for the wetting phase is shown in Figure 3.12c. We have fitted a second-order polynomial surface to P^c-S^w-a^{nw} and k_{rw}-S^w-a^{nw} simulation data of the sphere-and-tube network with loose-trapping assumption. Statistical properties of the model results and fitted surfaces are shown in Table 3.1. We see that the correlation coefficients are very high. We also found that the maximum

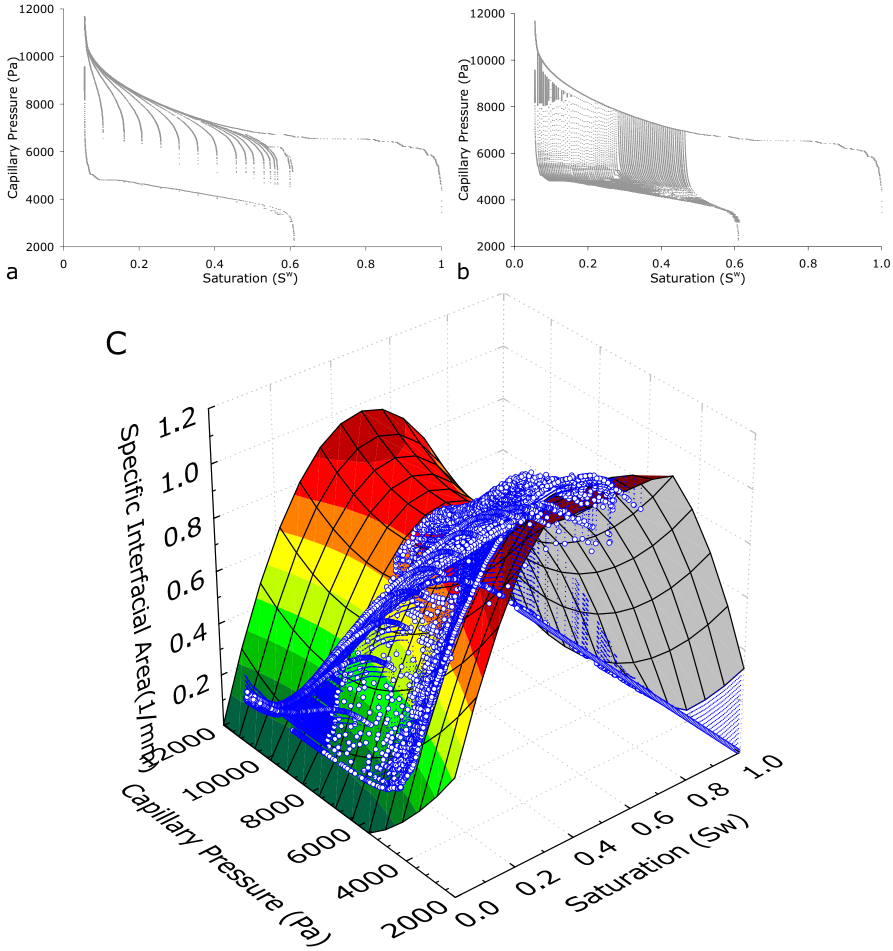

Figure 3.10: *Relationship among P^c (N/m^2), S^w, and a^{nw} $(1/m)$ for a) Drainage curves b) Imbibition curves (**c**) All P^c-S^w-a^{nw} points with fitted second-order polynomial surface.*

deviation happens during the primary drainage at high saturations. The equations of fitted surfaces are as follows (in SI unit):

$$a^{nw} = 849 + 3858S^w - 0.224P^c - 3992S^{w^2} + 0.006S^w \times P^c + (1.28E-5)P^{c^2}$$

$$k_{rw} = 1.26S^w - (4.39E-4)a^{nw} - 0.32S^{w^2} + (2.301E-4)S^w \times a^{nw}$$

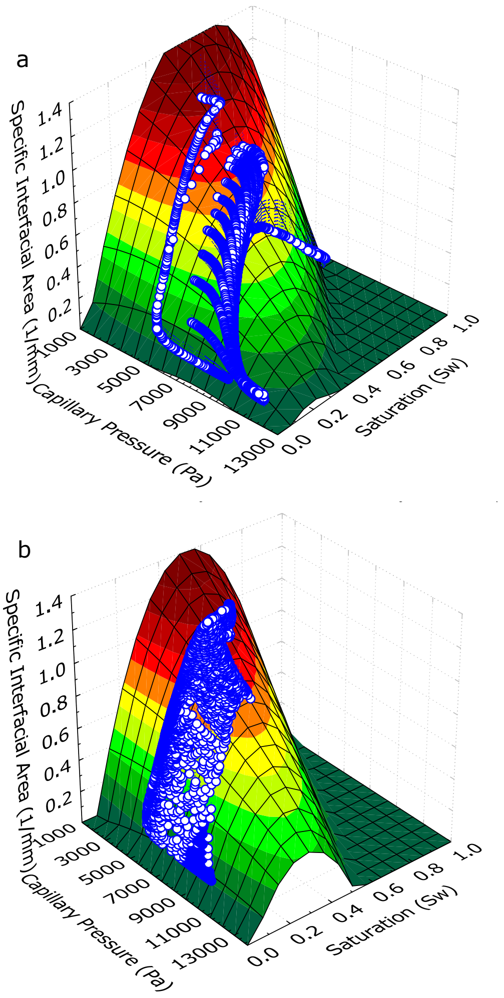

Figure 3.11: *a)* P^c*-*S^w*-*a^{nw} *drainage data points with fitted second-order polynomial surface b)* P^c*-*S^w*-*a^{nw} *imbibition data points with fitted second-order polynomial surface.*

3.5 Summary and conclusions

We have studied relationships among capillary pressure, saturation, and interfacial area (P^c-S^w-a^{nw}) as well as relative permeability, saturation, and interfacial area (k_{rw}-S^w-a^{nw}). To understand how network modelling algorithms influence the results, two different pore-network models have been developed; a tube network (similar to Fatts model) which has no pore bodies, and a sphere-and-tube network

Table 3.1: *Statistical properties of the model results and fitted surface*

Item	k_{rw}-S^w-a^{nw} Surface		P^c-S^w-a^{nw} Surface	
	R^2=0.991		R^2=0.956	
	Model Results	Fitted Surfaces	Model Results	Fitted Surfaces
No. of Data Points	566	566	11887	11887
Mean	0.160	0.158	534.0	529.9
St. Deviation	0.163	0.162	346.0	343.0

with both pore throats and pore bodies. Our results show that the oversimplification of the network influences the results significantly. In general, the sphere-and-tube network produces more realistic results than the tube network. The tube network is unable to produce hysteresis. Considering hysteresis in P^c-S^w relationship as a basis for resemblance of pore networks to the real porous media, we can conclude that the two network elements, namely pore throats and pore bodies, are required to produce hysteresis.

Based on the irreducible saturation for an uncorrelated pore size distribution with sphere-and-tube lattice geometry, we need about 40 nodes in each direction in order to have a representative network (REV). With an ensemble of 20 realizations, we could produce representative P^c-S^w-a^{nw} curves. The required size of ensemble decreases with increasing the network size.

Two different trapping algorithms have been employed: loose trapping (which mimics the escaping of wetting phase via corners of pores) and tight trapping (which assumes that the wetting phase trapped in a pore cannot escape). Trapping assumptions can influence significantly the form of S^w-a^{nw} curves as well as irreducible saturation. However, the trapping assumption is not important in wetting saturations larger than 55%. For the case of tight trapping, interfacial area increases monotonically with decreasing saturation. But, for the case of loose trapping, the variation is not monotonic and a maximum interfacial area can be observed at saturations around 25-35%, similar to the experiments on the real porous media. It implies that loose trapping assumption is more in agreement with real conditions.

Using data from the full range of scanning drainage and imbibition simulations, we have constructed P^c-S^w-a^{nw} and k_{rw}-S^w-a^{nw} surfaces. We have fitted a second-order polynomial to these surfaces, with correlation coefficients of 0.991 and 0.956, respectively. Furthermore, we have fitted a surface to the P^c-S^w-a^{nw} data points for drainage and imbibition, separately. These surfaces have been produced for two networks with different values of statistical distributions of pore bodies and pore throats. Results show that with increasing the overlapping part of the pore body and pore throat size distributions, the absolute difference between the two surfaces

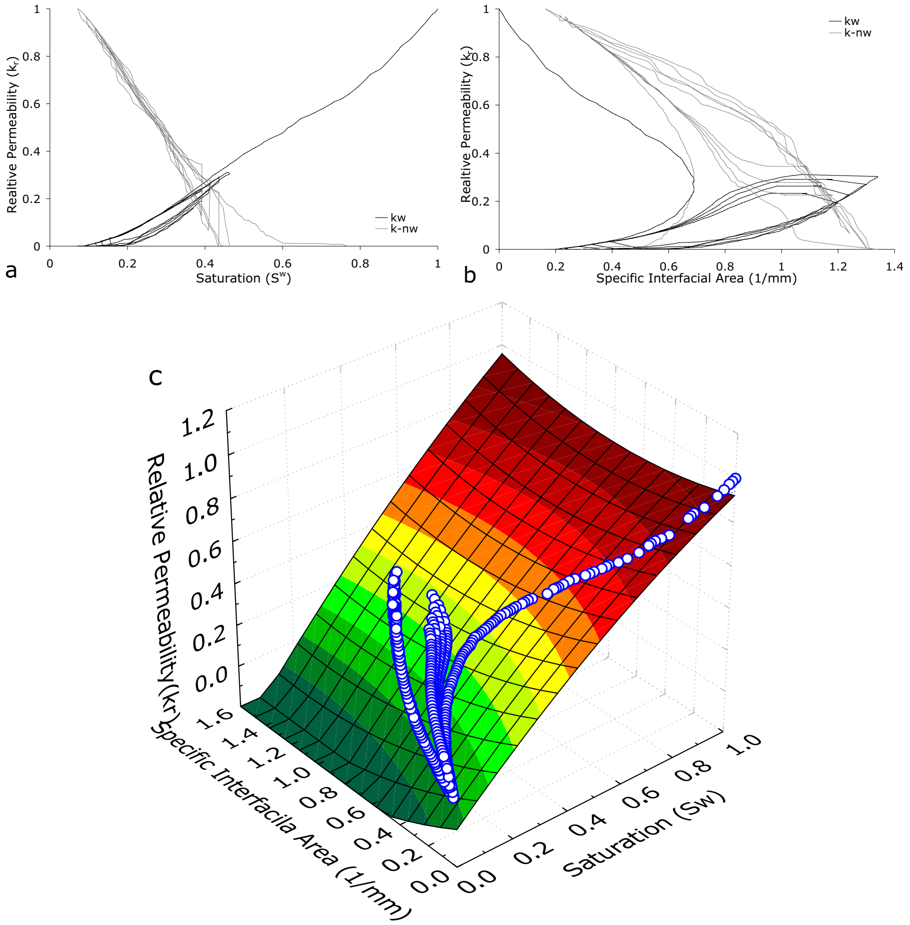

Figure 3.12: *Relationship among k_{rw}, S^w and a^{nw}. Solid lines correspond to the nonwetting phase and dashed lines correspond to the wetting phase. a) Main and scanning k_{rw}-S^w curves b) Main and scanning k_{rw}-a^{nw} curves (**c**) Fitted k_{rw}-S^w-a^{nw} surface with polynomial equation.*

decreases. This implies that in a real porous medium, where there is no clear distinction between pore bodies and pore throats, we can expect a smaller difference between the surfaces. Results of relative permeability-interfacial area show that there is a stronger hysteresis in krw-anw curves than in k_{rw}-S^w curves.

Results of this work suggest that in multiphase systems, interfacial area can be an essential variable in P^c-S^w and k_{rw}-S^w relationships. It can help in diminishing or eliminating the hysteresis that is commonly observed in P^c-S^w and k_{rw}-S^w curves.

Published as: Joekar-Niasar, V., Hassanizadeh, S.M., Pyrak-Nolte, L., Berentsen, C. – *"Simulating drainage and imbibition experiments in a high-porosity micro-model using an unstructured pore-network model,"* Water Resources Research, vol. 45, pp. W02430, 2009,doi:10.1029/2007WR006641.

Chapter 4

Pore-Network Model for a Micro-Model

> *Models are to be used, not believed.*
>
> H. Theil

Abstract

Development of pore-network models based on detailed topological data of the pore space is essential for predicting multiphase flow in porous media. In this work, an unstructured pore-network model has been developed to simulate a set of drainage and imbibition laboratory experiments performed on a two-dimensional micro-model. We used a pixel-based distance transform to determine medial pixels of the void domain of micro-model.

This process provides an assembly of medial pixels with assigned local widths that simulates the topology of the porous medium. Using this pore-network model, the capillary pressure-saturation and capillary pressure-interfacial area curves measured in the laboratory under static conditions were simulated. Based on several imbibition cycles, a surface of capillary pressure, saturation and interfacial area was produced. The pore network model was able to reproduce the distribution of the fluids as observed in the micro-model experiments. We have shown the utility of this simple pore-network approach for capturing the topology and geometry of the micro-model pore structure.

4.1 Objectives

One of the approaches for constructing the pore geometry from the imaging data is medial axis transform and skeletonization. Computationally, there are two general methods to find the medial axis of a given geometry: pixel-based and pixel-free methods (see e.g. *Brady and Asada*, 1984, *Chang et al.*, 1999, *Montanari*, 1969, *Saint-Marc et al.*, 1993). One may say that pixel-free methods are more precise than pixel-based methods since their computations are not implemented in a discrete domain. However, these methods also use pixelized input data acquired from imaging techniques that require approximations in order to transform the data into polyhedrons and lines. In these methods, mid-points or center lines of the pairs of contour elements bounding a shape are calculated analytically and are connected to generate the skeleton of a given geometry. Compared to pixel-free ones, pixel-based methods are usually simpler and easier to implement. However, since they are implemented on a discrete domain, they are not guaranteed to follow the exact medial axis. For skeletonization and finding medial axis, one may use different algorithms such as thinning algorithm (*Lam and Lee*, 1992, *Smith*, 1987), distance transformation, **DT** (introduced by *Rosenfeld and Pfalz*, 1968), and medial axis transform, MAT (introduced by *Blum*, 1967). Most of the existing pixel-based skeletonization methods use thinning techniques (*Lam and Lee*, 1992), which have been used extensively in many applications in biology, X-ray image analysis, finger print analysis, qualitative metallography, soil cracking pattern, automatic analysis of industrial parts as well as porous media (*Lam and Lee*, 1992). Distance transform has also many important applications in expanding or shrinking objects, reconstructing objects from parts of a given boundary (*Matsuyama and Phillips*, 1984) as well as for computing Voronoi diagrams *Ogniewicz and Ilg* (1992), *Ye* (1988). MAT methods have been used for computing many geometric properties (*Chandran et al.*, 1992, *Lee*, 1982, *Wu et al.*, 1986, 1988). In fields related to porous media, some researchers such as *Glantz and Hilpert* (2007, 2008), *Lindquist* (2002) have employed medial axis transform concept to extract topology and geometry of a porous medium. *Glantz and Hilpert* (2007) have applied their pixel-free approach to simulate a drainage experiment on a two-dimensional porous medium composed of circular grains. Subsequently, they simulated the P^c-S^w curve for a drainage experiment in a three-dimensional space porous medium (*Glantz and Hilpert*, 2008).

In this work, we use a pixel-based method to develop an unstructured pore-network model to simulate micro-model experiments performed by *Cheng* (2002). Their micro-model had a porosity $> 66\%$ and had irregular pore geometry. Porous media with high porosities (40% to 98%) are found in many industrial applications such as metallic thin-fiber material and metallic powder, which are used in the transportation industry (*Dubikovskaya et al.*, 1990), and in manufacturing capillary structures (*Reimbrecht et al.*, 2003). Due to these special features of the micro-model, conventional pore-network models with pore body and pore throat elements are not suitable. Thus, we have employed the medial pixel concept to extract the skeleton of the micro-model. We have used a pixelized distance transform to identify the medial pixels and the pore width at every pixel. As a result, the real pore geometry and topology is captured without losing significant information. With our pore network mode, we have simulated a set of quasi-static drainage and imbibition laboratory experiments performed on a two-dimensional porous micro-model porous (*Cheng et al.*, 2004). We demonstrate the capabilities of the model by simulating fluid configurations observed in the micro-model as well as by calculating capillary pressure-saturation (P^c-S^w) and interfacial area-saturation (S^w-a^{nw}) curves that agree well

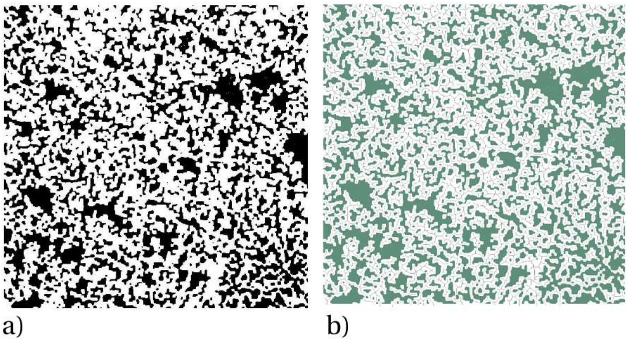

Figure 4.1: *a) Pattern of the micro-model, black color shows the solid b) Pore network model representation as an assembly of the medial pixels (1pixel≈0.3 μm)*

with the measured data. A P^c-S^w-a^{nw} surface for imbibition cycles also agreed with the experimental data.

4.2 Materials and experiments

Cheng (2002) and *Cheng et al.* (2004) performed fluid invasion experiments on two-dimensional micro-models with random pore structures. Details of the fabrication procedure and the experiments can be found in *Cheng* (2002). The main objective of the *Cheng* (2002) and *Cheng et al.* (2004) micro-model experiments was to investigate the conjecture of *Hassanizadeh and Gray* (1990) that capillary pressure (P^c) is not only a function of saturation (S^w), but also of interfacial area between non-wetting and wetting phases (a^{nw}). Their work provided experimental support for the theoretical prediction that the capillary-dominated subset plays a role analogous to a state variable. The goal of our study is to use pore network modelling to reproduce the fluid distributions and the P^c-S^w-a^{nw} relationship observed in their experiments based on the pore geometry of the micro-models.

The micro-model measured approximately 600μm × 600 μm with a constant depth of 1.28 μm (Figure 4.1).

The pores had a rectangular cross-section of variable width but with a constant height. The porosity of the porous medium was around 62%-64%. The micro-model was completely transparent which enabled direct visualization and imaging of fluid distributions within the pores using a microscope with a 16x objective and a CCD camera. From the images of the micro-model, fluid saturation, interfacial area and interfacial curvature were determined. During the experiments, the micro-model was placed horizontally on a microscope to avoid the gravitational effects. An external pressure transducer was used to measure the non-wetting phase (nitrogen) pressure. The wetting phase (decane) reservoir was open to atmosphere. In the two-phase displacement experiments of *Cheng et al.* (2004), nitrogen was used as the non-wetting phase and decane as the wetting phase. The contact angle of the wetting phase with the glass is 4.4° and with the photoresist material is 4.1°. The fluid-fluid interfacial tension is 24.7 dynes/cm. Images of fluid distributions in the micro-model were recorded for drainage and imbibition cycles.

At the start of a drainage experiment, the micro-model was saturated with the wetting phase (decane). Non-wetting phase (nitrogen) was injected into the model by manually increasing the nitrogen pressure in small increments to avoid sudden flooding of the micro-model. At each pressure step, the system was allowed to equilibrate. Then, an image and pressure reading were taken. A drainage experiment was continued until nitrogen gas reached the wetting reservoir. Contrary to standard capillary pressure cells, there was no hydrophilic membrane placed at the exit. So, the non-wetting phase entered the wetting reservoir (breakthrough) at which time the drainage experiment was halted. At the end of drainage test, there was still a significant amount of the wetting phase present in the micro-model. Then, an imbibition experiment was performed by reducing the non-wetting phase pressure in small increments and at each pressure step allowing the system to equilibrate. The imbibition experiment was continued until the micro-model was almost 100% saturated with the wetting phase. An archive of the images from the *Cheng et al.* (2004) experiments and other micro-model experiments (*Chen et al.*, 2007, *Pyrak-Nolte et al.*, 2008) have been placed on a website for downloading (*Pyrak-Nolte*, 2007).

Based on images of the experiments, fluid configurations during imbibition were more complicated than those observed from the drainage experiments. At the end of an imbibition experiment, no non-wetting fluid remained in the micro-model. This suggests that trapping mechanisms were absent in this system. In particular, fluid movement should have been piston-like with no snap-off occurring. However, images from imbibition experiments showed that cooperative filling of the pores by the wetting phase was dominant pore-filling mechanism in this micro-model pore structure. The image in Figure 4.2 shows an example of cooperative filling in the micro-model. During imbibition, the wetting-non-wetting interface spans several pores, whereas during drainage, the interfaces moved in individual pores.

4.3 Pore-network model description

To develop an unstructured pore network, a binary image of the air-filled micro-model is used. In the image, the pore space (void domain) and its boundaries (solid

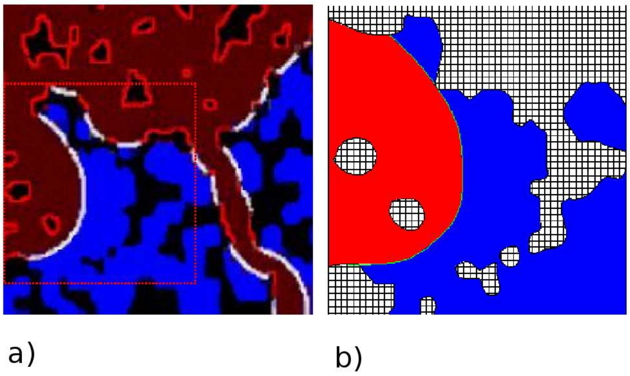

Figure 4.2: *An example of cooperative pore filling during imbibition (blue is wetting fluid, red is nonwetting fluid, hashed is the solid) a) An image of micro-model experiment b) Schematic presentation of cooperative-filling interface*

domain) are visible with a resolution of 0.6μm per pixel (Figure 4.1a). The skeleton of the micro-model, and the local pore width are needed to simulate the pore geometry. We have developed a pore-network model using a pixel-based distance transform to identify the medial pixels of pores, i.e., the pixels along the center of the channels that are equidistant from the pore channel walls. This approach is relatively simple compared to pixel-free methods.

4.3.1 Determination of medial pixels

We used a Distance Transform, **DT**, to generate a distance map from a binary image of the micro-model. Each pixel in the void domain was given a value indicating the shortest distance to the solid pixels (pore walls). Then, the value of each pixel was compared to the value of the neighboring pixels. A so-called flow operator (*Jensen and Domingue*, 1988) was applied to define the direction of the maximum gradient in a two-dimensional space. A search algorithm was used to indentify the medial pixels. A detailed explanation of the algorithm is given in Appendix B and an example of the procedure is shown in Figure 4.1(b).

4.3.2 Determination of fluids distribution

Our goal was to obtain the same fluids distributions using our pore network model as those observed in the micro-model. The fluids distribution is dictated by fluid pressures imposed on the model, the equilibrium of capillary forces within the pores, and the history of the displacement. During drainage, only those pores with

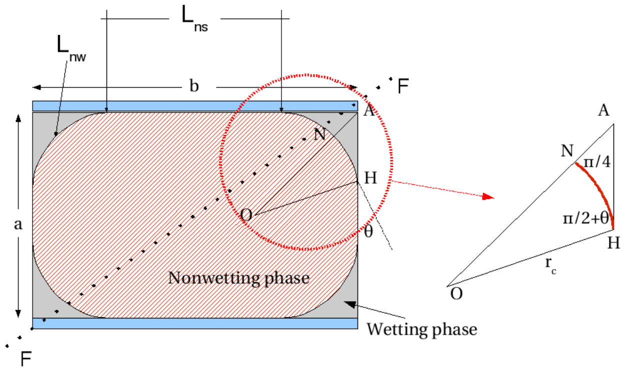

Figure 4.3: *Configuration of a meniscus in the corners of a rectangular pore. a is the depth of micro-model and b is the local pore width. Half of a corner meniscus with r_c radius of curvature has been magnified in the right side. Total length of contact line between solid and nonwetting phase is denoted by L_{ns} and total length of contact line between nonwetting phase and wetting phase is referred to as L_{nw}.*

entry capillary pressures smaller than the imposed capillary pressure were invaded by the non-wetting phase. The entry pressure varies among the pores because the pores in the micro-model have variable cross sections. Therefore, an entry pressure was calculated for each cross sections for all of the pores.

The entry pressure depends on the fluid-fluid interfacial tension(σ^{nw}), the pore size, pore geometry, and the contact angle (θ). As shown in Figure 4.3, the pores in the micro-model have a rectangular cross-section, and their boundary is partly glass and partly photoresist material. We denote the depth of the micro-model by a and the pore width by "b". Because the difference between the contact angles of the fluid-glass and of fluid-photoresist is insignificant ($\sim 0.3^\circ$ degree), we employ a single value of contact angle in our calculations. The entry pressure,P_e^c, for a pore with rectangular cross section is calculated from the following formula which is derived in Appendix D.

$$P_e^c = \sigma^{nw} \left(\frac{-(a+b)cos\theta + \sqrt{(a+b)^2 cos^2\theta + 4ab(\frac{\pi}{4} - \theta - \sqrt{2}cos(\frac{\pi}{4}+\theta)cos\theta)}}{4(\frac{\pi}{4} - \theta - \sqrt{2}cos(\frac{\pi}{4}+\theta)cos\theta)} \right)^{-1} \tag{4.1}$$

Thus, for a given P^c imposed on the micro-model, the fluid-fluid interface advances to all cross sections with an entry pressure less than P^c (i.e., $P_e^c \leq P^c$), provided the pore is connected to the wetting phase reservoir. If the interface reaches a diverging cross section, the rest of the pore will be filled up by the non-wetting phase. But, for a (partially) converging pore, the interface will stop at the location where the corresponding P^c_e is equal to P^c. It will only move farther after P^c is increased again. When the location of the interface is known, a local pore width is used to determine the planar arc length of the interface. Because the depth of the mico-model is constant, the interfacial area of the main terminal interface is simply the arc length times the micro-model depth. For imbibition, the reverse occurs. The wetting phase will re-enter smallest pores first. In a diverging pore, the meniscus will stop at a location whose local P^c_e is equal to P^c. Converging pores will be completely filled at once.

4.3.3 Trapping assumptions

In determining the displacement of one phase by another, we must take into account that we may have trapping of the wetting phase during drainage and trapping of the non-wetting phase during imbibition. In general, during drainage, trapping can occur in two ways. First, wetting phase always exists in the corners of a pore and the amount of wetting phase in the corners will decrease if P^c, is increased and if the corners are connected to the wetting reservoir. For this type of trapping, there is always an interface in the crevices called "corner meniscus". The second type of trapping is caused by the blockage of some pores. In this case, an interface spans the pore cross-section and it is called a "main terminal meniscus" (*Piri and Blunt*, 2005a). Because of the two-dimensionality of the micro-model and the resolution of images, only the second-type of trapping is visible. The corner menisci are not observed in the images and cannot be quantified from the images. Therefore, to simulate the analysis of the expeirments performed by Cheng et al (2004), our calculations do not take into account the wetting phase in the corners of the rectangular pores nor the interfacial area of the corner menisci.

Trapping of main terminal menisci can have a significant effect on fluids distribution and consequently on the interfacial area-saturation (a^{nw}-S^w) relationship (see e.g. *Joekar-Niasar et al.*, 2008). The trapping assumptions made for simulations of drainage and imbibition experiments are discussed separately. For drainage experiments, we can consider two different possibilities. One possibility is to assume that the wetting phase is never trapped. This can be justified based on the fact that the wetting phase, which always remains present in the corners of pores, provides a continuous path for the wetting phase to escape to its corresponding reservoir. This means that the wetting phase can be fully drained from all pores if the imposed capillary pressure is sufficiently high. Another possibility is to assume that the wetting-phase-filled corners of the pores do not act as conduits for the flow of the wetting phase. In this case, we can assume that the wetting phase gets trapped in pores that are not connected to the wetting phase reservoir through other (partially) filled pores. *Joekar-Niasar et al.* (2008) have shown that the shape of a^{nw}-S^w curve (calculated based on main menisci interface) is dictated by the trapping assumptions. A monotonic increase of interfacial area, with a decrease in saturation will be obtained if we allow trapping of main terminal menisci. A nonmonotonic a^{nw}-S^w curve, however, is found if we impose a loose or no trapping mechanism. This occurs because some main terminal interfaces will be reconnected. Such a reconnection has been observed in the experiments, as illustrated in Figure 4.4, which shows fluid configurations at two different pressures during the drainage experiment. Based on this observation, no trapping of the wetting phase is assumed in our simulations. But, to illustrate the effect of the trapping assumption, one of the drainage simulations has been shown with a simple trapping rule. Based on this rule, the wetting phase in a cell of the pore network is trapped if there is no neighboring cell filled with the wetting phase and connected to the wetting phase reservoir. Trapping mechanisms during imbibition are different and more complicated compared to those that occur during drainage. Previous studies have shown that displacement mechanisms during imbibition may be attributed to the following factors: a) pore size distribution, b) fluid occupancy in pore throats connected to a pore body, and/or c) pore throat to pore body diameter ratio. *Lenormand and Zarcone* (1983, 1984) have suggested different mechanisms for imbibition into a pore body that depends on the fluid topology of the neighboring pore throats. According to *Wardlaw and Yu* (1988) and *Ioannidis et al.* (1991), little variability of pore size, and small pore body to pore throat diameter ratio are factors that increase the effects of fluid topology in determining the non-wetting phase withdrawal sequence. Such local geometrical features result in a mechanism called cooperative filling. Figure 4.5 shows a schematic of interface configurations subjected to cooperative pore filling for two different cases. When the ratio of pore body to pore throat diameter is large (small pore throats), interfaces remain within a pore body. However, when the ratio of pore body to pore throat diameter is small, imbibition phenomena are controlled by the fluid topology, and the efficiency of wetting invasion increases significantly (*Mahmud and Nguyen*, 2006, *Vidales et al.*, 1998) and the effect of snap-off decreases. As observed in the micro-model experiments, there is no trapping at the end of the imbibition experiments. We conclude that snap-off is absent in the experiments and is not one of the major mechanisms of trapping of nonwetting phase (*Chatzis and Dullien*, 1981). Absence of snap-off occurs when the pore body to pore throat diameter ratio is small which results in an interface that bridges over several pores. This results in a large radius of curvature and consequently a low capillary pressure. The interface will maintain a stable position as well as continuity to the non-

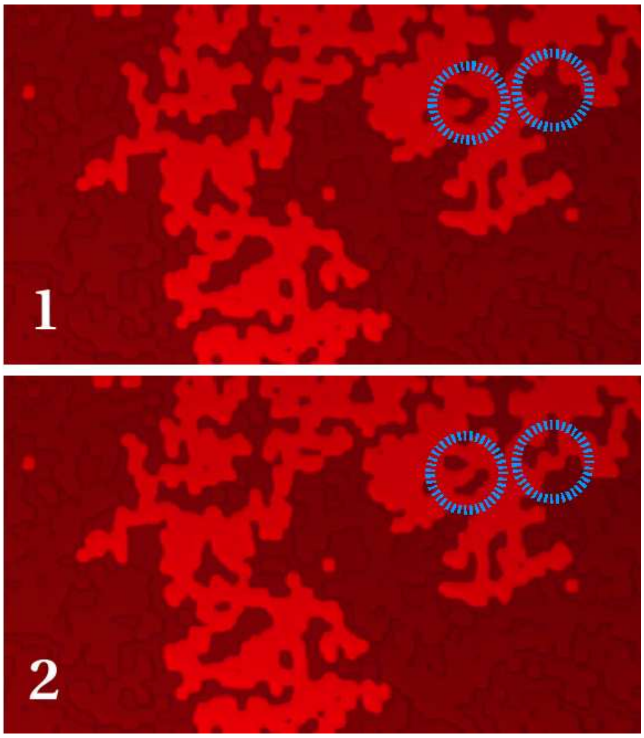

Figure 4.4: *Reconnection of main terminal interfaces due to under untrapped conditions. Two successive images during drainage experiment show that interfacial area can decrease due to the interfaces reconnection.*

wetting phase reservoir until the global capillary pressure during imbibition is reduced enough to allow invasion of wetting phase. Thus in cooperative filling, a low capillary pressure is required for the wetting phase to fill the pore body completely.

It is difficult and computationally expensive to capture the geometry of interfaces based on a cooperative filling mechanism when using a skeleton-based pore-network model. Thus, cooperative filling has not been modelled explicitly. However, its effect, namely the decrease in residual non-wetting saturation has been incorporated in the model using a local network rule, referred to as forced displacement. This rule allows invasion of the wetting phase into pore as long as it doe not break the continuity of the non-wetting phase connection to the non-wetting phase reservoir (i.e. no snap-off occurs during imbibition).

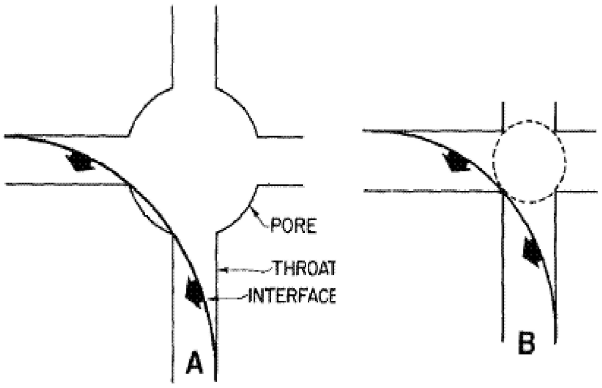

Figure 4.5: *Interfaces at positions of break-off in the pores with different pore to throat diameter ratios; (A) has larger ratio than (B) (Wardlaw and Yu, 1988)*

4.3.4 Simulation of experiments

The numerical analysis started with drainage simulations because the micro-models in the experiments were initially saturated with wetting phase. The wetting phase pressure was assumed to be zero in the entire pore network. Initially, the pressure of the non-wetting phase, and thus the network capillary pressure, was set equal to the entry capillary pressure of the largest pore(s) bordering the non-wetting phase reservoir. Then, the non-wetting phase pressure was increased incrementally. At each increment, only those pores connected to the non-wetting phase reservoir are invaded if their entry pressure was smaller than or equal to the imposed capillary pressure. At each displacement, saturation and specific interfacial area were calculated.

Drainage simulations were halted after the breakthrough of the non-wetting phase. Then, imbibition experiments were simulated by decreasing the non-wetting phase pressure in small steps. Imbibition always started from the smallest pores with the highest entry capillary pressure. At each imbibition step, the forced displacement rule was imposed. At the end of imbibition, the drainage simulation was repeated. We always obtained only the primary drainage curve because at the end of each imbibition cycle the non-wetting phase has completely exited the micro-model.

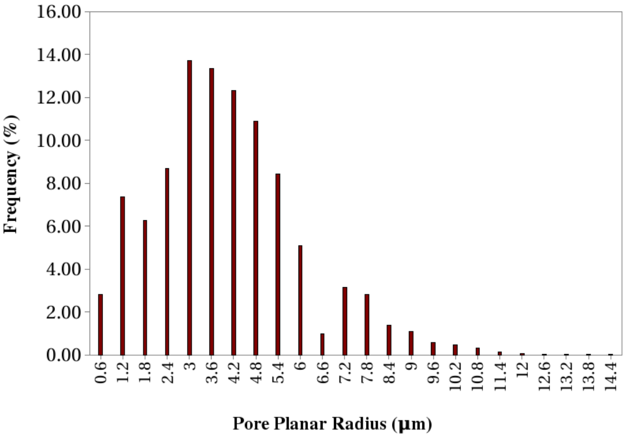

Figure 4.6: *Statistical distribution of radii of inscribed circles (half width of pore) of the network model*

4.4 Results and discussion

4.4.1 Network analysis

Because the depth of the micro-model was constant, a planar pore size distribution was used analyze the P^c-S^w curve behaviour. Figure 4.6 shows the histogram of pore widths assigned to the medial pixels of the image of the micro-model. For a rectangular cross section, Equation 4.1 gives the corresponding entry pressure as a function of the pore width. The resulting curve is plotted in Figure 4.7. For pore widths larger than 7μm, only small changes in the entry capillary pressure are required to invade the non-wetting phase into large pore widths because the depth of the micro-model (pore height - which controls the entry capillary pressure) is constant.

4.4.2 Fluids distribution snapshots

In Figure 4.8, snapshots of fluid distributions for different saturations from the micro-model experiments and the corresponding network simulations are shown for comparison. The simulations are based on the no-trapping assumption. The first two rows in Figure 4.8 show drainage results and the last two rows show imbibition results. We observe that the simulated fluid distributions qualitatively agree with the experimentally measured fluid configurations. Cooperative filling of the pores appears to dominate the fluid configurations in this micro-model.

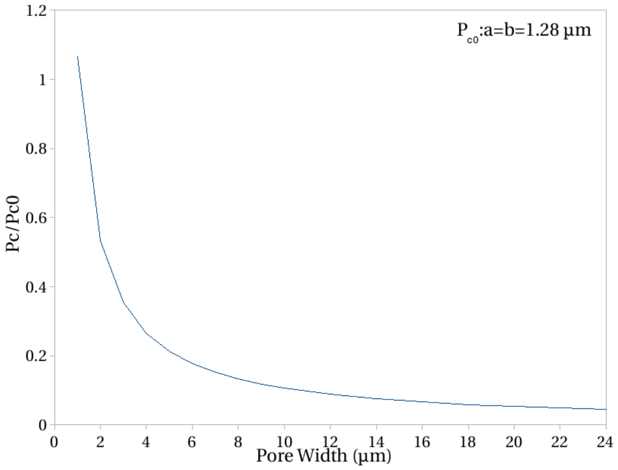

Figure 4.7: *Entry capillary pressure for a rectangular cross section as a function of pore width, normalized with respect to P_{c0}, which is the entry capillary pressure for a pore with a=b=1.28 μm*

4.4.3 P^c-S^w curves

In Figure 4.9, we compared P^c-S^w curves for drainage and imbibition obtained from our simulations with the measured curves from the micro-model experiments. Good agreement between the experimental data and the numerical simulations was obtained. It is interesting to note that portions of both the drainage and imbibition curves are flat. During drainge for saturations less than 0.83, the P^c-S^w curve are almost flat. This flat shape of the capillary pressure is caused by the spatial distribution of the micro-model pores. Pore constrictions act as bottlenecks that prevent the non-wetting phase from further invading the micro-model until the capillary pressure is high enough to breakthrough the bottleneck pore. After invading the bottleneck, a large region of the pore space is flooded at almost constant capillary pressure. Due to the absence of a hydrophilic membrane, breakthrough of non-wetting phase occurs at a relatively high saturation. This also means that the imbibition curve is not the main imbibition curve but a scanning curve. The flat part of the imbibition curve occurs above a saturation of 0.78. At this saturation, flooding of the micro-model by the wetting phase occurred at an almost constant capillary pressure of 39 kPa. This is the capillary pressure that corresponds to a meniscus with radius 1.28μm, i.e., the depth of micro-model.

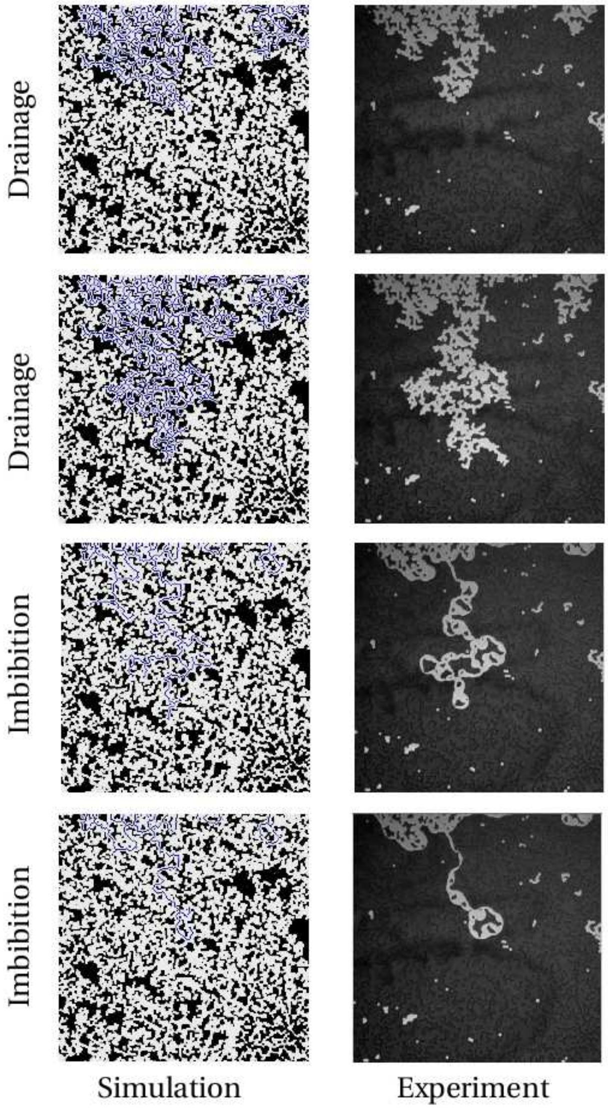

Figure 4.8: *Snapshots of the drainage and imbibition experiments, comparison between experiments and simulations*

4.4.4 a^{nw}-S^w relationship

In Figure 4.10, a^{nw}-S^w data points obtained from the pore-network model are compared to the measured anw S data. As mentioned earlier, pore-network computa-

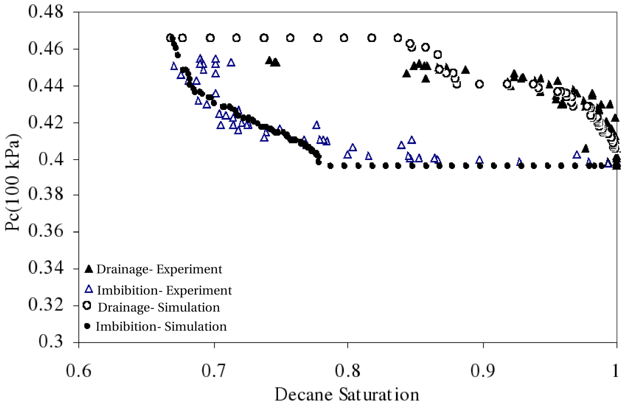

Figure 4.9: *Measured and simulated P^c-S^w data points for drainage and imbibition*

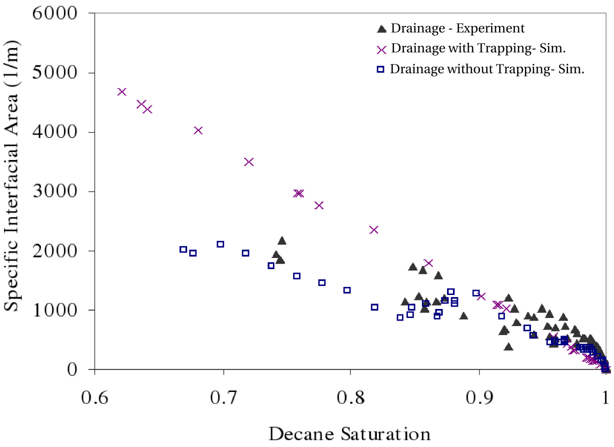

Figure 4.10: *a^{nw}-S^w points resulted from drainage experiments and simulations*

tions can be performed with two scenarios: with or without trapping. The effect of these two scenarios on the a^{nw}-S^w relationshipis shown in Figure 4.9. The points obtained from the no-trapping scenario are in good agreement with the experimental measurements. This indicates that the no-trapping assumption is valid for drainage. The a^{nw}-S^w curves were also calculated for many cycles of drainage and imbibition, invoking the no-trapping assumption for drainage and the forced displacement assumption for imbibition. The result is shown in Figure 4.11. Interfacial area is underestimated by the simulations for imbibition. We hypothesize that this is caused by

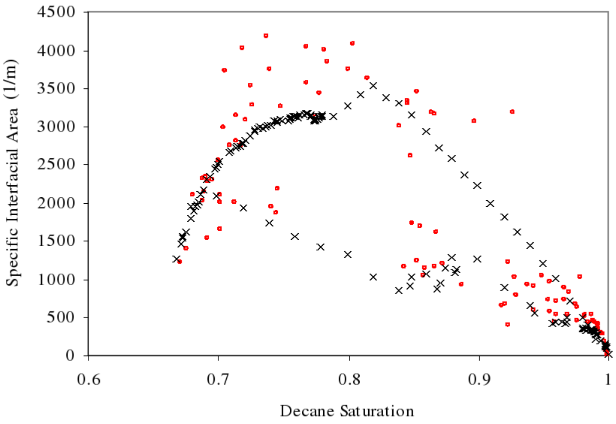

Figure 4.11: *Experimental and computational a^{nw}-S^w relationship for drainage and imbibition (circles show experiment data and crosses show simulation data). Interfacial area during drainage is much less than during imbibition*

not accounting for the cooperative filling that occurs during imbibition. Interfaces that span a number of pores (Figure 4.2) have a larger interfacial area than the interfaces that are confined within a single pore.

4.4.5 P^c-S^w-a^{nw} surface

Several researchers have computationally generated P^c-S^w-a^{nw} surfaces for either drainage or imbibition in lattice networks (*Held and Celia*, 2001, *Joekar-Niasar et al.*, 2008, *Reeves and Celia*, 1996) to investigate *Hassanizadeh and Gray* (1990) conjecture that that capillary pressure is not only a function of saturation, but also of interfacial area between non-wetting and wetting phases. In this paper, we produce a P^c-S^w-a^{nw} surface using both the main drainage curve and the imbibition scanning curves. A second-order polynomial surface was fitted separately to the experimental data and to the simulation data. A high correlation between the fitted surface and data was observed that corresponded to correlation coefficients for the simulations and experiments of 0.99 and 0.95, respectively. It has been observed that there are some fluctuations in the experimental data points, due to limitation in resolution of image acquisition and accuracy of pressure transducer. Using interpolation, a map of interfacial distribution within the P^c-S^w loop is obtained and is shown in Figure 4.12 for both simulations (Figure 4.12a) and experimental data (Figure 4.12b).

We have then subtracted these two maps to obtain a map of normalized differences (Figure 4.12c). The average normalized difference is 0.17 and it is larger

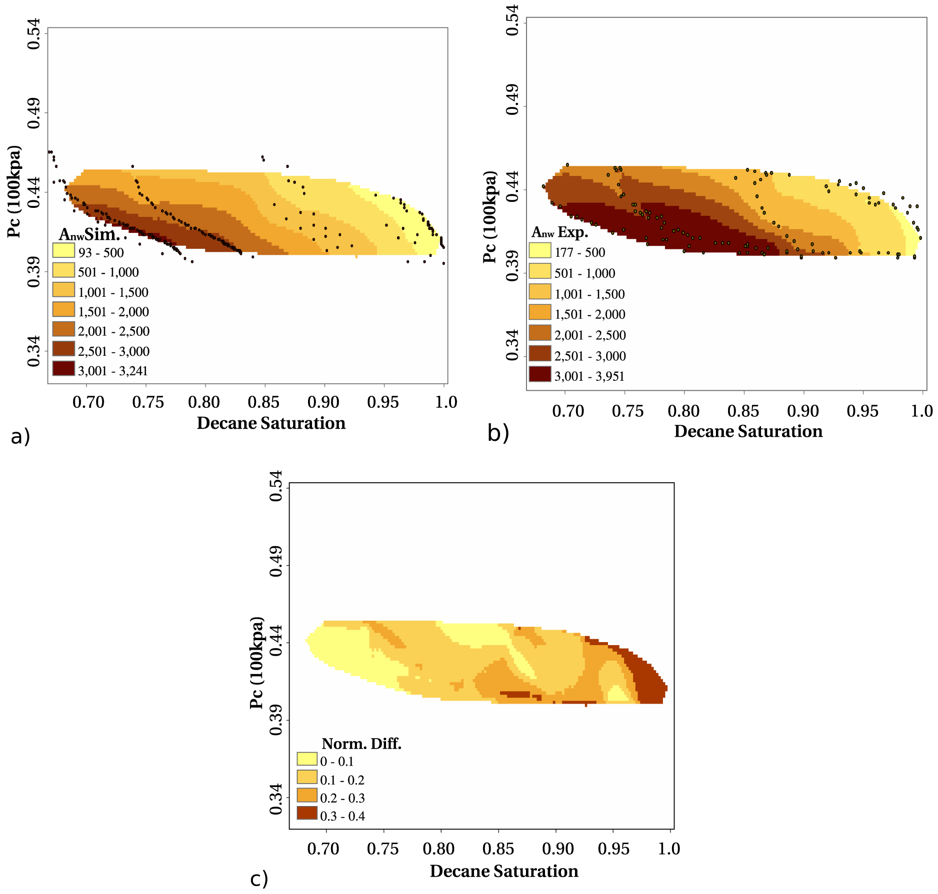

Figure 4.12: *Spatial distribution of specific interfacial area (1/m) for a) Simulations b) Experiments and c) Normalized differences between (a) and (b)*

only in a very small range at high saturations (0.97 to 1.00), where the magnitude of interfacial area is small. Based on the analysis done on interfacial area, it can be concluded that we have been able to define a single descriptive surface for the imbibition curves that also includes the main drainage curve. This conclusion is similar to that found experimentally by *Chen et al.* (2007). They showed experimentally that the P^c-S^w-a^{nw} surfaces obtained for drainage and imbibition were the same to within the experimental and analysis error (around 10%-15%). Our computational results and the work of *Chen et al.* (2007) suggest that data obtained from either the drainage process or the imbibition process are sufficient to generate the complete functional relationship among P^c-S^w-a^{nw}.

4.5 Summary and conclusion

In this work, an unstructured pore-network model was developed to simulate the drainage and imbibition experiments performed on a two-dimensional micro-model of a porous medium to produce P^c-S^w-a^{nw} surface. Development of the pore-network model was based on identifying the medial pixels of a pixelized image of the pore space in the micro-model. We have employed a simple approach based on distance transform (**DT**) to define medial pixels. Using this concept, geometry and topology of the micro-model are captured with an acceptable accuracy for use in a pore-network model. We have demonstrated the capability of the model by simulating the configuration of two immiscible fluids in a micro-model. Our analysis shows that capillary pressure of the micro-model is controlled by its depth, which is almost as small as the smallest pore width. In addition, the spatial distribution of pores with variable widths is such that a constriction (i.e., a bottleneck) controls the invasion of the non-wetting phase to a significant portion of the micro-model. Due to the rectangular cross-section of the pores, no trapping of the wetting phase occured during drainage. The wetting phase in the corners of invaded pores of the network was always connected to the outflow reservoir. This conclusion was checked by comparing the computationally obtained a^{nw}-S^w relationship for different assumptions to the a^{nw}-S^w relationship from the experiments. If there is trapping, a^{nw} would be monotonically increasing with decreasing saturation. However, if there is no trapping, the a^{nw}-S^w curve is parabolic in shape with a maximum value at an intermediate saturation (e.g. *Joekar-Niasar et al.*, 2008). The a^{nw}-S^w curve from the micro-model experiments had a parabolic shape, which confirms that no trapping occurred in micro-model drainage experiments. Finally using our pore-network model, we reproduced the observed patterns of fluid distribution in the micro-model for both drainage and imbibitions experiments. We also produced a P^c-S^w-a^{nw} surface for imbibition that approximates the measured surface very closely. This is very encouraging as it suggests that we can use our pore-network model as a predictive tool.

Published as: Joekar-Niasar, V., Prodanović, M., Wildenschild, D., Hassanizadeh, S.M. – *"Network Model Investigation of Interfacial Area, Capillary Pressure and Saturation Relationships in Granular Porous Media,"* Water Resources Research, 2010,doi:10.1029/2009WR008585

Chapter 5

Pore-Network Model for Glass Beads

> *The art of progress is to preserve order amid change and to preserve change amid order*
>
> Alfred North Whitehead, mathematician

Abstract

We have developed a new approach for generating pore throat cross sections of various shapes based on distributions of shape factors and radii of inscribed circles. These distributions are obtained from analysis of grains packing. General formulas for calculating geometrical properties and entry capillary pressure for given shape factor and inscribed circle radius are developed. These relationships are employed in a pore network, which has a number of special features. In particular, it is highly flexible in terms of location of pore bodies, variable coordination number, as well as variable cross-sectional shapes. The pore-network model is employed for simulating the equilibrium distribution of two fluids in a granular porous medium, under both drainage and imbibition conditions.

The pore-network model is verified by comparing simulation results with experimental data of quasi-static drainage and imbibition experiments in a glass-bead medium. The pore-level topology and geometrical description of pore bodies and pore throats, essential for building the network, are rigorously extracted from experimental data using image analysis (3DMA-Rock software). Calculated capillary pressure-saturation (P^c-S^w) and specific interfacial area-saturation (a^{nw}-S^w) curves show very good agreement with measured ones, for both drainage and imbibition. We show that the shape factor can significantly influence the form of macroscopic P^c-S^w and a^{nw}-S^w curves, if the length and volumes associated to the pore throats is considerable. Furthermore, using continuous generation of shape factor distribution, the model can be validated against the grain size distribution. After validating the model against experiments, in addition to primary and main curves, we simulate many scanning curves to generate P^c-S^w-a^{nw} surfaces for drainage and imbibition, separately. Results show that these two surfaces lie very close to each other, and the average normalized difference is small, in the range of simulations uncertainty. Our results illustrate that P^c-S^w-a^{nw} surfaces show very little hysteresis and, therefore, specific interfacial area can be considered as an essential variable for reducing or eliminating the hysteresis observed in P^c-S^w curves.

5.1 Introduction

5.1.1 Pore-network modeling

Among other sources, pore-scale information is very much needed for gaining insight in, and for fundamental understanding of, the physics of flow and transport in porous media. Thus, in recent years, various imaging techniques, such as X-ray computed microtomography (for recent overview see *Kaestner et al.*, 2008, *Wildenschild et al.*, 2002) and magnetic resonance imaging (MRI) have been employed to obtain detailed pore-scale information from many porous media. Combined with pore-scale modelling methods, such detailed information can be used to understand the interplay of various flow mechanisms and produce data for investigating macroscale theories. Depending on the pore-scale modelling technique, pore space geometry can be either used directly or as a simplified network of pores. Direct simulation techniques, such as Lattice-Boltzmann method (*Ahrenholz et al.*, 2008, *Porter et al.*, 2009, *Schaap et al.*, 2007, *Shan and Chen*, 1994), are computationally demanding. Thus, often pore-network models are used where the pore space is idealized as a network of “pore bodies” and “pore throats”.

Pore-network models - pioneered by *Fatt* (1956) - have been extensively used to study a variety of flow and transport phenomena in porous media. They can be divided into quasi-static and dynamic ones. Quasi-static pore-network models simulate only equilibrium states of drainage and imbibition processes without solving the pressure field (see e.g. *Fatt*, 1956). For a review of the literature, see *Celia et al.* (1995) and *Blunt* (2001). But, dynamic pore-network models simulate the transient behaviour of (multiphase) flow (see e.g. *Dahle and Celia*, 1999, *Dias and Payatakes*, 1986a, *Koplik and Lasseter*, 1985, *Nordhaug et al.*, 2003).

The main challenge in development of the structure of a pore network is to preserve essential features of the void space (relevant to multiphase flow). While representing the void space as a network of simplified geometries, it should be tractable for computations. Major characteristics of a pore network are its topology (i.e. positioning of pore bodies, and the number and orientation of links) and geometry of elements.

Regarding the topology, if pore bodies are centered at nodes of a regular lattice, the network is referred to as a “structured” network. The number of pore throats connected to a pore body is called “coordination number”. Many pore-network models have a coordination number of six, with pore throats oriented along the three principal directions of the lattice. We refer to these as regular networks. But, there are some network models with variable coordination number and with pore throats oriented in many directions (see e.g. *Joekar-Niasar et al.*, 2009, *Mogensen and*

Stenby, 1998, *Piri and Blunt*, 2005a, *Raoof and Hassanizadeh*, 2009, *Ryazanov et al.*, 2009).

Geometry of the network is represented by shape and size of pore bodies and pore throats. Commonly, all pore bodies in a pore-network model are assigned the same shape, such as sphere (e.g. *Bakke and Øren*, 1997, *Øren and Bakke*, 2002, *Reeves and Celia*, 1996) or cube (e.g. *Mogensen and Stenby*, 1998, *Patzek*, 2001). In yet some other models, no pore bodies are defined at all; i.e. no geometry is assigned to the connection points of pore throats. Instead, a variable cross section is assigned to each pore throat (see e.g. *Dias and Payatakes*, 1986a). However, an accurate representation of the exact geometry of large voids among grains in a real porous medium is not straight forward. Since pore bodies are the controlling elements during imbibition, any inaccuracy in representation of pore bodies increases the difficulty of simulation of the imbibition process.

Similarly, different choices are made for the shape of pore throats. In many models, all pore throats are assigned the same cross-sectional shape (e.g. *Reeves and Celia*, 1996). But pore networks where different cross-sectional shapes are assigned to various pore throats have been also developed. We refer to them as "mixed cross-sectional" pore networks (*Bakke and Øren*, 1997, *Øren and Bakke*, 2002, *Patzek*, 2001).

The cross-sectional shape of a pore throat is commonly parametrized by means of a shape factor. In two dimensions, the shape factor is defined as the ratio of cross-sectional area (A) to the square of the perimeter (P); $G = A/P^2$. The influence of shape factor on the entry capillary pressure, conductance, residual saturation, and interfacial area of a pore with triangular cross section was first studied by *Mason and Morrow* (1991). Since then, shape factor has been used for specification of pore throats shapes especially in quasi-static pore-network models.

Bakke and Øren (1997) developed a pore-network model with mixed cross sections for actual sandstones. However, the range of shape factor that was recovered in their model was very limited (to 0.0481, which corresponds to an equilateral triangle). In a model by *Man and Jing* (2000), pore throats were assigned star-shape cross section with four vertices. However, the authors chose pore throat cross sections in an arbitrary fashion and did not compare their P^c-S^w curves with experiments. *Patzek* (2001) developed a network with cubic pore bodies and four different polygonal cross sections for pore throats. He simulated relative permeability-saturation (k_r-S^w) and capillary pressure-saturation (P^c-S^w) relationships for *Bentheimer* sandstone. The author did not specify how the choice of specific cross-sectional shapes for pore throats and pore bodies was related to the sandstone geometrical properties. *Piri and Blunt* (2005a) developed a pore-network model for two- and three-phase flow for a mixed-wet porous medium. They chose circular, square, and triangular shapes for pore throat cross sections, and simulated relative permeability curves for *Berea* sandstone. *Sholokhova et al.* (2009) developed a model with three different cross sections (triangle, rectangle and ellipse) to study single-phase absolute permeability. They compared their results with the experimental data for *Fontainebleau* sandstone. *Ryazanov et al.* (2009) developed an unstructured irregular network with star-shape pore throats without including pore bodies. The structure were derived from image analysis of *Berea* sandstone.

In all above-mentioned pore-network models the full range of shape factor distribution was not continuously generated. Since, for $G > 0.0481$ triangular cross sections cannot be used, regular polygons are applied. Consequently, the resulting network has a stepped shape factor distribution instead of a continuous one. In fact, for a given shape factor, many different (combinations of) cross-sectional shapes are possible. Therefore, one should investigate the effect of number of vertices of a pore throat cross section on the macroscale porous media properties.

5.1.2 Objectives

The focus of this work is two-fold.

a. We develop a well-defined procedure for the selection of the cross-sectional shape of pore elements based on image analysis data. Contrary to the previous pore networks, in this work, the choice of pore cross sections is linked either to the local shape factor or to the overall shape factor distribution. This allows us to recover the full shape factor distribution continuously and avoid an arbitrary selection of polygonal cross sections. Furthermore, this approach gives us information about the gains size distribution, which can be checked against the actual grain size distribution.

We carefully select a mix of pore throat cross sections - irregular or regular hyperbolic polygons. This allows us to match pore-space topological and geometrical data obtained from micro-tomographic imaging for any given value of shape factor. We develop formulas for the entry capillary pressure of various shapes, which can be solved numerically. Pore bodies are represented by prolate spheroids. In this work, we have employed *3DMA-Rock* software (*Lindquist*, 2009) for image analysis.

b. Pore-network models have been mainly used to study standard concepts such as relative permeability and capillary pressure-saturation relationships. Here, we also study the role of fluid-fluid interfacial areas in elucidating and parameterizing capillary effects in a two-phase flow. In particular, we investigate the conjecture by *Hassanizadeh and Gray* (1990, 1993a) that specific interfacial area, a^{nw} (defined as the amount of fluid-fluid interfacial area per unit volume of the porous medium) is a major state variable in two-phase flow and the main variable for proper modelling of capillary hysteresis.

This conjecture has been investigated earlier by *Held and Celia* (2001), *Joekar-Niasar et al.* (2008, 2009), *Reeves and Celia* (1996) using pore-network models. *Held* *and Celia* (2001), *Reeves and Celia* (1996), and *Joekar-Niasar et al.* (2008) used regular structured pore networks with circular cross sections. *Reeves and Celia* (1996) and *Joekar-Niasar et al.* (2008) concluded that hysteresis can be significantly reduced by including a^{nw} to generate one surface defined $F(P^c, S^w, a^{nw}) = 0$. *Joekar-Niasar et al.* (2008) showed that with increase of aspect ratio (ratio of pore body radius to pore throat radius), effect of a^{nw} in reducing the hysteresis decreases. However, their results were not compared with experiments. All these models lack some major structural features such as angularity of the cross sections and irregularity of the network. Thus, it is not clear whether the conclusions would hold in a real porous media with an unstructured irregular and angular pore network.

The only published comparison between pore-network results and experimental data in this regard is the work by *Joekar-Niasar et al.* (2009) who simulated drainage and imbibition experiments, performed in a two-dimensional micromodel. They generated imbibition and drainage P^c-S^w-a^{nw} surfaces and found that including a^{nw} reduced hysteresis. Since the micro-model was two-dimensional and had high porosity, the experiments had very uncommon features as follow. The saturation of the wetting phase changed between 0.68 and 1.0, so the range of saturation in P^c-S^w-a^{nw} surface was too limited. Due to the high porosity and small aspect ratio, the nonwetting phase did not trap at all during imbibition (no snap-off). This is very uncommon in practice. Furthermore, due to two-dimensionality of the model, the hysteresis in P^c-S^w curves was not significant (only about 20%) and the flow path was restricted to a three-dimensional medium.

In this work, we have developed a three-dimensional irregular unstructured pore-network model and validated it against experimental data. Data were obtained from air-water drainage and imbibition experiments in a glass-bead column and reported in *Culligan et al.* (2004). We compare our results against measured capillary pressure-saturation (P^c-S^w) and specific interfacial area-saturation (a^{nw}-S^w) curves during both drainage and imbibition and found very good agreement. Then, we generated P^c-S^w-a^{nw} surfaces for drainage and imbibition and study the conjecture developed by *Hassanizadeh and Gray* (1990, 1993a).

5.2 Pore-network model

5.2.1 Pore network structure and geometry

We develop an irregular and unstructured pore-network model. Pore bodies are represented by prolate spheroids and pore throats by tubes with *n*-hyperbolic polygonal cross sections (*n* denotes the number of vertices). Pore throat cross sections do not vary along their lengths. The topological and geometrical properties of the pore

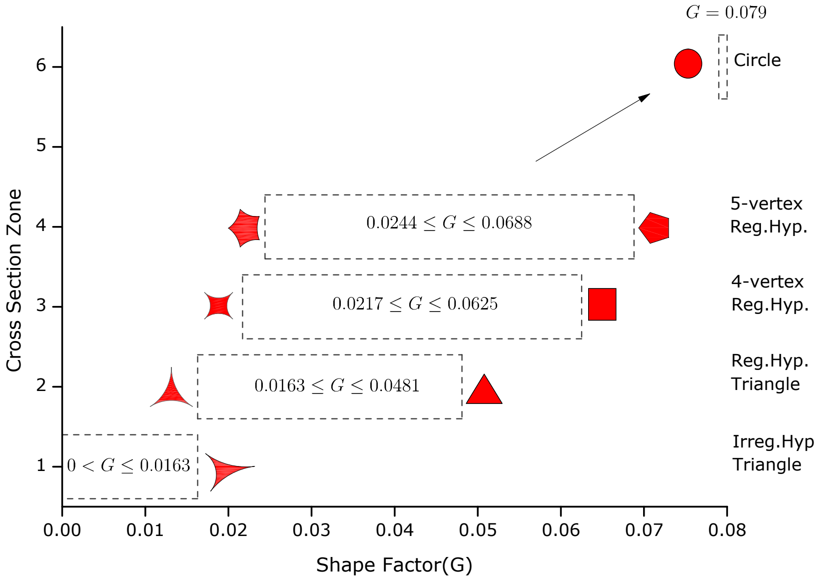

Figure 5.1: *Shape factor range for different cross sections; for each cross section zone (y-axis), the potential range of shape factor (G) has been shown in dashed-line.*

network are recovered from image analysis.

In the following parts, we present the formulations required for defining pore throat and pore body geometries.

Pore throats

Cross section determination Cross sections of pore throats are chosen such that the full range of shape factor, ($G = A/P^2$), calculated from image analysis, is recovered. The range of shape factor values for various cross sections is shown in Figure 5.1. Generally, with increasing of number of vertices, the shape factor increases as shown in Figure 5.1. A circle has the maximum shape factor, equal to 0.0795. For very elongated geometries (those with a small area but a large perimeter) the shape factor approaches zero.

In this study, we consider two general types for cross sections; irregular hyperbolic triangles ($n = 3$) and regular hyperbolic polygons with number of vertices $n \geq 3$ as shown in Figures 5.2(a) and (b), respectively. In irregular hyperbolic triangles, edges have different lengths (and radii of curvature). We consider only the case that the corner angles are zero. The range of shape factor values for various cross sections used in our network are shown in Figure 5.1. We choose irregular

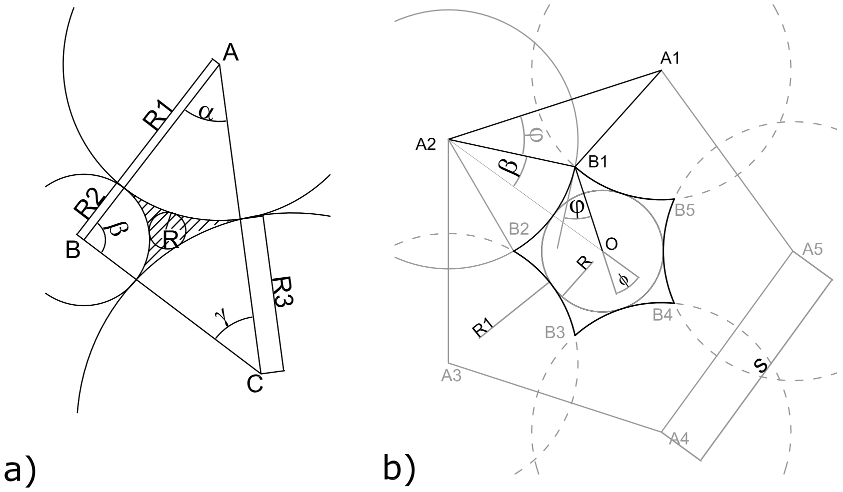

Figure 5.2: *Cross sections of pore throats for a) irregular hyperbolic triangle generated by three different tangential circles (soddy circles), b) regular hyperbolic polygon with five vertices. The hyperbolic polygon $B_{1..5}$ has an inscribed radius R and a half corner angle φ. The edge radius of curvature is R_1.*

hyperbolic triangles for shape factors less than 0.0163, and regular hyperbolic polygons otherwise. In regular hyperbolic polygons, all edges have the same length and the same radius of curvature. The corner angles are also equal and can be zero or larger (Figure 5.2(b)). For a given inscribed circle with radius R, by changing the corner angle, we can change the radius of curvature of edges, perimeter, area, and consequently shape factor G.

For a given cross section type, with increasing the corner angle from zero to the maximum possible value of $(\frac{n-2}{n}\pi)$, the cross section changes from a regular hyperbolic polygonal cross section to a regular polygonal cross section, and the shape factor increases. The choice of cross section type is based on the measured shape factor distribution of the pore throats acquired by image analysis. Geometrical properties and entry capillary pressures of these two general cross sections are obtained as described below.

Irregular hyperbolic triangles When three circles with different radii, namely R_1, R_2, R_3 are tangential to each other, they close off a specific geometrical shape among themselves (hatched region in Figure 5.2(a)). This is typically the cross section of a pore throat in a granular medium. This shape can be uniquely characterized by the radius of its inscribed circle R and its shape factor G. In principle, for a desired set of values for R and G, it is possible to calculate radii R_1, R_2, R_3, and angles α, β, and γ (shown in Figure 5.2(a)). The required equations, derived in Appendix E.1, are given below. They constitute a set of six nonlinear coupled equations that can be solved numerically using the *Newton-Raphson* method.

$$R = \frac{R_1R_2R_3}{R_1R_2 + R_2R_3 + R_1R_3 + 2\sqrt{R_1R_2R_3(R_1+R_2+R_3)}} \tag{5.1}$$

$$\sin\alpha = \frac{2\sqrt{R_1R_2R_3(R_1+R_2+R_3)}}{(R_1+R_2)(R_1+R_3)} \tag{5.2}$$

$$\sin\beta = \frac{2\sqrt{R_1R_2R_3(R_1+R_2+R_3)}}{(R_1+R_2)(R_2+R_3)} \tag{5.3}$$

$$\sin\gamma = \frac{2\sqrt{R_1R_2R_3(R_1+R_2+R_3)}}{(R_2+R_3)(R_1+R_3)} \tag{5.4}$$

$$\alpha+\beta+\gamma = \pi \tag{5.5}$$

$$G = \frac{\sqrt{R_1R_2R_3(R_1+R_2+R_3)} - 0.5(R_1^2\alpha + R_2^2\beta + R_3^2\gamma)}{(R_1\alpha + R_2\beta + R_3\gamma)^2} \tag{5.6}$$

Regular hyperbolic polygons (*n* vertices) A regular hyperbolic polygon is enclosed among three or more intersecting circles of equal radius. For example, Figure 5.2(b) shows a hyperbolic pentagonal cross section generated by five intersecting circles with radius R_1. A regular hyperbolic polygon is uniquely characterized by its inscribed radius R, shape factor G, and number of vertices n. Thus, for given R, G, and n, the following set of equations can be solved to determine R_1 and φ. φ is the angle between the tangent at a vertex and the line connecting the vertex to the center of the cross section.

$$G = \frac{\cos^2\varphi\cot\frac{\pi}{n} - \pi(\frac{1}{2}-\frac{1}{n}) + \varphi - 0.5\sin 2\varphi}{4n[\pi(\frac{1}{2}-\frac{1}{n}) - \varphi]^2} \tag{5.7}$$

$$R_1 = R\frac{\sin\frac{\pi}{n}}{\cos\varphi - \sin\frac{\pi}{n}} \tag{5.8}$$

Detailed explanation for the derivation of this set of equations is given in Appendix E.2. Note that for a regular polygon, $\varphi = \frac{\pi}{2} - \frac{\pi}{n}$, $R_1 = \infty$, and $G = \frac{\cot\frac{\pi}{n}}{4n}$.

Pore bodies

The pore bodies are chosen to have the shape of a prolate spheroid with equatorial radii *a* and *b*, where $a \le b$ (Figure 5.3). The volume of a prolate spheroid is equal to $\frac{4}{3}\pi a^2 b$.

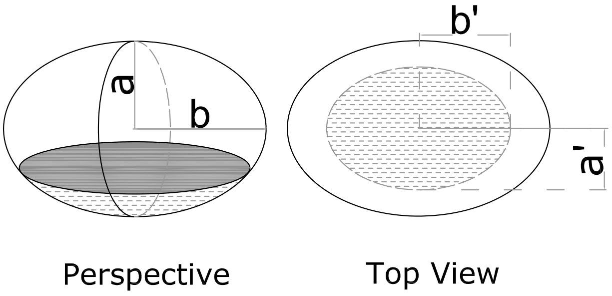

Figure 5.3: *Schematic configuration of an interface within a pore body (assumed as a prolate spheroid) during imbibition.*

5.2.2 Invasion criteria

In multiphase flow, the invasion is locally controlled by capillary pressure, i.e. the difference between nonwetting and wetting phase pressures. Pore throats control the invasion during drainage, and pore bodies during imbibition. Thus, network models require knowledge of the pore throat entry capillary pressure (for drainage), and the pore body filling capillary pressure (for imbibition).

Pore throat invasion

Figure C.1 shows the schematic cross section of a pore throat filled with nonwetting and wetting fluids. The fluid-fluid interface has a radius of curvature r_c. We denote the area occupied by the nonwetting phase by A_n and the length of contact lines between various phases by L_{ns}, L_{nw}, and L_{ws} (Figure C.1). The relationship between the entry capillary pressure (P_e^c) and geometrical parameters is found by examining force balance under equilibrium conditions (see Appendix C). This results in:

$$\frac{P_e^c}{\sigma^{nw}} = \frac{1}{r_c} = \frac{L_{nw} + L_{ns}\cos\theta}{A_n} \tag{5.9}$$

where, σ^{nw} is the interfacial tension. This equation is equally valid for regular and irregular hyperbolic polygons.

Irregular hyperbolic triangle According to Equation 5.9, L_{nw}, L_{ns}, and A_n should be known for a given cross section, in order to calculate r_c. The formulas for calculation of these terms are given in Table F.1 based on the geometries given in Figures F.1(a) and (b). Detailed explanation for the derivation of the these formulas is given in Appendix F.

Substitution of L_{nw}, L_{ns}, and A_n from Table F.1 into Equation 5.9 results in a highly nonlinear equation for r_c involving nine other unknowns, namely ε^i, ε^i_i, ε^i_{i+1} $(i = 1, 2, 3)$. That equation, therefore, has to be supplemented with the following nine equations:

$$\tan \varepsilon^i_i = \frac{r_c \sin \varepsilon^i}{R_i \cos(\theta + \varepsilon^i)}, i = 1, 2, 3 \tag{5.10a}$$

$$\tan \varepsilon^i_{i+1} = \frac{r_c \sin \varepsilon^i}{R_{i+1} \cos(\theta + \varepsilon^i)}, i = 1, 2, 3 \quad (\varepsilon^3_4 = \varepsilon^3_1, R_4 = R_1) \tag{5.10b}$$

$$\varepsilon^i + \varepsilon^i_i + \varepsilon^i_{i+1} = \frac{\pi}{2} - \theta, i = 1, 2, 3 \quad (\varepsilon^3_4 = \varepsilon^3_1) \tag{5.10c}$$

Thus, Equations 5.9 and 5.10 form a set of 10 equations to be solved for r_c, ε^i, ε^i_i, and ε^i_{i+1} $(i = 1, 2, 3)$. The resulting nonlinear system of equations has been solved numerically using NLEQ1S (*Nowak and Weimann*, 1991), which employs the global affine invariant Newton algorithm. Detailed explanation for the derivation of the set of equations is given in Appendix F. Once r_c is known, entry capillary pressure P^c_e can be calculated.

Regular hyperbolic polygon Figure F.1(c) shows the vertex of a regular hyperbolic polygon filled by the wetting phase. Similar to the approach used for irregular hyperbolic triangle and according to Figures 5.2(b) and F.1(c), L_{nw}, L_{ns}, and A_n may be written as functions of geometrical parameters, as derived in Appendix F and shown in Table F.1.

Substitution of L_{nw}, L_{ns}, and A_n in Equation 5.9 results in a nonlinear equation for r_c involving two other unknowns, namely ε and ε'. That equation, therefore, has to be supplemented with the following two equations in order to solve for r_c, ε, and ε'.

$$\frac{\sin \varepsilon}{\sin 2(\varphi + \varepsilon')} = \frac{R_1 \sin \varepsilon'}{r_c \sin(\varepsilon + \varepsilon' + \theta)} \tag{5.11a}$$

$$2\varepsilon' + \varepsilon = \frac{\pi}{2} - \theta - \varphi \tag{5.11b}$$

We solve this set of equations numerically using standard *Newton-Raphson* method.

Pore body filling

Since the entry capillary pressure of pore bodies is smaller than that of pore throats, pore bodies are filled spontaneously under drainage. However, during imbibition they are filled gradually. For the fluid-fluid interface shown in Figure 5.3, assuming that the interface is normal to the equatorial radius a, we can calculate the filling capillary pressure under imbibition. Here also, Equation 5.9 applies. A_n and L_{ns} are given by the following formulas:

$$A_n = \pi a' b' \tag{5.12a}$$

$$L_{ns} \approx \pi \sqrt{2(a'^2 + b'^2)} \tag{5.12b}$$

where a' and b' are shown in Figure 5.3. Based on Equations 5.9 and 5.12, and introducing $\Gamma = a/b = a'/b'$, it follows that

$$\frac{P^c}{\sigma^{nw}} = \frac{1}{r_c} = \frac{\sqrt{2(1+\Gamma^2)}}{a'}, \quad \Gamma = \frac{a}{b} = \frac{a'}{b'} \tag{5.13}$$

For a given r_c and a', we can approximate volume of the wetting fluid by:

$$V_w \approx \frac{4}{3}\pi a' b' (a - \sqrt{a^2 - a'^2}) \tag{5.14}$$

5.2.3 Translation of pore space data into the pore network

Relationships presented so far are employed in development of pore-network elements by analyzing 3-D microtomography images. We need the following information:

- Skeleton of the porous medium (connectivity information of pore bodies to pore throats)
- Pore body center coordinates and their coordination number.
- Pore unit volumes; this is the volume delineated by the narrowest cross sections of all pore throats connected to a pore body. Figure 5.4 shows schematically such a pore unit in two dimensions.
- Equatorial radii of pore bodies. Three principal diameters are determined for each pore unit by measuring the pore width through the centroid of pore unit in each of the principal directions. One half of the two smallest principal diameters are assigned as equatorial radii *a*, *b* of the representative prolate spheroids.
- Pore throat cross-sectional area and the corresponding shape factor. They should be determined so that the total volume of void space is conserved in the network model. Thus, length of pore throats in the pore-network model will be determined such that the volume of each and every pore-unit is the

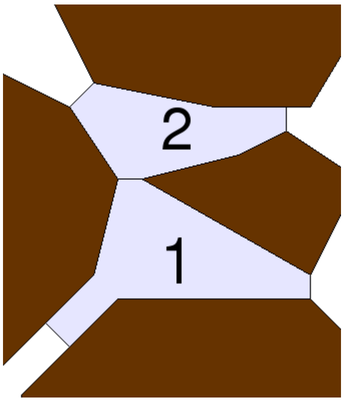

Figure 5.4: *Schematic presentation of pore units in bright color and grains in dark color.*

same as the volume of corresponding pore body and corresponding part of connected pore throats.

The procedure for generation of the pore-network model is as follows: In the first step, exact topology of the porous medium is translated into the pore network; i.e. skeleton of the porous medium resulted from image analysis is used to determine number of pore bodies, number of pore throats, and connectivity. Next, using a search algorithm and with sequential numbering of pore bodies and pore throats, the connectivity matrix (showing which pore body is connected to which pore throat) is generated. As a result, the coordination number distribution of the porous medium is generated in the pore network. Furthermore, in the analysis, we determine which pore throats are located on the boundary of the imaged section.

In the second step, local geometrical information is assigned to the pore network elements. The volumes of pore units are estimated by analysis of the 3-D microtomography images using *3DMA-Rock* software. Calculated equatorial radii a and b determine the volume (Section 5.2.1) of each pore body. The difference between the pore unit volume and pore body volume (referred to as "excess volume") should be assigned to the pore throats. Excess volume of each pore unit will determined the length of pore throats located in that pore unit. Knowing the cross-sectional area of pore throats from image processing and assuming that all pore throats within a pore unit have the same length, the length of pore throats belonging to a pore unit can be determined. Finally, the total length of a pore throat is obtained by adding the two pore throat lengths from the two neighboring pore units.

As the last step, cross section geometry of each pore throat should be determined. Using the shape factor and cross sectional area of pore throats, geometry of the cross

Table 5.1: *Specifications of air-water experiments in glass beads.*

Property	Value	Unit
Porosity	0.34	
Sample height (imaged section)	6.1×10^{-3}	m
Sample diameter	6.9×10^{-3}	m
Water dynamic density	1.002×10^{-3}	Pa.s
Air dynamic density	1.86×10^{-6}	Pa.s
Air-water interfacial tension (σ^{nw})	0.7275	N/m
contact angle (θ)	$0 - 4$	degree

sections can be determined using the approach proposed in Section 5.2.1.

We used *3DMA-Rock* software (*Lindquist*, 2009) for image analysis. This software employs a voxel-based medial axis approach to extract topological and geometrical properties of a porous medium. Detailed information about application of this software can be found in *Prodanović et al.* (2006, 2007).

5.3 Case study:two-phase experiments in packed glass beads

5.3.1 Materials and experiments

We analyze a set of air and water displacement experiments carried out in a synthetic porous medium (*Culligan et al.*, 2004). The medium consisted of packed soda lime glass beads with three size classes, 0.6, 0.85 and 1.0-1.4 mm in diameter. Porosity of the column was 34%. The beads were packed in a column of 7 mm in diameter and 70 mm in length. The column was connected to the atmosphere on the top, and to a water reservoir at the bottom. Experiment specifications are shown in Table 5.1. The column was packed dry and subsequently filled with water. Primary drainage, main imbibition, and main drainage experiments were performed. To prevent air from entering the water reservoir, a semi-permeable membrane was placed at the bottom of the column. Experiments were performed by pumping a known amount of water in or out of the medium. After shutting off the pump, the system was allowed to equilibrate. Then, fluid pressures were measured and a 5-*mm* section of the column was imaged using X-ray microtomography for each P^c-S^w point in the experiments (image voxel length was 17 μm). The three-dimensional images allowed to quantify fluids distribution and determine saturation and specific interfacial area

Table 5.2: *Classification of cross sections based on the shape factor distribution.*

Zone	Shape Factor (G)	Cross Section
1	$G < 0.0163$	irregular hyperbolic triangle (3 vertices)
2	$0.0163 \leq G < 0.0217$	regular hyperbolic triangle (3 vertices)
3	$0.0217 \leq G < 0.0244$	regular hyperbolic polygon (4 vertices)
4	$0.0244 \leq G < 0.0688$	regular hyperbolic polygon (5 vertices)
5	$0.0688 \leq G$	circle

for each equilibrium point. Water pressure was measured directly above and below the imaged section as well as in the water line outside of the column. This procedure was repeated multiple times in each cycle to obtain enough points to construct a complete drainage or imbibition curve.

5.3.2 Numerical simulations

As explained before, the imaged section of glass beads was translated into the pore-network model. Figure 5.5(a) shows the shape factor distribution for pore throat cross sections as computed with *3DMA-Rock*. Based on this shape factor distribution, we select the cross-sectional shapes as shown in Table 5.2. A small range of the distribution falls outside the theoretical upper limit (0.0795). This is attributed to the finite resolution of the image and the fact that the bottlenecks between pore units are not necessarily planar surfaces. This range is represented by circles in our model. Figure 5.5(a) shows that the majority of pore throats (97.2%) can be reproduced using regular hyperbolic polygonal cross sections with five vertices. Figure 5.5(b) shows the coordination number distribution of the glass beads sample as computed with *3DMA-Rock*. It should be noted that the most frequent coordination numbers are 3 and 4 for this medium. There is also a coordination number of 113, which is related to a large pore in the glass beads connected to many other neighboring pores. Results of image analysis shows that there are 367 pore bodies and 1302 pore throats. Total volume of the void space is 31.85 mm^3. Out of this volume, 26.64 mm^3 are assigned to the pore bodies and 5.21 mm^3 to the pore throats.

Boundary conditions

Pore throats connected to the side boundaries are closed in order to mimic the experiments. Reservoirs of fluids are each at a constant pressure. Top and bottom pore throats might be assumed to be connected to reservoirs of nonwetting fluid (air) and

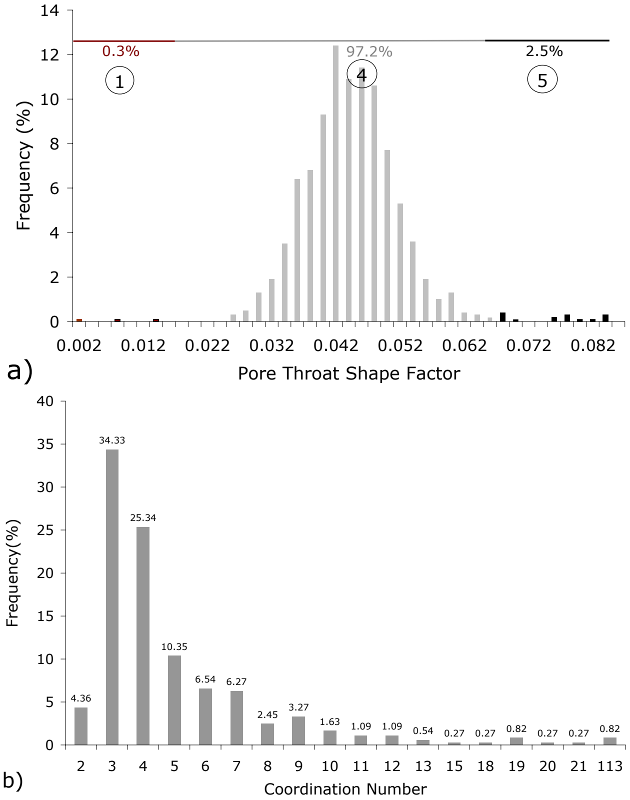

Figure 5.5: *a) Shape factor distribution for pore throats in the glass-bead medium. Pore throats classification (zone numbers are given in circles) has been made according to Table 5.2. b) Coordination number frequency (% number of pore bodies) of the glass beads sample.*

wetting fluid (water). As mentioned earlier, the scanned section simulated by our model is only a small part of a larger column. Since capillary forces are dominant in the experiments, there is a capillary fingering regime in the column. Thus only a few pores on the scanned column section are in contact with the invading phase reservoir. It means that our assumption for “connectivity of the boundary pores” to the nonwetting fluid reservoir is unclear. Two different assumptions for accessibility of the boundary pores might be considered: a) assuming all pores on the top boundary of the scanned section are in contact with the nonwetting fluid reservoir. b) assuming only one of more largest pores on the boundary of the scanned section are in contact with the nonwetting phase reservoir. The effect of these assumptions on P^c-S^w and a^{nw}-S^w curves and the correct choice in this regard will be discussed in Section 5.4.2.

Simulation of primary and main drainage

At the start of primary drainage, the pore network is fully saturated with the wetting phase (water). For the main drainage, the wetting phase is initially present in some pores, as determined at the end of an imbibition simulation. The pressure of the wetting phase reservoir is assumed to be zero and not changing. The pressure of the nonwetting phase reservoir is initially set to zero, and thus the imposed capillary pressure is also zero. Drainage simulation starts by increasing the pressure of the nonwetting phase reservoir to the entry capillary pressure P_e^c of the largest pore throat connected to the reservoir (Equation C.1). As the entry capillary pressure of a pore body is smaller than that of a pore throat, the controlling element is the pore throat. Thus, as soon as the pressure is high enough to enter a pore throat, because the pore throat has a constant cross section, nonwetting phase would occupy that pore throat and the connected pore body. When no other pores can be occupied in that pressure step, the corresponding capillary pressure, saturation, and interfacial area are calculated. The incremental increase in nonwetting phase pressure is continued, allowing for more pores to be occupied by the nonwetting phase. Simulation of drainage scanning curves is more complex than primary drainage curve. Since each drainage scanning curve starts from an equilibrium imbibition point, fluid configuration should be captured properly. There may be some trapped nonwetting phase at the beginning of drainage scanning curve. Therefore, a search algorithm is required to determine these trapped nonwetting blobs. Invasion can happen only from those pores which are in contact with the nonwetting reservoir, and in the process of invasion, they will connect to the trapped nonwetting phase blobs.

Simulation of imbibition

The fluid configuration at the end of the primary drainage simulations is used as the starting condition for main imbibition. The pressure of nonwetting phase reservoir is decreased, causing the nonwetting phase to recede. The replacement of the nonwetting phase by the wetting phase starts from those pore throats that have the highest entry pressure (smallest size). Since there are many pore throats with angular cross sections, the wetting phase is always present in the corners. With decreasing of the capillary pressure, the wetting phase content in the corners of pore throats will increase, eventually filling the pore throat. A pore throat with a noncircular cross section will be filled completely by the wetting phase only if the following criterion is met (*Vidales et al.*, 1998).

$$P^c \leq \frac{\sigma^{nw}}{R}(\cos\theta - \sin\theta) \tag{5.15}$$

Where R is the radius of inscribed circle. For circular cross sections, a pore throat will be fully filled if $P^c \leq 2\frac{\sigma^{nw}}{R}\cos\theta$. Once a pore throat connected to the wetting phase reservoir is filled, the wetting phase enters the neighboring pore body and stops at a position with a curvature corresponding to the imposed capillary pressure (for which a' is calculated from Equation 5.13). For sake of simplicity of geometrical configurations, we assume that only one interface may exist in each pore body. As the capillary pressure is decreased further, the wetting phase gradually fills the pore body. As soon as the interface radius is equal to the pore body maximum radius (Equation 5.13), the rest of the pore body and the connected pore throats fill up instantaneously by the wetting phase. Similar to the drainage experiment, for a given boundary pressure, when no other pores can be filled, capillary pressure, saturation, and interfacial area are calculated. Simulation of imbibition scanning curves is not different from main imbibition curve. The only difference is the starting wetting phase saturation.

The simulation of the full cycle of primary drainage and main imbibition took less than 2 minutes on Intel(R) CPU 6600, 2.4GHz with 2GB RAM.

Calculation of saturation, capillary pressure and specific interfacial area

Under static conditions, and in the absence of gravity, capillary pressures, P^c, at all interfaces are the same, equal to the difference between nonwetting and wetting fluid reservoir pressures, ($P^c = P^n - P^w$). Saturation of each phase can be easily calculated from the geometry and fluid occupancy of pore bodies and pore throats. We can also calculate the interfacial areas as we know the location of fluid-fluid interfaces within pore throats and pore bodies. Two different interface types may be identified: "*arc menisci* (AM)", formed along pore throat edges, and "*main terminal menisci* (MTM)", spanning the cross section of a pore body or a pore throat (*Mason and Morrow*, 1987). The area of "*AM*" is calculated from total length of nonwetting-wetting phase lines and length of pore throats. Behaviour of *MTM* during drainage and imbibition is different. During drainage, within a pore body filled with the nonwetting phase, there is *MTM* at the entrance of a pore throat, which is not invaded yet. Since the exact geometry of the interface is complicated, we approximate its area during drainage with that of the pore throat cross section; thus, effectively assuming a flat interface. However, during imbibition the *MTM* will be situated within a pore body. The area of a *MTM* within a prolate spheroidal pore body can be calculated

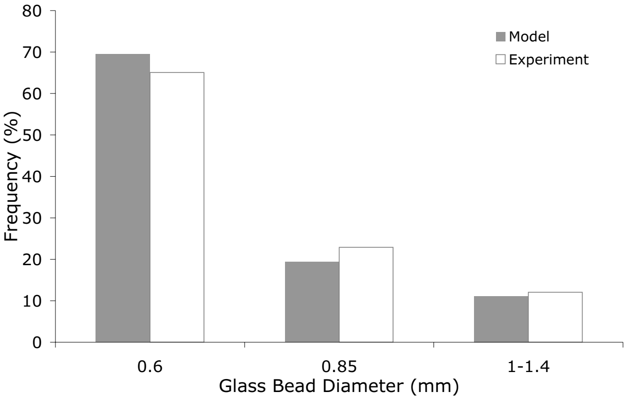

Figure 5.6: *Comparison between grain size distribution resulted from the model and the experimental data.*

using Equation 5.12(a) and the volume of the wetting phase can be calculated using Equation 5.14.

5.4 Results and discussions

5.4.1 Grain size distribution

The hyperbolic polygon shapes chosen for the pore throat cross sections in our model were characterized by semi-circular edges. In our model, radii of the edges were calculated from the shape factor distribution. The consistency of the pore-network model with the actual soil sample can be examined by comparing the calculated radii of edges and nominal grain size distribution as shown in Figure 5.6. The histogram distribution in Figure 5.6 has been generated for the three classes of grain size mentioned in the experimental data. There is a very good agreement between the model and the actual sample. This shows that generation of the cross sections in the model is consistent with grain sizes while the shape factor distribution is fully recovered from image analysis.

5.4.2 Effect of boundary pore connectivity

As explained in Section 5.3.2, not all boundary pores are necessarily connected to the nonwetting phase reservoir. We did some simulations to analyze effect of this connectivity boundary pore(s) on P^c-S^w and a^{nw}-S^w curves. Our analysis (not presented here) shows that assuming all boundary pores connected to the nonwetting phase has a significant influence on a^{nw}-S^w curve. If all pore bodies located on the boundary are assumed to be connected to the nonwetting phase reservoir, initially there will be a significant amount of interfacial area, which is not in agreement with data. But, if we assume only few of the largest boundary pore(s) be connected to the reservoir, creation of specific interfacial area occurs gradually as the pressure is increased. This analysis shows that the imaged section of glass-bead column is not so large to be insensitive to the boundary conditions. However, the effect of boundary condition on a^{nw}-S^w has been minimized by assuming the largest pore to be connected to the nonwetting phase reservoir.

5.4.3 Effect of shape factor and pore shape on P^c, S^w, and a^{nw}

As mentioned in Section 5.1, up to now only shape factor (G) has been introduced in the development of pore-network models. But, geometrical shape (number of vertices n) and shape factor (G) are the two parameters that control the entry capillary pressure (P^c_e), (corner) wetting phase saturation (ş^{w}), and specific interfacial area (ą^{nw}) associated with arc menisci (*AM*). These effects are illustrated for a single pore throat as well as for the whole network.

First, effects of n and G on entry capillary pressure, corner wetting phase saturation, and AM area for a single pore are shown. We consider a number of pore throats with a unit length, and the same cross-sectional area (A_{tot}). All pores have regular hyperbolic polygon shape with different values for G and n. Corner saturation is defined as the ratio of cross-sectional area of wetting phase to total cross-sectional area of a pore throat, A_w/A_{tot}. Figures 5.7(a) and 5.7(b) show variations of the corner saturation (ş^{w}) as a function of shape factor (G) and number of vertices (n) for two different situations, $r_c = 0.5R_{eq}$, and $r_c = 0.15R_{eq}$, respectively. R_{eq} is defined as the radius of a circle with area of A_{tot}, i.e. $R_{eq} = \sqrt{A_{tot}/\pi}$. These figures show that ş^{w} strongly depends on G and n. This dependence, however, decreases as G and/or n increase. At larger capillary pressures ($r_c = 0.15R_{eq}$), there is a non-monotonic dependence. As the number of vertices increases, more wetting phase can be kept in the corners (larger ş^{w}) for a given shape factor. In both cases, for large number of vertices, ş^{w} approaches zero because the cross section approaches a circle.

Although in this work the geometries of pore throats' cross sections have been idealized, these results may illustrate the origin of uncertainties in some applications of predictive pore-network models. If in a real porous medium the volume of pore throats compared with pore bodies is considerable, shape of the cross section can influence the accuracy of quantitative assessment. For instance, while in all simulations shown in Figure 5.7, cross section areas are the same, residual wetting phase saturations are significantly different for a given shape factor. This effect can

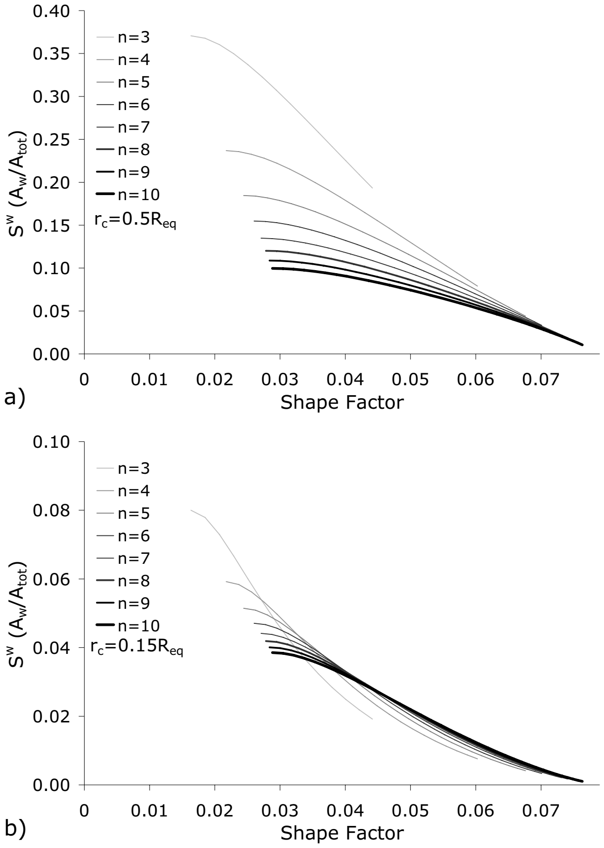

Figure 5.7: *Effect of shape factor and number of vertices on corner saturation, $\text{\c{s}}^{w}$, in a pore throat for a) Radius of curvature $r_c = 0.5R_{eq}$, b) Radius of curvature $r_c = 0.15R_{eq}$. All cross sections have the same cross-sectional area A_{tot}.*

be even more significant for quantitative assessment of relative permeability curves, where $k^{\alpha} \propto S^{\alpha}$. As Figure 5.7 shows at small capillary pressures (high wetting phase saturation), effect of shape of cross sections is important. Simulations of relative permeabilities using pore-network models show that the largest inaccuracies occur at high saturations, especially for the wetting phase permeability (e.g. *Blunt et al.*, 2002, *Valvatne and Blunt*, 2004). This implies that for predictive pore-network modelling, in addition to G, the number of vertices (n) should be included in the development of pore networks.

Fluid-fluid interfacial area in a pore throat contributes to the AM area. For a single pore throat, effect of G and n on AM is investigated by examining $\text{\k{a}}^{nw}$, defined

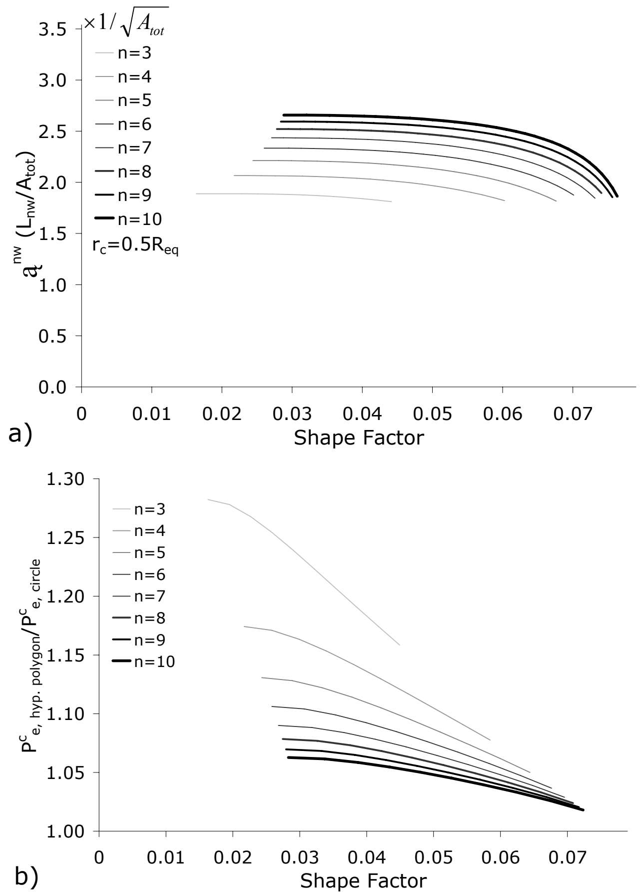

Figure 5.8: *Effect of shape factor and number of vertices on a) nonwetting-wetting corner specific interfacial area* $ą^{nw}$ *in a pore throat for radius of curvature* $r_c = 0.5R_{eq}$*, b) entry capillary pressure. Entry capillary pressures have been normalized with the entry capillary pressure for a circular tube with cross-sectional area equal to* A_{tot}*. All cross sections have the same cross-sectional area denoted by* A_{tot}*.*

as the ratio of the length of nonwetting-wetting line (L_{nw}) to the total cross-sectional area, A_{tot}. Variations of $ą^{nw}$ with G and n for $r_c = 0.5R_{eq}$ is shown in Figures 5.8(a). As it can be observed, $ą^{nw}$ varies monotonically with G values and increases as the number of vertices increases. With increase of capillary pressure (decrease of r_c), corner specific interfacial area decreases. Our analysis (not presented here) shows that with the increase of P^c by a factor of three, the specific interfacial area decreases by about half. Effect of geometrical shape and shape factor on specific interfacial area will be important in those porous media that have long pore throats. In such porous media, *AM* area can be even smaller that AM area. This has been shown by *Raeesi and Piri* (2009); depending on the geometry and topology of a porous medium, interfacial area associated with the arc menisci can be larger than the interfacial area associated with the area of MTM. *Raeesi and Piri* (2009) have simulated AM and MTM area in two mixed cross-sectional pore-network models based on *Berea* sandstone and *Saudi Aramco* sandstone, and show that the area of AM is larger than the area of MTM.

Finally, the effect of G and n on entry capillary pressure for a single pore throat is shown in Figure 5.8(b). Here, entry capillary pressures have been normalized with the entry capillary pressure for a circular tube with the same cross-sectional area (A_{tot}). It is evident that the entry capillary pressure decreases monotonically with the increase in G and/or n. Obviously, as the number of vertices increases, the entry capillary pressure approaches that of a circular cross section.

To see the effect of shape of cross section on macroscale P^c-S^w and a^{nw}-S^w curves, we have simulated drainage experiments with three different networks consisting of circular cross sections, mixed polygonal cross sections, and mixed hyperbolic polygonal cross sections. Figures 5.9(a) and 5.9(b) show P^c-S^w and a^{nw}-S^w curves, respectively, compared to the experimental data. It is obvious that including the hyperbolic polygonal cross section significantly improves the agreement between simulations and experiments, especially for P^c-S^w curves.

In simulations shown in Figure 5.9, all networks have the same skeleton (coordination number distribution), void volume, and pore throat cross sectional area distribution. Since the network is small (364 pore bodies), effect of pore geometries are pronounced. A network with all pores having circular cross sections cannot recover the shape factor distribution. So, for a given cross-sectional area, it results in a smaller entry capillary pressure than the other shapes. In addition, there is no saturation associated with the wetting phase in the corners. The difference between results for a mixed polygonal network and mixed hyperbolic polygonal network for large saturations is not significant. However, at small saturations, smallest pores need to be invaded. Obviously for high capillary pressures, a network with hyperbolic polygonal cross sections can keep more wetting phase in the corners compared with other types of networks. Effect of n on the specific interfacial area values over the whole domain is not very significant. This is because in glass beads, the volume of pore throats compared with the volume of pore bodies is not significant. Thus, area of *AM* is much smaller than the area of MTM.

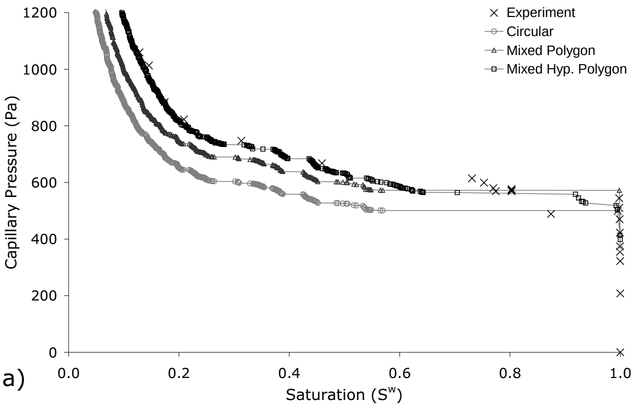

a)

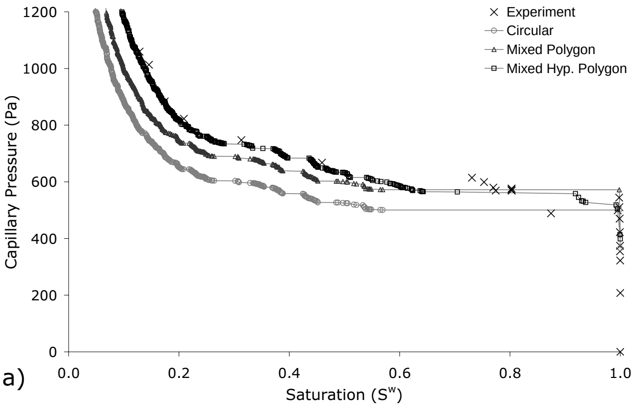

a)

Figure 5.9: *Effect of selection of pore throat cross section on a) P^c-S^w drainage curve and b) a^{nw}-S^w drainage curve.*

5.4.4 P^c-S^w and a^{nw}-S^w curves

We employ insights obtained from the study of effects of boundary pores and cross section geometry to simulate the experimental data. Thus, P^c-S^w and a^{nw}-S^w curves have been obtained for primary drainage and main imbibition processes using a network with mixed hyperbolic polygonal pore throats and a single pore connected to the boundary. Results are shown in Figures 5.10(a) and 5.10(b). The agreement with measured curves are excellent. This is a particularly significant result for imbibition curves as many pore-network models have had difficulty to match imbibition data points for capillary pressure.

Figure 5.10(a) shows that there is a strong hysteresis in P^c-S^w curves resulted from drainage and imbibition (up to 100%). The magnitude of this hysteresis is

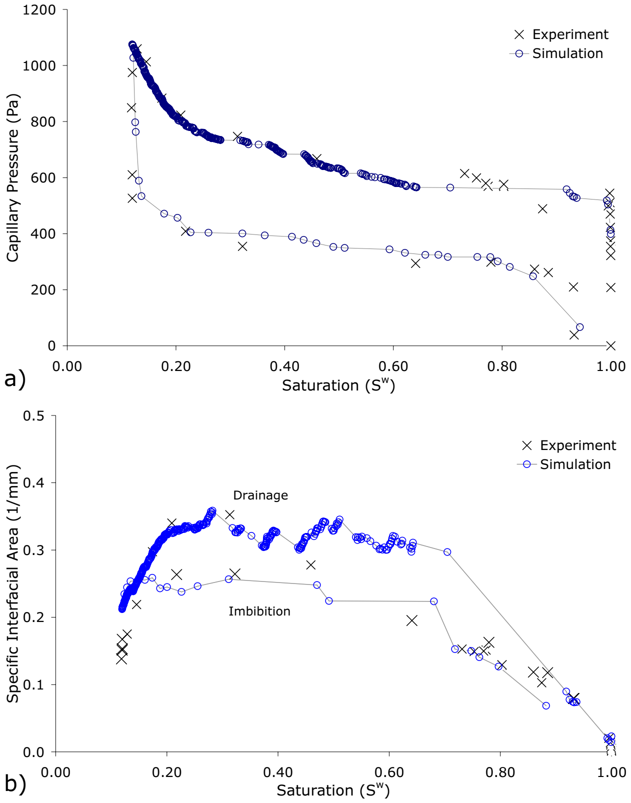

Figure 5.10: *Comparison between simulations and experiments for drainage and imbibition a) P^c-S^w curves b) a^{nw}-S^w curves.*

larger than that of P^c-S^w curves resulted from sand pack columns (*Valvatne and Blunt*, 2004); which is due to the larger aspect ratio of pores in glass bead packing.

Compared with P^c-S^w curves, there is more discrepancies between a^{nw}-S^w curves especially during imbibition. This is due to the small size of the domain and simplified geometries assumed for the interface. Nevertheless, accuracy of the model in prediction of a^{nw} is good. Such model can be a powerful tool for generating input data such as P^c-S^w-a^{nw} surface needed for new macroscopic multiphase flow simulators such as *Niessner and Hassanizadeh* (2008, 2009). They solved multiphase flow and transport equations including interfacial area as a new state variable.

5.4.5 P^c-S^w-a^{nw} surfaces

After having validated the model against experimental data, we can use it to investigate role of specific interfacial area in removing or reducing the hysteresis in capillary pressure-saturation curves. We have simulated many scanning loops of drainage and imbibition and have calculated equilibrium values of P^c, S^w, and a^{nw}. Results are plotted in Figures 5.11(a) and (b) for drainage and imbibition, respectively, where contours of a^{nw} are shown in P^c-S^w plane. The shade coding shows specific interfacial area for a given pair of capillary pressure and saturation. The natural neighbor interpolation method (*Sibson*, 1981) has been used to generate the surfaces. The corresponding surfaces have been depicted in Figures 5.11(a) and (b) by showing contour lines of equal specific interfacial area. The correlation coefficient between the two surfaces was found to be 95%. Next, the difference between imbibition and drainage surfaces has been normalized by drainage surface as plotted in Figure 5.11(c). As it can be observed, the maximum difference in main loop of drainage and imbibition curves is about 25%. The average normalized difference over the entire surface is about 15%. To investigate in more detail causes of difference between drainage and imbibition surfaces, we have included normalized difference between experimental data and simulations (Figure 5.11(d)). The average normalized difference in this figure is 19%, which is very close to the average difference calculated in Figure 5.11(c) with similar spatial trend in error variation. We should note that the maximum difference is observed in the range of capillary pressure-saturation where no data point exists. Thus, it could be mainly an artifact of the interpolation. A similar trend was found by *Joekar-Niasar et al.* (2009) (Figure 12c, page 10), which was also due to lack of imbibition data points in that region. Comparing Figure 5.11(c) with 5.11(d), one can observe that the difference between the simulated drainage and imbibition surfaces is very close to the uncertainty range of modelling procedure.

The maximum differences in P^c-S^w and a^{nw}-S^w curves in micro-model simulations of *Joekar-Niasar et al.* (2009) were about 20% and 300%, respectively. None of these values are common in real three-dimensional porous media. Nevertheless, the reduction in difference between $a^{nw} = f(P^c, S^w)$ surfaces over the whole loop of drainage and imbibition ($S^w \in [0.65, 1]$) was considerable (*Joekar-Niasar et al.*, 2009). In this work, the maximum differences between P^c-S^w and a^{nw}-S^w curves (i.e. the hysteresis effect) are 100% and 50%, respectively. Whereas, the difference between $a^{nw} = f(P^c, S^w)$ surfaces over the whole loop of drainage and imbibition ($S^w \in [0.15, 1]$) is about 15%. This is a major reduction of hysteretic behaviour. Thus, we can conclude that $a^{nw} = f(P^c, S^w)$ surfaces are almost identical within experimental and computational uncertainties; i.e. the hysteresis in P^c-S^w-a^{nw} surfaces

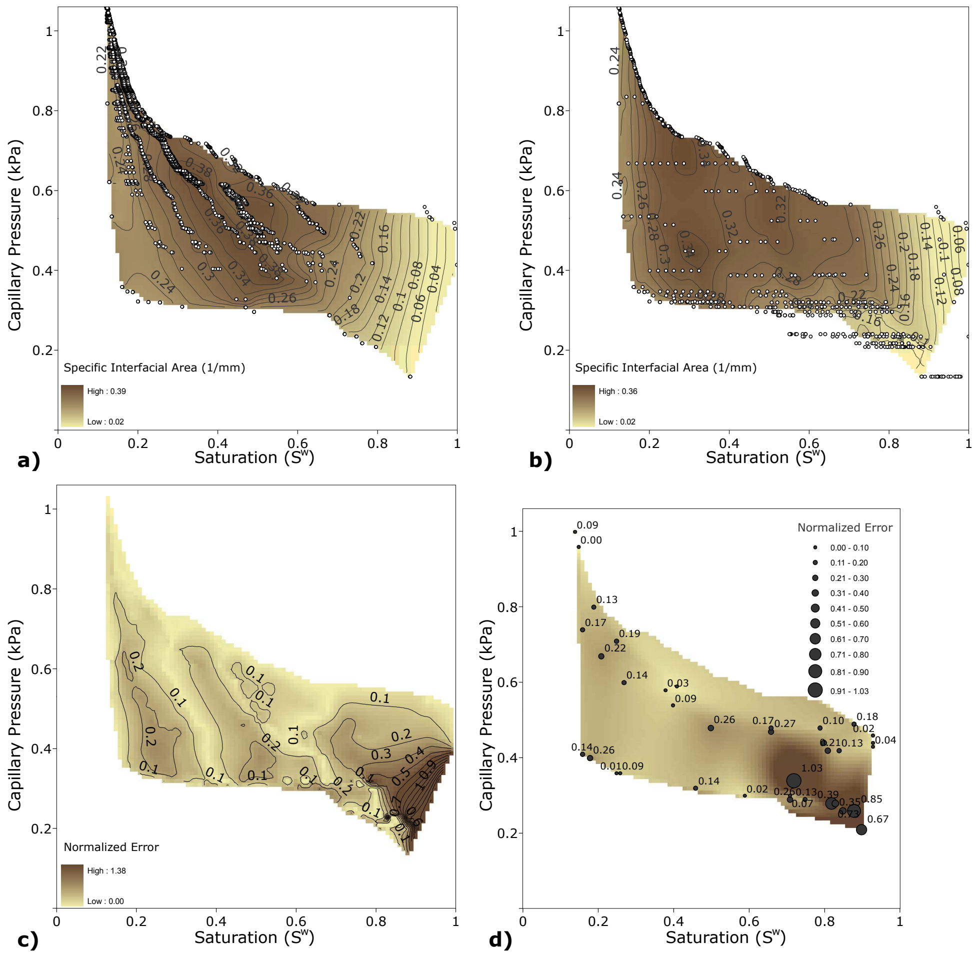

Figure 5.11: *Contours of specific interfacial area and normalized differences shown in the capillary pressure-saturation plane. a) Simulated P^c-S^w-a^{nw} surface for drainage, b) Simulated P^c-S^w-a^{nw} surface for imbibition, c) Difference between (a) and (b) normalized by (a), d) Difference between simulations and experimental data normalized by experimental data. Color coding in (a) and (b) shows specific interfacial area, and in (c) and (d) it shows the normalized difference. All surfaces have been generated using natural neighboring interpolation.*

for the main loop is negligible. One should note that these results are related to a three-dimensional unstructured and irregular porous medium, which is topologically and geometrically very different from previous works such as *Held and Celia* (2001), *Joekar-Niasar et al.* (2008, 2009), *Reeves and Celia* (1996).

5.5 Summary and conclusions

One of the goals of the study has been to determine whether shape factor alone is enough to characterize the pore geometry of a granular porous medium. In particular, the role of actual shape of pores is investigated.

In this paper, a geometry-based approach has been proposed for generation of pore throat cross sections so that the whole range of shape factor distribution can be reproduced. Three different general shapes for pore throats have been considered: irregular hyperbolic triangles, regular hyperbolic polygons, and circles. General formulas for calculation of geometrical properties and entry capillary pressure of these geometries are derived. Effects of shape factor as well as cross-sectional shape on entry capillary pressure, corner saturation and corner interfacial area have been investigated for a single pore throat. We have shown that in addition to shape factor, the shape of cross section (number of vertices) has a significant effect on entry capillary pressure, corner saturation, and arc menisci area. These parameters can be very important in porous media with long pore throats and may contribute significantly to the total pore volume.

We have developed an irregular unstructured mixed cross-sectional pore-network model, with the pore bodies in the shape of prolate spheroids and pore throats having a mix of cross sectional shapes described above. The model has been used for simulating drainage and imbibition experiments carried out by *Culligan et al.* (2004) in a glass-bead column. The capability of the pore-network model for simulating a real porous medium has been successfully verified, as we reproduce the measured P^c-S^w and a^{nw}-S^w curves very well. Moreover, grain size distribution inferred from our pore-network model is in close agreement with the measured distribution. We have shown that the inclusion of shape factor distribution and cross-sectional shape in the generation of pore network significantly influence P^c-S^w curves. Depending on the number of vertices of a cross section and volume and length associated with the pore throats, shape factor distribution and cross-sectional shape can significantly influence a^{nw}-S^w curves.

Another goal of this work is to investigate the role of specific interfacial area in reducing the hysteresis in P^c-S^w curves for a real porous medium. Using this pore-network model, we have generated P^c-S^w-a^{nw} surfaces for drainage and imbibition, separately. Comparison between these two surfaces shows that they are highly correlated ($r^2 = 0.95$), and the normalized difference is small, in the range of uncertainty of model calculations. Our results show that in glass beads with unstructured irregular network with mixed cross sections, the hysteresis in P^c-S^w-a^{nw} curves is much smaller than the hysteresis in P^c-S^w curves. The largest relative error between $a^{nw} = f(P^c, S^w)$ surfaces is found at large saturations, where the specific interfacial area is very small. Finally, we emphasize that the proposed approach for generating pores cross sections, based on the continuous recovery of shape factor distribution, is essential for the development of predictive pore-network models.

Part III

Dynamic Simulations

Published as: Joekar-Niasar, V., Hassanizadeh, S. M., Dahle, H. K. – *"Non-equilibrium Effects in Capillarity and Interfacial Area in Two-Phase Flow: Dynamic Pore-Network Modeling"* Journal of Fluid Mechanics, 2010, doi:10.1017/S0022112010000704.

Submitted as: Joekar-Niasar, V., Hassanizadeh, S. M. – *"Fluid-fluid interfacial area under nonequilibrium conditions"* IXVIII International Conference on Computational Methods in Water Resources, 2010.

Chapter 6

Nonequilibrium Effects in Capillarity and Interfacial Area

Observations always involve theory.

Edwin Hubble, astronomer

Abstract

Current theories of two-phase flow in porous media are based on the extended Darcy's law, and an algebraic relationship between capillary pressure and saturation. Both of these equations have been challenged in recent years, primarily based on theoretical works using a thermodynamic approach, which have led to new governing equations for two-phase flow in porous media. In these equations, new terms appear related to the fluid-fluid interfacial area and non-equilibrium capillarity effects. Although there has been a growing number of experimental works aimed at investigating the new equations, a full study of their significance has been difficult as some quantities are hard to measure and experiments are costly and time consuming. In this regard, pore-scale computational tools can play a valuable role. In this paper, we develop a new dynamic pore-network model for simulating two-phase flow in a porous medium. Using this tool, we investigate relationships among average capillary pressure, average phase pressures, saturation, and specific interfacial area. We provide evidence that average capillary pressure-saturation-interfacial area points fall on a single surface regardless of flow conditions and fluid properties. We demonstrate that the traditional capillary pressure-saturation relationship is not valid under dynamic conditions, as predicted by the theory. Instead, one has to employ the non-equilibrium capillary theory, according to which the fluids pressure difference is a function of the time rate of saturation change. We study behaviour of non-equilibrium capillarity coefficient, specific interfacial area, and its production rate versus saturation and viscosity ratio.

A major feature of our pore-network model is a new computational algorithm, which considers capillary diffusion. Pressure field is calculated for each fluid separately, and saturation is computed in a semi-implicit way. This provides more numerical stability, compared with previous models, especially for unfavorable viscosity ratios and small capillary number values.

6.1 Objectives

The focus of this work is two-fold. The major goal is to investigate theories for two-phase flow in porous media including interfacial area and the side-goal is to present a new numerical algorithm for two-phase dynamic pore-network modelling.

Investigation of theories for two-phase flow In the extended theories of two-phase flow in porous media, there are new variables and parameters, which are experimentally difficult to be investigated. Major objectives of this work are as follows:

- Investigation of uniqueness of Equation 1.6 under equilibrium and non-equilibrium conditions during drainage.
- Investigation of the validity of Equation 1.7.
- Proposing an explicit formula for the dependence of the interfacial area production term (in Equation 1.4) on saturation and its time rate of change.

Hassanizadeh and Gray (1993b) state that P^c-S^w-a^{nw} relationship is supposed to be an intrinsic property of the fluids-solid system and valid under all thermodynamic conditions. The latter issue has not been investigated yet as all measurements of the P^c-S^w-a^{nw} relationship have been carried out under equilibrium conditions. So, one goal of the present paper is to determine specific interfacial area, average capillary pressure, and saturation under various dynamic conditions as well as quasi-equilibrium situation, albeit for drainage only, and determine whether all data points fall on a single a^{nw}-P^c-S^w surface.

Equation 1.7 has been the subject of many studies in recent years, both computationally (see e.g. *Dahle et al.*, 2005, *Das et al.*, 2006, *Gielen et al.*, 2005, *Manthey et al.*, 2005) and experimentally (see e.g. *Berentsen and Hassanizadeh*, 2006, *Bottero and Hassanizadeh*, 2006, *Hassanizadeh et al.*, 2004, *O'Carroll et al.*, 2005, *Oung et al.*, 2005). Nevertheless, there are still open questions regarding the dependency of τ on various factors. In the present paper, we investigate the dependency of τ on saturation as well as fluids viscosity ratio.

Regarding Equation 1.4, although there has been considerable progress in recent years in finding ways of measuring specific interfacial area (see e.g. *Brusseau et al.*, 1997, 2006, *Chen et al.*, 2007, *Chen and Kibbey*, 2006, *Cheng et al.*, 2004, *Costanza-Robinson and Brusseau*, 2002, *Culligan et al.*, 2004, 2006), there is yet no experimental (or computational) study of the interface production term. One of the goals of the present paper is to study the dynamics of fluid-fluid interfaces and to provide insight in the dependence of this production term on other primary variables. In particular, the dependence of E^{nw} on saturation and its time rate of change and viscosity ratio will be studied. This term is very important because it prescribes the appearance and disappearance of interfaces as the two-phase flow occurs.

Computational improvement of two-phase dynamic pore-network modelling Despite the fact that numerous dynamic pore-network models have been proposed over the years, the quasi-static models have remained dominant, largely because of computational tractability. In particular, the strong nonlinearity at the pore-scale causes severe stability problems in dynamic pore-network models. In this paper, we propose a computational algorithm, which is different from the previous dynamic pore-network models, in the following aspects:

(a) Similar to *Thompson* (2002), and in contrast to all other dynamic pore-network models, we assign a separate pressure field to each phase within both pore bodies and pore throats, and include local capillary pressures in pore bodies. We include a snap-off criterion to account for the effect of pore geometry on flow.

(b) The computational algorithm for saturation update is improved in order to have numerical stability in simulations even for capillary-dominated flow. A semi-implicit approach is used in the saturation update. Thus, the resulting set of equations for fluid pressures contain both advection-type terms (corresponding to viscous forces) and diffusion-type terms (corresponding to capillary forces). This gives more versatility to our formulation so that competition between viscous forces and capillary forces is properly modelled. We will show that in contrast to previous studies (see e.g. *Al-Gharbi and Blunt*, 2005, *Thompson*, 2002), we can obtain a full consistency between fluid occupancy at equilibrium resulted from quasi-static simulations and dynamic simulations for the same boundary conditions.

(c) We improve significantly computational efficiency in pressure field calculations. Using total pressure definition (phase pressures weighted with saturation), calculation of phase pressures is done in a cheaper way compared with previous dynamic pore-network models. In addition, the model has been tested for both favorable and unfavorable viscosity ratios, which is numerically stable.

(d) Tracking fluid-fluid interfaces in pore throats is computationally expensive. Allocating zero filling time for pore-throats allows us to model a much larger domain. On the other hand, we consider infinite conductance (zero flow resistance) in pore bodies.

6.2 Classification of dynamic pore-network models

Dynamic pore-network models differ among themselves in three main features: network structure, geometry of the elements, and computational algorithm for solving the pressure field. A brief description of these features in various dynamic pore-network models developed so far is given in this section.

6.2.1 Network structure

The network structure is characterized by the positioning of nodes and the number and orientation of links. If the nodes are positioned at the vertices of a regular lattice, the network is referred to as a "structured" one, and otherwise it is "unstructured". If all nodes have the same number of links connected, the networked is "isotropic", and otherwise it is "anisotropic". Dynamic pore-network models developed to date are mostly structured and isotropic. However there are some cases, which are structured and anisotropic (e.g. *Mogensen and Stenby*, 1998), unstructured and isotropic (e.g. *Blunt and King*, 1991, *King*, 1987), and unstructured and anisotropic (e.g. *Koplik and Lasseter*, 1985, *Thompson*, 2002).

6.2.2 Geometry of the elements

Conventional pore-network models consist of pore bodies, which are connected to each other by pore throats. Geometry of pore-network models can be studied based on two different aspects of these network elements: volumes and cross-sectional shapes assigned to them.

First, volumes assigned to elements: In this regard, there are three different types of network models as described below.

i) Pore bodies have volume but no resistance; pore throats have negligible volume but offer resistance to flow. This assumption will help to save computation time and memory in simulations, since it is not necessary to track interfaces within pore throats. Also, pressure drop within pore bodies can be neglected so that a single pressure values can be assigned to (each fluid within) a pore body. Examples are the works by *Blunt and King* (1990), *Gielen et al.* (2005).

ii) Both pore bodies and pore throats have volume and resistance. Almost none of dynamic pore-network models reported in the literature correspond to this case. The only exceptions, to our knowledge, are *Mogensen and Stenby* (1998) and *Singh and Mohanty* (2003). However, they have not shown gains of their models compared with previous ones.

iii) A pore body and a pore throat are combined into one element that has both volume and resistance. Combined pore throat-pore body elements may have a varying cross section. No specific properties, such as volume and resistance, are assigned to the connection points. This structure has been used in pore-network models of Payatakes and co-workers (see e.g. *Dias and Payatakes*, 1986a,b, *Valvanides et al.*, 1998) as well as in works by *Aker et al.* (1998a,b), *Al-Gharbi and Blunt* (2005), *Dahle and Celia* (1999), *Knudsen and Hansen* (2002), *Knudsen et al.* (2002), among others.

Second, geometry of elements, cross section; The geometry chosen for pore bodies and pore throats has consequences for the computational algorithm. Due to the significant simplicity of circular cross section, most dynamic network models have a circular cross section. However, there are a few models with angular cross sections. *Valvanides et al.* (1998) and *Al-Gharbi and Blunt* (2005) have assumed triangular cross sections, whereas *Mogensen and Stenby* (1998), *Hughes and Blunt* (2000), *Singh and Mohanty* (2003) and *Gielen et al.* (2005) have assumed cubic pore bodies, and parallelopiped pore throats. *Pereira et al.* (1996), *Van der Marck et al.* (1997), and *Thompson* (2002) have also considered other angular cross sections. The main reason for using angular cross sections is to allow existence of corner flow along edges of a pore element. In angular cross sections, it is possible to have two fluids simultaneously present at any given cross section, with the wetting phase filling the corners.

6.2.3 Computational algorithms

There are two general algorithms for solving the pressure field in a dynamic pore-network model, single-pressure and two-pressure algorithms. These are explained in detail in the following.

Single-pressure algorithm In this algorithm, regardless of the occupancy of pore bodies, a single pressure is assigned to each pore body. This single-pressure algorithm is generally applied in following three different approaches.

i) It is assumed that each pore body or pore throat is occupied by one fluid only at a time. This is generally applied to networks with circular cross sections (e.g. *Aker et al.*, 1998a,b, *Van der Marck et al.*, 1997).

ii) It is assumed that both fluids can be present within a pore body but not within a pore throat. Then, it is assumed that the local capillary pressure is negligible. Therefore, to each pore element a single pressure is assigned (e.g. *Gielen et al.*, 2005).

iii) It is assumed that an equivalent fluid can be defined having a single pressure. Thus, pore bodies and pore throats are filled with the equivalent fluid and an equivalent conductivity is assigned to each pore throat (e.g. *Al-Gharbi and Blunt*, 2005, *Mogensen and Stenby*, 1998).

In all three approaches, the following volume balance equation for pore bodies is solved:

$$\sum_{j=1}^{N_i} Q_{ij} = 0 \tag{6.1}$$

where, N_i is the number of pore throats connected to pore body i, and Q_{ij} $\left[L^3T^{-1}\right]$ is the volumetric fluxes through pore throat *ij*. This flux is calculated by means of *Washburn* equation (*Washburn*, 1921):

$$Q_{ij} = K_{ij}^{eq}\left(\Delta p_{ij} - p_{ij}^{c}\right) \tag{6.2}$$

$$\Delta p_{ij} = p_i - p_j \tag{6.3}$$

where, K_{ij}^{eq} $\left[M^{-1}L^4T\right]$ is an equivalent conductivity, which is a function of the pore throat radius, pore throat length, fluid viscosities and location of the meniscus in the pore throat; and p_{ij}^{c} $\left[ML^{-1}T^{-2}\right]$ is the effective capillary pressure (depending on the number of interfaces located) between pore bodies *i* and *j*.

Obviously, corner flow is not included in *Washburn* formulation. Nevertheless, Equation 6.2 has been modified and used for angular cross sections, using concept of equivalent phase (see approach *iii* above). It is assumed that a pore throat is filled simultaneously by two fluids, each fluid having its own conductivity. In the pore bodies on the two sides of a pore throat, each phase has its own pressure, which drives the flow. But, to simplify the problem and decrease computational effort, a single (virtual) pressure is assigned to the two fluids in pore bodies. Equation 6.1 is then applied to calculate the flow. It is assumed that a pore throat is filled with a single fluid with the equivalent conductivity K_{ij}^{eq}. This is achieved by averaging conductivities of phases using the rule of equivalent resistor for electrical resistor circuits. So, instead of solving for two pressure fields, one can solve for a single pressure field (see e.g. *Al-Gharbi and Blunt*, 2005, *Bravo et al.*, 2007, *Mogensen and Stenby*, 1998).

The advantage of single-pressure approach is that it simplifies the problem and reduces computational effort. But, it also has some disadvantages. For example, no local capillary pressure for pore bodies can be defined. This means that no information from the interface behaviour under dynamic conditions can be gained using this type of dynamic pore-network models. Moreover, this approach exhibits some inconsistent behaviours in fluids occupancy in the network. In particular, snapshots of fluid occupancy obtained from quasi-static and dynamic pore-network models, for the same boundary conditions, are not the same. If we do not assign any dynamics to the contact angle, one would expect to obtain the same equilibrium fluid occupancy resulting from quasi-static pore-network model as from a dynamic pore-network model for the same boundary conditions. However, *Al-Gharbi and Blunt*

(2005) showed that employing the concept of equivalent phase pressure solver induced an inconsistent behaviour in fluid occupancy in their dynamic pore-network model.

Two-pressure algorithm In this algorithm, when a pore body is filled with two fluids, each fluid is assumed to have its own pressure. To our knowledge, this concept was employed for the first time by *Thompson* (2002), who defined variable local capillary pressures in pore bodies and solved the pressure field for both phases separately. The local capillary pressure for pore body *i* is defined as:

$$p_i^c = p_i^n - p_i^w = f(s_i^w) \tag{6.4}$$

A flux Q_{ij}^α is assigned in a pore throat *ij* for each phase separately. Then, Equation 6.1 is replaced by following total volume balance for pore *i*:

$$\sum_{j=1}^{N_i} (Q_{ij}^n + Q_{ij}^w) = 0 \tag{6.5}$$

Moreover, a separate volume balance for each phase in a pore body is employed:

$$V_i \frac{\Delta s_i^\alpha}{\Delta t} = -\sum_{j=1}^{N_i} Q_{ij}^\alpha, \quad \alpha = w, n \tag{6.6}$$

where, V_i is the volume of pore body *i*, s_i^α is the saturation of phase α in pore body *i*, and Q_{ij}^α is the volumetric flux of phase α in pore body *i*, given by Equation 6.7. The latter is given by an equation similar to *Washburn* formula:

$$Q_{ij}^\alpha = -K_{ij}^\alpha \mathit{\Delta} p_{ij}^\alpha, \quad \alpha = w, n \tag{6.7}$$

where K_{ij}^α is a function of geometry and fluid occupancy of pore throats. This formulation allows us to include mechanisms related to the local capillary pressure (such as snap-off, counter-current flow) in simulations.

6.3 Model description

In this paper, we employ the two-pressure algorithm. The procedure and results are described in detail below.

6.3.1 Model features

Structure and geometry For predictive purposes, where pore-network models are used to simulate a specific porous medium, the network should be based on the real connectivity of pores (topology), aspect ratio (i.e. pore body radius divided by pore throat radius), and shape of pores (geometry). Due to the following reasons, structure of network (coordination number) can be considered as a minor issue in this study. a) We are interested in studying qualitative behaviour of new theories of two-phase flow, and we prefer to eliminate effects of heterogeneities in our simulations. b) *Mogensen and Stenby* (1998) studied effects of pores connectivity (coordination number) and aspect ratio using pore-network modelling. They found that with increase of capillary number, effect of variation of coordination number on dynamics of the system and residual saturation decreases. c) For theoretical purposes, generally regular lattice with fixed coordination number has been used, which computationally is simpler than the irregular unstructured networks.

Our pore-network model has a three-dimensional regular lattice structure with fixed coordination number of six. Pore bodies have cubic shape and pore throats have square cross sections. Figure 6.1 shows a schematic presentation of two pore bodies and the connected pore throat. The size distribution of pore bodies is given by a truncated log-normal distribution, with no spatial correlation, expressed by:

$$f(R_i;\sigma_{nd}) = \frac{\sqrt{2}exp\left[-\frac{1}{2}\left(\frac{ln\frac{R_i}{R_m}}{\sigma_{nd}}\right)^2\right]}{\sqrt{\pi\sigma_{nd}^2}R_i\left[erf\left(\frac{ln\frac{R_{max}}{R_m}}{\sqrt{2\sigma_{nd}^2}}\right)-erf\left(\frac{ln\frac{R_{min}}{R_m}}{\sqrt{2\sigma_{nd}^2}}\right)\right]} \tag{6.8}$$

in which R_i is the radius of inscribed sphere in a pore body (so, the cube side length is $2R_i$), R_{min} is the the lower range of truncation, R_{max} is the upper range of truncation, R_m is the mean of inscribed sphere radii, and σ_{nd} is the standard deviation. Radius and length of pore throats connecting the pore bodies are determined based on the size of neighboring pore bodies. Spacings between the layers of the network in *x*-, *y*- and *z*-directions are chosen to be variable. Let the spacings between layers *i* and *i+1* in the three directions be denoted by $\lambda_{x,i}$, $\lambda_{y,i}$, and $\lambda_{z,i}$. Then, designating each pore body by its lattice indices, namely i, j, and k, lattice spacings are defined as follows:

$$\lambda_{x,i} = \max\{R(i,j,k)+R(i+1,j,k) : j=1,n_y, k=1,n_z\}, i=1,n_x \tag{6.9a}$$

$$\lambda_{y,j} = \max\{R(i,j,k)+R(i,j+1,k) : i=1,n_x, k=1,n_z\}, j=1,n_y \tag{6.9b}$$

$$\lambda_{z,k} = \max\{R(i,j,k)+R(i,j,k+1) : i=1,n_x, j=1,n_y\}, k=1,n_z \tag{6.9c}$$

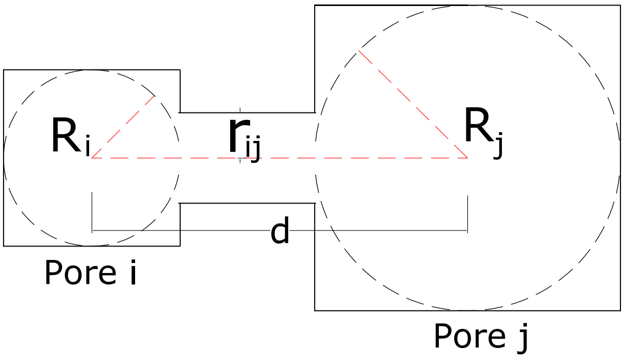

Figure 6.1: *Geometrical configuration for determining the pore throat radius (r_{ij}) based on pore bodies radii, R_i and R_j.*

where n_x, n_y, and n_z denote the number of pore bodies in x, y, and z directions, respectively. Then, length of the pore throats is determined. Based on the length of a pore throat and sizes of its neighboring pore bodies, the size of that pore throat cross section is determined (for more detailed explanation refer to *Joekar-Niasar et al.*, 2008). Consider two pore bodies *i* and *j*, with a centre-to-centre distance *d* (see Figure 6.1), and inscribed pore radii R_i and R_j, respectively. We define the dimensionless $\widetilde{R_i}$ and $\widetilde{R_j}$ as follows:

$$\widetilde{R_i} = R_i/d, \quad \widetilde{R_j} = R_j/d \tag{6.10}$$

We can calculate dimensionless inscribed radius of the pore throat *ij*, $\widetilde{r_{ij}}$, as follows:

$$\widetilde{r_{ij}} = \varrho_i \varrho_j (\varrho_i^{1/n} + \varrho_j^{1/n})^{-n}, n > 0 \tag{6.11}$$

$$\varrho_i = \frac{\widetilde{R}_i \sin(\pi/4)}{(1 - \widetilde{R}_i \cos(\pi/4))^n} \tag{6.12}$$

$$\varrho_j = \frac{\widetilde{R}_j \sin(\pi/4)}{(1 - \widetilde{R}_j \cos(\pi/4))^n} \tag{6.13}$$

where n is a parameter, which can control ratio between the radii of pore bodies and pore throat. It should be larger than zero. Larger n results in smaller pore throats. In this work, we select $n = 0.1$ to have a significant overlapping between pore body and pore throat radii distributions. Resulted aspect ratio varies between 2.2 and 3.4.

Boundary conditions It is assumed that the network is connected to a nonwetting phase reservoir on one side and a wetting phase reservoir on the other side. Dirichlet boundary conditions are imposed at these boundaries. We refer to difference between the two boundary pressures as the global pressure difference P^c_{global}. After breakthrough of the pore throat *ij* at the lower boundary by the nonwetting fluid, we assign the same capillary pressure to both sides of the outlet pore throat, determined by the upstream pore body; $p^c_i = p^c_j$. Side boundary conditions are assumed to be periodic.

Assumptions The following assumptions are imposed in the computational algorithm and network development:

- The volume of pore throats is negligible compared to the volume of pore bodies. Thus, the time required for filling a single pore throat is negligible compared to that of a pore body. Also, this volume is not included in the computation of network saturation.
- Hydraulic resistance to flow in pore bodies is assumed to be negligible compared to that of pore throats.
- Fluids are assumed immiscible and incompressible, and the solid matrix is assumed to be rigid.
- Flow in the pore throats is assumed to have low Reynolds number such that transient effects can be neglected at pore scale. This allows us to use *Washburn* equation for fluid fluxes through pores.
- No gravity effect has been considered in the simulations. Flow occurs due to the pressure difference across the boundaries. Adding gravity does not constitute any major complication in the code. But it does not affect results and conclusions.

System parameters and specifications Tables 6.1 and 6.2 show the fluid properties and network specifications used in the simulations, respectively.

6.3.2 Local rules

Capillary pressures for pore bodies and pore throats Since pore bodies in our model are cubic, the wetting phase is always residing in the corners and along edges (see Figure G.1). The saturation of the pore body (i.e. volume of the wetting fluid divided by the volume of the pore body) depends on the prevailing capillary pressure. For a given capillary pressure, curvature of the interface in the vertices and edges of the cube can be calculated and, consequently, the corresponding saturation can be

Table 6.1: *Fluid properties in the simulations*

Specification	Symbol	Value	Unit
Contact angle	θ	0.0	degree
Interfacial tension	σ^{nw}	0.0725	kgs^{-2}
Wetting fluid viscosity	μ^{w}	0.001	$kgm^{-1}s^{-1}$
Non-wetting fluid viscosity	μ^{n}	0.0001,0.001, 0.01	$kgm^{-1}s^{-1}$

Table 6.2: *Network parameters*

Specification	Symbol	Value	Unit
Lattice dimension		3D: 35×35×35	-
(2D only for Figure 6.8)		2D:70×70	
Lattice size		3D: 6×6×6	mm^3
		2D:12.5×12.5	mm^2
Min. pore body inscribed radius	R_{min}	0.0408	mm
Max. pore body inscribed radius	R_{max}	0.234	mm
Mean pore body inscribed radius	R_m	0.114	mm
Standard deviation		0.169	mm

estimated. In Appendix G, details of derivation of the (local) p_i^c-s_i^w relationship for a cubic pore body are presented. The resulting equation for p_i^c in terms of the radius R_i of the inscribed sphere of the pore body i and the local wetting phase saturation, is:

$$p_i^c(s_i^w) = \frac{2\sigma^{nw}}{R_i(1 - \exp(-6.83 s_i^w))} \tag{6.14}$$

A capillary pressure should be also assigned to a pore throat once it is invaded and both phases are present. We assume that capillary pressure in a pore throat is equal to the capillary pressure of the upstream pore body.

Minimum wetting phase saturation in a pore body Obviously it is impossible to displace the wetting phase from the corners of a cube completely. We assume that each pore body has a minimum saturation $s_{i,min}^w$, that depends on the imposed global pressure difference (P_{global}^c defined in §6.3.1) as well as the blockage of the invading fluid. The capillary blockage of invading fluid ($P_{e_{block}}^c$) is also a global variable, defined to be the minimum entry capillary pressure of all pore throats that are connected to the nonwetting phase and not invaded yet. Thus, using the p_i^c-s_i^w relationship given by Equation 6.14, the local minimum wetting phase saturation in a pore body may be determined as follows:

$$s_{i,min}^w = -\frac{1}{6.83}\ln(1 - \frac{1}{R_i}\frac{2\sigma^{nw}}{\min\{P_{global}^c, P_{e_{block}}^c\}}) \tag{6.15}$$

Entry capillary pressure for a pore throat We assume that a pore throat will be invaded by the nonwetting phase when the capillary pressure in a neighboring pore body becomes larger than the entry capillary pressure of the pore throat. The latter can be calculated as follows (due to *Ma et al.* (1996), *Mayer and Stowe* (1965), *Princen* (1969a,b, 1970)):

$$p_{e,ij}^c = \frac{\sigma^{nw}}{r_{ij}}\left(\frac{\theta + \cos^2\theta - \pi/4 - \sin\theta\cos\theta}{\cos\theta - \sqrt{\pi/4 - \theta + \sin\theta\cos\theta}}\right) \tag{6.16}$$

where r_{ij} is the radius of inscribed circle of the pore throat cross section, and θ is the contact angle.

Conductivities of pore throats Conductivities of pore throats are determined based on the fluid occupancy and size of the pore throat. One of the following two different states may occur during drainage.

a) Pore throat is occupied by the wetting phase only. For this case, the following equation was obtained by *Azzam and Dullien* (1977):

$$\begin{aligned} K_{ij}^w &= \frac{\pi}{8\mu^w l_{ij}}(r_{ij}^{eff})^4 \\ K_{ij}^n &= 0 \end{aligned} \tag{6.17}$$

where μ^w is the viscosity of the wetting phase, l_{ij} is the length of pore throat, and

$$r_{ij}^{eff} = \sqrt{\frac{4}{\pi}}r_{ij} \tag{6.18}$$

b) Pore throat is invaded by the nonwetting phase, thus both phases may be flowing. Then, following *Ransohoff and Radke* (1988) we can write:

$$K_{ij}^w = \frac{4-\pi}{\beta\mu^w l_{ij}}(r_{ij}^c)^4 \tag{6.19}$$

$$K_{ij}^n = \frac{\pi}{8\mu^n l_{ij}}(r_{ij}^{eff})^4 \tag{6.20}$$

where

$$r_{ij}^c = \frac{\sigma^{nw}}{p_{ij}^c} \tag{6.21}$$

$$r_{ij}^{eff} = \frac{1}{2}\left(\sqrt{\frac{r_{ij}^2 - (4-\pi)r_{ij}^{c^2}}{\pi}} + r_{ij}\right) \tag{6.22}$$

In Equation 6.19, β is a resistance factor that depends on geometry, surface roughness, crevice roundness and other specifications of the cross section. Detailed explanation about β can be found in *Zhou et al.* (1997). As mentioned earlier, the pore throat capillary pressure p_{ij}^c is set equal to the capillary pressure of the upstream pore body.

Snap-off During drainage, if the local capillary pressure in a pore throat becomes smaller than a critical value of capillary pressure (defined below), the corner interfaces become unstable and snap-off will occur. Ignoring dynamics of contact angle, the criterion for snap-off in a square cross section pore throat has been defined as follows (*Vidales et al.*, 1998):

$$p_{ij}^c \leq \frac{\sigma^{nw}}{r_{ij}}(\cos\theta - \sin\theta) \tag{6.23}$$

After snap-off, the pore throat will be filled with the wetting phase again, and nonwetting-phase becomes disconnected, receding in the neighboring two pore bodies.

6.3.3 Computational procedure

Pressure field solver Equations 6.4, 6.6, and 6.7 form a determinate set to be solved for s_i^w, p_i^w, and p_i^n. But, to reduce the computational demand, the equations are reformulated in terms of total pressure (saturation-weighted average pressure, $\bar{p}_i$) defined in each pore body as:

$$\bar{p}_i = s_i^w p_i^w + s_i^n p_i^n \tag{6.24}$$

Using Equation 6.4 and $s_i^n + s_i^w = 1$, we get the following equations for pressures of wetting and nonwetting phases:

$$p_i^w = \bar{p}_i - s_i^n p_i^c \tag{6.25}$$

$$p_i^n = \bar{p}_i + s_i^w p_i^c \tag{6.26}$$

For each pore body i, we know that the summation of fluxes of the two phases should be zero, as specified by Equation 6.5. Substituting from Equation 6.7 into Equation 6.7, we obtain:

$$\sum_{j=1}^{N_i} \left[K_{ij}^n(p_i^n - p_j^n) + K_{ij}^w(p_i^w - p_j^w)\right] = 0 \tag{6.27}$$

Substituting Equation 6.25 and Equation 6.26 in Equation 6.27 results in an equation for $\bar{p}_i$:

$$\begin{aligned}&\sum_{j=1}^{N_i}(K_{ij}^w + K_{ij}^n)(\bar{p}_i - \bar{p}_j) = \\ &-\sum_{j=1}^{N_i}[(K_{ij}^n s_i^w - K_{ij}^w(1 - s_i^w))p_i^c + (K_{ij}^w(1 - s_j^w) - K_{ij}^n s_j^w)p_j^c]\end{aligned} \tag{6.28}$$

In this equation, the right-hand side as well as the coefficients of the left-hand side depend on local saturation only. This linear system of equations is solved for $\bar{p}_i$ by diagonally-scaled biconjugate gradient method using SLATEC mathematical library (*Fong et al.*, 1993).

Saturation update After calculating $\bar{p}_i$, pressure of phases can be back-calculated explicitly using Equation 6.25 and Equation 6.26. Then Equation 6.7 can be used to calculate Q_{ij}^α. Afterwards, Equation 6.6 can be solved for new saturations in an explicit way based on saturation values from the previous time step. This procedure, however, will result in numerical problems for a capillary-dominated flow regime, as mentioned in *Thompson* (2002). He found that the explicit saturation update was not numerically stable for very small capillary numbers and he could not successfully simulate the capillary-dominated flow. In addition, he could not observe consistency between near-equilibrium snapshots resulted from dynamic simulations and quasi-static ones. Therefore, we have developed a semi-implicit approach to control the nonlinearities under such flow conditions. Summing Equation 6.7 for the two phases, and writing p_i^w in terms of p_i^n and p_i^c, we obtain the following relationship for the total flux $Q_{ij}^{tot} = Q_{ij}^n + Q_{ij}^w$ through a pore throat:

$$Q_{ij}^{tot} = (K_{ij}^n + K_{ij}^w)(p_i^n - p_j^n) - K_{ij}^w(p_i^c - p_j^c) \tag{6.29}$$

Then, defining $K_{ij}^n + K_{ij}^w = K_{ij}^{tot}$ and resubstituting for Q_{ij}^n from Equation 6.7, we can write:

$$Q_{ij}^{tot} = \frac{K_{ij}^{tot}}{K_{ij}^{n}} Q_{ij}^{n} - K_{ij}^{w}(p_i^c - p_j^c) \tag{6.30}$$

Rewriting the above equation for Q_{ij}^n, we get a formula analogous to the fractional-flow equation:

$$Q_{ij}^{n} = \frac{K_{ij}^{n}}{K_{ij}^{tot}} Q_{ij}^{tot} + \frac{K_{ij}^{w} K_{ij}^{n}}{K_{ij}^{tot}} (p_i^c - p_j^c) \tag{6.31}$$

Substituting Equation 6.31 in the Equation 6.6 results:

$$V_i \frac{\Delta s_i^w}{\Delta t} - \sum_{j=1}^{N_i} \left(\frac{K_{ij}^{n}}{K_{ij}^{tot}} Q_{ij}^{tot} + \frac{K_{ij}^{w} K_{ij}^{n}}{K_{ij}^{tot}} (p_i^c - p_j^c) \right) = 0 \tag{6.32}$$

The capillary pressure term can be approximated to the first order by

$$p_i^c - p_j^c = \frac{\partial p_{ij}^c}{\partial s_{ij}^w} (s_i^w - s_j^w) \tag{6.33}$$

where, $\frac{\partial p_{ij}^c}{\partial s_{ij}^w}$ is calculated from the upstream pore body.

Finally, after substitution of Equation 6.33 in Equation 6.32, we get the following discretized form of a semi-implicit equation for saturation update:

$$\begin{aligned} &V_i \frac{(s_i^w)^{k+1} - (s_i^w)^k}{\Delta t} - \\ &\sum_{j=1}^{N_i} \left(\frac{K_{ij}^{n}}{K_{ij}^{tot}} Q_{ij}^{tot} + \frac{K_{ij}^{w} K_{ij}^{n}}{K_{ij}^{tot}} \frac{\partial p_{ij}^c}{\partial s_{ij}^w} \left((s_i^w)^{k+1} - (s_j^w)^{k+1} \right) \right) = 0 \end{aligned} \tag{6.34}$$

where superscript k denotes time step level. In this equation, all coefficients are evaluated at time step k, so that equation above may be recast into a linear equation matrix:

$$\begin{aligned} \left(\frac{V_i}{\Delta t} - \sum_{j=1}^{N_i} \frac{K_{ij}^{n} K_{ij}^{w}}{K_{ij}^{tot}} \frac{\partial p_{ij}^c}{\partial s_{ij}^w} \right) (s_i^w)^{k+1} + \left(\sum_{j=1}^{N_i} \frac{K_{ij}^{n} K_{ij}^{w}}{K_{ij}^{tot}} \frac{\partial p_{ij}^c}{\partial s_{ij}^w} \right) (s_j^w)^{k+1} = \\ \frac{V_i}{\Delta t} (s_i^w)^k + \sum_{j=1}^{N_i} \frac{K_{ij}^{n}}{K_{ij}^{tot}} Q_{ij}^{tot} \end{aligned} \tag{6.35}$$

One should note that since Q_{ij}^{tot} and K_{ij}^{α} are calculated from time step k, this scheme is not fully implicit. Here also the diagonally-scaled biconjugate gradient method from SLATEC mathematical library (*Fong et al.*, 1993) is used.

Time step The time step is determined on the basis of time of filling of pore bodies by the nonwetting phase or wetting phase, denoted by Δt_i. The wetting phase saturation of a pore body varies between 1 and $s^w_{i,min}$ as we assume that a pore body may be drained down to the minimum saturation. On the other hand, we allow for imbibition to occur locally in some pore bodies, in which case the wetting phase saturation in a pore body can go back to 1. Then, the global time step will be the minimum value of all local time steps. So, we calculate Δt_i for all pore bodies, depending on the process, from the following:

$$\Delta t_i = \begin{cases} \frac{V_i}{q^n_i}(s^w_i - s^w_{i,min}) & \text{for local drainage, } q^n_i > 0 \\ \frac{V_i}{q^n_i}(1 - s^w_i) & \text{for local imbibition, , } q^n_i < 0 \end{cases} \tag{6.36}$$

where, the accumulation rate of the nonwetting phase is defined as $q^n_i = \sum_{j=1}^{N_i} Q^n_{ij}$. Then, the time step is chosen to be the minimum Δt_i.

$$\Delta t_{global} = min\{\Delta t_i\} \tag{6.37}$$

It should be noted that we have imposed a truncation criterion of 10^{-6} for saturation when it is close to $s^w_{i,min}$ or 1. Also note that in Equation 6.36, there is a correspondence between saturation change (numerator) and the accumulation rate of nonwetting phase (denominator). That is, when local saturation is close to the limits, the accumulation rate of nonwetting phase is also very small. This means that Δt_i always remains finite and nonzero.

6.4 Drainage simulations and analysis

6.4.1 General procedure

Initially, the network is fully saturated with the wetting phase. Simulation of drainage starts with raising the pressure of the nonwetting phase reservoir. When the global pressure difference, P^c_{global}, becomes larger than the entry pressure of the largest pore throat connected to the nonwetting phase reservoir, drainage starts. In quasi-static simulations, the global pressure difference is increased incrementally. At the end of each step, when there is no flow (static conditions), the overall saturation of the network is determined. Then, global pressure difference is increased again.

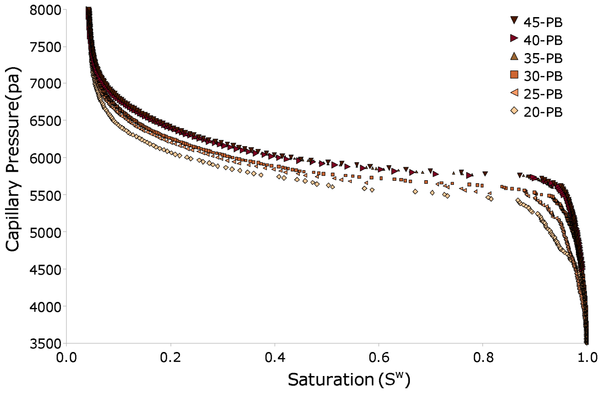

Figure 6.2: *Quasi-static* P^c*-*S^w *curves for different network sizes.*

In order to have representative results for a network with a given statistical distribution, the network must have a minimum size, corresponding to the REV (Representative Elementary Volume)(*Bear*, 1972). REV size was determined by performing quasi-static drainage simulations for a network with different sizes but with the same statistical parameters. Results are shown in Figure 6.2. It is evident that P^c-S^w curve changes with the network size until a network size of 35×35×35 pore bodies. For larger network sizes, the curves are almost identical. Therefore, a network with 35 pore bodies in each direction was used in our simulations.

6.4.2 Averaging procedure

Our simulations result in local-scale variables such as pressure, saturation, and fluxes. These have to be averaged over the network to obtain macroscopic variables. Average saturation is simply defined as follows.

$$S^w = \frac{V^w}{V^w + V^n} = \frac{\sum_{i=1}^{n_{pb}} s_i^w V_i}{\sum_{i=1}^{n_{pb}} V_i} \qquad (6.38)$$
$$S^n = 1 - S^w$$

in which n_{pb} is the total number of pore bodies. The total flux across any given surface is equal to the sum of fluxes of all pore throats intersecting that surface. The averaging of pressure is, however, less straightforward. Commonly, average pressure is obtained using an intrinsic phase average operator (see e.g. *Whitaker*, 1977). However, recently it has been shown that the intrinsic phase average pressure introduces numerical artefacts when both pressure and saturation are spatially variable (see *Nordbotten et al.*, 2007, 2008). Instead, a centroid-corrected averaging operator has been suggested by *Nordbotten et al.* (2008) to alleviate problems associated with intrinsic phase averaging. Nevertheless in this work, we still use intrinsic phase average for a pore body *i* with volume of V_i and α-phase pressure of p_i^α as, this is still most commonly used:

$$P^\alpha = \frac{1}{\delta V^\alpha}\int_{\delta V^\alpha} P^\alpha dV = \frac{\sum_{i=1}^{n_{pb}} p_i^\alpha s_i^\alpha V_i}{\sum_{i=1}^{n_{pb}} s_i^\alpha V_i}, \alpha = n, w \tag{6.39}$$

Commonly, the macroscale capillary pressure is defined to be the difference in the average pressures of nonwetting and wetting phases. But as we show later, this is not a correct definition of macroscopic capillary pressure. Here, we propose to define macroscopic capillary pressure based on the average of local capillary pressures of pore bodies, weighted by the corresponding interfacial area, A_i^{nw}:

$$P^c = \frac{\sum_{i=1}^{n_{pb}} p_i^c A_i^{nw}}{\sum_{i=1}^{n_{pb}} A_i^{nw}} \tag{6.40}$$

Calculation of interfacial area in pore bodies is explained in Appendix H.

6.5 Results and discussion

6.5.1 Quasi-static vs. dynamic simulation

As explained before, previous dynamic pore-network models failed to simulate very slow flow (very small capillary numbers) properly. As *Thompson* (2002) and *Al-Gharbi and Blunt* (2005) found that application of dynamic pore-network models for very small capillary numbers (relatively low flow velocities) was not numerically successful and severe instability problems were observed. To show capability of the proposed algorithm in simulating capillary dominated flow, P^c-S^w curve has been produced using the dynamic pore-network model with very small nonwetting phase reservoir pressure increments. Simultaneously, for the same network P^c-S^w curve has been generated using a quasi-static pore-network model. As it can be observed in Figure 6.3, the equilibrium points resulted from both models are the same. That is, if there is no dynamic effect in contact angle, there will be a full agreement between quasi-static and dynamic pore-network models. We found that equilibrium fluid configurations resulted from both models (not shown here) are the same. This simulation was done for a 20-pore body cubic lattice network. The simulation took 46 hours on Intel(R) CPU 6600, 2.4GHz with 2GB RAM, which is

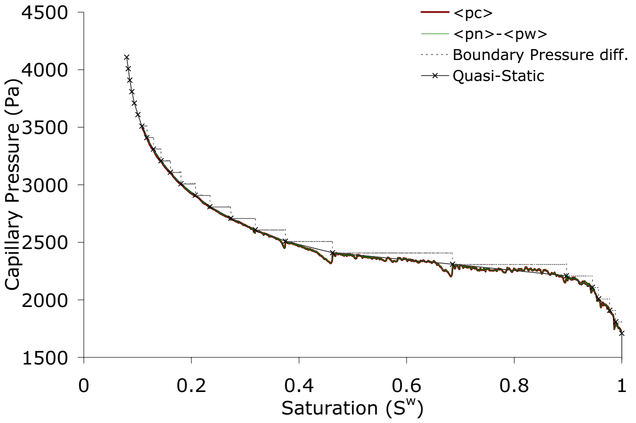

Figure 6.3: *Comparison between equilibrium points resulted from quasi-static and dynamic pore network models for the same boundary conditions in a 20-pore body cubic lattice network.*

significantly more time-consuming compared with viscous-dominated flow.

Figure 6.3 shows some interesting features resulted by interfaces behaviour in a near-to-equilibrium system. Average phase pressure difference, $P^n - P^w$ (Equation 6.39), and average capillary pressures P^c (Equation 6.40) are the same, and their values are fluctuating around the quasi-static model P^c-S^w curve. The dips visible in Figure 6.3 are due to the relaxation of the interfaces behind the invading fronts. This phenomenon has been observed in micromodel experiments reported by *Pyrak-Nolte* (2007). However, as we increased the aspect ratio (radius of pore body to radius of pore throat), these dips disappeared, but more fluctuations in dynamic P^c-S^w curve were observed.

6.5.2 Non-equilibrium effects in average phase pressures

In this section, we investigate the validity of non-equilibrium capillarity in Equation 1.7 and the behavior of non-equilibrium capillarity coefficient (τ). To do so, we have determined the change of saturation with time under various dynamic conditions and have prepared corresponding plots of average phase pressure difference versus saturation.

As explained before, by imposing a large global pressure difference on the network domain, it is possible to simulate dynamic two-phase flow drainage experiments. We have considered two fluids with three different viscosity ratios ($M = \mu^n/\mu^w = 0.1, 1, 10$) and five different global pressure difference values (10, 15, 20, 25 and 30 kPa). Computational time increases with decrease of viscosity ratio and decrease of global pressure difference. The simulations took about 10 to 70 hours on Intel(R) CPU 6600, 2.4GHz with 2GB RAM.

Commonly, for viscosity ratios less than unity, the displacement shows instability. We found that for given flow conditions, saturation changes with time for $M = 1$ and $M = 10$ were very similar. The breakthrough saturations for $M = 1$ and $M = 10$, were not so different for different global pressure differences. While, for $M = 0.1$, the breakthrough saturation decreased significantly for larger global pressure differences. Breakthrough saturation for favorable viscosity ratio were smaller than the unfavorable viscosity ratio (in the same network), due to the stable front invasion for $M \geq 1$ and viscous fingering for $M < 1$.

Curves of average fluid pressure difference (based on Equation 6.39) versus average saturation are shown in Figure 6.4. It is clear that the curves are strongly dependent on boundary conditions. The differences in fluid pressures are found to be higher for larger global pressure differences, which also lead to larger saturation changes. This behaviour agrees with Equation 1.7, which suggests larger pressure differences for large saturation changes under drainage.

As it can be observed in Figure 6.4, higher viscosity ratio can also cause higher pressure build-up. Higher viscosity ratios mean less snap-off occurs and fewer pores will be partially filled and disconnected from the reservoir. The decline in the fluid pressure differences as residual saturation is approached, is due to the nonwetting phase breaking through the outflow boundary of the averaging window. After breakthrough, average phase pressure difference decreases due to the direct connection of nonwetting phase to the lower (outflow) boundary, which entraps wetting phase in the corners. Thus wetting fluid will gain a higher pressure compared to non-trapped wetting phase. Consequently, the average pressure difference approaches the P^c-S^w curve. Decline in the fluid pressure differences as residual saturation in the averaging window is reached, has been studied analytically by *Nordbotten et al.* (2008) who found qualitatively the same behaviour.

According to Equation 1.7, the deviation of the macroscopic pressure difference from the macroscopic capillary pressure is related to the time rate of change of saturation. *Hassanizadeh and Gray* (1993a) have suggested that τ is a non-negative nonequilibrium capillarity coefficient that may still depend on saturation. To implement this equation for practical purposes, it is crucial to determine the dependency of this coefficient on medium and/or fluid properties. To compute τ, first a set of $\partial S^w/\partial t$ values is calculated for a given saturation (and constant M). Then, from corresponding curves in Figure 6.4, P^c and $P^n - P^w$ are found at that saturation (for a given viscosity ratio M). This results in a graph of $P^n - P^w - P^c$ vs. $\partial S^w/\partial t$ (not shown here) for the given saturation values and viscosity ratios. The slopes of the resulting curves gives the values of τ at different saturations. Results are plotted in

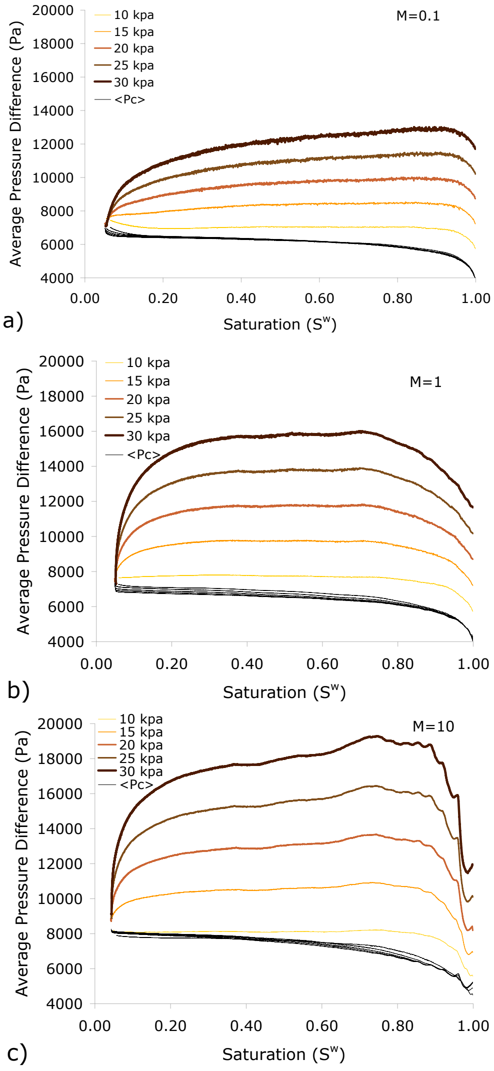

Figure 6.4: *Average phase pressure difference curves,* $P^n - P^w$*, calculated using Equation 6.39 and average capillary pressure curves,* P^c*, calculated using Equation 6.40 for five different global pressure differences and viscosity ratios a)* $M = 0.1$*, b)* $M = 1$ *and c)* $M = 10$*.*

Figure 6.5. It is evident that the dynamic effect is stronger for higher viscosity ratios. This is because for viscous fluids, it takes much larger time for the equilibrium fluid configuration to be reached. Decrease of τ after breakthrough is not relevant and is not a property of the porous medium, but is due to the drainage front reaching the

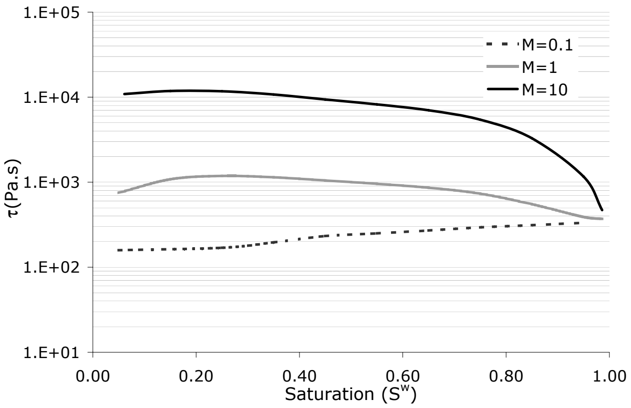

Figure 6.5: *Variation of non-equilibrium capillarity coefficient, τ, as a function of saturation for different viscosity ratios $M = 0.1, 1, 10$. The vertical axis is shown in logarithmic scale.*

boundary of the domain (see also the explanation given in relation to the decline of pressure differences at low saturation in Figure 6.4). For M≥1, non-equilibrium capillarity coefficient increases with decrease of wetting phase saturation, which is similar to the findings of *Mirzaei and Das* (2007) in their column-scale drainage simulations (using a continuum model) for favorable viscosity ratio. But, this trend is reversed for $M = 0.1$. This trend can be interpreted based on the empirical equation suggested by *Stauffer* (1978) for unsaturated soil. Based on the drainage experiments done on fine sand in an air-water system, he suggested the following equation.

$$\tau = \frac{\alpha \epsilon \mu}{\lambda k} \left(\frac{p^c}{\rho g} \right)^2 \tag{6.41}$$

where α is assumed to be a constant equal to 0.1 for granular soils, ϵ is porosity, μ is the water viscosity, λ and p^c are the coefficients in *Brooks-Corey* formula (*Brooks and Corey*, 1964), k is the saturated permeability, ρ is the water mass density, and g is the gravity. For the case of two-phase flow, μ can be replaced by μ_{eff}, the saturation-weighted average viscosity of the two-fluids, which is very much dependent on the flow regime. For a stable invasion, where a piston-like movement is dominant, viscosity can be weighted linearly with saturation: $\mu_{eff} = \mu^n S^n + \mu^w S^w$. However, for viscous fingering regime, some researchers such as *Koval* (1963) have suggested some other empirical relationships for effective viscosity (see e.g. *Fayers et al.*, 1990). In all equations, effective viscosity is suggested to be a function of saturation. Considering $\tau \propto \mu_{eff}$, it can be concluded that $\partial\tau/\partial S^w \propto \partial\mu_{eff}/\partial S^w$. The term $\partial\mu_{eff}/\partial S^w$ will be positive for unfavorable viscosity ratio, since both wetting phase saturation and effective viscosity decrease with decreasing of wetting phase saturation. In addition, difference between magnitudes of $\partial\tau/\partial S^w$ for different viscosity ratios is significant. From Figure 6.5, we can determine that $\partial\tau/\partial S^w$ for $M = 10$ is almost 10 times larger than that of $M = 1$. This is qualitatively consistent with Equation 6.41, where effective viscosity for $M = 10$ is almost 10 times larger than that of $M = 1$ for intermediate and low range of wetting phase saturation.

6.5.3 On the existence of P^c-S^w-a^{nw} surface

As discussed in § 1.1 (page 1), the main underlying concept in Equation 1.7 is that capillary pressure is an intrinsic property of the fluids-solid system, and thus it should be a function of state variables only (namely, saturation, temperature, and specific interfacial area); it should not depend on initial or boundary conditions and other parameters that control transient flow conditions such as viscosity. Here, we investigate this conjecture for the case of primary drainage.

First, consider the average capillary pressure P^c defined by Equation 6.40. Plots of P^c versus average saturation under various dynamic conditions are shown in Figure 6.6(a), where also the quasi-static capillary pressure is plotted. It is evident that average capillary pressure-saturation relationship is not unique, as depends on transient flow conditions as well as fluids viscosity ratio. This apparently contradicts the concepts presented above according to which capillary pressure curve is an intrinsic property of the fluids-solid system. But, in fact the theory prescribes that the capillary pressure is a function of specific interfacial area as well as saturation (see e.g. *Hassanizadeh and Gray*, 1993a, *Held and Celia*, 2001, *Joekar-Niasar et al.*, 2008, 2009, *Reeves and Celia*, 1996). So, differences observed in P^c-S^w curves could be due to the fact that specific interfacial area is different under different dynamic conditions.

Figure 6.6(b) shows specific interfacial area values for different viscosity ratios at different saturations for a three-dimensional network used in previous simulations. In addition, relationship between specific interfacial area and saturation resulted from static simulations has been shown as a thick solid line. According to the conjecture of *Hassanizadeh and Gray* (1993b), if P^c-S^w-a^{nw} surface were an intrinsic property of the porous medium, all the points for all non-equilibrium and equilibrium conditions should be located on a single surface. To investigate this, a second-order polynomial surface was fitted to all P^c-S^w-a^{nw} data points presented in Figures 6.6(a) and 6.6(b), which is shown in Figure 6.6(c). Note that the selection of a polynomial function for fitting is arbitrary and only for simplicity in presentation. This surface is highly correlated with the data points ($R^2 = 0.95$ and the average relative error is about 14%). The behaviour of the surface is very similar

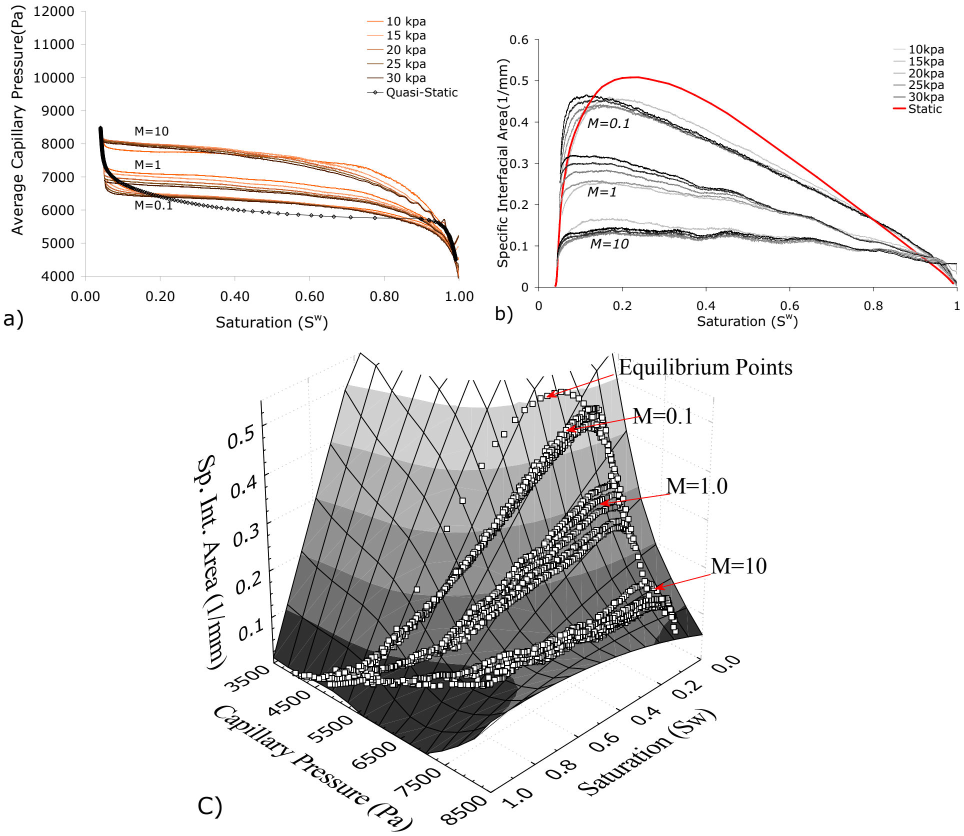

Figure 6.6: *a) Macroscopic capillary pressure, defined by Equation 6.40, for five different global pressure differences and three different viscosity ratios* $M = 0.1, 1, 10$ *compared with quasi-static capillary pressure curve in a 3D (35×35×35) network, b) Quantitative comparison between quasi-static and dynamic specific interfacial area-saturation curves for the same fluid-solid properties and boundary conditions mentioned in (a). c) A second-order polynomial surface fitted to all* P^c-S^w-a^{nw} *data points resulted from dynamic and quasi-static simulations shown in (a) and (b)* ($R^2 = 0.95$).

to the P^c-S^w-a^{nw} surfaces shown in *Held and Celia* (2001), *Joekar-Niasar et al.* (2008, 2009), *Porter et al.* (2009), *Reeves and Celia* (1996), although they only simulated P^c-S^w-a^{nw} equilibrium points.

The uniqueness of P^c-S^w-a^{nw} surfaces under all equilibrium and non-equilibrium conditions, drainage and imbibition processes has not been yet fully investigated. We have used DYPOSIT model (with the properties given in the next chapter) to generate P^c-S^w-a^{nw} surface data points under primary drainage and main imbibition processes. The data points have been plotted for drainage and imbibition processes separately, as shown in Figures 6.7(a) and (b), respectively. As it can be observed, data points resulted from drainage simulations create a well-behaved surface. This trend is less visible for imbibition simulations due to the limited range of saturation, covered by the experiments. However, there is still a smooth and meaningful trend in variation of interfacial area with capillary pressure and saturation. The interesting aspect of these results is that although the data points are resulted from different viscosity combinations ($M = 0.1, 1, 10$), all the points are still located in a well-behaved surface. Qualitatively there is a reasonable agreement between the trends of both data sets. Obviously, with the increase of wetting fluid saturation, specific interfacial area decreases.

As Figure 6.6(b) shows, specific interfacial area has larger values for smaller viscosity ratios, as a result of instability and fingering. For unfavorable viscosity ratio ($M = 0.1$), local entry capillary pressures of pore throats and their connectivity (topology and geometry) control the invasion. According to results shown in Figure 6.6(b), the largest specific interfacial area has been created in the quasi-static simulation, where only capillary forces are controlling the invasion. In other words, it seems that for a given saturation value, with decrease of viscous forces compared with capillary forces, more interfacial area is created.

Significant variation of specific interfacial area with viscosity ratio and flow conditions in Figure 6.6(b) suggests that invasion mechanism and system parameters have a major effect on interfacial area evolution under dynamic conditions. This is illustrated in Figure 6.8, where we have shown different snapshots of fluid distribution for drainage. These simulations were performed in a two-dimensional network with size of 70×70 pore bodies. Snapshots are shown for $P^c_{global} = 20kPa$ and at wetting phase saturations of 0.9, 0.5 and 0.3. As shown in Figure 6.8, under favorable conditions ($M \geq 1$), interface front is stable with less fingering. For small global pressure difference, more fingering occurs compared to high global pressure differences for a given (favorable) viscosity ratio. This is because, with more invasion of the nonwetting fluid, more energy dissipation occurs and consequently at low saturations more fingering can occur. Under unfavorable conditions ($M < 1$), however even large global pressure difference can not stabilize the interface front. This is because front basically follows the local variations in pore throat sizes within the pore-network (*Aker et al.*, 1998b).

6.5.4 Production rate of specific interfacial area vs. saturation

As explained in § 1.1, in the new theory of two-phase flow, the interfacial area production term E^{nw} (Equation 1.4) plays a significant role. Since there is no quan-

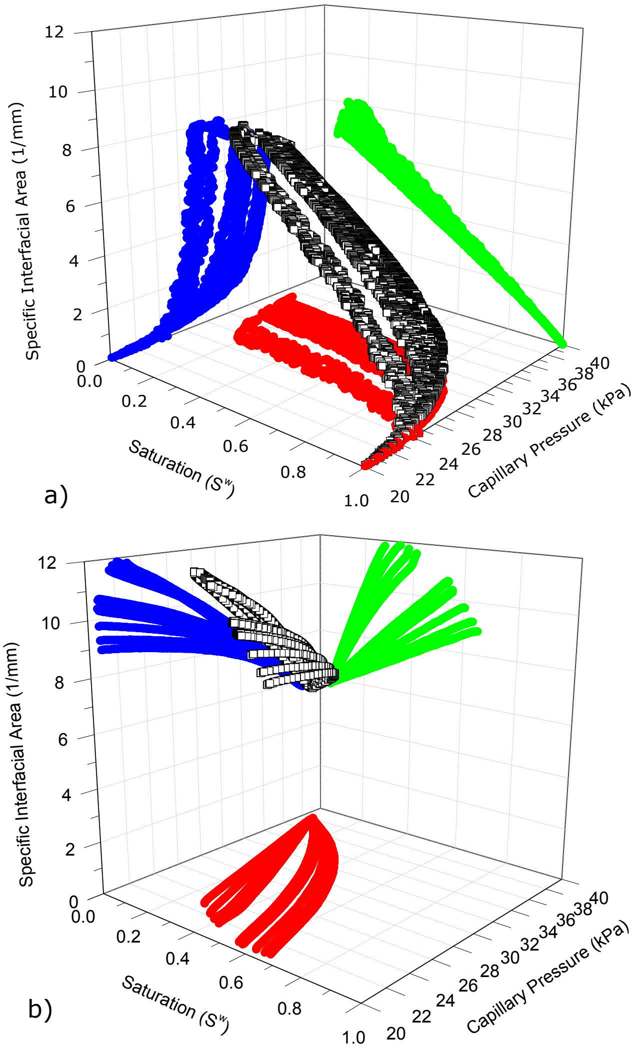

Figure 6.7: *Three-dimensional presentation of all data points resulted from a) drainage and b) imbibition simulations.*

titative information available about this term yet, we have used our pore-network model to get some insight about its dependence on other primary variables. In particular, the dependency of E^{nw} on saturation and its time rate of change, and on viscosity ratio will be studied.

The procedure for the estimation of E^{nw} is as follows. If in Equation 1.4, we neglect the advective flux term, the production term may be calculated as the rate

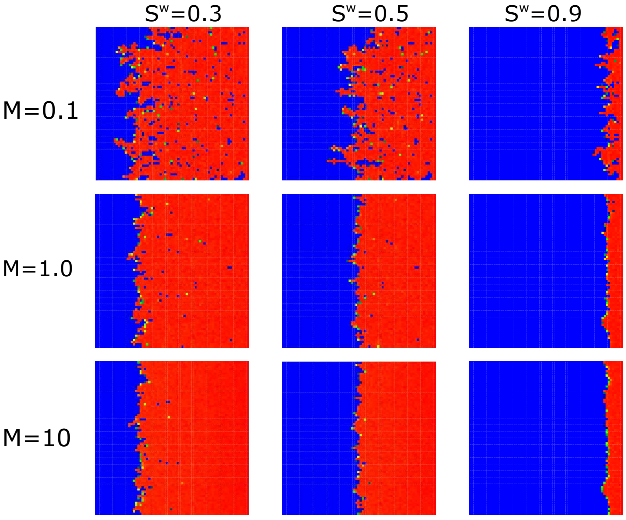

Figure 6.8: *Qualitative comparison of macroscopic interface topology for* $M = 0.1, 1$ *and* 10 *in a 2D (70×70) network at three different saturations.*

of change of specific interfacial area with time. The production rate of specific interfacial area (E^{nw}) is plotted as a function of saturation in Figure 6.9. It is evident that E^{nw} decreases with the decreasing of saturation. We also see that it is much larger for $M = 0.1$ than for $M = 10$ and $M = 1$. Figure 6.9 also shows that E^{nw} depends on the imposed boundary pressure, which in turn causes different rate of change of saturation, $\frac{\partial S^w}{\partial t}$. Therefore, based on Figure 6.9 and change of saturation with time, one can construct a relationship between E^{nw} and $-\frac{\partial S^w}{\partial t}$ for different saturations. The results (not presented here) show that at saturations lower than 0.9, we can roughly define a linear relationship between E^{nw} and $-\frac{\partial S^w}{\partial t}$:

$$E^{nw} = -G\frac{\partial S^w}{\partial t} \tag{6.42}$$

where $G\left[L^{-1}\right]$ is a material coefficient, which itself is a function of saturation as well as viscosity ratio, as shown in Figure 6.10. We suggest a linear relationship between G and saturation: $G(S^w, M) = a + b.S^w$, where values of "a" and "b" depend on viscosity ratio and are reported in Figure 6.10. A relationship similar to Equation 6.42 was employed by *Niessner and Hassanizadeh* (2008) in a model based on the new theory of two-phase flow.

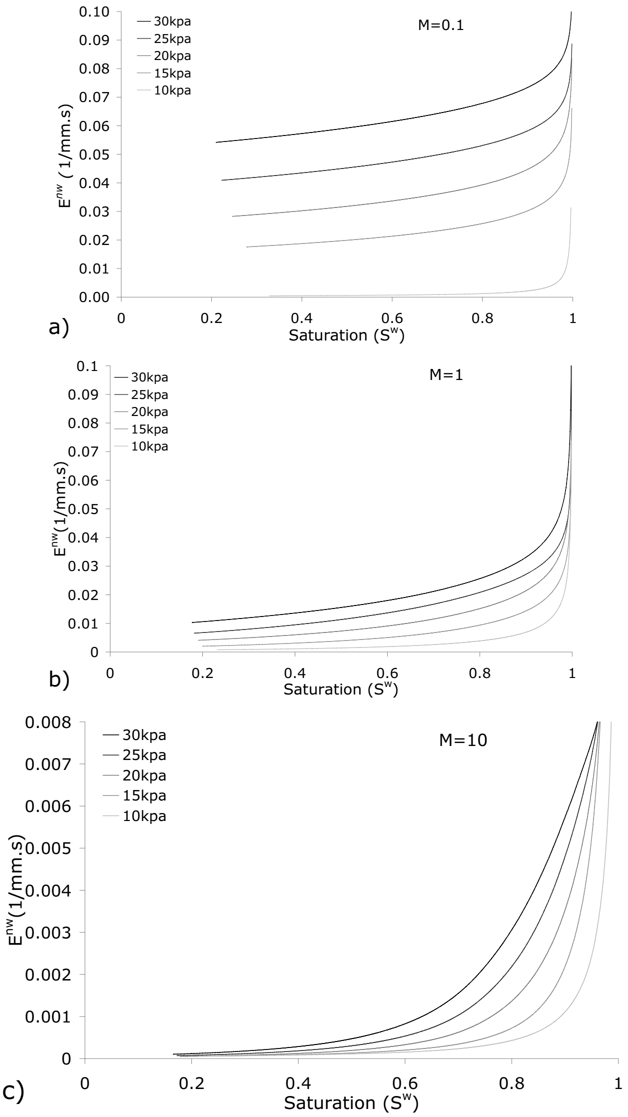

Figure 6.9: *Plots of production rate of specific interfacial area* E^{nw}*, versus saturation for a)*$M = 0.1$ *b)*$M = 1$ *c)*$M = 10$ *and for various values of global pressure difference.*

6.6 Summary and conclusions

A DYnamic POre-network model for SImulating Two-phase flow in a porous medium, referred to as *DYPOSIT* has been developed. The combination of features

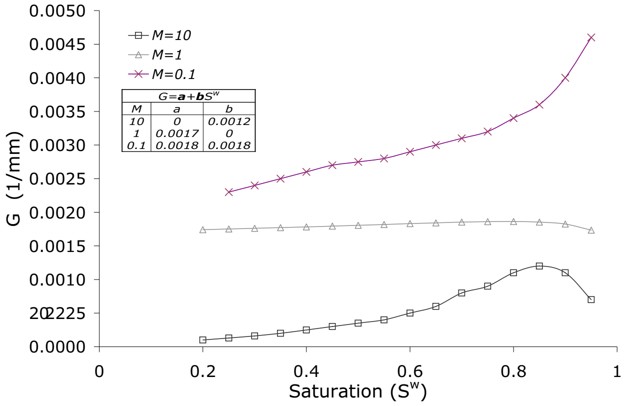

Figure 6.10: *Relationship between G and the wetting phase saturation for different viscosity ratios.*

included in this model has not been offered in previous network models. The network elements have square cross sections, as a result of which both phases can be simultaneously present within a pore body or pore throat. Local capillary pressure in the pore elements is taken into account. Two different pressure fields are assigned to each phase and solved using a robust algorithm. The model is numerically stable for a wide range of viscosity ratios and under different dynamic conditions (viscous dominated or capillary dominated). The model is used to simulate drainage experiments with Dirichlet boundary conditions. It is applied to study dynamics of specific interfacial area, average capillary pressure, average phase pressure differences, functionality of non-equilibrium capillarity coefficient as well as production rate of interfacial area.

Macroscopic capillary pressure is defined as the average of local capillary pressure at all interfaces weighted with the area of the interface. We have shown that neither average capillary pressure-saturation curves, nor specific interfacial area-saturation curves, are not unique, but they depend on flow dynamics as well as fluid-solid properties. However, it is shown that capillary pressure-saturation-interfacial area surface for primary drainage is an intrinsic property of the porous medium, independent of fluid properties and dynamic conditions. The difference between average phase pressures, however, is found to be dependent on boundary pressures and time rate of change of saturation as prescribed by the dynamic capillary theory. Our results illustrate that the non-equilibrium capillarity coefficient is a function of saturation as well as viscosity ratio.

Dynamics of interfacial area show that with decrease of the viscosity ratio, specific interfacial area increases, which is a consequence of the invasion mechanism.

However, in all dynamic cases, specific interfacial area is smaller than that under quasi-static conditions. With decrease of the viscosity ratio, effect of the intrinsic properties of medium (geometry and topology) on the creation of interfacial area increases. The production rate of specific interfacial area for different viscosity ratios has been studied and quantified. With the decrease of the viscosity ratio, production rate of the specific interfacial area increases. The production rate is found to have an almost linear relationship with the time rate of change of saturation. This linearity coefficient is a function of saturation as well as the viscosity ratio. The dynamic pore-network model developed here is capable of simulating complex problems of flow of two fluid phases in porous media including non-equilibrium capillarity effects and dynamics of interfaces. In future research, our model will be applied to a larger domain in order to simulate column experiments and investigate validity of full system of equations of extended Darcy's law Equations 1.1 and 1.2.

Submitted as: Joekar-Niasar, V., Hassanizadeh, S. M. – *"Effect of fluids properties on non-equilibrium capillarity effects; dynamic pore-network modelling"* International Journal of Multiphase Flow, 2010.

Chapter 7

Capillarity Effects under Drainage and Imbibition

> *The scientist is not a person who gives the right answers, he's one who asks the right questions.*
>
> Claude Lévi-Strauss, anthropologist

Abstract

We have developed a DYnamic POre-network model for SImulating Two-phase flow in porous media (DYPOSIT). Employing improved numerical and geometrical features in the model provides a physical-based pore-scale simulator. This computational tool is applied in several numerical experiments (primary and main drainage, main imbibition) to investigate validity of the central equation in classical two-phase flow simulations, called capillary pressure curve. Traditional multiphase formulations state that macroscopic capillary pressure is only a function of saturation. Some theoretical and experimental studies have shown that this assumption is invalid and capillary pressure is also related to the variation of saturation with time in the domain, referred to as "non-equilibrium effect". In this study, effect of fluid properties and macroscopic interface topology on the qualitative behaviour of non-equilibrium capillarity coefficient as well as its uniqueness under different processes (drainage, imbibition) have been investigated. Although, at pore scale local equilibrium conditions for fluid-fluid interfaces (constant contact angle, validity of Young-Laplace Equation) are assumed, non-equilibrium effects can be observed in average fluids pressure difference, which is resulted from the macroscopic interface topology. Other aspects of the dynamics of two-phase flow such as trapping, saturation profile, etc are also studied.

7.1 Introduction

Non-equilibrium capillarity coefficient

Equation 1.7 (page 3) has been the subject of many studies in recent years, computationally using Darcy-scale models (see e.g. *Das et al.*, 2006, *Manthey et al.*, 2005), and pore-scale models (see e.g. *Dahle et al.*, 2005, *Gielen et al.*, 2005, *Joekar-Niasar et al.*, 2010a) as well as experimentally (see e.g. *Berentsen and Hassanizadeh*, 2006, *Bottero*, 2009, *Bottero and Hassanizadeh*, 2006, *Camps-Roach et al.*, 2010, *Hassanizadeh et al.*, 2004, *O'Carroll et al.*, 2005, *Oung et al.*, 2005). *Hassanizadeh et al.* (2002) reviewed extensively the experimental works in which non-equilibrium effects have been observed.

Dahle et al. (2005) developed a bundle-of-tube model to investigate the variation of τ with variance of radii distribution and with saturation under drainage process. They found that τ increases with decrease of wetting fluid saturation and with increase of variance. In another study, *Joekar-Niasar et al.* (2010a) investigated variation of τ with viscosity ratio (M) and saturation during drainage using a dynamic pore-network model. Viscosity ratio is defined as the ratio of nonwetting fluid viscosity (μ^n) to the wetting fluid viscosity (μ^w). *Joekar-Niasar et al.* (2010a) found a similar trend for variation of τ with saturation as *Dahle et al.* (2005) did. In addition, they found that larger values of viscosity ratio results in larger values of τ. In another study, *Manthey et al.* (2005) studied variation of τ with permeability, heterogeneity and entry capillary pressure during drainage. They employed a continuum-scale two-phase simulator in which local capillary pressure was defined based on *Brooks-Corey* relation. Based on volumetric phase averaging, they determined the magnitude and behaviour of τ.

Although some aspects of non-equilibrium capillarity effect has been studied, there is still much room for further studies. There is still no study on the combined effect of saturation, effective viscosity, and viscosity ratio on the variation of τ or on the presence of hysteresis on τ-S^w relationship.

Objectives

The main objectives of this paper are as follow:

- Developing a dynamic pore-network model for simulating two-phase flow (DYPOSIT) with improved numerical algorithms for computing pressure fields and updating the saturation. Using this algorithm, the transient behaviour of capillary pressure under different flow regimes and viscosity ratios can be simulated. To mimic large pore spaces among the solid grains in a granular medium, the shape of pore bodies has been selected as truncated octahedrons. This is a modification of the geometry compared with *Joekar-Niasar et al.* (2010a), in which pore bodies were represented as cubes.

- Studying the evolution of average fluids pressure difference ($P^n - P^w$) with time and saturation under favorable ($M \geq 1$) and unfavorable ($M < 1$) conditions for primary and main drainage as well as main imbibition processes.

- Analysis of the validity of Equation 1.7 during imbibition as well as drainage. Up to now, behaviour of τ has been studied only during primary drainage. We are interested in analyzing existence of τ under conditions where the local equilibrium at interfaces is still assumed (so, for example, dynamics of contact angle is neglected).
- Analysis of the variation of τ with viscosity ratio and saturation during primary and main drainage and main imbibition.

7.2 Model description

7.2.1 Model features

Structure and geometry We have also developed a regular three-dimensional lattice network with fixed coordination number of six. Pore bodies and pore throats are presented by "truncated octahedron" and "parallelepiped", respectively. This allows simultaneous existence of both fluids in a single pore element. The octahedron pore bodies can be unequally truncated since they are connected to pore throats of different sizes, as shown in Figure 7.1(a). Truncated parts of the octahedron have the shape of square pyramids with base width of $2r_{ij}$ (where r_{ij} is equal to the radius of inscribed circle of the pore throat ij) as shown in Figure 7.1(a). The radius of the inscribed sphere of a pore body, R_i, and the radius of the inscribed circle of the cross section of pore body, R'_i, are shown in Figure 7.1(b). It should be noted that $R_i = \frac{\sqrt{6}}{3}R'_i$. A cross section through the vertices of a pore body and the pore throat connecting them is shown in Figure 7.1(c). The size distribution of pore bodies is specified by a truncated log-normal distribution, with no spatial correlation, expressed by Equation 6.8. Spacings between the pore body layers of the network in *x*-, *y*- and *z*-directions are chosen to be variable. Let the spacings between layers k and $k+1$ in the three directions be denoted by $\lambda_{x,k}$, $\lambda_{y,l}$, and $\lambda_{z,m}$. Then, designating each pore body by its lattice indices, namely k, l, and m, lattice spacings are given as follow:

$$\lambda_{x,k} = \sqrt{2}\max\{R'(k,l,m) + R'(k+1,l,m) : l = 1, n_y, m = 1, n_z\}, k = 1, n_x \quad (7.1a)$$

$$\lambda_{y,l} = \sqrt{2}\max\{R'(k,l,m) + R'(k,l+1,m) : k = 1, n_x, m = 1, n_z\}, l = 1, n_y \quad (7.1b)$$

$$\lambda_{z,m} = \sqrt{2}\max\{R'(k,l,m) + R'(k,l,m+1) : k = 1, n_x, l = 1, n_y\}, m = 1, n_z \quad (7.1c)$$

where n_x, n_y, and n_z denote the total number of pore bodies in x, y, and z directions, respectively. If there is no spacing between vertices of square cross sections shown in Figure7.1(c), the distance between centres of pore bodies will be equal to $\sqrt{2}$ times

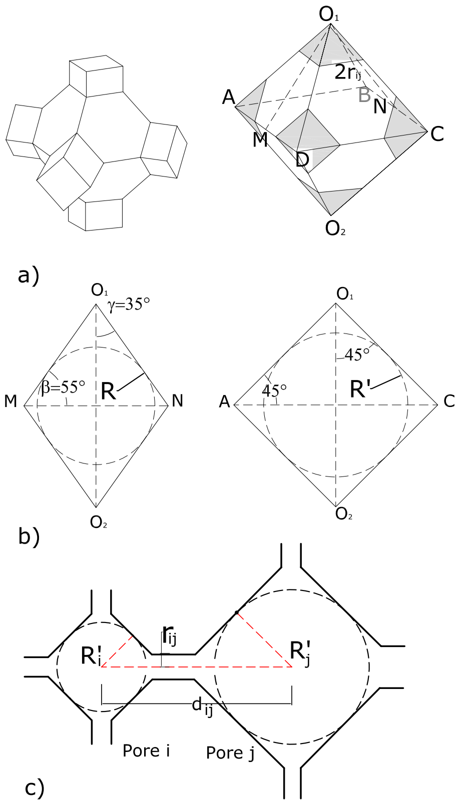

Figure 7.1: *a) Schematic presentation of a pore body and its connected pore throats. Truncated parts of the pore body have the width of $2r_{ij}$, which is the inscribed radius of pore throat ij. b) Cross sections of the pore body along the vertices and through the edges. Radius of inscribed sphere is denoted by R and radius of inscribed circle in the cross section along vertices is denoted by R' c) Cross section of two pore bodies and connected pore throats. Geometrical configuration for determining the pore throat radius (r_{ij}) based on pore bodies radii, $R'_i = \frac{\sqrt{6}}{2}R_i$ and $R'_j = \frac{\sqrt{6}}{2}R_j$.*

the summation of cross section inscribed radii. Based on the length of a pore throat and sizes of its neighboring pore bodies, radius of the inscribed circle in a pore throat cross section is determined (for more detailed explanation, see *Joekar-Niasar et al.*, 2008, and § 6.3.1, page 154).

Fluids and network parameters and specifications Table 7.1 shows fluids and network properties used in the simulations. Viscosity of the nonwetting fluid is kept constant and equal to 0.001 and viscosity ratio is defined as the $M = \frac{\mu^n}{\mu^w}$. Statistical

Table 7.1: *Fluid and network properties used in the simulations.*

Parameter	Symbol	Value	Unit
Contact angle	θ	0.0	degree
Interfacial tension	σ^{nw}	0.0725	kgs^{-2}
Wetting fluid viscosity	μ^w	0.0001,0.001, 0.01	$kgm^{-1}s^{-1}$
Non-wetting fluid viscosity	μ^n	0.001	$kgm^{-1}s^{-1}$
Total no. of pore bodies in flow direction	n_z	45	-
Total no. of pore bodies in lateral directions	n_x, n_y	35	-
Domain Size	-	1.9×1.9×2.37	mm^3
Permeability	K	1.43×10^{-12}	m^2

Table 7.2: *Statistical properties of the radii of inscribed spheres of pore bodies (R_i), and of inscribed circle of pore throats r_{ij}, and aspect ratio distribution R_{asp}.*

Specifications	R_i (mm)	r_{ij} (mm)	R_{asp}
min	0.0077	0.0048	1.55
max	0.0200	0.0162	4.00
mean	0.0125	0.0084	2.25
st. deviation	0.0028	0.0017	0.38

properties of pore bodies, pore throats, and aspect ratio distributions are shown in Table 7.2. Aspect ratio is defined as pore body inscribed sphere radius divided by pore throat radius. Corresponding to Table 7.2, Figures 7.2(a) and (b) show the aspect ratio distribution as well as pore body-pore throat size distributions, respectively . Aspect ratio is controlled by the parameter n given in Equation 6.11. In this work, we have set $n = 1.0$.

7.2.2 Local rules

Details about the governing equations can be found in §6.3.3, page 159. The local rules are given in the following sections.

Capillary pressure curves for pore bodies and pore throats Local capillary pressure within a pore is a function of the curvature of fluid-fluid interface through

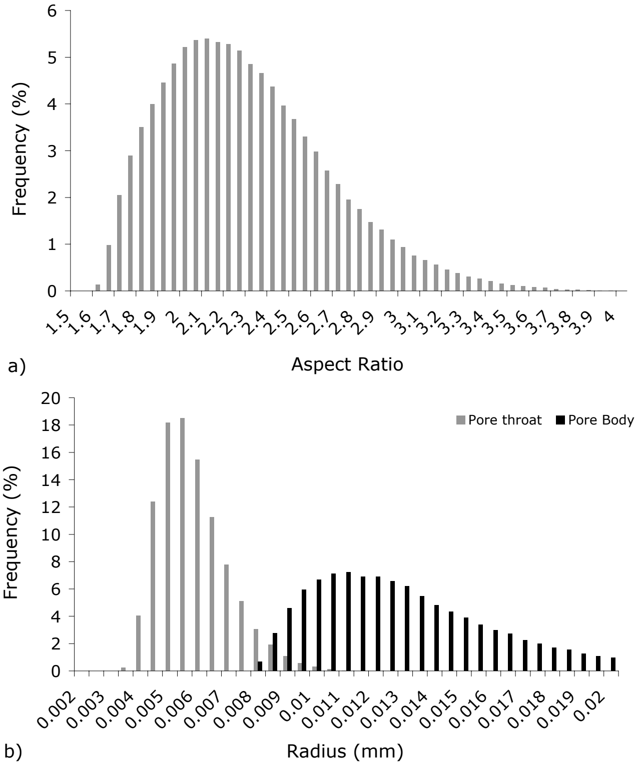

Figure 7.2: *Network geometry properties a) Aspect ratio distribution b) Pore body and pore throat distributions.*

Young-Laplace equation, regardless of whether drainage or imbibition occurs. However, during imbibition, topology of fluid-fluid interfaces is much more complicated.

Interfaces may be categorized in two different types: "*arc menisci* (AM)", formed along the edges, and "*main terminal menisci* (MTM)", spanning the pore throat cross section during drainage (*Mason and Morrow*, 1987). Behaviour of "*MTM*" during drainage and imbibition is different. During drainage, a *MTM* is formed at the entrance to a pore throat within a pore body filled with the nonwetting fluid. However, during imbibition a *MTM* can be formed such that it spans over a pore body and connected pore throats; this is referred to as "cooperative filling" (*Lenormand and Zarcone*, 1984).

In any case, for a given fluid-fluid interface position within a pore body, we can determine corresponding capillary pressure and saturation. Therefore, for a given pore body, a unique relationship between capillary pressure and local saturation can be obtained. Local p_i^c-s_i^w curves for drainage and imbibition are discussed and derived below.

Drainage During drainage, the invasion of a pore throat by the nonwetting fluid, and consequently the movement of main terminal menisci, is controlled by the entry capillary pressure. In drainage, an interface is located within a pore body. If a pore body is filled with both fluids, the wetting fluid is residing along edges of the pore bodies (see Figures I.1(b) and (c) in I.1). The saturation of the pore body (i.e. volume of the wetting fluid divided by the volume of the pore body) depends on the prevailing capillary pressure. For a given capillary pressure, the curvature of interfaces in the edges of the pore body can be calculated and, consequently, the corresponding saturation can be estimated. In I.1, details of derivation of the (local) p_i^c-s_i^w relationship for an octahedron pore body are presented.

The resulting p_i^c-s_i^w relationship in terms of the radius R_i of the inscribed sphere of the pore body i and other geometrical parameters is:

$$p_i^c = 2\sigma^{nw}\kappa_i, \quad \kappa_i = \begin{cases} (\frac{1}{r_{ij}} - \frac{1}{R_i})(\frac{s_i^w - s_i^{dr}}{1-s_i^{dr}})^{3.5} + \frac{1}{R_i} & s_i^w \geq s_i^{dr} \\ \frac{1}{R_i}\left(\frac{s_i^w}{s_i^{dr}}\right)^a, a = \frac{1}{2.98 s_i^{dr} - 3.85} & s_i^{min} < s_i^w < s_i^{dr} \end{cases} \tag{7.2}$$

in which, s_i^{dr} is the wetting fluid saturation corresponding to the inscribed sphere of the pore body, given by Equation I.2, and s_i^{min} is the minimum possible saturation in a simulation given by Equation 7.3. The resulting curve is shown in Figure I.2(a).

Obviously, it is impossible to completely displace the wetting fluid from the corners of a pore body. We assume that each pore body has a minimum saturation $s_{i,min}^w$, which depends on the imposed global pressure difference (P_{global}^c defined in § 7.3.2) as well as the blockage of the invading fluid. The capillary pressure blockage of the invading fluid ($P_{e_{block}}^c$) is also a global variable, defined to be the minimum entry capillary pressure of all pore throats neighbouring the vicinity of the nonwetting fluid but not invaded by it yet. Thus, using the p_i^c-s_i^w relationship given by Equation 7.2, the local minimum wetting fluid saturation in a pore body may be determined as follows:

$$s_{i,min}^w = s_i^{dr}\left(\frac{R_i}{2\sigma^{nw}}\min\{P_{global}^c, P_{e_{block}}^c\}\right)^{2.98 s_i^{dr} - 3.85} \tag{7.3}$$

A capillary pressure should be also assigned to a pore throat once it is invaded and both fluids are present. We assume that the capillary pressure of a pore throat p_{ij}^c is equal to the capillary pressure of the upstream pore body.

Imbibition During imbibition, locations of interfaces are not only controlled by the geometry of pore bodies and pore throats, but also by local fluid configuration in pore throats connected to a pore body (*Lenormand and Zarcone*, 1984). One of the mechanisms that controls configuration of fluid-fluid interfaces in a pore body during imbibition is "cooperative pore filling". *Lenormand and Zarcone* (1984) observed in micro-model experiments that, depending on the number of pore throats filled with the nonwetting fluid, the topology of local main terminal interface can change. They defined a so-called *I*-mechanism for pore filling, where *I* represents number of pore throats filled with the nonwetting fluid. They showed that with the decrease of *I*, radius of interface may decrease, resulting in an increase of local capillary pressure as shown schematically in Figure 7.3. Some researchers such as *Hughes and Blunt* (2000), *Øren et al.* (1998) suggested simple algebraic equations for pore filling mechanism, regardless of the geometry of pore bodies and pore throats. These relations do not apply to all pore spaces. For example, they do not apply to high-porosity domains with small aspect ratio, such as micro-model experiments of *Pyrak-Nolte* (2007) , as illustrated in simulations of the imbibition process by *Joekar-Niasar et al.* (2009).

We define local capillary pressure-saturation relationship as a function of saturation as well as pore throats filling. Details of derivation of local p_i^c-s_i^w relationship during imbibition are given in I.2. Finally, we have suggested the following relationships which results in a trend consistent with experimental observations of *Lenormand and Zarcone* (1984):

$$\begin{aligned} p_i^c &= 2\sigma^{nw}\kappa_i \\ \kappa_i &= \begin{cases} \left(\frac{1}{r_{ij}} - \frac{1}{R_i}\left(\frac{s_i^{imb}}{s_i^{dr}}\right)^a\right)\left(\frac{s_i^w - s_i^{imb}}{1-s_i^{imb}}\right)^{3.5} + \frac{1}{R_i}\left(\frac{s_i^{imb}}{s_i^{dr}}\right)^a & s_i^w \geq s_i^{imb} \\ \frac{1}{R_i}\left(\frac{s_i^w}{s_i^{dr}}\right)^a, a = \frac{1}{2.98 s_i^{dr} - 3.85} & s_i^{min} < s_i^w < s_i^{imb} \end{cases} \end{aligned} \tag{7.4}$$

where s_i^{imb} is the pore body saturation at which one pore throat is still filled with the nonwetting fluid. It should be noted that this saturation is not predetermined in the simulations. Its value for each pore body will be determined during the simulation.

Other local rules such as entry capillary pressure, pore throat conductivities and snap-off conditions are given in § 6.3.2, page 156.

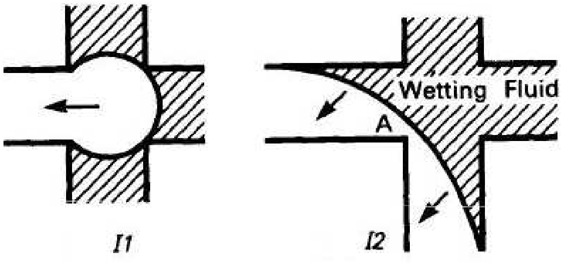

Figure 7.3: *Pore filling mechanisms during imbibition referred to I-mechanism. Wetting fluid is shown as hashed areas. With decrease of number of pore throats filled with the nonwetting phase, radius of the interface may decrease. Consequently capillary pressure assigned to the interface can increase (due to Lenormand and Zarcone, 1984).*

7.3 Simulations and analysis

7.3.1 Network size

To analyze Darcy-scale equations using pore-network models, the size of the pore-network should be at least one REV. REV size was determined by performing quasi-static drainage simulations in networks with different sizes but with the same statistical parameters. Our simulations show that the REV size for these statistical parameters is a cube with length of 35 pore bodies. However, we have added five buffer layers at each boundary to reduce the boundary effect. Thus the network has a length of 45 pore bodies along the main flow direction. The buffer layers are not included in the averaging window.

7.3.2 Boundary conditions

For our simulations, we assume that the network is connected to a nonwetting fluid reservoir on one side and a wetting fluid reservoir on the other side. Fluid pressures are specified at these boundaries. Side boundary conditions are assumed to be periodic.

For drainage and imbibition simulations the following procedure is followed:

a) Drainage: Pressure at the nonwetting fluid reservoir is fixed to P^n_{top} and pressure at the wetting fluid reservoir is fixed to zero. The difference between the two boundary pressures during drainage is referred to as "global pressure difference" P^c_{global}=P^n_{top}. After the nonwetting fluid breaks into the wetting fluid reservoir a boundary condition for its pressure is needed. One may choose to set it equal to the wetting fluid boundary pressure. But, this will cause an unrealistic relaxation of the nonwetting fluid pressure field throughout the network. Instead, we have chosen to set the gradient of capillary pressure within an invaded pore throat (connected to the wetting fluid boundary) to be equal to zero ($\frac{\partial P^c_{ij}}{\partial l_{ij}}$).

b) Imbibition: Similar to the drainage process, pressure at the nonwetting fluid reservoir is fixed to P^n_{top} and pressure at the wetting fluid reservoir is fixed to zero. However, P^n_{top} should be so small that imbibition process can occur continuously. During imbibition similar to the drainage, it is assumed that $\frac{\partial p^c_{ij}}{\partial l_{ij}} = 0$ as long as a pore throat at the nonwetting fluid boundary is filled with both fluids.

7.3.3 Drainage simulations

For primary drainage, the network is initially fully saturated with the wetting fluid. Simulation of drainage starts with raising the pressure of the nonwetting fluid reservoir, and establishing a global pressure difference, P^c_{global}, across the network. When the pressure difference is larger than the entry pressure of the largest pore throat connected to the nonwetting fluid reservoir, drainage starts. In quasi-static simulations, the nonwetting fluid reservoir pressure is increased in incremental steps so that the network is invaded in steps. At the end of each step, when there is no flow (static conditions), the overall saturation of the network and average specific interfacial area are determined. Then, global pressure difference is increased again. In dynamic simulations, the imposed P^c_{global} is so large that the whole network (or a large part of it) could be flooded in one step. The simulations are continued till the change of average saturation in a selected averaging window is negligible.

For main drainage simulations, the initial saturation occupancy is based on the last snapshot of the quasi-static main imbibition experiment. The simulation procedure is otherwise similar to the primary drainage simulation.

7.3.4 Imbibition simulations

Consider a pore network filled by the nonwetting fluid at the end of a (main or primary) drainage experiment. The wetting fluid is still present along edges of pore bodies and pore throats. Starting from an equilibrium condition, all pore bodies have the same capillary pressure. The global capillary pressure is decreased by reducing the nonwetting fluid reservoir pressure or increasing the wetting fluid reservoir pressure. A decrease in the global capillary pressure causes the interfaces to relax gradually and main imbibition experiment will start. The imbibition simulation will stop when all pore throats at the outflow boundary (nonwetting fluid reservoir) are fully filled with the wetting fluid.

For the quasi-static imbibition simulations, an approach similar to the drainage has been employed. Averaging procedure has been explained in details in § 6.4.2, page 163.

7.4 Results and discussion

7.4.1 Non-equilibrium capillarity effects

As mentioned in the Introduction, in standard models of two-phase flow in porous media, the difference in fluid pressures, $P^n - P^w$, is assumed to be a function of saturation. In this section, we show that the curves of $P^n - P^w$ versus S^w depend strongly on boundary conditions and dynamics of the system, as shown by *Yang et al.* (2009) for bundle-of-tube model. We performed a large number of dynamic primary drainage, main drainage, and main imbibition simulations for fluids with different viscosity ratios and under a range of global pressure difference values. For every simulation, we calculated the variations of average saturation and the "fluids pressure difference" with time. From those results, plots of $P^n - P^w$ versus saturation were made.

For primary and main drainage simulations, three different global pressure differences were imposed over the domain: 45, 60 and 90 kPa. The entry capillary pressure is 15 kPa. For main imbibition, four different global pressure differences were imposed over the domain, equal to +5, 0, -5, -10 kPa. Also, all simulations were performed for three different viscosity ratios (ratio of viscosity of the nonwetting fluid to that of the wetting fluid): $M = 0.1, 1$, and 10. Computational time increased with decrease of viscosity ratio and decrease of global pressure difference. Each simulation can take 24 to 72 hours on Intel(R) CPU 6600, 2.4GHz with 2GB RAM.

Plots of $P^n - P^w$ as well as P^c versus average saturation, S^w, are shown in Figure 7.4. It is clear that the curves of $P^n - P^w$ versus S^w strongly depend on boundary conditions. The behaviour of average fluids pressure difference compared with P^c-S^w curve is in agreement with Equation 1.7: at a given saturation, the fluids pressure difference is larger than the capillary pressure during drainage and smaller during imbibition. The differences are larger for larger nonwetting fluid boundary pressure during drainage and for large wetting fluid boundary pressure during imbibition. These curves are used later to calculate non-equilibrium capillarity coefficient, τ.

Resulting $P^n - P^w$ curves also depend strongly on viscosity ratio and effective viscosity. In order to explain this, let us define the effective viscosity as $\mu_{eff} = \mu^n S^n + \mu^w S^w$. It must noted that this definition is most suitable for a stable invading front where a piston-like movement is dominant. For unstable fronts

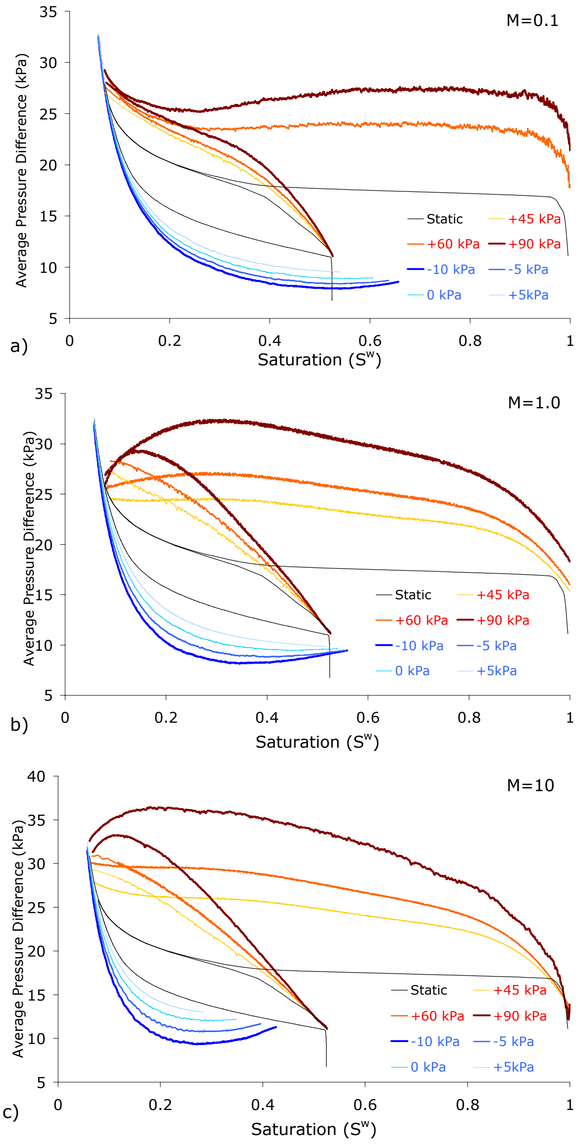

Figure 7.4: *Average phase pressure difference curves, $P^n - P^w$, calculated using Equation 6.39 (page 164) and P^c-S^w curves for three different global pressure differences during primary and main drainage and four different global pressure differences during primary imbibition for viscosity ratios a) $M = 0.1$, b) $M = 1$ and c) $M = 10$ and for $\mu^n = 0.001 Pa.s$.*

e.g. in a viscous fingering regime, some researchers, such as *Koval* (1963), have suggested other empirical relationships for effective viscosity (see e.g. *Fayers et al.*, 1990). During both drainage and imbibition, the effective viscosity changes considerably if fluid viscosities are not equal. During primary drainage, effective viscosity is initially equal to μ^w, which is chosen to be different in simulations with different viscosity ratios (i.e. nonwetting fluid saturation is kept constant and μ^w is varied to get various M values). As the drainage proceeds effective viscosity decreases for $M = 0.1$ and increases for $M = 10$. At the end of drainage, the effective viscosity is almost equal to μ^n.

Figure 7.4 shows the effect of viscosity ratio and μ_{eff} on the transient behaviour of fluids pressure difference. During drainage, initially (i.e. at higher saturations), $P^n - P^w$ is larger for small M and smaller for larger M (for equal μ^n). This is due to the fact that the pressure drop over the whole domain for $M = 10$ is smaller than the other cases. The decline in the fluids pressure difference during drainage as residual saturation is approached, as an artefact of the intrinsic phase averaging. As the nonwetting fluid invades the network, the wetting fluid pressure behind the invasion front increases along with the nonwetting fluid pressure. As a result, after breakthrough, the average fluid pressure difference may even decrease. Consequently, the average pressure difference approaches the $P^c - S^w$ curve.

7.4.2 Effect of viscosity ratio on fluid distribution

Fluid entrapment at pore scale, and consequently fluid distribution at macro-scale is controlled by pore- scale invasion mechanisms, such as piston-like movement and snap-off. The importance of these mechanisms varies depending on the process (drainage or imbibition). For instance, snap-off is more important during imbibition than drainage, since the nonwetting fluid is the receding one. As a result, at the end of imbibition process, a significant amount of the nonwetting fluid remains behind as the residual saturation. Due to the importance of imbibition in reservoir engineering, the dependence of residual saturation on capillary number, viscosity ratio, contact angle and pores aspect ratio has been studied significantly (see e.g. *Dias and Payatakes*, 1986a,b, *Hughes and Blunt*, 2000, *Mogensen and Stenby*, 1998, *Vizika et al.*, 1994).

In this section, the effects of capillary number, global pressure difference, and viscosity ratio on snap-off and residual saturation and saturation profile are studied. Because in simulations with constant boundary pressure, flow rate, and thus capillary number change continuously, first we performed some additional imbibition simulations with a constant wetting fluid flux boundary condition. In this simulations, a constant pressure at the nonwetting fluid boundary and a constant flux at the wetting fluid boundary were specified. By performing imbibition simulations at various fluxes, the nonwetting fluid residual saturation was determined as a function of capillary number (plotted in Figure 7.5), for the (imbibition favorable) case of $M = \frac{\mu^n}{\mu^w} = 0.1$. This figure shows that with the increase of capillary number, the residual nonwetting fluid saturation decreases. The largest decrease occurs for capillary numbers between 10^{-6} and 10^{-4}. At higher capillary numbers, the snap-off mechanism is suppressed.

In our main simulations, with constant boundary pressures, capillary number varied significantly as imbibition occurred. This is made apparent in Figure 7.6, where capillary number is plotted for various viscosity ratios and global pressure difference values as a function of wetting fluid saturation during imbibition. It is evident that the largest variation occurs in the case of $M = 10$. This case is also the most sensitive to the global pressure difference. A larger global pressure difference results in higher capillary number and thus a lower residual nonwetting fluid saturation. This is because with the increase of capillary number, the probability of snap-off decreases and consequently flooding efficiency increases.

Similar effects can be observed when examining the average saturation profile along the network, shown in Figure 7.7. Here, the saturation is averaged over a cross section of the network located at position x and then plotted against x/l at different times, and for two different viscosity ratios. An interesting result here is the non-monotonic behaviour of saturation for $M = 10$. This is because snap-off is suppressed with invasion of the wetting fluid as the capillary number increases. Moreover, the saturation front for the case of $M = 10$ is steeper than for $M = 1.0$. This is because the resident nonwetting fluid is more viscous for $M = 10$ than for $M = 1.0$ and thus local imbibition is resisted. The fact that viscosity ratio greatly affects fluid occupancy in the network is illustrated in Figure 7.7(c) where the histogram of the local pore body saturation at the end of imbibition process, for $\Delta P = -10kPa$, is shown. It is clear that with the decrease of viscosity ratio (more viscous wetting fluid), less snap-off occurs and larger flooding efficiency is resulted. To show the effect of viscosity ratio on saturation profile during drainage, saturation profiles for $M = 1.0$ and 0.1 for $\Delta P = 45kPa$ have been shown in Figure 7.8. As it can be seen, for $M = 0.1$, the invading front is unstable and the slope of the front is much smaller than for $M = 1.0$. The comparison between invasion front for these two cases shows how significant the effect of local heterogeneities on saturation profile is. Consequently, the flooding efficiency is smaller for $M = 0.1$ compared with $M = 10$. However, due to the fact that, during imbibition, snap-off is the major mechanism that controls the entrapment of the nonwetting fluid, effect of viscosity ratio on residual saturation is more significant during imbibition than drainage.

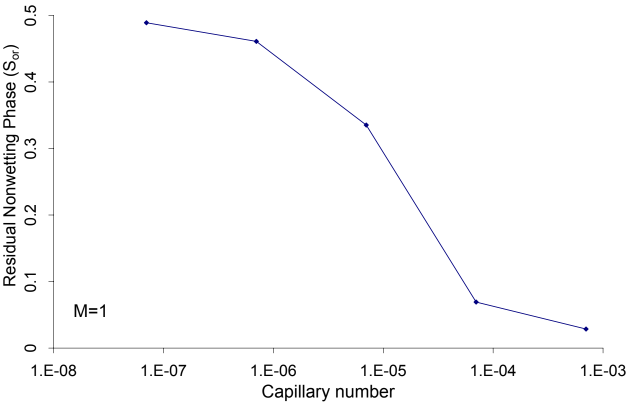

Figure 7.5: *Effect of capillary number on residual nonwetting saturation for* $M = 1.0$.

7.4.3 Dependence of τ on viscosity ratio and saturation

According to Equation 1.7, the deviation of non-equilibrium fluids pressure difference from the macroscopic capillary pressure is related to the time rate of change of saturation. *Hassanizadeh and Gray* (1993a) have suggested that the non-equilibrium capillarity coefficient, τ, is a non-negative function of saturation. For the application of this equation for practical purposes, it is crucial to determine the dependency of this coefficient on medium and/or fluid properties. To compute τ at a given saturation, a plot of $P^n - P^w$ versus $\partial S^w/\partial t$ at that saturation must be made. This is done by starting from one of the graphs is Figure 7.4 for a given viscosity ratio. At a given saturation, different values of $P^n - P^w - P^c$ can be obtained pertaining to different global pressure differences. Corresponding values of $\partial S^w/\partial t$ are known for that saturation. Note that such plots are made for drainage and imbibition separately, whereby the corresponding (drainage or imbibition) P^c-S^w curve is used to calculate $P^n - P^w - P^c$.

By plotting $P^n - P^w - P^c$ versus $\partial S^w/\partial t$ at various values of S^w and fitting a linear relationship to the data points, τ is found as the slope of the fitted line. Results for primary and main drainage as well as for main imbibition are plotted in Figures 7.9(a) and (b), respectively. Under drainage, the fitted line passed through the origin for different M values, as it should. However, under imbibition, there was an intercept. This means that for the curve to go through the origin ($P^n - P^w - P^c = 0$ and $\partial S^w/\partial = 0$) a nonlinear relationship should be employed. However, with increase of the pressure gradient, this nonlinearity decreases, as the capillary forces are suppressed by the viscous forces. Two different aspects of these data are important; a) order of magnitude of the non-equilibrium capillarity coefficient τ b) its variation with saturation for different viscosity ratios.

Values of τ obtained here (ranging from 100 to $1000 Pa.s$ for $M = 1.0$) are in agreement with results obtained in other pore-network modelling studies as shown in Table 7.3. The dimensions of our network correspond to a porous medium sample size of $1.9 \times 1.9 \times 1.9 mm^3$ with an intrinsic permeability of $1.43 \times 10^{-12} m^2$. While the permeability corresponds to a fine sand, the sample size is very small. The general understanding is that the magnitude of τ increases with the size of the observation or averaging window and is inversely correlated with permeability. *Dahle et al.* (2005), using a bundle-of-tube model, concluded that τ value can be proportional to L^2, where L is the length of averaging window. A similar result was found by *Manthey et al.* (2005) based on simulations at continuum scale. In laboratory experiments by *Hassanizadeh et al.* (2004), the value of τ for a fine sand sample of $3cm$ in height was found to be $5 \times 10^5 Pa.s$. The pressure measurements were actually done by transducers with a diameter of around one centimeter. Using similar transducers in experiments with the same fine sand, *Bottero and Hassanizadeh* (2006) found a τ-value of around 1-2 $\times$ 10^5 $Pa.s$. But, when *Bottero* (2009) upscaled the results to the column scale ($18cm$), the average τ-value was found to be 1-2 $\times$ 10^6 $Pa.s$.

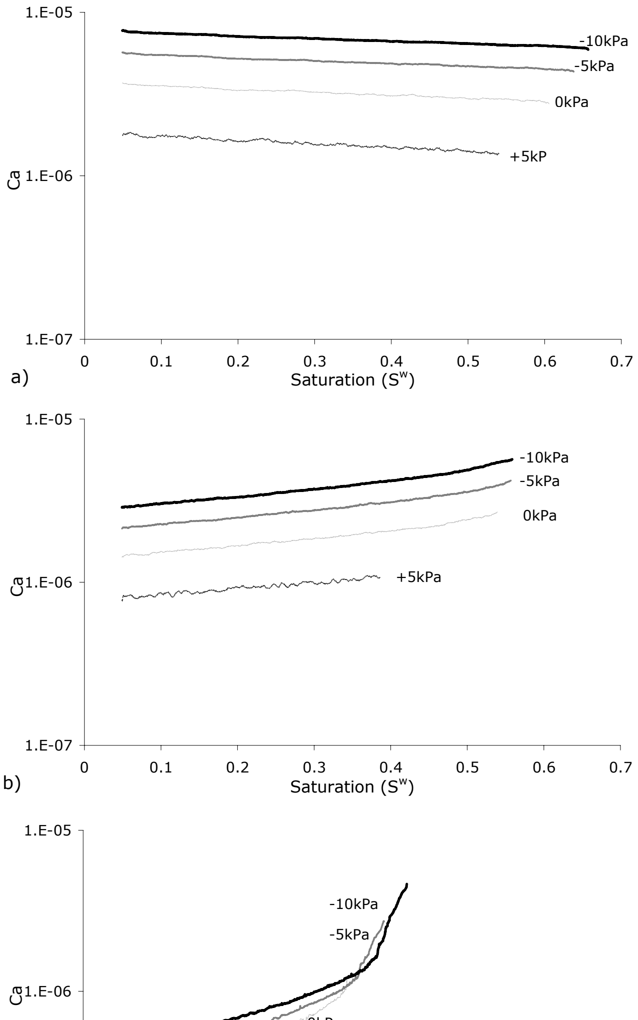

Figure 7.6: *Variation of capillary number during imbibition under constant pressure boundary conditions for a)* $M = 0.1$ *,b)* $M = 1.0$ *,c)* $M = 10$ *and* $M = \mu^n/\mu^w$*. With decrease of nonwetting phase saturation for* $M = 1.0$ *and* $M = 10$*, flow rate of wetting phase increases.*

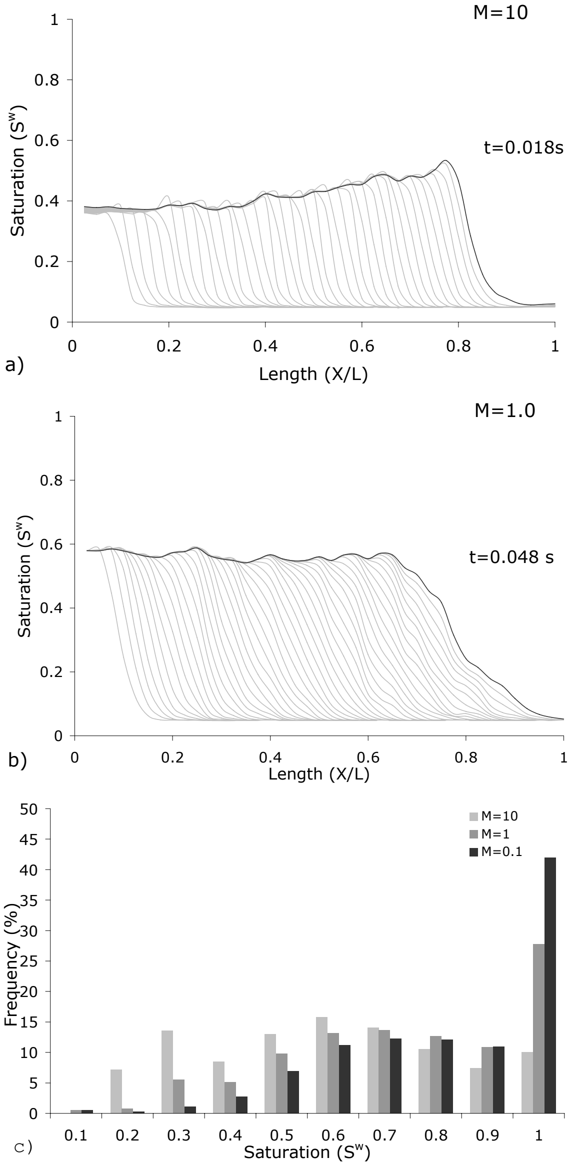

Figure 7.7: *Wetting phase saturation profiles for $\Delta P = -10kPa$ for a) $M = 10$ and b) $M = 1$. Dark-colored curves show the wetting phase saturation distribution at the time of breakthrough of the wetting phase. Light-colored curves show the saturation profile at earlier times. c) Distribution of local saturation of pore bodies at the end of main imbibition simulations for $M = 0.1, 1, 10$ for $\Delta P = -10kPa$. For $M = 0.1$, more pore bodies are fully imbibed compared with $M = 1$ and 10.*

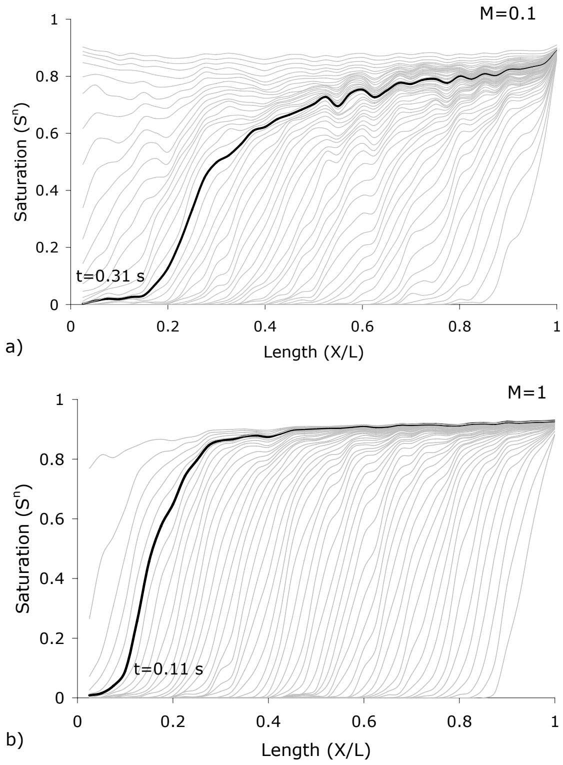

Figure 7.8: *Effect of viscosity ratio on invasion process during drainage. Traveling wave of saturation during dranage for $\Delta P = 45kPa$ for a) $M = 0.1$ and b) $M = 1$. For $M = 0.1$ the invasion front is unstable and effect of porous medium topology to create viscous fingering is obvious.*

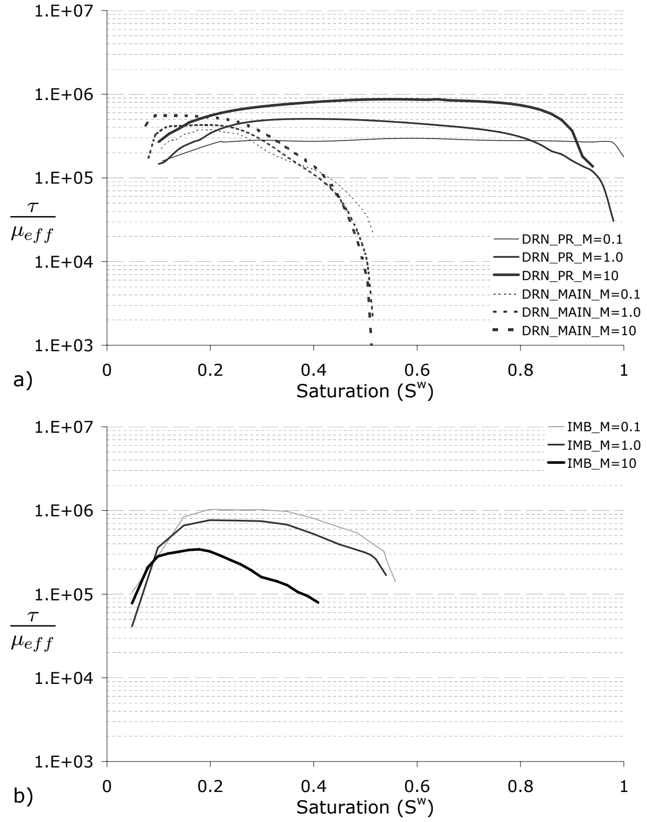

Figure 7.9: *Variation of normalized non-equilibrium capillarity coefficient, $\frac{\tau}{\mu_{eff}}$, as a function of saturation for different viscosity ratios $M = 0.1, 1, 10$ for a) primary and main drainage, b) main imbibition simulations. The vertical axis is in logarithmic scale and $\mu_{eff} = (1 - S^w)\mu^n + S^w\mu^w$.*

Table 7.3: *Values of τ in literature for computational and experimental works.*

Reference	**Exp. Type**	**Process**	**Fluids**	**M**	P^d**(kPa)**	**K (**m^2**)** $\times 10^{-12}$	τ **(**$Pa.s$**)**	$\frac{\partial \tau}{\partial S^w}$	**Domain Dimensions (**cm**)**
Dahle et al. (2005)	BTM	Drain	-	1	0.8	4.7	274	$\ll 0$	0.1 (L)
Gielen et al. (2005) *Gielen* (2007)	PNM	Drain	Oil-water	10	5	-	1.2×10^5	< 0	$0.3 \times 0.3 \times 1$
Joekar-Niasar et al. (2010a)	PNM	Drain	-	1,10	4	150	900,2750	$\ll 0$	$0.5 \times 0.5 \times 0.5$
Joekar-Niasar et al. (2010a)	PNM	Drain	-	0.1	4	150	350	$\gg 0$	$0.5 \times 0.5 \times 0.5$
Das et al. (2007)	CM	Drain	Oil-PCE-Water	> 0.6	1.2	5	10^5 to 10^7	$\ll 0$	
Manthey et al. (2004)	Lab	Drain	PCE-Water	0.9	5.58	3	2 to 7×10^4	< 0 > 0	-
O'Carroll et al. (2005)	Lab	Drain	PCE-Water	0.8	2.1	15.8	5.64×10^7	$\ll 0$	5.07(D),9.62(L)
O'Carroll et al. (2005)	Lab	Drain	PCE-Water	0.8	2.4	12.6	1.99×10^7	$\ll 0$	5.07(D),9.62(L)
Bottero and Hassanizadeh (2006) *Bottero* (2009)	Lab	Drain	PCE-Water	0.9	6	-	10^5 to 10^7	$\ll 0$	9.8 (D),19(L)
Camps-Roach et al. (2010)	Lab	Drain	Air-Water	0.02	2.2	53	2×10^5to10^6	$\gg 0$	10 (D),20(L)
Camps-Roach et al. (2010)	Lab	Drain	Air-Water	0.02	4.6	14.7	10^5to8×10^5	$\gg 0$	10 (D),20(L)

BTM: Bundle of tubes, PNM: Pore-network model, CM: Continuum model, Lab: Laboratory experiment
D: Diameter, L: Length

Figure 7.9 shows that the dynamic effect is stronger for larger effective viscosity values ($\tau(M = 0.1) > \tau(M = 1) > \tau(M = 10)$). This agrees with the explanation given by *Barenblatt et al.* (2003), who stated that dynamic effects in capillary pressure are related to the finite time required for the fluids in the pore structure to rearrange themselves. Indeed, for larger effective viscosity values, more time is required for fluids to reach the equilibrium condition, which corresponds to a larger τ value. *Entov* (1980) has reported that $\tau \propto \frac{\mu l^2}{k \Delta P^c}$, in which k is the permeability, μ is the (effective) viscosity, l is the length of the averaging domain, and ΔP^c is the deviation from the equilibrium capillary pressure for a given saturation.

Results show that For $M \geq 1$, non-equilibrium capillarity coefficient increases with decrease of wetting fluid saturation, which is similar to most findings as reported in Table 7.3. This was found by *Bottero and Hassanizadeh* (2006) for PCE-water ($M = 0.9$), *Mirzaei and Das* (2007) in their column-scale drainage simulations (using a continuum model) as well as *Joekar-Niasar et al.* (2010a) in their pore-network model simulations for favorable viscosity ratio. But, this trend is reversed for $M = 0.1$ as reported in *Camps-Roach et al.* (2010), *Joekar-Niasar et al.* (2010a). *Camps-Roach et al.* (2010) found that τ decreases with decrease of saturation for air-water drainage experiments. These trends are in agreement with the empirical equation suggested by *Stauffer* (1978) for unsaturated soil. Based on drainage experiments done on fine sand in an air-water system. His equation can be modified for two-phase flow in the following simple manner:

$$\tau = \frac{\alpha \epsilon \mu_{eff}}{\lambda k} \left(\frac{P_d^c}{\rho g} \right)^2 \tag{7.5}$$

where α is a constant, ϵ is porosity, λ and P_d^c are the coefficients in *Brooks-Corey* formula (*Brooks and Corey*, 1964), k is the saturated permeability, ρ is the water mass density, and g is the gravity. This equation suggests that the change of τ with saturation is proportional to the change of μ_{eff} with saturation. Recalling the simple linear algebraic equation for μ_{eff} (although it is not valid for all invasion regimes), we can write:

$$\frac{\partial \mu_{eff}}{\partial S^w} = \mu^w - \mu^n \tag{7.6}$$

, which means that $\frac{\partial \tau}{\partial S^w}$ ($\propto \frac{\partial \mu_{eff}}{\partial S^w}$) is negative for $M > 1$ and positive for $M < 1$:

$$\frac{\partial \tau}{\partial S^w} \propto \begin{cases} \mu^w - \mu^n \leq 0 & , M \geq 1 \\ \mu^w - \mu^n > 0 & , M < 1 \end{cases}$$

7.5 Summary and conclusion

We have developed a DYnamic POre-network model for SImulating Two-phase flow (DYPOSIT) to investigate non-equilibrium effects in pressure field under different dynamic conditions. The pore-network model consists of truncated octahedron pore bodies and parallelepiped pore throats. The angularity in cross sections allows for simultaneous flow of both nonwetting and wetting fluids. This means that capillary diffusion in the network is properly taken into account. The pressure field is computed for each fluid separately to consider counter-current flow within pore throats. To improve numerical stability of the model under capillary dominated flow, a semi-implicit algorithm is employed. This allows us to simulate flow dynamics for different flow regimes and viscosity ratios for drainage as well as imbibition.

Several numerical simulations for primary drainage, main imbibition, and main drainage are implemented. We find that in spite of the fact that we have not included local-scale dynamics of the interface (such as dynamics of contact angle), the average fluids pressure difference is significantly distinct from the capillary pressure. We have calculated non-equilibrium capillarity coefficient (τ) versus saturation for three different viscosity ratios under Dirichlet boundary conditions. Our analysis shows that deviation of fluids pressure difference from capillary pressure, mainly originates from the invasion mechanism. It means that in capillary fingering regime or viscous fingering regime less dynamic effect is resulted compared with stable front regime. Furthermore, our analysis shows a strong dependence of τ on viscosity ratio as well as effective viscosity. Due to this fact, τ values under drainage and imbibition processes are different.

Variation of τ with saturation is strongly dependent on the viscosity ratio. This is in agreement with laboratory experiments reported in Table 7.3. We have analyzed uniqueness of τ value under drainage and imbibition processes. Although the order of magnitude of τ during drainage and imbibition for a given viscosity ratio does not change significantly, the curves for primary drainage and main imbibition are not identical. This is due to the fact that effective viscosities and viscosity ratios are different under drainage and imbibition. It is known that viscosity ratios smaller than one can create unstable invading front during both drainage and imbibition. This has been also illustrated by our simulations. Moreover, we have shown that snap-off is highly related to the viscosity ratio and capillary number. A viscous fingering during imbibition under Dirichlet boundary conditions creates non-monotonic distribution of trapped nonwetting fluid. With invasion of the wetting fluid during imbibition, flooding efficiency increases and less nonwetting fluid remains in the domain.

The size of the averaging window used here was 35×35×35 pore bodies. This represents one Representative Elementary Volume (REV) and it sufficed for the purpose of investigating non-equilibrium capillarity effect. For the study of Darcy's law and the role of interfacial area in the modelling multiphase flow, a larger domain must be used. It should be so large that gradients in average pressure, saturation, interfacial area, etc can be calculated. The model is robust and computationally efficient to make this possible. Further applications of this model will be presented in further publications.

Submitted as: Joekar-Niasar, V., Hassanizadeh, S. M. – *"Specific Interfacial Area; the Missing State Variable in Two-Phase Flow"* Water Resources Research, 2010

Chapter 8

Role of Specific Interfacial Area in Two-Phase Flow

> *What is is what must be.*
>
> Gottfried Wilhelm von Leibnitz, philosopher and mathematician

Abstract

It is widely accepted that the description of multiphase flow in porous media has some major shortcomings. In the classical Darcy's equation for multiphase flow in porous media, it is assumed that the gravity and the gradient in fluid pressure are the only driving forces and resistance to the flow is parameterized by a coefficient called (relative) permeability, which is considered to be a function of saturation. It is conceivable that, in multiphase flow, other driving forces may also exist. This would mean that such non-equilibrium effects are lumped into a permeability coefficient. Indeed, many studies have shown that the relative permeability coefficient generally depends not only on saturation, but also pressure gradient and/or flow rate, viscosity ratio, flow history, etc. Through the application of rational thermodynamics a theory of two-phase flow had been developed in which interfacial areas were introduced as separate thermodynamic entities and their macroscale effects were explicitly included. This theory includes new driving forces whose significance need to be established yet. Due to the experimental limitations, the behavior and validity of these equations have not been investigated in detail. We employ the DYPOSIT model - a DYnamic POre-network SImulator for Two-phase flow - to analyze and quantify the extended theories for two-phase flow in porous media. A long pore network was used, which represents as a one-dimensional porous medium column. This model provides pore-scale distribution of local phase pressures, capillary pressure, interfacial area, saturation, and flow rate. Using averaging operators, this information is upscaled and one-dimensional macroscale distributions of these variables are obtained. This information is used then to analyze the behavior of extended equations.

Results show that the classical two-phase flow equations fail to described the transient behaviour of two-phase flow. Transient phase permeability especially for nonwetting fluid is very different from that steady-state permeability curves. Including interfacial area, the coefficients in extended equations are quantified and parameterized. Variations of the coefficients as a function of saturation are very well-behaved. Furthermore, using

the new coefficients it is possible to explain either transient or steady-state flow regimes, which is a new achievement.

8.1 Objectives

The purpose of this work is to provide insights into the behaviour and potential significance of various terms in the extended theories of two-phase flow in porous media, presented above. We implement transient drainage simulations in a long pore network representing a one-dimensional column. Then, a moving REV averaging procedure is formulated that results in the macroscale fields of fluids pressures, velocities, saturation, and specific interfacial area. With extensive analysis of these data, functional dependencies and magnitudes of coefficients $\Psi^{\alpha a}$, $\Psi^{\alpha S}$, $\Psi^{\alpha a}$, Ψ^{nw}, K^{nw}, and E^{nw} are obtained.

8.2 Model description

The dynamic pore-network model DYPOSIT is used here. Details of the model are given in *Joekar-Niasar et al.* (2010a). Here, a summary of main features, equations, and algorithms are provided.

8.2.1 Structure and geometry

The network is based on a regular three-dimensional lattice with fixed coordination number of six. Table 8.1 shows fluid and network properties used in the simulations. Length of the network in the flow direction is equal to 210 pore bodies. Over the network cross section normal to the flow direction, there are 30× 30 pore bodies. We select a viscosity ratio (defined as μ^n/μ^w) equal to one.

Pore bodies and pore throats are represented by “cubes” and “parallelepipeds”, respectively. The size distribution of pore bodies is specified by a truncated log-normal distribution, with no spatial correlation. Statistical properties of radii of pore body inscribed spheres, pore throat inscribed circles, and aspect ratio distributions are shown in Table 8.2. Aspect ratio is defined as the pore body inscribed sphere radius divided by pore throat radius. Corresponding to Table 8.2, Figures 8.1(a) and (b) show the pore body and pore throat size distributions as well as aspect ratio distribution.

Parameter	Symbol	Value	Unit
Contact angle	θ	0.0	degree
Interfacial tension	σ^{nw}	0.0725	kgs^{-2}
Wetting fluid viscosity	μ^{w}	0.001	$kgm^{-1}s^{-1}$
Non-wetting fluid viscosity	μ^{n}	0.001	$kgm^{-1}s^{-1}$
Total no. of pore bodies in flow direction	n_z	210	-
Total no. of pore bodies in lateral directions	n_x, n_y	30	-
Network Size	-	$7.28\times1.08\times1.08$	mm^3
Permeability	K	6.56×10^{-12}	m^2
Entry capillary pressure	P_d^c	14	kPa

Table 8.1: *Fluid and network properties used in the simulation.*

Specifications	R_i (mm)	r_{ij} (mm)
min	0.008	0.005
max	0.018	0.013
mean	0.012	0.008
st. deviation	0.003	0.0017

Table 8.2: *Statistical properties of the radii of inscribed spheres in pore bodies (R_i) and inscribed circles in pore throats r_{ij}.*

8.3 Simulations and analysis

8.3.1 Network size and boundary conditions

To analyze Darcy-scale equations using pore-network models, size of the pore-network should be at least one REV. The REV size was determined by performing

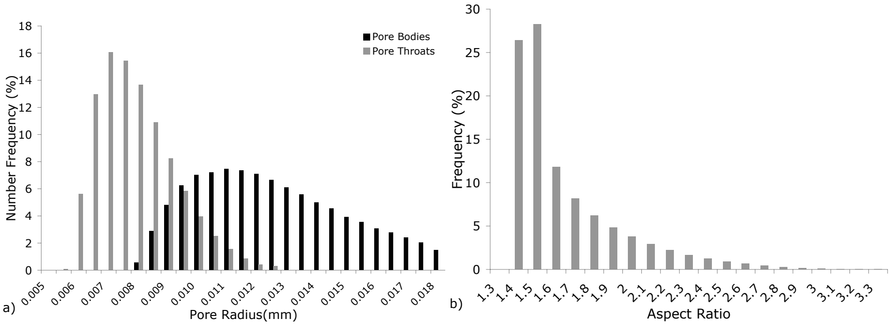

Figure 8.1: *Network geometry properties a) Pore body and pore throat size distributions b) Aspect ratio distribution.*

quasi-static drainage simulations in networks with different sizes but the same statistical parameters. Our simulations showed that the REV size for these statistical parameters is a cube with 30 pore bodies in each directions. So, the cross section was selected to be 30×30 pore bodies and the length of the model in the flow direction was chosen to be 210 pore bodies. The simulation of drainage process in this network took more than three weeks using one processor of an *AMD Opteron 2218* computer with 6GB RAM.

For our simulations, we assumed that the network was connected to a nonwetting phase reservoir on one side and a wetting phase reservoir on the other side. Phase pressures were specified at these boundaries. Side boundary conditions were assumed to be periodic.

Dirichlet boundary conditions were assigned to the inflow and outflow boundaries. The pressure of the nonwetting phase reservoir was denoted by P^n_{top} and the pressure of the wetting phase reservoir was set to zero. The difference between the two boundary pressures during drainage is referred to as "global pressure difference" P^c_{global}. P^c_{global} in our simulation was set to $30kPa$. Once the nonwetting phase reached a pore throat at the wetting-phase boundary, it was assumed that the gradient of capillary pressure within the invaded pore throat was equal to zero ($\frac{\partial p^c_{ij}}{\partial l_{ij}} = 0$). This was done to prevent a sudden relaxation of interfaces after breakthrough of the nonwetting fluid.

8.3.2 Drainage simulations

The network was assumed to be initially fully saturated with the wetting phase. Simulation started with raising the pressure of the nonwetting phase reservoir to P^n_{top}, and establishing a global pressure difference, P^c_{global}, across the network. When the imposed pressure difference was larger than the entry pressure of the largest pore throat at the nonwetting phase reservoir boundary, drainage would start. In quasi-static simulations, the nonwetting phase reservoir pressure was increased in incremental steps so that the network would be invaded in steps. At the end of each step, when there was no flow (static conditions), the overall saturation and the specific interfacial area were determined. Then, the global pressure difference was increased again. Each global pressure difference corresponds to a saturation value. The capillary pressure-saturation data points formed the quasi-static P^c-S^w curve. In transient simulations, the imposed P^c_{global} was chosen to be so large that the whole network could be flooded in one transient step. The simulations were continued till the change of average saturation in the whole network was not significant.

8.3.3 Steady-state phase permeability curves

Relative permeability for each phase is commonly determined from steady-state flow experiments as a function of average saturation. A steady-state flow experiment at a given average saturation (or a given capillary pressure) was simulated as follows. As described above, in quasi-static simulations, we obtained an equilibrium configuration of fluids in the network at a given P^c_{global}. That equilibrium configuration was frozen and a small pressure gradient for each phase imposed across the selected section of the network, where both phases formed a continuous path. The pressure gradient was chosen such that the imposed P^c_{global} was kept unchanged at the boundaries. Also, it was assumed to be so small that fluid configurations were not affected. Therefore, Equations 6.4-6.7 would apply with the left-hand side of Equation 6.6 (mentioned in page 153) being zero. The solution of resulting equations provided steady-state pressure fields for the two phases. Then, total flow through the network for each phase was calculated. Then. following classical Darcy's law, the phase permeability K^α was calculated as $-\mu^\alpha v^\alpha/(\partial p^\alpha/\partial x)$. One should note that since the pore throats have square cross sections, wetting fluid is always connected to the reservoir but its conductance decreases with increase of global capillary pressure P^c_{global}.

8.3.4 Averaging procedure and averaging operators

Our simulations resulted in the fields of local variables, such as pressures, saturations, and fluxes, at consecutive time steps. These were then averaged over an averaging domain moving along the network. That is, at any given time, t, the averaging domain was moved along the network pore layer by pore layer; thus, determining average variables as a function of distance x (position of the center of the averaging domain, see Figure 8.2). This allowed us to obtain gradients of average variables as well as their time derivatives. The averaging domain size was chosen to be 30×30×30 pores, which we had determined to be the REV size. Thus, for our network with the length of 210 pore bodies, this procedure resulted in 180 values for each average variable, at any given time. Average values were determined for saturation, specific interfacial area, pressure, fluid velocities, and interface velocity, following formulas presented below.

Average saturation was simply defined as the ratio of the total volume of the

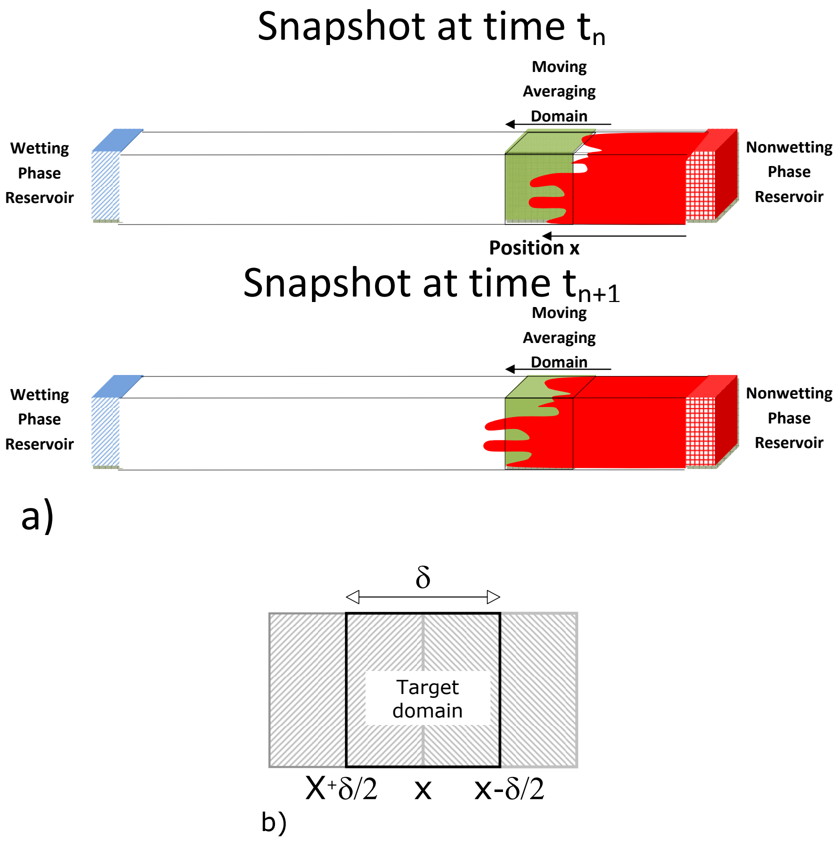

Figure 8.2: *a) Schematic presentation of averaging domain moving along the flow direction. b) For calculating the gradient of average variables, average values at two neighbouring domains centered at* $x - \delta/2$ *and* $x + \delta/2$ *are used.*

wetting phase present within the averaging domain to the total pore volume.

$$S^w = \frac{\sum_{j=1}^{n^{pb}} s_j^w V_j}{\sum_{j=1}^{n^{pb}} V_j} \tag{8.1}$$

$$S^n = 1 - S^w$$

where V_j is the volume of pore body j and n^{pb} is the total number of pore bodies of the averaging domain centered at x. The gradient of saturation for domain was calculated from the average saturations of domains centered at $x - \delta/2$ and $x + \delta/2$, as shown in Figure 8.2(b):

$$\frac{\partial S^w}{\partial \mathrm{x}} = \frac{S^w_{x+\delta/2} - S^w_{x-\delta/2}}{\delta}. \tag{8.2}$$

where δ is the length of the averaging domain.

The averaging of pressure is less straightforward. Commonly, average pressure is obtained using an intrinsic phase average operator (see e.g. *Whitaker*, 1977). However, recently it has been shown that the intrinsic phase average pressure introduces numerical artefacts when both pressure and saturation are spatially variable (see *Korteland et al.*, 2009, *Nordbotten et al.*, 2007, 2008). Instead, a centroid-corrected averaging operator has been suggested by *Nordbotten et al.* (2008) to alleviate problems associated with intrinsic phase averaging. Nevertheless, in this work, we decided to use intrinsic phase average, as it is still the most commonly used operator. This choice does not affect the issues and concepts studied here.

$$P^\alpha = \frac{\sum_{j=1}^{n^{pb}} p_j^\alpha s_j^\alpha V_j}{\sum_{j=1}^{n^{pb}} s_j^\alpha V_j}, \alpha = n, w \tag{8.3}$$

Specific interfacial area was calculated by summing all interfacial areas in an averaging domain divided by its total volume:

$$a^{nw} = \frac{\sum_{j=1}^{n^{pb}} A_j^{nw}}{V} \tag{8.4}$$

where A_j^{nw} is fluid-fluid interfacial area in a pore body j. Gradients of fluids pressures and specific interfacial area over the domain were also calculated using equations similar to 8.2. The average phase velocity for the domain centered at x was defined as follows:

$$v^\alpha = \frac{\sum_{j=1}^{n^{pth}} v_j^\alpha s_j^\alpha V_j}{\sum_{j=1}^{n^{pth}} s_j^\alpha V_j}, \alpha = n, w \tag{8.5}$$

where v_j^α is the local velocity in the pore throat j for fluid α, and V_j is the volume of the pore throat j. This velocity is averaged over the pore throats considering their orientations.

The macroscopic velocity of fluid-fluid interfaces can be determined in two different ways: it can be based either on the average of velocities of individual interfaces or on the time rate of change of the centroids of all interfacial areas within the averaging domain. Considering the first option, it is indeed possible to calculate the velocity of individual interfaces within the network. However, this velocity fluctuates strongly. The reason is that interfaces move in the form of Haines jump. As long as the local capillary pressure is smaller than the entry capillary pressure of a pore throat, the pore interface is stagnant. But, once the interface moves it moves very fast. At any given time, only few interfaces can move, which temporarily may have large velocities. These velocities depend on the global capillary pressure, interfacial tension, pore size, as well as viscosity ratio. *Lu et al.* (1995) found that for ethanol-air system with a viscosity of 0.0119 $Pa.s$, in a pore with radius of 0.05 cm, the velocity of capillary rise can reach 20 cm/s. So, these velocities are not really representative of all fluid-fluid interfaces in the averaging domain. We believe that the second option is physically more acceptable and in line with the classical definition of the average velocity of a collection of masses: it is equal to the time rate of change of their centre of mass. Therefore, we have chosen to determine the macroscale velocity of interfaces from the position of centre of mass of interfaces in the averaging domain in two consecutive time steps. Given the fact that we assumed that fluid-fluid interfaces have a constant mass density, the macroscopic interfacial velocity was defined as follows:

$$\mathrm{w}^{nw} = \frac{1}{t^{k+1} - t^{k}} \left(\left(\frac{\sum_{j=1}^{n^{pb}} \mathrm{x}_j A_j^{nw}}{\sum_{j=1}^{n^{pb}} A_j^{nw}} \right)^{k+1} - \left(\frac{\sum_{j=1}^{n^{pb}} \mathrm{x}_j A_j^{nw}}{\sum_{j=1}^{n^{pb}} A_j^{nw}} \right)^{k} \right) \tag{8.6}$$

where x_j denoted the position of interfaces in pore body j, the superscript k denotes the time step. Note that in this calculation, only the interfaces in the pore bodies were included. Interfaces in pore throats, did not move from one time step to another.

For calculating the divergence of product of interfacial area and its velocity, $\nabla(a_i^{nw}\mathrm{w}_i^{nw})$, appearing in Equation 1.4, we employ the 1-D equivalent of the divergence theorem:

$$\frac{\partial(a^{nw}\mathrm{w}^{nw})}{\partial x} = \frac{1}{\delta} \left(\sum_{j=1}^{n^{pb}} (A_j^{nw} w_j^{nw})|_{\text{D.B.}} - \sum_{j=1}^{n^{pb}} (A_j^{nw} w_j^{nw})|_{\text{U.B.}} \right) \tag{8.7}$$

where $U.B.$, and $D.B.$ denote the downstream and upstream boundaries, respectively.

8.4 Results and discussion

The extended two-phase flow equations involve new variables such as velocity of fluid-fluid interfaces or their rate of production, as well as new coefficients. In this

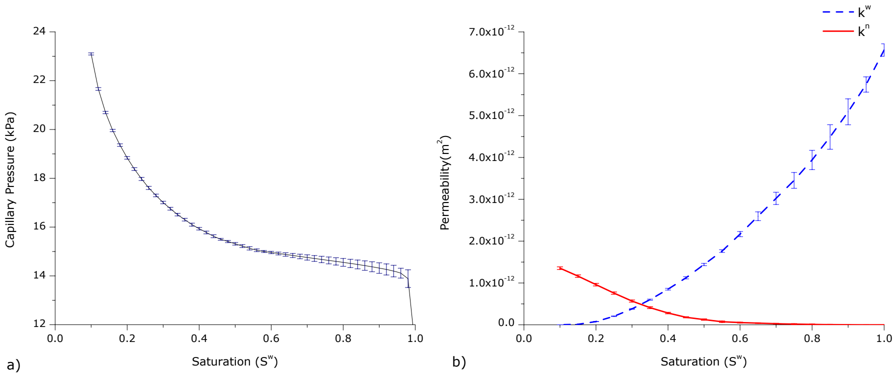

Figure 8.3: *Averaged characteristic curves for a moving averaging domains along the domain. The bars at each saturation show the minimum and maximum value resulted at that saturation. a) Capillary pressure-saturation curve b) Permeability for each fluid versus saturation.*

section, the behaviour of these new variables are investigated and values of new coefficients are quantified. The major interest in this work is to gain an insight into the role of fluid-fluid interfaces in the description of two-phase flow.

8.4.1 Investigation of Darcy's law

Equilibrium conditions

As explained in the previous section, capillary pressure-saturation (P^c-S^w) curves were determined under quasi-static conditions and phase permeability-saturation (k^α-S^w) curves were obtained through steady-state flow simulations of primary drainage. These curves were computed for each and every moving averaging domain along our network. As a result of this procedure, 180 average curves were produced. The mean of resulting curves are shown in Figures 8.3, where the range of variations is shown by vertical bars. It is obvious that there is no significant variation in these characteristic curves over the whole network.

Under no-flow conditions, we have $v^\alpha = 0$ and $\frac{\partial P^\alpha}{\partial x} = 0$, but we may still have gradients in saturation and specific interfacial area. Thus, from Equation 1.1, as there is no gravity in our simulations, we obtain:

$$\frac{\Psi^{\alpha S}}{\Psi^{\alpha a}} = -\frac{a^{nw}_{,x}}{S^w_{,x}} \quad \alpha = w, n \tag{8.8}$$

From our simulation results, we can calculate the r.h.s of this equation for many

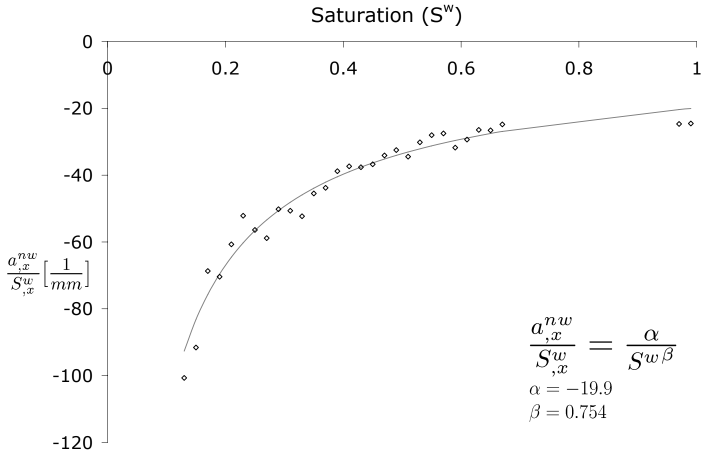

Figure 8.4: *Variation of $a^{nw}_{,x}$ versus $S^{nw}_{,x}$ for all snapshots using Equations 8.2,8.1, and 8.4.*

averaging domains along the network, under various conditions. The results are plotted in Figure 8.4 for the wetting phase. It is evident that this curve is well-behaved and it can be fitted with a simple formula:

$$\frac{\Psi^{wS}}{\Psi^{wa}} = \frac{\alpha}{S^{w\beta}}[1/mm] \tag{8.9}$$

where α has the dimension of [1/L] and β is a dimensionless coefficient. For the curve presented in Figure 8.4, we have $\alpha = -19.9mm^{-1}$ and $\beta = 0.574$.

Transient conditions; standard Darcy's law

The relative permeability curve, measured under steady state flow conditions, is also used in the standard flow conditions, is als used in the standard Darcy's law under transient flow conditions. Here, we show that this assumption is generally not valid. In our transient simulations, we determined the phase permeability K^α by calculating $-\mu^\alpha v^\alpha/\partial P^\alpha/\partial x$ for many averaging domains along the network (the same procedure that we followed to obtain curves shown in Figure 8.3). The mean of resulting curves are plotted in Figure 8.5, along with the steady-state curves.

It is evident that steady-state and transient curves are significantly different. specially for the nonwetting phase, the transient permeability curve is totally different from steady-state curve. In particular, it has a non-monotonic behavior and is much larger than the steady-state values for medium and high wetting phase saturations.

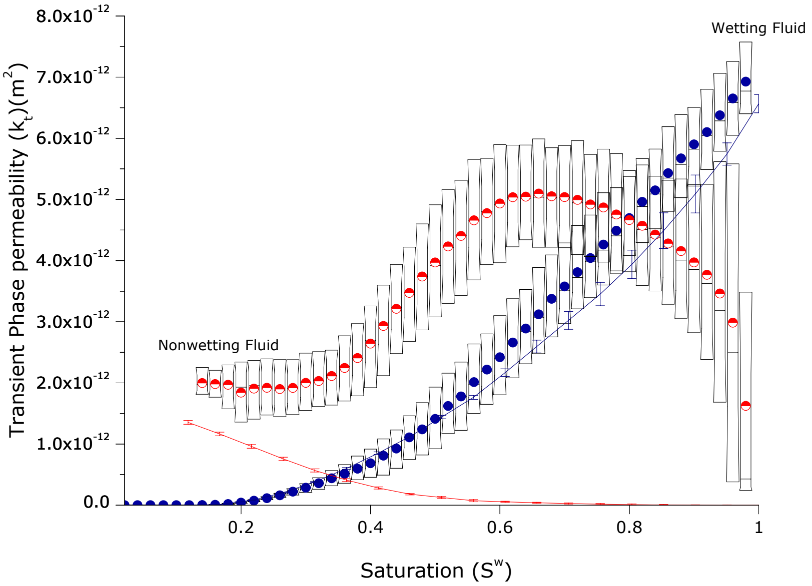

Figure 8.5: *Ratio of α-phase flux to the α-phase pressure gradient under transient conditions, referred to as transient phase permeability. It is compared with steady-state permeability curves. The bars show the range of variation of* 10 *to* 90% *of the data points at the given saturation.*

This is also the range that fluid-fluid interfaces are generated and the system is very dynamic.

As mentioned above, the permeability values are determined for a large number of averaging domains. The variations from the mean values are shown by means of vertical bars for the steady-state curve and by vertical boxes for the transient curves. The boxes in Figure 8.5 show the 10% and 90% probability of the occurrence for all transient phase permeabilities. As it can be seen, there is a huge variation in the magnitude of the transient phase permeability. As mentioned before, in our simulations capillary number was variable; it decreased with the invasion of the nonwetting fluid.

Also, it can be observed that under transient flow conditions, for $S^w > 0.5$, the there is linear relationship between the transient wetting phase permeability and saturation. This is qualitatively in agreement with steady-state experimental observations of *Constantinides and Payatakes* (1996) and simulation results of *Tsakiroglou et al.* (2003) who observed that with the increase of capillary number (increase of viscous forces), the nonlinear behaviour of relative permeability decreases.

Furthermore, we note that as the residual saturation is approached, the transient nonwetting phase permeability also approaches the steady-state values. This is because the fluids configuration is well developed under those conditions, and non-equilibrium effects become negligible. The foregoing results point to the fact that the standard Darcy's law is not valid under transient flow conditions. We therefore investigate the role of additional terms in the extended Darcy's law given by Equation 1.1.

Transient conditions; extended Darcy's law

As mentioned before, many computational and experimental studies have shown that the relative permeability in the classical Darcy's law strongly depends on transient flow variables such as flow velocity and/or pressure gradient. We believe this is because pressure gradient is not the only driving force for two-phase flow. Indeed, as suggested by Equation 1.1, gradients in saturation and specific interfacial area also contribute to the flow. But, because they are absent in classical Darcy's law, their role has to be taken over by the relative permeability. In order to investigate this conjecture, we use results of transient conditions to determine the significance of extra terms in Equation 1.1. First, the values of coefficients $\Psi^{\alpha S}$ and $\Psi^{\alpha a}$ need to be determined.

In the previous subsection, the ratio of $\frac{\Psi^{\alpha S}}{\Psi^{\alpha a}}$ for each phase was obtained; thus, only two independent coefficients (one coefficient per phase) should be determined. Once again, for any given set of boundary conditions, v^α, $P^\alpha_{,x}$, $a^{nw}_{,x}$, and $S^w_{,x}$ can be calculated. With K^α already known as a function of S^w for steady-state simulations, the other two coefficients can be calculated. The results are shown Figure 8.6. As it can be observed, the variation of material parameters, $\Psi^{\alpha a}$ and $\Psi^{\alpha S}$ with saturation is very well behaved. One should note that values of these parameters are resulted from many different averaging domains, with very different capillary numbers. It means that transient conditions of the system does not influence significantly the variation of these parameters. The large variations in the values of these parameters at large saturations are strongly dependent on the size of the averaging domain. With the increase of the size of averaging domain, these variations will decrease.

To show the importance of the gradient of pressure compared to the new terms in the extended Darcy's law, we have presented their ratio in Figure 8.7. In Figure 8.7(a), the ratio $\frac{P^w_{,x}}{-\Psi^{wa}a^{nw}_{,x}-\Psi^{wS}S^w_{,x}}$ versus saturation, and in Figure 8.7(b) the ratio $\frac{-\Psi^{na}a^{nw}_{,x}+\Psi^{nS}S^w_{,x}}{P^n_{,x}}$ versus saturation have been presented. It is clear that the effect of the new terms is basically negligible for the wetting phase, but very significant for the nonwetting phase. This means that the deviation of the fluid flux calculated from

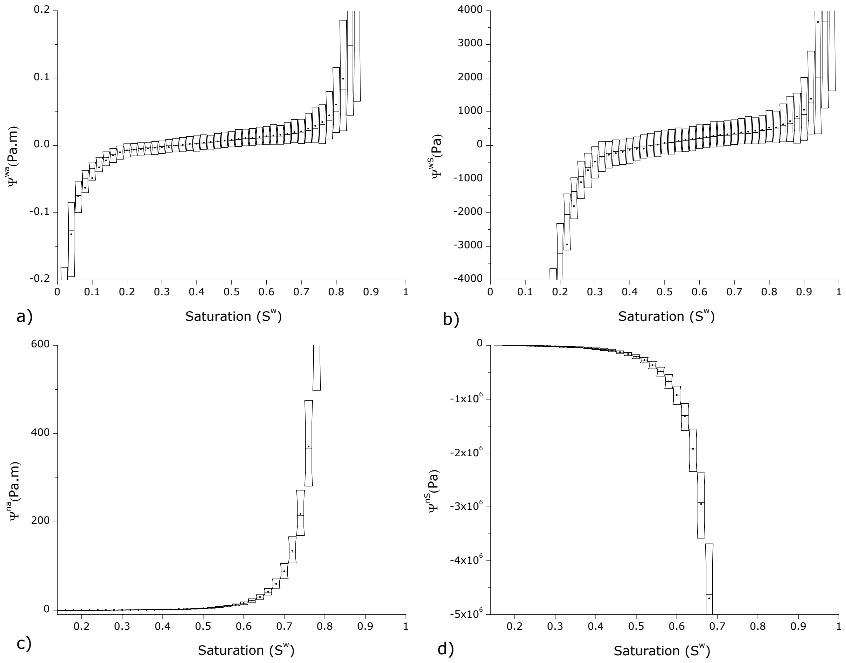

Figure 8.6: *Variation of material properties presented in Equation 1.1 based on the moving averaging domain analysis of the simulations. a)*Ψ^{wa} *b)*Ψ^{wS} *c)*Ψ^{na} *d)*Ψ^{nS}*. Description of the bars are given in caption of Figure 8.5.*

the classical Darcy's law from the "true value" is not as significant for the wetting phase as for the nonwetting fluid flux. In Figure 8.7(b), the ratio $\frac{-\Psi^{na}a^{nw}_{,x}+\Psi^{nS}S^{w}_{,x}}{P^{n}_{,x}}$ starts from a very large number at high saturations, and decreases as steady-state conditions are approached. This implies that for an improved estimation of fluid fluxes under transient conditions, especially for nonwetting fluid, the gradient of the interfacial area and saturation should be included.

8.4.2 Interfacial area equations

The introduction of specific interfacial area as a state variable into the theories of multiphase flow necessitates new set of governing equations to model its evolution. These are given by Equations 1.2 and 1.4. These equations also involve new material properties, which are the macroscopic interface velocity, interfacial conductivity tensor, macroscale interfacial tension, material coefficient Ψ^{nw}, and the interfacial production term E^{nw}. In this section, results of transient drainage simulations are

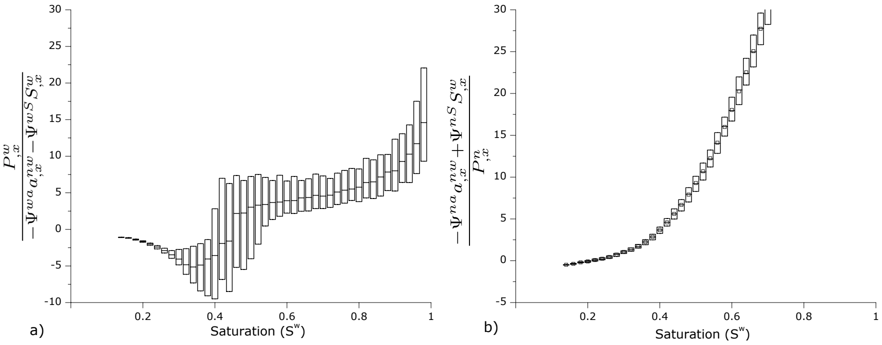

Figure 8.7: *Ratio of gradient of fluid pressure to the other added terms in Equation 1.1 for a) Wetting fluid b) Nonwetting fluid. On should note that for clear illustration the ratio is inverse in figure (b).*

used to calculate these properties and investigate their behavior.

Macroscopic interface velocity

Using Equation 8.6, the macroscopic interface velocity was calculated for many averaging domains with time. We then looked into possible relationships between interface velocity and other quantities. We found a meaningful relationship with the saturation and time rate of change of saturation. The resulting plot is shown in Figure 8.8(a). As it can be observed, there is an almost linear relationship between the interface velocity and time rate of saturation change. We should point out the small negative interface velocities obtained at large saturations. This is caused by the fact that when interfaces have just entered the averaging domain, it is possible that local and temporary imbibition occurs, i.e. the nonwetting fluid may temporarily move back and out of the domain. In the intermediate saturation range, the interface velocity reaches its maximum value. *Nordhaug et al.* (2003) also calculated variation of interface velocity with saturation, using a pore-network model with circular cross sections and a size of $10 \times 10 \times 50$ pore bodies, elongated in flow direction. They studied variation of the interface velocity under different dynamic conditions (capillary number and viscosity ratio). Although the algorithm for calculation of interface velocity in their network was different from our approach, they got a qualitatively similar behavior for interface velocity especially under capillary-dominated flow conditions. However, due to the small size of their averaging domain ($10 \times 10 \times 10$ pores), there was a boundary effect in their results, which caused an overshoot of interface velocity at large saturations ($S^w > 0.9$).

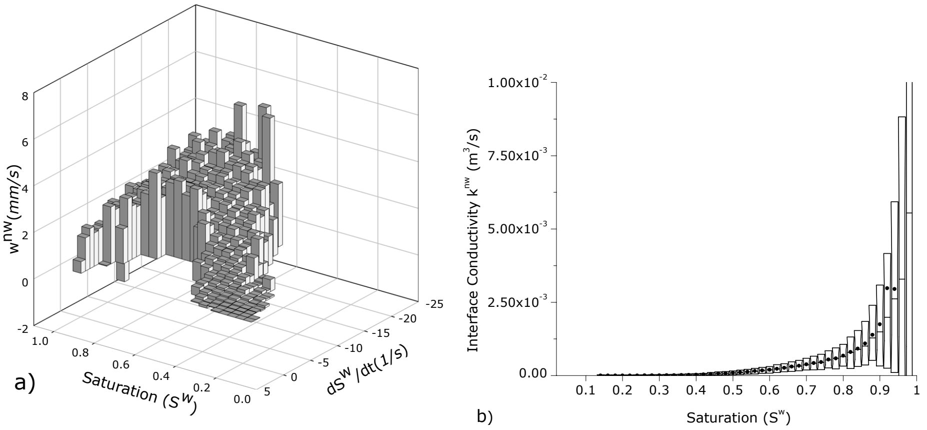

Figure 8.8: *a) Dependence of macroscopic interface velocity on saturation and change of saturation with time, calculated using Equation 8.6 for all simulation snapshots and averaging domains, b) Variation of interface conductivity with saturation resulted from analysis of all moving averaging domains in time and space. Description of the bars is given in the caption of Figure 8.5.*

Interface conductivity and material coefficient Ψ^{nw}

After calculating fluid-fluid interface velocities at different saturations under variable dynamic conditions, it is possible to estimate the conductivity of interfaces. To lump effect of interfacial tension in the interface conductivity term, for a one-dimensional domain we can rewrite Equation 1.2 as follows:

$$w^{nw} = -k^{nw}(a^{nw}_{,x} + \psi^{nw} S^{w}_{,x}) \tag{8.10}$$

where $k^{nw}[L^3/T] = \sigma^{nw} K^{nw}$ and $\psi^{nw} = \Psi^{nw}/\sigma^{nw}$. First, the coefficient ψ^{nw} is obtained from the equilibrium conditions, where the interfaces do not move and w^{nw} is equal to zero. Under these conditions, we have:

$$\psi^{nw} = -\frac{a^{nw}_{,x}}{S^{w}_{,x}} = -\frac{\alpha}{S^{w\beta}} \tag{8.11}$$

where the r.h.s of this equation follows from Equation 8.9. Next, the interfacial conductivity k^{nw} can be determined from Equation 1.2, under transient conditions. All terms in Equation 1.2 can be calculated for a large number of averaging domains and at various times; allowing us to find values of k^{nw} for a wide range of dynamic conditions. The result is plotted as a function of average saturation in Figure 8.8(b). It is evident that the interface conductivity is an increasing function of wetting fluid saturation. One should note that, except for the range of $S^w > 0.9$, the variation in values of interface conductivity estimated under various transient conditions is not significant. This shows that this coefficient is a reasonably well-behaved function of saturation under a wide range of dynamic conditions. Larger variations of interface conductivity for $S^w > 0.9$ is due to the variations of interface velocity, and having negative values in Figure 8.8(a), which is caused by local temporary imbibition during the early stages of invasion. This effect reduces dramatically as soon as the nonwetting phase saturation becomes significant in the averaging domain.

Production rate of interfacial areas

We use Equation 1.4 to calculate the production term, E^{nw}. Thus, we have to estimate the change of specific interfacial area with time ($\partial a^{nw}/\partial t$) as well as the flux of interfacial area ($\partial(a^{nw}w^{nw})/\partial x$). Both of these quantities can be calculated for a large number of averaging conditions. The resulting production rate is plotted in Figure 8.9 as a function of average saturation and its time rate of change. This figure shows that E^{nw} depends linearly on the time rate of saturation change. Furthermore, it reaches its maximum value in the range of intermediate saturations. This is due to greater possibilities for the creation of invasion sites at intermediate saturations. At high wetting fluid saturations, only few pores are filled with the nonwetting fluid, thus small amount of interfacial area is created. With the invasion of the nonwetting fluid, more pores will be filled, each of them acting as the launching site for the invasion of many other pores by the nonwetting fluid. This causes a faster creation of interfacial area. Eventually the interfacial area associated with the main terminal interfaces will start to become less and less, as many of them will coalesce with each other. Thus, the production rate of specific interfacial area will decrease.

8.5 Concluding remarks

We have simulated two-phase drainage experiments using a long dynamic pore-network model, called DYPOSIT, under constant pressure boundary conditions. The model has a cross section of 30×30 pore bodies and 210 pore bodies in flow direction. The analyses are based on volumetric averaging in a moving averaging domain with the size of 30×30×30 pore bodies. The averaging is done along the domain in many time steps. Because of imposed boundary conditions (i.e. constant pressures) the flow velocity varies considerably with time as the nonwetting fluid invades the domain. As a result, the capillary number also change through the network with time from 2×10^{-5} to 5×10^{-7}. So the calculated material properties are

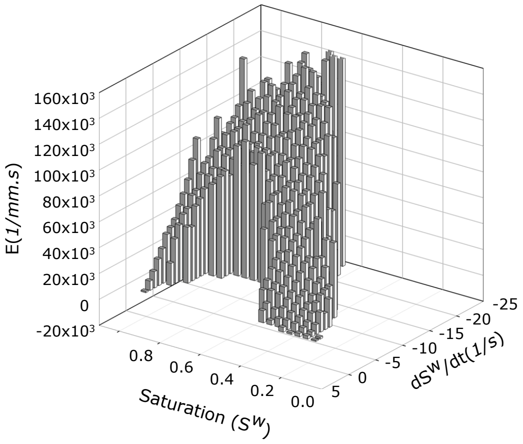

Figure 8.9: *Dependence of production rate of specific interfacial area versus saturation and change of saturation with time based on Equation 1.4 and calculated using Equations 8.4 and 8.7 for all simulation snapshots and averaging domains.*

obtained for a wide range of capillary numbers.

We have used our results to investigate thermodynamically-based theories of two-phase flow in porous media, where the fluid-fluid specific interfacial area is included as a new state variables. First, we have showed that if the standard Darcy's law is used under transient conditions, then the phase conductivity of the nonwetting phase will be a nonmonotonic function of saturation. Also, the wetting phase conductivity determined under transient conditions will be significantly different from the steady-state phase conductivity. We believe this is because of the fact that in the standard Darcy's law the pressure gradient is assumed to be the only driving force for the flow. But, we know that in two-phase flow, the movement of interfaces and energies associated with them significantly affect the flow of phases. The new terms in the extended Darcy equation are believed to account for such effects. These terms introduce gradients in the saturation and specific interfacial area as extra driving forces. We have shown that including these terms allows us to use steady-state relative permeability curve for transient flow conditions. We have determined the values of material coefficients associated with extra terms. We have found that they are well-behaved functions of saturation. Next, various coefficients appearing in the equations governing the evolution of interfaces were determined. One of these coefficients was the interface conductivity. Our results show that interface conductivity is an increasing function of wetting phase saturation. We have also determined the rate of production of specific interfacial area. Our results show a linear relationship between production rate of fluid-fluid interfaces and change of saturation with time.

It is also shown that although interfaces may have high velocities at the moment of Haines jump, the macroscopic interface velocities are strongly correlated with the time rate of saturation change. Variation of macroscopic interfacial velocity with saturation - in an averaging domain - is nonmonotonic, having a maximum in the intermediate saturations.

These analyses lead us to a new understanding that including gradient of interfacial area and gradient of saturation in the new equations can implicitly account for the moving boundary between the two fluids during drainage. This feature is absent in the classical equations for two-phase flow. Dependence of the new parameters on fluid and porous medium properties is an important issue, which should be investigated in future. It must be noted that here we did not investigate the non-equilibrium capillarity effect (the second term in the r.h.s of Equation 1.7) as this was done extensively in an earlier work by *Joekar-Niasar et al.* (2010b) and *Joekar-Niasar and Hassanizadeh* (2010).

Chapter 9

Concluding Remarks

> *The important thing is never to stop questioning.*
>
> Albert Einstein, physicist

9.1 Towards a better understanding of multiphase flow

Understanding the physics of multiphase flow in porous media is important in many fields such as hydrogeology, reservoir engineering, biomechanical engineering, fuel cells, and other industrial applications. Current theories of multiphase flow are based on Darcy's law, which assumes that the only driving forces for flow of each fluid are the gravity and the gradient in fluid pressure. The resisting force is assumed to be linearly proportional to the relative fluid velocity with respect to the solid. One may expect many other factors to affect the balance of forces in the case of multiphase flow. Among these are interfacial forces that govern the distribution of interfaces in the porous medium. In fact, through the application of rational thermodynamics, *Hassanizadeh and Gray* (1990, 1993a) developed a theory of two-phase flow in which interfacial areas were introduced as separate thermodynamic entities, possessing mass, momentum, and energy. They derived momentum balance equations not only for phases, but also for interfaces, and macroscale effects of interfacial forces were explicitly included.

Some of the equations proposed in the extended Darcy's law, such as "non-equilibrium capillarity effect in fluid pressures difference" and "role of interfacial area is removing hysteresis in capillary pressure curves" have been partially studied numerically or experimentally. But the full set of equations has not been analyzed. The full set of equations can be summarized in the following conjectures.

- In multiphase flow in porous media, gravity and fluid pressure gradient are not the only forces. There are other sources of forces, such as interfacial forces.

- Capillary pressure and saturation are related to each other through fluid-fluid interfacial area to generate a unique surface under drainage and imbibition.

Thus, interfacial area can remove the hysteresis observed in P^c-S^w curves under drainage and imbibition.

- There is not a unique capillary pressure-saturation curve. Depending on the time rate of saturation change, different capillary pressure-saturation curves can be resulted.

To understand the physics of the problem and evaluate these hypotheses, pore-network modelling technique has been employed. This technique allows us to simulate the flow processes at pore scale. The pore-scale information can be averaged to obtain macroscale data for further analysis. Since pore-network modelling is computationally cheaper than the other pore-scale simulators (such as Lattice Boltzmann, Smooth Particle Hydrodynamics, etc), it allows us to simulate large domains.

Two different objectives have been followed in this research.

9.2 Theory analysis

The behavior of extended Darcy's law has been studied using different pore-network models. Role of specific interfacial area in removing hysteresis has been investigated by quasi-static pore-network models in three different porous media: hypothetical porous media, a two-dimensional micro-model, a glass-bead column.

The hypothetical network was structured and regular. Pore bodies and pore throats were represented by sphere and circular tubes. Using this model, the relationships among capillary pressure, saturation, and interfacial area (P^c-S^w-a^{nw}) as well as relative permeability, saturation, and interfacial area (k_r^w-S^w-a^{nw}) were studied. The results showed that aspect ratio has a major effect on significance of hysteresis in P^c-S^w and k_r^w-S^w curve, so that in a tube network (no pore body), hysteresis was almost eliminated. Furthermore, trapping mechanism can influence significantly the form of S^w-a^{nw} curves as well as irreducible saturation. Using data from the full range of scanning drainage and imbibition simulations, we have constructed P^c-S^w-a^{nw} and k_r^w-S^w-a^{nw} surfaces. Results show that with decreasing the pore aspect ratio, the absolute difference between the two surfaces decreases, and basically interfacial area can diminish or eliminate the hysteresis that is commonly observed in P^c-S^w and k_r^w-S^w curves. But, since the network was idealized, more detailed investigation based on a more realistic porous medium was required.

Thus, this conjecture was analyzed in a two-dimensional micro-model. An unstructured pore-network model was developed to simulate the drainage and imbibition experiments performed on a two-dimensional micro-model of a porous medium to produce P^c-S^w-a^{nw} surface. Our analysis showed that capillary pressure of the micro-model was controlled by its depth, which was almost as small as the smallest pore width. Using the pore-network model, we reproduced the observed patterns of fluid distribution in the micro-model for both drainage and imbibitions experiments. We also produced a P^c-S^w-a^{nw} surface for imbibition that approximates the measured surface very closely. This is very encouraging as it suggests that we can use our pore-network model as a predictive tool for testing the behaviour of micro-models, before manufacturing.

Finally, the role of interfacial area in removing the hysteresis was investigated for a glass-bead column. In this case study, the porous medium was completely unstructured and irregular. In addition, the cross sections of the pores were angular, which allows simultaneous existence of both fluids. Using the generated pore-network model, P^c-S^w-a^{nw} surfaces for drainage and imbibition were produced, separately. Comparison between these two surfaces showed that they are highly correlated ($r^2 = 0.95$), and the normalized difference is small, in the range of uncertainty of model calculations. Our results show that in glass beads with unstructured irregular network with mixed cross sections, the hysteresis in P^c-S^w-a^{nw} curves is much smaller than the hysteresis in P^c-S^w curves. The largest relative error between $a^{nw} = f(P^c, S^w)$ surfaces is found at large saturations, where the specific interfacial area is very small.

To investigate the non-equilibrium capillarity effects and their dependence, a DYnamic POre-network Simulator for Two-phase flow (DYPOSIT) was developed. It was applied to study dynamics of specific interfacial area, average capillary pressure, average phase pressure differences, functionality of non-equilibrium capillarity coefficient as well as production rate of interfacial area. Macroscopic capillary pressure was defined as the average of local capillary pressure at all interfaces weighted with the area of the interface. We showed that neither average capillary pressure-saturation curves, nor specific interfacial area-saturation curves, are not unique, but they depend on flow dynamics as well as fluid-solid properties. However, it is shown that capillary pressure-saturation-interfacial area surface for primary drainage is an intrinsic property of the porous medium, independent of fluid properties and dynamic conditions. The difference between average phase pressures, however, is found to be dependent on boundary pressures and time rate of change of saturation as prescribed by the dynamic capillary theory. We found that in spite of the fact that we have not included local-scale dynamics of the interface (such as dynamics of contact angle), the average fluids pressure difference is significantly distinct from the capillary pressure. Our results illustrate that the non-equilibrium capillarity coefficient is a function of saturation as well as viscosity ratio. Dynamics of interfacial area show that with decrease of the viscosity ratio, specific interfacial area increases, which is a consequence of the invasion mechanism. However, in all dynamic cases, specific interfacial area is smaller than that under quasi-static conditions. With decrease of the viscosity ratio, effect of the intrinsic properties of medium (geometry and topology) on the creation of interfacial area increases. The production rate of specific interfacial area for different viscosity ratios has been studied and quantified. With the decrease of the viscosity ratio, production rate of the specific interfacial area increases. The production rate is found to have an almost linear relationship with the time rate of change of saturation. This linearity coefficient is a function of saturation as well as the viscosity ratio.

In another set of simulations, several numerical experiments for primary drainage, main imbibition, and main drainage are implemented. We calculated non-equilibrium capillarity coefficient (τ) versus saturation for three different viscosity ratios under Dirichlet boundary conditions. Our analysis shows that deviation of fluids pressure difference from capillary pressure, mainly originates from the invasion mechanism. It means that in capillary fingering regime or viscous fingering regime less dynamic effect is resulted compared with stable front regime. Furthermore, our analysis shows a strong dependence of τ on viscosity ratio as well as effective viscosity. Due to this fact, τ values under drainage and imbibition processes are different. Variation of τ with saturation is strongly dependent on the viscosity ratio. This is in agreement with laboratory experiments reported in Table 7.3. We have analyzed uniqueness of τ value under drainage and imbibition processes. Although the order of magnitude of τ during drainage and imbibition for a given viscosity ratio does not change significantly, the curves for primary drainage and main imbibition are not identical. This is due to the fact that effective viscosities and viscosity ratios are different under drainage and imbibition. It is known that viscosity ratios smaller than one can create unstable invading front during both drainage and imbibition. This has been also illustrated by our simulations. Moreover, we have shown that snap-off is highly related to the viscosity ratio and capillary number. A viscous fingering during imbibition under Dirichlet boundary conditions creates non-monotonic distribution of trapped nonwetting fluid. With invasion of the wetting fluid during imbibition, flooding efficiency increases and less nonwetting fluid remains in the domain.

Finally, the pore-network model was employed to simulate drainage process in a long domain. The model had a cross section of 30×30 pore bodies and 210 pore bodies in flow direction. Different aspects of the fluid-fluid interfaces such as their velocity (and dependence on change of saturation with time) and production rate have been analyzed. Results show a linear relationship between production rate of fluid-fluid interfaces and change of saturation with time. It is also shown that although interfaces may have high velocities at the moment of Haines jump, the macroscopic interface velocities are strongly correlated with the time rate of saturation change. Variation of macroscopic interfacial velocity with saturation - in an averaging window - is nonmonotonic, having a maximum in the intermediate saturations.

Given the fact that intrinsic phase averaging is the most common approach, transient two-phase drainage and extended two-phase flow equations (proposed by *Hassanizadeh and Gray* (1990, 1993a)) have been investigated using this averaging operator. Macroscopic analysis of transient two-phase drainage shows that, as expected, there is a significant dynamic effect on fluid permeabilities, especially on nonwetting-fluid transient permeability. This can not be captured properly using the classical two-phase flow equations. On the other hand, *Hassanizadeh and Gray* (1990, 1993a) have conjectured that specific interfacial area should be explicitly included in the governing equations for an adequate description of the multiphase flow in porous media. However, these equations include new coefficients, which are not well defined in terms of the macroscopic fluid and solid properties. Averaging all the variables and relating them to the averaged fluxes given in Equation 1.1, we quantified the coefficients $\Psi^{\alpha S}$ and $\Psi^{\alpha a}$ (given in Equation 1.1) so that the equality between averaged flux and gradients of saturation, interfacial area, and pressures can be obtained. The dependence of new coefficients on saturation seems very well-behaved. In spite of the fact that the capillary number varies during the simulations, the dependencies of the parameters on the averaged saturation seem independent of the dynamics of the system.

These analyses lead us to a new understanding that including gradient of interfacial area and gradient of saturation in the new equations can implicitly account for the moving boundary between the two fluids during drainage. This feature is absent in the classical equations for two-phase flow. Dependence of the new parameters on fluid and porous medium properties is an important issue, which should be investigated in future.

9.3 Improving pore-network modelling technique

From the technical point of view, new geometrical and computational approaches were developed. These methodologies provide more accurate representative pore-network models for specific cases and predictive purposes.

For generation of two-dimensional pore-network model based on the image, a medial axis-based approach was employed. A simple approach based on distance transform (**DT**) was employed to define medial pixels. Using this concept, geometry and topology of the micro-model are captured with an acceptable accuracy for use in a pore-network model. We have demonstrated the capability of the model by simulating the configuration of two immiscible fluids in a micro-model. The capability of the pore-network model for simulating a real porous medium has been successfully verified, as we reproduce the measured P^c-S^w and a^{nw}-S^w curves very well.

For granular porous media, a new approach for generation of cross sections based of shape factor distribution was proposed. We studied whether shape factor alone is enough to characterize the pore geometry of a granular porous medium. A geometry-based approach was proposed for generation of pore throat cross sections so that the whole range of shape factor distribution can be reproduced. Three different general shapes for pore throats have been considered: irregular hyperbolic triangles, regular hyperbolic polygons, and circles. General formulas for calculation of geometrical properties and entry capillary pressure of these geometries were derived. Effects of shape factor as well as cross-sectional shape on entry capillary pressure, corner saturation and corner interfacial area were also investigated for a single pore throat. We showed that in addition to shape factor, the shape of cross section (number of vertices) has a significant effect on entry capillary pressure, corner saturation, and arc menisci area. These parameters can be very important in porous media with long pore throats and may contribute significantly to the total pore volume. We have developed an irregular unstructured mixed cross-sectional pore-network model, with the pore bodies in the shape of prolate spheroids and pore throats having a mix of cross sectional shapes described above. The model has been used for simulating drainage and imbibition experiments carried out by *Culligan et al.* (2004) in a glass-bead column. The capability of the pore-network model for simulating a real porous medium has been successfully verified, as we reproduce the measured P^c-S^w and a^{nw}-S^w curves very well. Moreover, grain size distribution inferred from our pore-network model is in close agreement with the measured distribution. We have shown that the inclusion of shape factor distribution and cross-sectional shape in the generation of pore network significantly influence P^c-S^w curves. Depending on the number of vertices of a cross section and volume and length associated with the pore throats, shape factor distribution and cross-sectional shape can significantly influence a^{nw}-S^w curves. Finally, we emphasize that the proposed approach for generating pores cross sections, based on the continuous recovery of shape factor distribution, is essential for the development of predictive pore-network models.

Up to now many dynamic pore-network models fail to simulate capillary-dominated flow or unfavorable conditions, due to the numerical problems. We have developed a DYnamic POre-network model for SImulating Two-phase flow (DYPOSIT) during drainage and imbibition under different dynamic conditions (capillary numbers and viscosity ratios). The combination of features included in this model has not been offered in previous network models. The network elements have square cross sections, as a result of which both phases can be simultaneously present within a pore body or pore throat. Pore throats are represented by parallelepiped, and pore bodies can be represented by truncated octahedron or cube. Local capillary pressure in the pore elements is taken into account. Two different pressure fields are assigned to each phase and solved using a robust algorithm. To improve numerical stability of the model under capillary dominated flow, a semi-implicit algorithm is employed. This allows us to simulate flow dynamics for different flow regimes and viscosity ratios for drainage as well as imbibition.

As a future step, the dynamic pore-network model can be developed to a more realistic representative porous media. Employing the hyperbolic cross sections in the dynamic pore-network models can be a step forward. Furthermore, there are still many complexities and questions in the extended two-phase flow equations that worth to be studied. These can include the effect of fluid and porous medium properties on the behaviour of the involved parameters, effect of averaging operator on them and finally, the effect of size of the domain on the macroscopic behaviour of the the parameters.

Part IV

Appendices

Appendix A

Calculation of Pore Throat Radii

For our sphere-and-tube network, we specify a size distribution for the pore bodies. Then, the radius of a pore throat is determined from the radii of the two neighboring pore bodies. We do this following a scheme adopted from *Acharya et al.* (2004) and explained below.

Consider two pore bodies *i* and *j*, with a center-to-center distance *d* (see Figure A.1a), and pore sizes R_i and R_j, respectively. Along the line connecting the centers of the two nodes, we can define the dimensionless coordinate ξ:

$$\xi = x/d, \quad 0 \leq \xi \leq 1 \tag{A.1}$$

We consider two arbitrary curves with order of $n > 0$, tangent to the pore bodies (see Figure A.1) with the following equations:

$$\rho_1(\xi) = \rho_i(1-\xi)^n, \quad for \quad 0 \leq \xi \leq 1 \tag{A.2}$$

$$\rho_2(\xi) = \rho_j \xi^n, \quad for \quad 0 \leq \xi \leq 1 \tag{A.3}$$

where parameters ρ_i and ρ_j (see Figure A.1b) need to be determined following the procedure explained below. The points of contact of these curves with the pore bodies *i* and *j* are denoted by *a* and *c*, respectively. The points *a* and *c* are determined so that the angle between the radii passing through these points and the horizontal axis is $\pi/4$. The two curves intersect each other at point *b*. The projections of these points on the dimensionless coordinate axis ξ are denoted by $\widetilde{a}$, $\widetilde{b}$ and$\widetilde{c}$ (see Figure A.1b). At point *b*, we have $\rho_1(\widetilde{b}) = \rho_2(\widetilde{b})$. So using Equations A.2 and A.3 we can determine $\widetilde{b}$:

$$\rho_1(1-\widetilde{b})^n = \rho_j \widetilde{b}^n \longrightarrow \widetilde{b} = \frac{(\rho_i/\rho_j)^{1/n}}{1+(\rho_i/\rho_j)^{1/n}} \tag{A.4}$$

We now need to calculate $\rho_\alpha(\alpha = i, j)$. From geometrical considerations, we can write for pore body *i*:

$$\widetilde{a} = \widetilde{R_i}\cos(\pi/4), \rho_1(\widetilde{a}) = \widetilde{R_i}\sin(\pi/4) \tag{A.5}$$

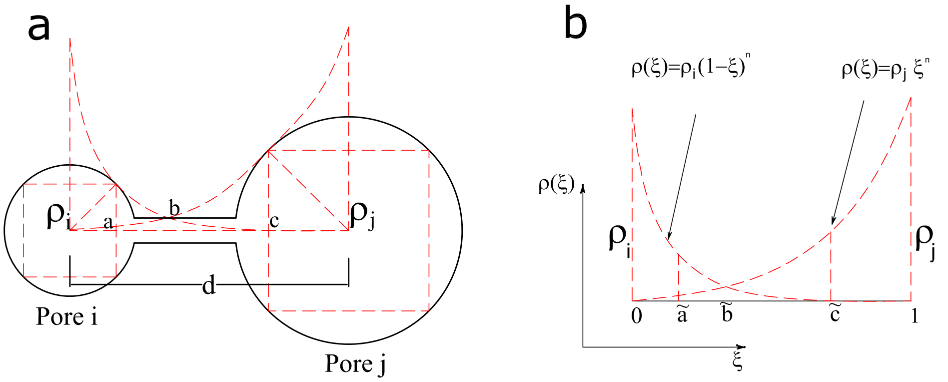

Figure A.1: *Geometrical configuration of relationship between pore body and pore throat radii in sphere-and-tube network a) Geometrical configuration for determining the pore throat radius. b) Schematic definition of functions used for determining the radius of pore throat. Radius of pore throat is determined at intersection of the two curves (point b) using the dimensionless configuration in (b)*

where $\widetilde{R}_\alpha = \widetilde{R}_\alpha/d$ is the dimensionless radius. In addition, from Equation A.3 we can write:

$$\rho_1(\widetilde{a}) = \rho_i(1-\widetilde{a})^n \tag{A.6}$$

Substituting Equation A.5 in Equation A.6, we can calculate ρ_i:

$$\rho_i = \frac{\widetilde{R}_i \sin(\pi/4)}{(1-\widetilde{R}_i \cos(\pi/4))^n} \tag{A.7}$$

In a similar fashion, ρ_j is calculated:

$$\rho_j = \widetilde{R}_j \sin(\pi/4)/(1-\widetilde{R}_j \cos(\pi/4))^n \tag{A.8}$$

Combining Equations A.8, A.3, and A.4, the radius at the intersection point b, which is taken to be the pore throat size, will be given by:

$$\rho(b) = \rho_i\rho_j(\rho_i^{1/n} + \rho_j^{1/n})^{-n}, n > 0 \tag{A.9}$$

Appendix B

Determination of Medial Pixels

Our approach for identifying medial pixels is explained in three parts. First, the micro-model domain decomposition is introduced. Then, the distance transform (**DT**) is explained, and finally a flow operator, which is used for determining the medial pixels, is covered.

a) Micro-model domain decomposition Let $\Omega_t \in \mathbb{R}^2$ include all pixels existing in the micro-model domain including solid domain $\Omega_s \in \mathbb{R}^2$ and void domain $\Omega_v \in \mathbb{R}^2$. Void domain can include two different phase domains: nonwetting phase $\Omega_{nw} \in \mathbb{R}^2$ and wetting phase $\Omega_w \in \mathbb{R}^2$. Thus, we may write:

$$\Omega_v := \Omega_{nw} \cup \Omega_w \tag{B.1}$$

$$\Omega_t := \Omega_v \cup \Omega_s := \Omega_{nw} \cup \Omega_w \cup \Omega_s \tag{B.2}$$

As a short-hand notation, we can write:$\Omega_t := \bigcup \Omega_\alpha \, : \, \alpha = w, nw, s$. Each pixel i, shown as P_i^α, belongs to a domain α. In a two-dimensional domain, P_i^α can have a maximum of eight neighbors which belong to domain α. The set of those pixels neighboring P_i^α and belonging to the domain α, is denoted by $\mathbb{N}_i^\alpha$. In addition, total number of elements of set $\mathbb{N}_i^\alpha$ is denoted by $|\mathbb{N}_i^\alpha|$.

Thus, boundary pixels for the domain α can be identified as follows:

$$\partial\Omega_\alpha := \{P_i^\alpha \in \Omega_\alpha : |\mathbb{N}_i^\alpha| < 8\}, \alpha = nw, w, s \tag{B.3}$$

For example, pixel P_0 is not a boundary pixel in Figure B.1(a), but in Figure B.1(b) it is a boundary pixel.

b) Distance transform Let the Euclidean distance between the centers of two pixels P_i^α and P_j^α be denoted by $d(P_i^\alpha, P_j^\alpha)$. Distance tranform, **DT**, is calculated as the minimum Euclidean distance between the center of a pixel in the void domain and pixels of solid boundary.

$$DT(P_i^v) = \min\{d(P_i^v, P_j^s) : \forall P_j^s \in \partial\Omega_s\} \tag{B.4}$$

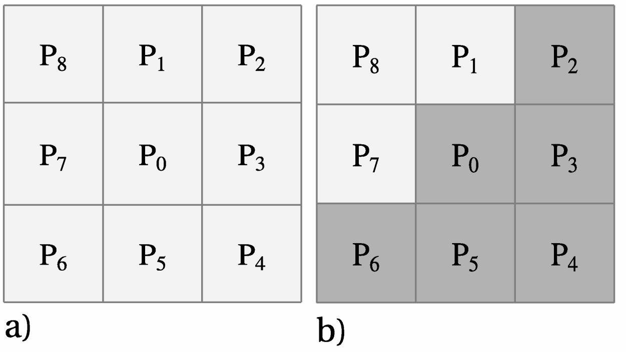

Figure B.1: *Definition of a boundary pixel, a)*P_0^α *is not a boundary pixel* $|\mathbb{N}_i^\alpha| = 8$ *b)*P_0^α *is a boundary pixel,*$|\mathbb{N}_i^\alpha| = 5 < 8$*, colors show the arbitrary phases.*

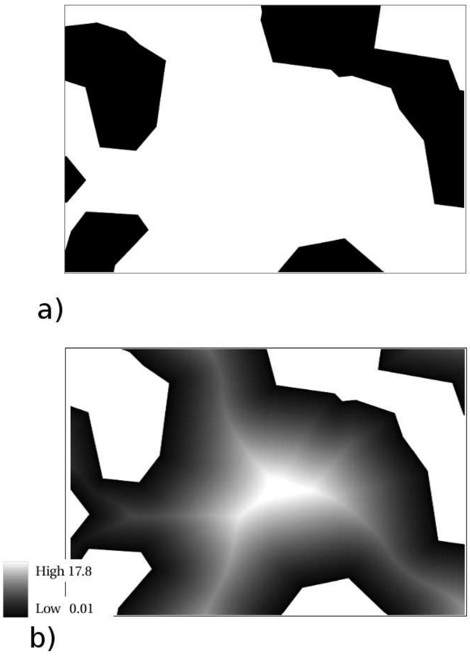

Figure B.2: *a) Binary presentation of a porous medium, black is the solid domain and white is the void domain b) Spatial distribution of the distance transform*

Result of distance transformation for a given void domain (e.g. Figure B.2a) will be a distance map as shown in Figure B.2(b). In this figure, pixels with a larger distance from the nearest solid boundary pixels are shown in a brighter color.

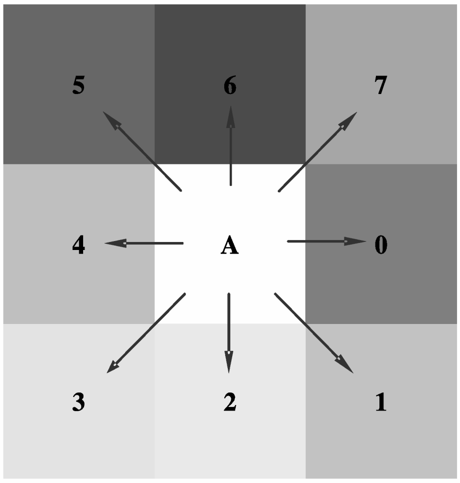

Figure B.3: *Direction numbering for flow operator; the same color code is used in Figure B.4 and B.5.*

c) Flow operator Within the distance map, each pixel located in the void domain will have a distance value larger than zero. If we assign this value as the height of that pixel, we can create a mountain chain. The ridge of mountain chain is the locus of pixels with the largest **DT** value (i.e. the largest distance from solid boundary). To determine pixels located on the ridge, a flow operator is defined. Flow operator, **F**, is used to determine the direction (*DIR*) of maximum downward slope between the centers of a pixel and its neighboring pixels (*Jensen and Domingue*, 1988). Since each pixel of void domain has at most eight neighbors in the void domain, there will be a maximum of eight possible directions as shown in Figure B.3. Flow operator can be written as follows:

$$\mathbf{F}(P_i^v) = DIR(\max\{\frac{DT(P_i^v) - DT(P_j^v)}{d(P_i^v - P_j^v)} : j \in \mathbb{N}_i^v\}) \tag{B.5}$$

Let the complete set of $\mathbf{F}(P_i^v)$ consisting of non-repeating members be denoted by $\mathbb{F} := \{0, 1, 2, 3, 4, 5, 6, 7\}$ and its cardinality,$|\mathbb{F}|$, is of maximum eight. For example, Figure B.4(b) shows the flow operator implemented on a hypothetical distance map presented in Figure B.4(a). In this figure, pixel (4,2), for example has three different types of neighbors, namely 2, 6, and 7; thus $\mathbb{F}_{(4,2)} := \{2, 6, 7\}$ and $|\mathbb{F}_{(4,2)}| = 3$. All pixels with a common flow direction form a direction cluster; e.g. there are four direction clusters in Figure B.4(b), each designated with its own color. This color code is used in examples shown in Figures B.3 to B.5. Thus, flow operator, **F**, creates

index	1	2	3	4	5	6	7	8	9
1	13.37	13.28	13.20	13.08	12.88	12.69	12.52	12.35	12.20
2	13.77	13.68	13.60	13.43	13.24	13.06	12.89	12.73	12.58
3	14.16	14.08	13.98	13.79	13.60	13.42	13.26	13.10	12.96
4	14.16	14.08	13.98	13.87	13.77	13.68	13.59	13.48	13.34
5	13.77	13.68	13.59	13.48	13.37	13.28	13.20	13.09	12.98
6	13.37	13.28	13.20	13.09	12.98	12.89	12.80	12.70	12.59
7	12.98	12.89	12.80	12.70	12.59	12.49	12.41	12.31	12.20

a)

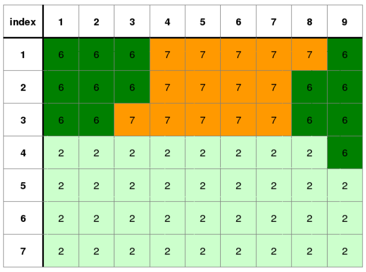

index	1	2	3	4	5	6	7	8	9
1	6	6	6	7	7	7	7	7	6
2	6	6	6	7	7	7	7	6	6
3	6	6	7	7	7	7	7	6	6
4	2	2	2	2	2	2	2	2	6
5	2	2	2	2	2	2	2	2	2
6	2	2	2	2	2	2	2	2	2
7	2	2	2	2	2	2	2	2	2

b)

Figure B.4: *An example: a) Spatial distribution of distance transform b) Result of flow operator based on distribution in (a)*

durection clusters (i.e. clusters of pixels with a common flow direction). Each cluster will be bounded by its boundary pixels. These pixels may see solid boundary pixels in their neighboring cells (e.g. close circles in Figure B.5) or may see more than one type of other clusters in their neighboring cells (e.g. open circles in Figure B.5). Finally, using a search algorithm, it is possible to find the medial pixels (e.g. the dashed path crossing through the open circles in Figure B.5).

Due to the variability of the pore width in the domain, image analysis should be done at such a resolution that pixel size is smaller than the minimum pore width. The finer the discretization of the domain is, the more precise the pore network will be. In our study, each pixel has a size of 0.3μm. Sensitivity analysis, based on the P^c-S^w curves has shown that this resolution is in acceptable range for generation of the pore network model.

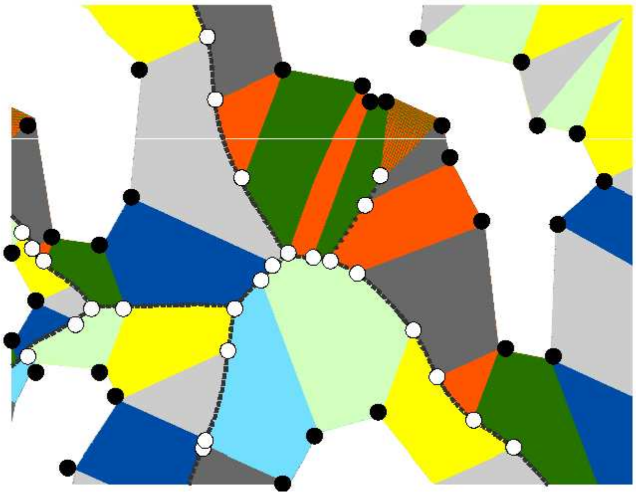

Figure B.5: *Result of flow operator for domain presented in Figure B.2, dashed path represents medial path required for the simulation. Close circles show those cluster boundary pixels, neighboring solid domain pixels. Open circles show cluster boundary pixels, where at least three different clusters are neighboring each other.*

Appendix C

Balance of Forces for an Interface

Calculation of entry capillary pressure for various cross sections is based on the MS-P (*Mayer-Stowe-Princen*) method, suggested by *Ma et al.* (1996), *Mayer and Stowe* (1965), *Princen* (1969a,b, 1970), which follows from the balance of forces for contact lines. When the nonwetting phase invades a tube with an angular cross section, the wetting phase remains behind in the corners along the tube. The longitudinal curvature of the resulting fluid-fluid interface inside the tube is zero. For a regular hyperbolic polygonal cross section, let radius of curvature of the interface within the cross section be denoted by r_c (see Figure C.1). Then, the entry capillary pressure is equal to:

$$P_e^c = P^n - P^w = \frac{\sigma^{nw}}{r_c} \tag{C.1}$$

in which, P^n is pressure of the nonwetting phase, and P^w is the pressure of the wetting phase. Now, consider an *nw*-interface formed at the entrance of the tube. This interface will move into the tube (i.e. nonwetting phase invades the tube) only if the entry capillary pressure given by Equation C.1 is reached. At that instance, the

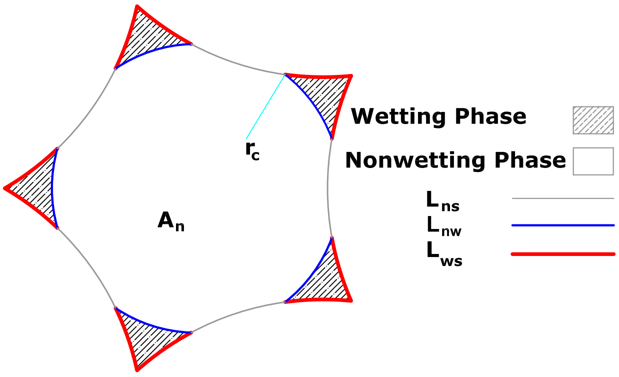

Figure C.1: *A typical regular hyperbolic polygonal cross section filled with the wetting and nonwetting phases. The nonwetting-wetting interface has a radius of curvature denoted by* r_c *and the nonwetting area is denoted by* A_n.

following balance of forces for the interface can be written:

$$(P^n - P^w)A_n = L_{nw}\sigma^{nw} + L_{ns}\sigma^{ns} - L_{ns}\sigma^{ws} \tag{C.2}$$

where A_n is that part of a cross section filled with nonwetting phase, L_{ns} is the total length of solid-fluid-fluid contact line, L_{nw} is the total length of arc cut through the fluid-fluid interface in the corners.

From Young equation, we have the following relationship:

$$\sigma^{ns} = \sigma^{nw} cos\theta + \sigma^{ws} \tag{C.3}$$

Substituting Equation C.3 in Equation C.2 will result in:

$$(P^n - P^w)A_n = \sigma^{nw}(L_{nw} + L_{ns}\cos\theta) \tag{C.4}$$

Combination of Equations C.1 and C.4 results in:

$$\frac{L_{nw} + L_{ns}\cos\theta}{A_n} = \frac{1}{r_c} \tag{C.5}$$

In Equation C.5, L_{nw} and L_{ns} depend on cross-sectional geometry and also fluid occupancy. Geometrical relationships between these terms and r_c should be calculated for each cross-sectional group separately as shown in Section 5.2.2.

Appendix D

Entry Capillary Pressure for a Rectangular Cross Section

In this appendix, the equation for entry capillary pressure of a tube with rectangular cross section is derived. In a rectangular cross section with the corner angle of $\pi/2$ and contact angle of θ, we consider the half corner angle as shown in Figure 4.3. Then, we can write the following geometrical relations:

$$AH = \sqrt{2}\cos(\pi/4+\theta)r_c \tag{D.1}$$

To calculate the area covered by the nonwetting phase,A^{nw}, we need to substitute the areas of the four corners filled by the wetting phase for the rectangular area,ab, First, area of half-corner triangle will be:

$$s_{\triangle AHO} = (\sqrt{2}/2)r_c^2\cos(\pi/4+\theta)\cos\theta \tag{D.2}$$

Area of ANH is calculated as follows:

$$S_{AHN} = (\sqrt{2}/2)r_c^2\cos(\pi/4+\theta)\cos\theta - 0.5r_c^2(\pi/4-\theta) \tag{D.3}$$

Considering the total area of a rectangular, $S = ab$, total area of nonwetting fluid is:

$$A^{nw} = ab - 4r_c^2[\sqrt{2}\cos(\pi/4+\theta)\cos\theta - (\pi/4-\theta)] \tag{D.4}$$

In addition, we will have:

$$L_{nw} = 8r_c(\pi/4-\theta) \tag{D.5}$$

$$L_{ns} = 2(a+b) - 8\sqrt{2}\cos(\pi/4+\theta)r_c \tag{D.6}$$

Substituting Equations D.4, D.5 and D.6 in Equation C.5 will result:

$$\frac{8(\pi/4-\theta)r_c + [2(a+b) - 8\sqrt{2}\cos(\pi/4+\theta)r_c]\cos\theta}{ab - 4r_c^2[\sqrt{2}\cos(\pi/4+\theta)\cos\theta - (\pi/4-\theta)]} = \frac{1}{r_c} \tag{D.7}$$

This equation can be solved for r_c to obtain:

$$r_c = \frac{-(a+b)\cos\theta + \sqrt{(a+b)^2\cos^2\theta + 4ab[\frac{\pi}{4} - \theta - \sqrt{2}\cos(\frac{\pi}{4}+\theta)\cos\theta]}}{4(\frac{\pi}{4} - \theta - \sqrt{2}\cos(\frac{\pi}{4}+\theta)\cos\theta)} \tag{D.8}$$

Finally, entry capillary pressure can be calculated using Equations C.1 and C.1.

Appendix E

Geometry of Hyperbolic Polygons

E.1 Irregular hyperbolic triangles

For a set of *Soddy circles* shown in Figure 5.2(a), the inscribed radius, R, can be determined based on the radii of the three tangent circles.

$$R = \frac{R_1 R_2 R_3}{R_1 R_2 + R_2 R_3 + R_1 R_3 + 2\sqrt{R_1 R_2 R_3 (R_1 + R_2 + R_3)}} \tag{E.1}$$

The area of the $\triangle ABC$ may be written as follows:

$$A_{\triangle ABC} = \sqrt{R_1 R_2 R_3 (R_1 + R_2 + R_3)} \tag{E.2}$$

On the other hand, using laws of sines in $\triangle ABC$, we can write the following three equations:

$$\begin{gathered} \frac{R_1 + R_2}{\sin\gamma} = \frac{R_2 + R_3}{\sin\alpha} = \frac{R_1 + R_3}{\sin\beta} = \frac{(R_1 + R_2)(R_2 + R_3)(R_1 + R_3)}{2\sqrt{R_1 R_2 R_3 (R_1 + R_2 + R_3)}} \\ \alpha + \beta + \gamma = \pi \end{gathered} \tag{E.3}$$

The area and perimeter of the irregular hyperbolic triangle, the hatched part of Figure 5.2(a), is denoted by as $A_{hatched}$ and $P_{hatched}$, respectively. They can be written:

$$A_{hatched} = \sqrt{R_1 R_2 R_3 (R_1 + R_2 + R_3)} - 0.5(R_1^2\alpha + R_2^2\beta + R_3^2\gamma) \tag{E.4}$$

$$P_{hatched} = R_1\alpha + R_2\beta + R_3\gamma \tag{E.5}$$

Finally, the shape factor, G, can be calculated, as:

$$G = \frac{\sqrt{R_1 R_2 R_3 (R_1 + R_2 + R_3)} - 0.5(R_1^2\alpha + R_2^2\beta + R_3^2\gamma)}{(R_1\alpha + R_2\beta + R_3\gamma)^2} \tag{E.6}$$

For given values of G and R, we can solve Equations E.1,E.3 and E.6 numerically, using *Newton-Raphson* method, to calculate R_1,R_2, R_3, α, β, and γ.

E.2 Regular hyperbolic polygons

To relate the shape factor to geometry of a cross section, the area and perimeter should be calculated. The area of the *n*-hyperbolic polygon ($B_1..B_n$) in Figure 5.2(b) can be calculated as follows:

$$A_{B_1..B_n} = A_{A_1..A_n} - n \times A_{\triangle A_1 A_2 B_1} - n \times A_{\triangleleft A_2 B_1 B_2} \tag{E.7}$$

Because $\angle A_2 B_1 O = \pi/2 + \varphi$ and $\phi = \pi/n$, we obtain:

$$\beta = \pi(\frac{1}{2} - \frac{1}{n}) - \varphi \tag{E.8}$$

In addition, we note that $\tan\phi = \tan\frac{\pi}{n} = \frac{R_1 \sin\beta}{R + R_1(1-\cos\beta)}$, which results in:

$$R_1 = R\frac{\sin\frac{\pi}{n}}{\cos\varphi - \sin\frac{\pi}{n}} \tag{E.9}$$

The area of a n-polygon, with edge length s is:

$$A_{A_1..A_n} = \frac{n}{4}s^2 \cot\pi/n = nR_1^2\cos^2\varphi\cot\frac{\pi}{n} \tag{E.10}$$

and the areas of $\triangle A_1 A_2 B_1$ and $\triangleleft A_2 B_1 B_2$ may be written as follows, respectively:

$$A_{\triangle A_1 A_2 B_1} = 0.5R_1^2 \sin 2\varphi \tag{E.11}$$

$$A_{\triangleleft A_2 B_1 B_2} = R_1^2\beta \tag{E.12}$$

Using Equations E.9, E.10,E.11, and E.12, Equation E.7 may be written as:

$$A_{B_1..B_n} = \frac{nR^2\sin^2\frac{\pi}{n}}{(\cos\varphi - \sin\frac{\pi}{n})^2}\left[\cos^2\varphi\cot\frac{\pi}{n} - \pi(\frac{1}{2} - \frac{1}{n}) + \varphi - 0.5\sin 2\varphi\right]. \tag{E.13}$$

Then, the perimeter of a *n*-hyperbolic polygon is obtained from:

$$P_{B_1..B_n} = 2nR\frac{\sin\frac{\pi}{n}}{\cos\varphi - \sin\frac{\pi}{n}}[\pi(\frac{1}{2} - \frac{1}{n}) - \varphi] \tag{E.14}$$

Based on Equations E.13 and E.14, the shape factor can be written as follows:

$$G = \frac{A}{P^2} = \frac{\cos^2\varphi\cot\frac{\pi}{n} - \pi(\frac{1}{2} - \frac{1}{n}) + \varphi - 0.5\sin 2\varphi}{4n[\pi(\frac{1}{2} - \frac{1}{n}) - \varphi]^2} \tag{E.15}$$

For given values of n and G, Equation E.15 can be solved numerically to calculate φ and subsequently the geometry of the cross section will be define from Equation E.9.

Appendix F

Entry Capillary Pressure for a Hyperbolic Cross Section

F.1 Irregular hyperbolic triangles

Consider the vertex *i* of an irregular hyperbolic triangle filled by the wetting phase, shown in Figure F.1. We need to calculate the area of the wetting phase in the corner as well as the length of nonwetting-wetting interface. Let ε_j^i denote the angle made by the tangent at vertex i and line connecting vertex i to the intersection of interface with edge j (e.g. line BN or BN' in Figure F.1). Also, let ε^i denote the angle between the tangent to the interface at its intersection with the edge i and the line connecting both ends of the interface (line NN' in Figure F.1). Then in the triangle $\triangle BNN'$, we can write:

$$\varepsilon^i + \varepsilon_1^i + \varepsilon_2^i = \frac{\pi}{2} - \theta, (i = 1, 2, 3) \tag{F.1}$$

, where θ is the fluid-fluid-solid contact angle.

Based on law of sines, we have:

$$\frac{\overline{BN}}{\sin(\varepsilon^i + \varepsilon_2^i + \theta)} = \frac{\overline{BN'}}{\sin(\varepsilon^i + \varepsilon_1^i + \theta)} = \frac{\overline{NN'}}{\sin(\varepsilon_1^i + \varepsilon_2^i)} \tag{F.2}$$

Radii of arcs BN, BN', and NN are R_1, R_2, and r_c, respectively. Since angles $\angle N'ON$, $\angle ABN$, and $\angle BA'N'$ are denoted by ε^i, ε_1^i, ε_2^i, respectively, we may rewrite Equation F.2, as follows:

$$R_1 \tan\varepsilon_1^i = R_2 \tan\varepsilon_2^i = \frac{r_c \sin\varepsilon^i}{\cos(\theta + \varepsilon^i)}, i = 1, 2, 3 \tag{F.3}$$

Now, the area of the wetting phase (hatched part in Figure F.1(b)) should be calculated. That is equal to the area of the triangle BNN' minus the total areas of the circular segments created by chords BN, BN', and NN', denoted by A_{BN}^{cs}, $A_{BN'}^{cs}$,

$A^{cs}_{NN'}$, respectively:

$$A^i_w = A_{\triangle BNN'} - A^{cs}_{BN} - A^{cs}_{BN'} - A^{cs}_{NN'} \tag{F.4}$$

With some manipulation, we can write the following equation for A^i_w.

$$\begin{aligned} A^i_w = 2r_cR_1 \sin\varepsilon^i \sin\varepsilon^i_1 \cos\varepsilon^i_2 \quad & -R^2_1(\varepsilon^i_1 - 0.5\sin 2\varepsilon^i_1) \\ & -R^2_2(\varepsilon^i_2 - 0.5\sin 2\varepsilon^i_2) \\ & -r^2_c(\varepsilon^i - 0.5\sin 2\varepsilon^i) \end{aligned} \tag{F.5}$$

Next, the area of that part of pore throat cross section filled by the nonwetting phase (A_n in Figure F.1) can be calculated by subtracting the total wetting phase area from the pore cross-sectional area (given by Equation E.4), $A_{hatched}$:

$$A_n = A_{hatched} - \sum_{i=1}^{3} A^i_w \tag{F.6}$$

Total length of the nonwetting-wetting interface, L_{nw}, would be estimated simply as follows:

$$L_{nw} = 2r_c \sum_{i=1}^{3} \varepsilon^i \tag{F.7}$$

Using Equation E.5 and considering the geometry given in Figure F.1, the length of the nonwetting-solid interface can be calculated.

$$L_{ns} = R_1\alpha + R_2\beta + R_3\gamma - 2\sum_{i=1}^{3}\left(R_i\varepsilon^i_i + R_i\varepsilon^{i-1}_i\right), \varepsilon^0_1 = \varepsilon^3_1 \tag{F.8}$$

Substituting Equations F.6, F.7, and F.8 in Equation C.5 results in a new equation, which relates all $\varepsilon^i_j|i = 1,2,3, j = 1,2$ and $\varepsilon^i|i = 1,2,3$ to the radius of curvature of the interface r_c. Te resulting equation, together with Equations F.1 and F.3, can be solved numerically to calculate r_c. Subsequently, it is possible to calculate the entry capillary pressure from Equation C.1.

F.2 Regular hyperbolic polygons

The procedure for calculation of entry capillary pressure for a regular hyperbolic polygonal cross section, is similar to the method used for regular hyperbolic polygonal cross sections. There are few differences in geometry that should be taken into consideration. Considering Figure F.1(c), since the geometry is regular, $R_1 = R_2 = .. = R_n$. Therefore, all $\varepsilon^i_j = \varepsilon'$, ($j = 1, 2, i = 1, 2, .., n$) are equal and denoted by ε'. In addition, $\angle NBN'$ in Figure F.1(c) will be equal to $2(\varepsilon' + \varphi)$. The angle ε' is referred to the angle made by the tangent at a vertex and line connecting the vertex to the intersection of interface and edge. For $\triangle BNN'$ we can write $2\varepsilon' + \varepsilon = \frac{\pi}{2} - \theta - \varphi$. Based on the law of sines in $\triangle BNN'$ we may write:

$$\frac{r_c \sin\varepsilon}{\sin 2(\varphi + \varepsilon')} = \frac{R_1 \sin\varepsilon'}{\sin(\varepsilon + \varepsilon' + \theta)}, \quad 2\varepsilon' + \varepsilon = \frac{\pi}{2} - \theta - \varphi \tag{F.9}$$

Next, for the area of the wetting phase, A^i_w, we can write:

$$\begin{aligned} A^i_w = 2r_c R_1 \sin\varepsilon \sin\varepsilon' \cos(\varepsilon' + \varphi) \quad & -2R_1^2(\varepsilon' - 0.5\sin 2\varepsilon') \\ & -r_c^2(\varepsilon - 0.5\sin 2\varepsilon) \end{aligned} \tag{F.10}$$

Knowing the area of a regular hyperbolic cross section from Equation E.13, $A_{B_1..B_n}$, the area of the nonwetting phase in this cross section can be calculated as follows:

$$A_n = A_{B_1..B_n} - nA^i_w \tag{F.11}$$

The total length of the nonwetting-wetting interface,L_{nw} , is simply given by:

$$L_{nw} = 2nr_c\varepsilon \tag{F.12}$$

According to Equation E.14, the total length of L_{ns} is given by:

$$L_{ns} = P_{B_1..B_n} - 4nR_1\varepsilon' \tag{F.13}$$

Substituting Equations F.11, F.12, and F.13 in Equation C.5 results in a new equation, which relates ε' and ε to the radius of curvature of the interface r_c. The resulting equation and Equation F.9 can be solved numerically to calculate r_c. Finally, the entry capillary pressure is calculated from Equation C.1.

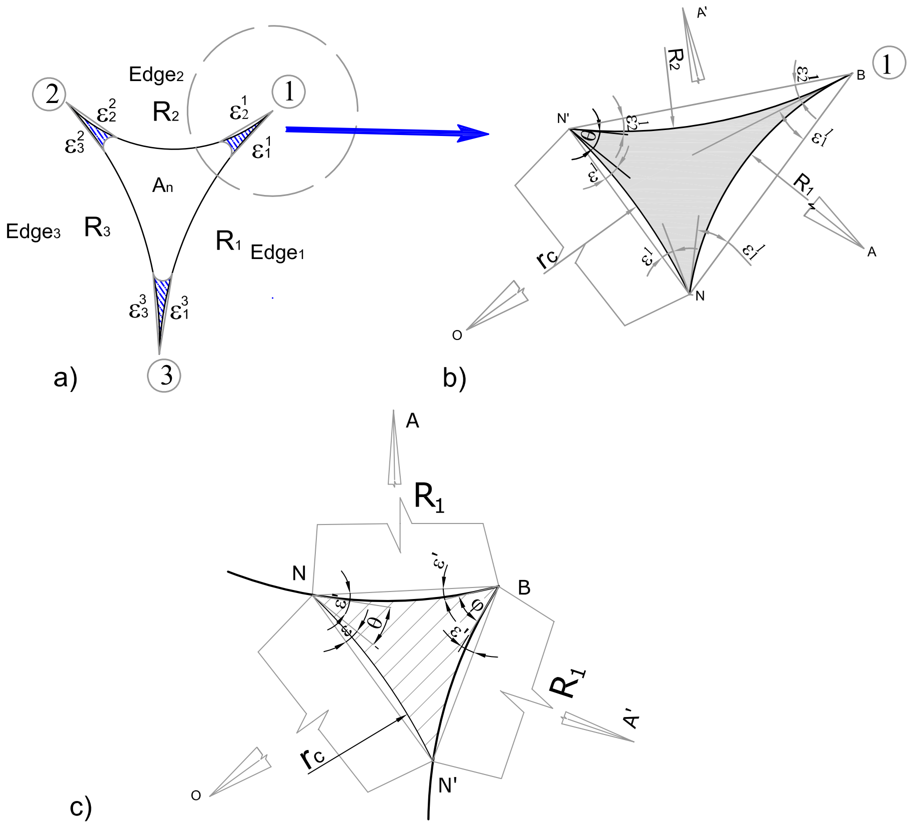

Figure F.1: *a) Schematic presentation of interfaces in an irregular hyperbolic triangle b) Geometry of an interface and wetting phase in vertex 1. Center of the arcs with radii R_1, R_2, and r_c are denoted by A, A', and O, respectively (see also Figure 5.2(a)). The angle ε_j^i is referred to the angle made by the tangent at vertex i and line connecting vertex i to the intersection of interface with edge j. The angle ε^i is referred to the angle between the tangent to the interface at its intersection with the edge i and the line connecting both ends of the interface. c) Geometry of a fluid-fluid interface and the wetting phase in the vertex of a regular hyperbolic polygon. The geometry is defined by half corner angle, φ, contact angle, θ, interface radius of curvature, r_c, inscribed radius R, and edge radius of curvature, R_1 (see also Figure 5.2(b))*

Table F.1: *Formulas for A_n, L_{ns} and L_{nw} for different cross sections.*

Irregular Hyperbolic Triangle	Regular Hyperbolic Polygon
$A_n = \sqrt{R_1 R_2 R_3 (R_1 + R_2 + R_3)}$	$A_n = \frac{nR^2 \sin^2 \frac{\pi}{n}}{(\cos\varphi - \sin\frac{\pi}{n})^2} \left[\cos^2\varphi \cot\frac{\pi}{n} - \pi(\frac{1}{2} - \frac{1}{n}) + \varphi - 0.5\sin 2\varphi\right]$
$-0.5(R_1^2\alpha + R_2^2\beta + R_3^2\gamma)$	$-2nr_c R_1 \sin\varepsilon \sin\varepsilon' \cos(\varepsilon' + \varphi)$
$-\sum_{i=1}^{3} \left[2r_c R_i \sin\varepsilon^i \sin\varepsilon_i^i \cos\varepsilon_{i+1}^i\right]$	$+2nR_1^2(\varepsilon' - 0.5\sin 2\varepsilon')$
$+\sum_{i=1}^{3} \left[R_i^2(\varepsilon_i^i - 0.5\sin 2\varepsilon_i^i)\right]$	$+nr_c^2(\varepsilon - 0.5\sin 2\varepsilon)$
$+\sum_{i=1}^{3} \left[R_{i+1}^2(\varepsilon_{i+1}^i - 0.5\sin 2\varepsilon_{i+1}^i)\right]$	
$+\sum_{i=1}^{3} \left[r_c^2(\varepsilon^i - 0.5\sin 2\varepsilon^i)\right]$,	
$(\varepsilon_4^3 = \varepsilon_1^3, R_4 = R_1)$	
$L_{ns} = R_1\alpha + R_2\beta + R_3\gamma$	$L_{ns} = 2nR\frac{\sin\frac{\pi}{n}}{\cos\varphi - \sin\frac{\pi}{n}}[\pi(\frac{1}{2} - \frac{1}{n}) - \varphi] - 4nR_1\varepsilon'$
$-2\sum_{i=1}^{3}\left(R_i\varepsilon_i^i + R_i\varepsilon_i^{i-1}\right), (\varepsilon_1^0 = \varepsilon_1^3)$	
$L_{nw} = 2r_c\sum_{i=1}^{3}\varepsilon^i$	$L_{nw} = 2nr_c\varepsilon$

Appendix G

p_i^c-s_i^w Relationship for a Cubic Pore Body

Consider a cube with its inscribed sphere radius equal to R_i; so the edge length is equal to $2R_i$. If the nonwetting phase volume is larger than the volume of inscribed sphere (i.e. $s^w_{insc.} \leq 1 - \frac{\pi}{6} = 0.48$), the fluid interfaces are pinned into the corners. However, for $s^w_{insc.} > 1 - \frac{\pi}{6} = 0.48$, they are not pinned into the corners. Therefore, for the variation of local capillary pressure with saturation, we identify two different zones as shown in figure G.3, and described below.

G.1 Capillary pressure for $0 < s_i^w \leq 0.48$ (zone I)

In a cube, interfaces can be formed along its 12 edges as well as in its 8 corners as shown in figure G.1. Edge interfaces form part of a cylindrical surface. Therefore, they have only one finite radius of curvature. Corner interfaces form part of a spherical surface and thus, have two identical finite curvatures. Assuming a contact angle of zero, edge interfaces form one fourth of a cylinder whereas corner interfaces are one eighth of a sphere (see figure G.1). Let us denote the radius of curvature of corner interfaces by $rc_{i,1}$. Then, the total volume of the wetting phase in the corners

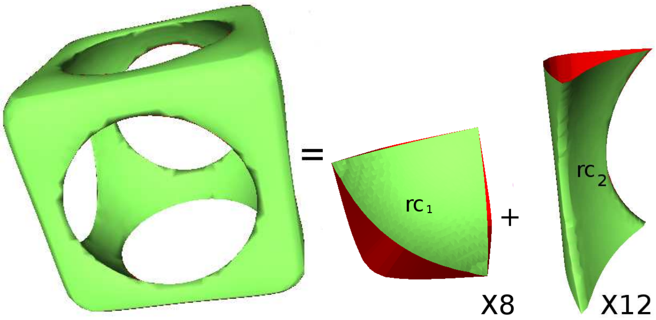

Figure G.1: *A pore body occupied by the nonwetting phase (in the middle) and the wetting phase in corners and edges. There are wetting-nonwetting interfaces in 8 corners with mean radius of* $rc_{i,1}$ *and in 12 edges with mean radius of* $rc_{i,2}$.

would be equal to the volume of a cube with dimensions $2rc_{i,1}$ minus the volume of a sphere with radius $rc_{i,1}$:

$$V^w_{corner} = (8 - \frac{4}{3}\pi)rc^3_{i,1} \tag{G.1}$$

Length of an edge interface is equal to the cube size, $2R_i$, minus two times the radius of corner interfaces:

$$L_{edge} = 2(R_i - rc_{i,1}) \tag{G.2}$$

Thus, if we denote the radius of curvature of an edge interface by $rc_{i,2}$, the total volume of wetting phase in the edges will be:

$$V^w_{edge} = 12L_{edge}rc^2_{i,2}(1 - \frac{\pi}{4}) \tag{G.3}$$

Total volume of wetting phase in the pore body is thus obtained by summing (G.1) and (G.3):

$$V^w_i = (8 - \frac{4}{3}\pi)rc^3_{i,1} + 24(R_i - rc_{i,1})rc^2_{i,2}(1 - \frac{\pi}{4}) \tag{G.4}$$

Since we assume that the capillary pressure in a pore body is the same everywhere, the capillary pressures of edge and corner interfaces must be equal. Thus, $p^c_i = \frac{2\sigma^{nw}}{rc_{i,1}} = \frac{\sigma^{nw}}{rc_{i,2}}$, which gives $rc_{i,1}$ and $rc_{i,2}$ in terms of p^c_i. Substituting for $rc_{i,1}$ and $rc_{i,2}$ in (G.4) and dividing both sides by the total volume of the cubic pore body, $8R^3_i$, we obtain the following p^c_i-s^w_i relationship for a pore body if $s^w_i \leq 0.48$:

$$s^w_i = \frac{(2 + \frac{1}{6}\pi)(\frac{2\sigma^{nw}}{p^c_i})^3 + (6 - \frac{3}{2}\pi)R_i(\frac{2\sigma^{nw}}{p^c_i})^2}{8R^3_i} \tag{G.5}$$

The case of $rc_{i,1} = R_i$ corresponds to the situation that the nonwetting phase occupies the inscribed circle of the pore body.

G.2 Capillary pressure for $0.48 < s^w_i \leq 1$ (zone II)

When the fluid interfaces are not pinned into the corners, one may choose from the following two approaches:

a) The simplest approach is to assign a constant capillary pressure equal to $2\sigma^{nw}/R_i$ to the pore body if $s^w_i \geq 0.48$ as shown in figure G.3 (the horizontal line in zone II).

b) A second approach is to assume that a capillary pressure varies with saturation. At the moment of invasion of nonwetting fluid into a pore body, the local capillary pressure is close to the (entry) capillary pressure of the pore throat from which the fluid enters th pore body (figure G.2). So, it is larger than the entry capillary pressure of the pore body, which is associated with that of inscribed circle. As the interface moves into the pore body, it will expand and its capillary pressure decreases. We assume that the interface goes through the following stages:

- First, as it enters the pore body, its radius remains unchanged, equal to the radius of the pore throat, r_{ij} (interface 1 in figure G.2(a)). So, for the range $s_i^w \geq 1-\frac{2}{3}\pi(\frac{r_{ij}}{2R_i})^3$, the local capillary pressure will be equal to the entry capillary pressure of the pore throat; $p_i^c = p_{e,ij}^c$.

- From this point on, the radius of interface increases. For a given radius of curvature $rc_{i,1}$, the nonwetting fluid will be present within a truncated sphere, as shown in figure G.2(b). Defining $\widetilde{rc}_{i,1} = rc_{i,1}/2R_i$ and $\widetilde{r}_{ij} = r_{ij}/2R_i$, s_i^w can be calculated as follows:

$$s_i^w = 1 - \frac{\pi}{8}\left(\frac{2}{3}\widetilde{rc}_{i,1}^3 - \widetilde{rc}_{i,1}^2\sqrt{\widetilde{rc}_{i,1}^2 - \widetilde{r}_{ij}^2} + \frac{1}{3}\left(\widetilde{rc}_{i,1}^2 - \widetilde{r}_{ij}^2\right)^{\frac{3}{2}}\right) \qquad \text{(G.6)}$$

and $p_i^c = \frac{2\sigma^{nw}}{rc_{i,1}}$.

- At some point, the interface touches the sides of the pore body cube. Its radius of curvature is then equal to R_i (interface 2 in figure G.2(a)) and wetting phase saturation at this point is obtained from (G.6) by setting $rc_{i,1} = 1$; it is $s_i^w = 1 - \frac{\pi}{12} + \frac{\pi}{8}\sqrt{1-\widetilde{r}_{ij}^2} - \frac{\pi}{24}(1-\widetilde{r}_{ij}^2)^{3/2}$. From this point on, the nonwetting phase is contact with the side walls of pore body (relative to the pore throat) and it continues moving into the pore body, at the constant radius, until it is fully inscribed within the pore body. So, the wetting phase saturation reduces to 0.48. In this range the local capillary pressure remains constant equal to $p_i^c = \frac{2\sigma^{nw}}{R_i}$.

A plot of the local capillary pressure as a function of saturation for these two approaches has been shown in figure G.3. As it can be observed, depending on the size of pore throat, the second approach can result in different p_i^c-s_i^w curves. With the increase of ratio of pore throat to pore body radii, the curves from the two approaches get closer to each other.

G.3 Local p_i^c-s_i^w relationship for the full range of saturation

Finally, to investigate effect of these two assumptions on average behaviour of the model during drainage, a number of simulations were performed, with viscosity ratio set equal to 0.1 and the global pressure difference (P_{global}^c) set to $10kPa$. Change

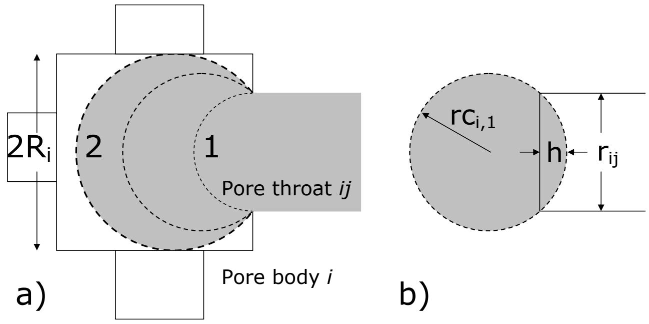

Figure G.2: *a) Expansion of an interface into a pore body before inscribing in it b) Parameterization of the interface for calculating the volume of nonwetting phase, h is the height of dome inside a pore throat (truncated part of the sphere), rc_1 is the radius of the expanding nonwetting sphere, and r_{ij} is the pore throat radius.*

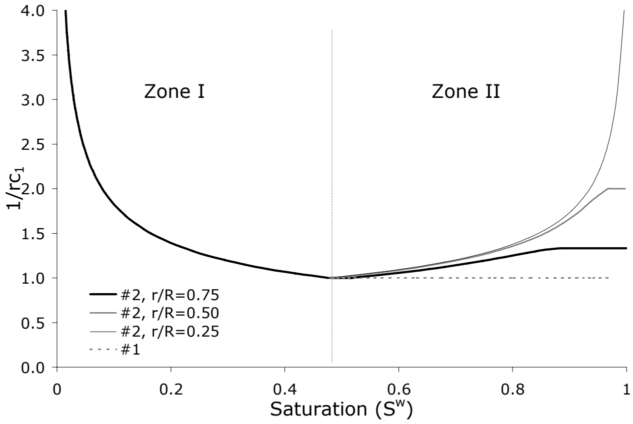

Figure G.3: *Local p_i^c-s_i^w curve during drainage for approach #1 (broken curve) and approach #2 (continuous curves). For approach #2 three different curves for three different aspect ratios have been shown.*

of saturation with time as well as change of average capillary pressure with saturation are shown in figure G.4. As it can be observed the choice of local capillary pressure curve for the range $0.48 \leq s_i^w \leq 1$ is really small. This is due to the fact that only few pores are partially filled in this range. As the simulation with the second approach is more time-consuming (it requires smaller time steps), we have used the curve from the first approach in all simulations in this paper.

The resulting $p_i^c - s_i^w$ curve for the full range of saturation was fitted by the

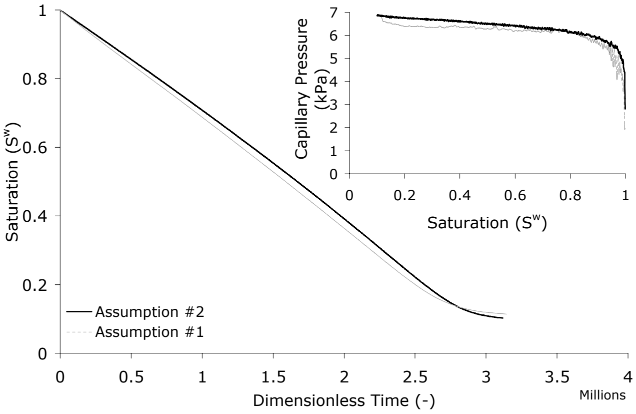

Figure G.4: *Effect of local p_i^c-s_i^w curve on variation of saturation and capillary pressure versus time ($M = 0.1, P^c_{global} = 10kPa$, $\overline{r/R} = 0.45$).*

following continuous function:

$$p_i^c = \frac{2\sigma^{nw}}{R_i(1 - exp(-6.83s_i^w))} \tag{G.7}$$

The radius of curvature of corner interfaces is then approximated by the following formula:

$$rc_{i,1} = \frac{2\sigma^{nw}}{p_i^c} = R_i(1 - exp(-6.83s_i^w)) \tag{G.8}$$

Appendix H

A_i^{nw}-s_i^w Relationship for a Cubic Pore Body

As mentioned earlier, the volume of pore throats is assumed to be negligible compared to the volume of pore bodies. Thus, we neglected saturation of fluids in the pore throats. Similarly, we have not considered the interfacial area present in pore throat corners in our calculations.

There are two different types of capillary interfaces is a pore body, interfaces in corners and edges, and interfaces covering the entrance of pore throats that are not invaded yet. These two types are referred to as "corner interfaces" (arc menisci) and "main terminal menisci", respectively (*Mason and Morrow*, 1987).

H.1 Corner interfaces

Given a pore body with inscribed radius R_i filled with nonwetting and wetting phases, nonwetting phase volume can be smaller or larger than the inscribed sphere volume. If the nonwetting phase volume is smaller than or equal to the volume of inscribed sphere, we assume that it occupies a sphere, whose radius is $R_{i,eq} = R_i(\frac{6}{\pi}(1 - s_i^w))^{1/3}$. The corresponding interfacial area will be $4\pi R_{i,eq}^2$. If the nonwetting phase volume is larger than or equal to the volume of inscribed sphere, the wetting phase occupies geometries that were described in Appendix G. The interfaces will have the mean radius given by (G.8). Therefore, total interfacial area in corners of a pore body will be equal to $4\pi R_{i,eq}^2 + 6\pi R_{i,eq}(R_i - R_{i,eq})$ for nonwetting phase saturations larger than the inscribed sphere. The results are summarized as follows:

$$R_{i,eq} = \begin{cases} R_i(\frac{6}{\pi}(1 - s_i^w))^{1/3} & s_i^w \geq 0.48 \\ R_i(1 - exp(-6.83 s_i^w)) & s_i^w < 0.48 \end{cases} \tag{H.1}$$

$$A_i^{nw} = \begin{cases} 4\pi R_{i,eq}^2 & s_i^w \geq 0.48 \\ 4\pi R_{i,eq}^2 + 6\pi R_{i,eq}(R_i - R_{i,eq}) & s_i^w < 0.48 \end{cases} \tag{H.2}$$

H.2 Main terminal menisci

Consider a pore body *i*, partially occupied by the nonwetting phase, and a pore throat *ij*, which is not invaded yet. Opening of the pore throat *ij* is thus covered by a meniscus, to which we refer to as "main terminal meniscus". The geometry of the main terminal meniscus is simply assumed to be a part of a sphere with a radius of curvature R_{dm} equal to $2\sigma^{nw}/p_i^c$ similar to the interface within the pore throat in figure G.2(b). Thus, the area of the main terminal meniscus will be equal to $8\pi\left(\frac{\sigma^{nw}}{p_i^c}\right)^2\left(1-\sqrt{1-(\frac{r_{ij}p_i^c}{2\sigma^{nw}})^2}\right)$.

Appendix I

Local p_i^c-s_i^w Relationship for an Octahedron Pore Body

I.1 Local p_i^c-s_i^w relationship under drainage

Consider the octahedron shown in Figure 7.1 to be associated with pore body i. As mentioned earlier, the size of a pore body is specified by the radius of inscribed sphere of the octahedron, R_i. So the length of a typical edge O_1A is equal to $\alpha_i = \sqrt{6}R_i$. Total volume of an an octahedron is then given by $V_{oct.hed_i} = \frac{\sqrt{2}}{3}a_i^3 = 4\sqrt{3}R_i^3$. Next, consider the corners to be truncated by pore throats connecting to the pore body. A pore throat ij results in a pyramid with square base and edge length $2r_{ij}$ to be cut off the octahedron (r_{ij} is the radius of inscribed circle of the pore throat). The height of the pyramid will be equal to $\sqrt{2}r_{ij}$.Thus, the volume of the truncated section is equal to $\frac{4\sqrt{2}}{3}r_{ij}^3$. So, the volume of the truncated octahedron forming pore body i is given by:

$$V_i = 4\sqrt{3}R_i^3 - \frac{4\sqrt{2}}{3}\sum_{j\in\mathbb{N}_i} r_{ij}^3 \tag{I.1}$$

During primary drainage, the wetting fluid saturation of a pore body varies from 1 to residual value S_i^{min} specified below. An important intermediate saturation corresponds to the situation that the nonwetting fluid fills up the inscribed sphere of the pore body. Denoted by s_i^{dr}, the corresponding wetting fluid saturation is given by:

$$s_i^{dr} = 1 - \frac{4\pi R_i^3}{3V_i} = 1 - \frac{\pi R_i^3}{3\sqrt{3}R_i^3 - \sqrt{2}\sum_{j\in\mathbb{N}_i} r_{ij}^3} \tag{I.2}$$

For the derivation of local capillary pressure-saturation curves, we identify two different ranges as described below.

I.1.1 Capillary pressure for the range $s_i^{dr} \leq s_i^w \leq 1$ (zone 1)

We assume that the entrance of nonwetting fluid into a pore body and the position of fluid-fluid interface may be idealized by sequences shown in Figure I.1(a). Position 1 shows the moment of invasion of nonwetting fluid into the pore body. The interface has the same radius of curvature as when it was in the pore throat ij and the local capillary pressure is the same as the (entry) capillary pressure of the pore throat, denoted by $p_{e,ij}^c$ (the starting point of p_i^c-s_i^w curve in Figure I.2(a) at $s_i^w = 1$). We assume that as the interface moves into the pore body, its radius remains unchanged until position 2 is reached. At this point, the saturation of nonwetting fluid in the pore body is equal to $\frac{2}{3}\pi\frac{r_{ij}^3}{V_i}$. Thus, for the range $1 \geq s_i^w \geq 1 - \frac{2}{3}\pi\frac{r_{ij}^3}{V_i}$, the local capillary pressure will be constant equal to the entry capillary pressure of the pore throat; $p_i^c = p_{e,ij}^c$ (see the plateau in Figure I.2(a)). As the interface moves into the pore body, it will expand and its capillary pressure decreases (interface 3 in Figure I.1(a)). To simplify the geometry of the interface, we assume that from this saturation onwards, the nonwetting fluid fills up a sphere of increasingly larger radius until it fills up the inscribed sphere of the pore body, at which point the wetting fluid saturation is s_i^{dr} given by Equation I.2.

If the radius of such an intermediate sphere is r_i^c, then the wetting fluid saturation in this range is given by the following relation:

$$s_i^w = 1 - \frac{4\pi r_i^{c3}}{3V_i} \tag{I.3}$$

In this range, as r_i^c increases, the local capillary pressure, given by $p_i^c = 2\sigma^{nw}/r_i^c$ decreases until s_i^{dr} is reached (see Figure I.2).

The irregular shape of the resulting curves is approximated by the following formula for the range 1 to s_i^{dr} for sake of computational efficiency.

$$s_i^w = s_i^{dr} + (1 - s_i^{dr})\frac{1 - s_i^{dr} - \frac{4\pi r_i^{c3}}{3V_i}}{1 - s_i^{dr} - \frac{4\pi r_{ij}^3}{3V_i}} \tag{I.4}$$

I.1.2 Capillary pressure for the range $0 < s_i^w \leq s_i^{dr}$ (zone 2)

Once the nonwetting fluid fills the inscribed sphere, and after that, the wetting fluid will be present only along the edges of the pore body. So, interfaces will be formed along pore body's 12 edges as well as in the opening of pore throats not invaded by the nonwetting fluid yet. The latter interfaces are formed in the vertices of the truncated octahedron (where non-invaded pore throats are connected). Edge and vertex interfaces are shown in Figures I.1(b) and (d), respectively.

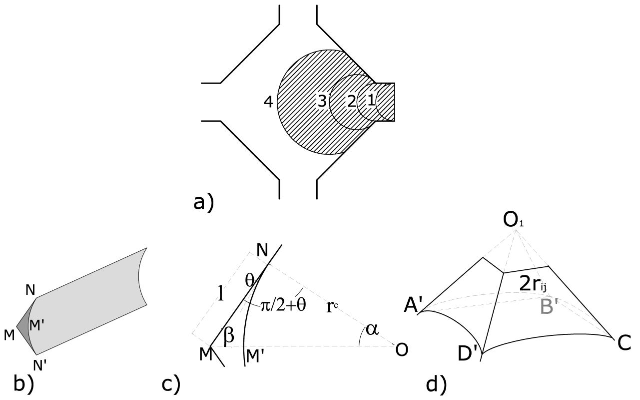

Figure I.1: *Schematic presentation of interfaces in a pore body a) Expansion of an interface into a pore body before filling the inscribed sphere b) and c) Interface geometry along the edges d) Interface geometry in a vertex of pore body when the corresponding pore throat is filled with wetting phase.*

Edge interfaces form part of a cylinder (with only one finite radius of curvature), and vertex interfaces form part of a spherical surface. When all pore throats have been invaded by the nonwetting fluid, there will be no vertex interface in a pore body.

Let the radius of edge interfaces be denoted by r_i^c. We assume that the radius of curvature of interfaces along the edges is negligible compared r_i^c. As shown in Figure I.1(b), we denote the half corner angle of all edges by β and half angle of interfaces by α. We can show that $\sphericalangle NMO = \beta = 0.5\cos^{-1}(-1/3) = 0.9553$, and $\sphericalangle NOM = \alpha = (0.61548 - \theta)$. For given β and r_i^c, area of the $MNM'N'$ is equal to $2 \times (A_{\triangle MNO} - A_{\triangleleft ONM'})$, which are themselves defined as follow:

$$A_{\triangle MNO} = 0.5 r_i^{c2} \frac{\sin\alpha\cos\theta}{\sin\beta} \tag{I.5}$$

$$A_{\triangleleft ONM'} = 0.5 r_i^{c2} \alpha \tag{I.6}$$

Consequently, the cross-sectional area of residual wetting fluid may be written as:

$$A_i^{wet} = r_i^{c2} \left(\frac{\sin\alpha\cos\theta}{\sin\beta} - \alpha \right) \tag{I.7}$$

Total length of edges filled with the wetting fluid is given by:

$$L_i = 12\sqrt{6}R_i - 8\sum_{j\in\mathbb{N}_i} r_{ij} \tag{I.8}$$

With the total pore body volume given by Equation I.1, the saturation of wetting fluid in the pore body is determined as:

$$s_i^w = \frac{3\sqrt{2}r_i^{c2}\left(3\sqrt{6}R_i - 2\sum_{j\in\mathbb{N}_i} r_{ij}\right)\left(\frac{\sin\alpha\cos\theta}{\sin\beta} - \alpha\right)}{3\sqrt{6}R_i^3 - 2\sum_{j\in\mathbb{N}_i} r_{ij}^3} \tag{I.9}$$

This relation is valid only when all pore throats connected to the pore body i are invaded by the nonwetting fluid, so that there is no vertex interface in that pore body. This may not be the case when the nonwetting fluid has filled only the inscribed sphere of the pore body ($r_i^c = R_i$) for which $s_i^w = s_i^{dr}$ given by Equation I.2. In fact, substituting $r_i^c = R_i$ in Equation I.9, results in a saturation different from s_i^{dr}. We denote this saturation by s_i^*. Forcing saturation to vary between s_i^{dr} and s_i^{min} (the latter one was defined by Equation 7.3), results in the following equation:

$$\begin{aligned} s_i^w \quad &= \quad s_i^{min} + \frac{s_i^{dr} - s_i^{min}}{s_i^* - s_i^{min}} \times \\ &\left[\frac{3\sqrt{2}\left(3\sqrt{6}R_i - 2\sum_{j\in\mathbb{N}_i} r_{ij}\right)\left(\frac{\sin\alpha\cos\theta}{\sin\beta} - \alpha\right)}{4\kappa_i^2(3\sqrt{6}R_i^3 - 2\sum_{j\in\mathbb{N}_i} r_{ij}^3)} - s_i^{min}\right] \end{aligned} \tag{I.10}$$

This relationship is shown as a thick curve in Figure I.2(a).

I.1.3 Local p_i^c-s_i^w relationship for the full range of saturation

Finally, to reduce the computational efforts, we have chosen to fit one single curve to p_i^c for the full range of saturation. Equation 7.2 shows the fitted p_i^c-s_i^w relationship for the full range of saturation in a pore body. This relationship is shown by a thin curve in Figure I.2(a).

I.2 Local p_i^c-s_i^w relationship under imbibition

Local variation of capillary pressure is much more complex under imbibition than drainage. As mentioned in Section 6.3.2, interface topology, and consequently capillary pressure in a pore body are controlled by the number of pore throats which are

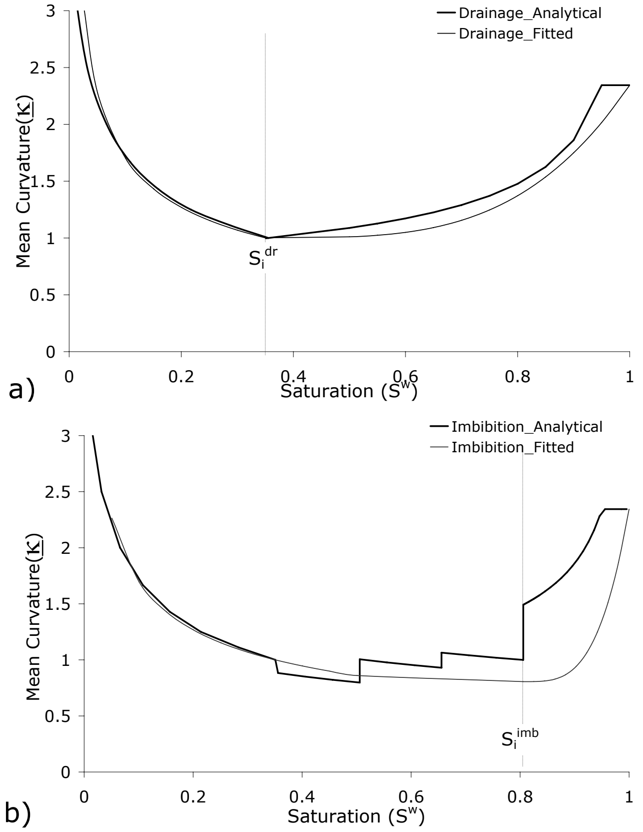

Figure I.2: *Local p_i^c-s_i^w curves during drainage (a) and imbibition (b). Thick curves show the analytical calculations and thin curves show the fitted curves.*

still (partially) filled by the nonwetting fluid. Introducing Z as the total number of pore throats connected a pore body, and I as the number of pore throats (partially filled by the nonwetting fluid), the following zones are introduced to defining local p_i^c-s_i^w relationship:

- All pore throats are (partially) filled by the nonwetting fluid, $I = Z$ (Zone 1)
- More than one of the pore throats and not all of them are (partially) filled by the nonwetting fluid, $1 < I < Z$ (Zone 2)
- Only one pore throat is (partially) filled by the nonwetting fluid, $I = 1$ (Zone 3)

I.2.1 All pore throats (partially) filled by the nonwetting fluid, $I = Z$ (zone 1)

In this range all pore throats are (partially) filled by the nonwetting fluid and p_i^c-s_i^w relationship is the same as Zone 2 ($0 < s_i^w \leq s_i^{dr}$) for drainage process. Thus, p_i^c-s_i^w curve follows the same curve shown in Figure I.2(a) till one of the pore throats is fully filled by the wetting fluid.

I.2.2 More than one of the pore throats and not all of them (partially) filled by the nonwetting fluid, $1 < I < Z$ (zone 2)

As long as all the pore throats are (partially) filled by the nonwetting fluid, the wetting fluid will be present only along the 12 edges of the pore body. When nonwetting fluid recedes completely from one of the pore throats, an interface will be created in the opening of that pore throat. This vertex interfaces is shown in Figure I.1(d). For simplicitly, we assume that all wetting fluid's volume existing in that pore body will remain in that vertex. If nonwetting fluid recedes from two or more pore throats, the wetting fluid will be distributed among them. Knowing the volume of the wetting fluid and the number of pore throats nonwetting fluid has receded from, radius of the curvature of the interface can be estimated. Refer to Figure I.1(d), let's denote the length of edge of pyramid $O_1A'B'C'D'$ base by a'. We can calculate a' based on the geometry of pore body, pore throats, and the number of pore throats partially filled with nonwetting fluid (I), as follows:

$$a' = \left[\frac{3\sqrt{2}}{6-I} s_i^w V_i + \frac{8}{6-I} \sum_{j=1}^{6-I} r_{ij}^3 \right]^{1/3} \tag{I.11}$$

in which V_i can be calculated from Equation I.1. Using the value of a', mean radius of caurvature of the interface is given by $r_i^c = \frac{a'}{2\cos(\theta + \sin^{-1}\frac{\sqrt{3}}{3})}$. As it can be seen with decrease of I, a' will decrease and consequently capillary pressure will increase. This trend is shown schematically in Figure I.2(b) as a step-wise curve. The jumps in the curve occur when the nonwetting fluid recedes from one of the pore throats (I decreases), and refer to Equation I.11, radius of curvature decreases. We follow this trend till only one of the pore throats remains filled with the nonwetting fluid.

There is a qualitative consistency between the trend of this local p_i^c-s_i^w curve with the experimental observations of *Lenormand and Zarcone* (1984), who observed with decrease of number of pore throats (partially) filled with the nonwetting fluid, local capillary pressure may increase.

I.2.3 Only one pore throat (partially) filled by the nonwetting fluid, $I = 1$ (zone 3)

When only one of the pore throats is (partially) filled with the nonwetting fluid, the behaviour of the interface follows the explanations given in Zone I during drainage.

I.2.4 Local p_i^c-s_i^w relationship for the full range of saturation

As mentioned before, the variation of capillary pressure with saturation is very irregular and it depends on the fluid occupancy of pore throats. The thick curve in Figure I.2(b) shows an example of this curve for a pore body. But, handling such a discontinuous curve in the pore-network model is nontrivial. Thus, to reduce the computational efforts, we have chosen to fit one single curve to p_i^c for the full range of saturation. Equation 7.4 shows the fitted p_i^c-s_i^w relationship for the full range of saturation in a pore body. This relationship is shown by a thin curve in Figure I.2(b). The fitted curve results decrease of capillary pressure with increase of saturation to a minimum capillary pressure. This minimum capillary pressure occurs at a saturation corresponding to the start of Zone 3 during imbibition, where only one pore throat is (partially) filled by the nonwetting fluid. We denote this saturation by s_i^{imb} as shown in Figure I.2(b).

Bibliography

Acharya, R. C., S. E. A. T. M. van der Zee, and A. Leijnse (2004), Porosity–permeability properties generated with a new 2-parameter 3d hydraulic pore-network model for consolidated and unconsolidated porous media, *Advances in Water Resources*, *27*, 707–723.

Ahrenholz, B., J. Tölke, P. Lehmann, A. Peters, A. Kaestner, M. Krafczyk, and W. Durner (2008), Prediction of capillary hysteresis in a porous material using lattice-boltzmann methods and comparison to experimental data and a morphological pore network model, *Advances in Water Resources*, *31*(9), 1151–1173, doi:DOI: 10.1016/j.advwatres.2008.03.009.

Aker, E., J. Maloy, A. Hansen, and G. G. Batrouni (1998a), A two-dimensional network simulator for two-phase flow in porous media, *Transport in Porous Media*, *32*, 163–186.

Aker, E. K., K. J. Maloy, and A. Hansen (1998b), Simulating temporal evolution of pressure in two-phase flow in porous media, *Physical Review E*, *58*, 2217–2226.

Al-Futaisi, A., and T. W. Patzek (2003), Extension of hoshenkopelman algorithm to non-lattice environments, *Physica A*, *321*, 665–678.

Al-Gharbi, M. S., and M. J. Blunt (2005), Dynamic network modeling of two-phase drainage in porous media, *Phys Rev E Stat Nonlin Soft Matter Phys*, *71*, 016,308 – 016,308, doi: 10.1103/PhysRevE.71.016308.

Al-Raoush, R. I., and C. S. Willson (2005a), Extraction of physically realistic pore network properties from three-dimensional synchrotron x-ray microtomography images of unconsolidated porous media systems, *Journal of Hydrology*, *300*, 44–64.

Al-Raoush, R. I., and C. S. Willson (2005b), A pore-scale investigation of a multiphase porous media system, *J. Contam. Hydrology*, *77*, 67–89.

Anwar, A. H. M. F., M. Bettahar, and U. Matsubayashi (2000), A method for determining air–water interfacial area in variably saturated porous media, *J. Contam. Hydrol.*, *43*, 129–146.

Avraam, D. G., and A. C. Payatakes (1995), J. fluid mech., *Flow regimes and relative permeabilities during steady-state two-phase flow in porous media*, *293*, 207–236.

Avraam, D. G., and A. C. Payatakes (1995a), Generalized relative permeability coefficients during steady-state, two-phase flow in porous media and correlation with the flow mechanisms, *Transport in Porous Media*, *20*, 135–168.

Avraam, D. G., and A. C. Payatakes (1999), Flow mechanisms, relative permeabilities and coupling effects in steady-state two-phase flow in porous media. the case of strong wettability, *Ind Eng Chem Res.*, *38*, 778–786.

Avraam, D. G., G. B. Kolonis, T. C. Roumeliotis, G. N. Constantinides, and A. C. Payatakes (1994), Steady-state two-phase flow through planar and non-planar model porous media, *Transport in Porous Media*, *16*, 75–101.

Azzam, M. I. S., and F. A. L. Dullien (1977), Flow in tubes with periodic step changes in diameter: a numerical solution, *Chem. Eng. Sci.*, *32*, 1445–1455.

Bakke, S., and P.-E. Øren (1997), 3-d pore-scale modelling of sandstones and flow simulations in the pore networks, *SPE Journal*, *2*(2), 136–149.

Barenblatt, G., T. Patzek, and D. Silin (2003), The mathematical model of nonequilibrium effects in water-oil displacement, *SPE Journal*, *8*(4), 409–416.

Bear, J. (1972), *Dynamics of fluids in porous media*, Elsevier, New York.

Bear, J., D. Zaslavsky, and S. Irmay (1968), *Physical Principles of Water Percolation and Seepage*, z.uitg, Paris.

Berentsen, C. W. J., and S. M. Hassanizadeh (2006), On the equivalence of measured and averaged pressures in porous media, 16th International Conference on Computational Methods in Water Resources.

Blum, H. (1967), A transformation for extracting new descriptors of shape, in *Models for the Perception of Speech and Visual Form*, edited by W.-D. W., pp. 362–380, MIT Press, Cambridge, Mass.

Blunt, M., and P. King (1990), Macroscopic parameters from simulations of the pore scale flow, *Physical Review A*, *42*, 4780–4788.

Blunt, M., and P. King (1991), Relative permeabilities from two- and three- dimensional pore-scale network modelling, *Transport in Porous Media*, *6*, 407–433.

Blunt, M., and H. Scher (1995), Pore-level modeling of wetting, *Physical Review E*, *52*, 6387–6403.

Blunt, M., P. King, and H. Scher (1992), Simulation and theory of two-phase flow in porous media, *Physical Review A*, *46*, 7680–7702.

Blunt, M., M. D. Jackson, M. Piri, and P. H. Valvatne (2002), Detailed physics, predictive capabilities and macroscopic consequences for pore-network models of multiphase flow, *Advances in Water Resources*, *25*, 1069–1089.

Blunt, M. J. (2001), Flow in porous media - pore-network models and multiphase flow, *Current Opinion Colloid Interface Sci.*, *6*, 197–207.

Bottero, S. (2009), Advances in theories of capillarity in porous media, Ph.D. thesis, Utrecht University.

Bottero, S., and S. M. Hassanizadeh (2006), Experimental and numerical study to investigate dynamic capillary pressure effect in two-phase flow in porous media, 16th International Conference on Computational Methods in Water Resources.

Brady, M., and H. Asada (1984), Smoothed local symmetries and their implementation, *Int. J. Robotics Res.*, *3*, 36–61.

Bravo, M. C., M. Araujo, and M. E. Lago (2007), Pore network modeling of two-phase flow in a liquid-(disconnected) gas system, *Physica A*, *375*, 1–17.

Brooks, R. H., and A. T. Corey (1964), Hydraulic properties of porous media, *Tech. Rep. Hydrol. Pap. No. 3*, Colo. State Univ.

Brusseau, M. L., J. Popovicova, and J. A. K. Silva (1997), Characterizing gas–water interfacial and bulk-water partitioning for gas phase transport of organic contaminants in unsaturated porous media, *Environ. Sci. Technol.*, *31*, 1645–1649.

Brusseau, M. L., S. Peng, G. Schnaar, and M. S. Constanza-Robinson (2006), Relationships among air–water interfacial area, capillary pressure, and water saturation for a sandy porous medium, *Water Resources Research*, *42*, W03,501, doi:10.1029/2005WR004058.

Burganos, V. N., and A. C. Payatakes (1992), Knudsen diffusion in random and correlated networks of constricted pores, *Chem. Eng. Sci.*, *47*, 1383–1400.

Camps-Roach, G., D. M. OCarroll, T. A. Newson, T. Sakaki, and T. H. Illangasekare (2010), Experimental investigation of dynamic effects in capillary pressure: Grain size dependency and upscaling, *Water Resources Research*, *submitted*.

Celia, M. A., P. C. Reeves, and L. A. Ferrand (1995), Recent advances in pore scale models for multiphase flow in prous media, *Reviews of Geophysics*, *33 (S1)*, 1049–1058.

Chandran, S., S. K. Kim, and D. M. Mount (1992), Parallel computational geometry of rectangles, *Algorithmica*, *7*, 25–49.

Chang, F., Y. C. Lu, and T. Pavlidis (1999), Feature analysis using line sweep thinning algorithm, *IEEE Trans. Pattern Anal. Mach. Intell.*, *21*, 145–158.

Chaouche, M., N. Rakotomalala, D. Salin, B. Xu, and Y. C. Yortsos (1994), Capillary effects in drainage in heterogeneous porous media: continuum modelling, experiments and pore network simulations, *Chemical Engineering Science*, *49*, 2447–2466.

Chatzis, I., and F. A. L. Dullien (1981), Mercury porosimetry curves of sandstones, mechanisms of mercury penetration and withdrawal, *Powder Technology*, *29*, 117–125.

Chen, D. Q., L. J. Pyrak-Nolte, J. Griffin, and N. J. Giordano (2007), Measurement of interfacial area per volume for drainage and imbibition, *Water Resources Research*, *43*, W12,504, doi: 10.1029/2007WR0060217.

Chen, J. D., and D. Wilkinson (1985), Pore-scale viscous fingering in porous media, *Physical Review Letters*, *55*, 1892–1896.

Chen, L., and T. C. G. Kibbey (2006), Measurement of air-water interfacial area for multiple hysteretic drainage curves in an unsaturated fine sand, *Langmuir*, *22*, 6874–6880.

Cheng, J. T. (2002), Fluid flow in ultra-small structures, Ph.D. thesis, Purdue University, West Lafayette, Indiana.

Cheng, J. T., L. J. Pyrak-Nolte, and D. D. Nolte (2004), Linking pressure and saturation through interfacial area in porous media, *Geophysical Research Letters*, *31*, L08,502, doi: 10.1029/2003GL019282.

Coles, M. E., et al. (1998), Developments in synchrotron x-ray microtomography with applications to flow in porous media, *SPE Reservoir Evaluation & engineering*, *1*, 288–296.

Constantinides, G. N., and A. C. Payatakes (1991), A theoretical model of collision and coalescence of ganglia in porous media, *J. Colloid Interface Sci.*, *141*, 486–504.

Constantinides, G. N., and A. C. Payatakes (1996), Network simulation of steady-state two-phase flow in consolidated porous media, *AIChE Journal*, *42*, 369–382.

Constantinides, G. N., and A. C. Payatakes (2000), Effects of precursor wetting films in immiscible displacement through porous media, *Transport in Porous Media*, *38*, 291–317.

Costanza-Robinson, M. S., and M. L. Brusseau (2002), Air–water interfacial areas in unsaturated soils: evaluation of interfacial domains, *Water Resources Research*, *38*, 13–1.

Culligan, K. A., D. Wildenschild, B. S. B. Christensen, W. Gray, M. L. Rivers, and A. F. B. Tompson (2004), Interfacial area measurements for unsaturated flow through a porous medium, *Water Resources Research*, *40*, W12,413, doi:10.1029/2004WR003278.

Culligan, K. A., D. Wildenschild, B. S. B. Christensen, W. Gray, M. L. Rivers, and A. F. B. Tompson (2006), Pore-scale characteristics of multiphase flow in porous media: A comparison of air–water and oil–water experiments, *Advances in Water Resources*, *29*, 227–238.

Dahle, H. K., and M. A. Celia (1999), A dynamic network model for two-phase immiscible flow, *Computational Geosciences*, *3*, 1–22.

Dahle, H. K., M. A. Celia, and S. M. Hassanizadeh (2005), Bundle-of-tubes model for calculating dynamic effects in the capillary-pressure-saturation relationship, *Transport in Porous Media*, *58*, 5–22, doi:10.1007/s11242-004-5466-4.

Das, D., R. Gauldie, and M. Mirzaei (2007), Dynamic effects for two-phase flow in porous media: Fluid property effects, *AIChE Journal*, *53*(10), 2505–2520.

Das, D. B., M. Mirzaei, and N. Widdows (2006), Non-uniqueness in capillary pressure–saturation–relative permeability relationships for two-phase flow in porous media: Interplay between intensity and distribution of random micro-heterogeneities, *Chemical Engineering Science*, *61*, 6786–6803.

Dias, M. M., and A. C. Payatakes (1986a), Network models for two-phase flow in porous media part 1. immiscible microdisplacement of non-wetting fluids, *J. Fluid Mechanics*, *164*, 305–336.

Dias, M. M., and A. C. Payatakes (1986b), Network models for two-phase flow in porous media part 2. motion of oil ganglia, *J. Fluid Mechanics*, *164*, 337–358.

DiCarlo, D. A. (2006), Quantitative network model predictions of saturation behind infiltration fronts and comparison with experiments, *Water Resource Research*, *42*, W07,408, doi: 10.1029/2005WR004750.

Dubikovskaya, A. A., O. V. Kirichenko, and V. G. Lapshin (1990), High-porosity thin-fiber metallic material, *Materials Science*, *25*, 372–373.

Dullien, F. A. L. (1992), *Porous Media: Fluid Transport and Pore Structure*, 574 pp., Academic Press Inc.,U.S.; 2Rev Ed edition, San Diego.

Entov, V. M. (1980), Theory of nonequilibrium effects associated with the flow of nonuniform fluids in porous media, *Fluid Dynamics*, *15*(3), 365–369, doi:10.1007/BF01089969.

Fatt, I. (1956), The network model of porous media, i. capillary pressure characteristics, *Petroleum Trans. AIME*, *207*, 144–159.

Fayers, F. J., M. J. Blunt, and M. A. Christie (1990), Accurate calibration of emperical viscous fingering models, 2nd European Conference on the Mathematics of Oil Recovery, pp. 45–55, 75015 Paris.

Fenwick, D. H., and M. J. Blunt (1998), Network modeling of three-phase flow in porous media, *SPE Journal*, *3*, 86–97.

Figus, C., Y. Le Bray, S. Bories, and M. Prat (1999), Heat and mass transfer with phase change in a porous structure partially heated continuum model and pore network simulations, *International Journal of Heat and Mass Transfer*, *42*, 2557–2569.

Fong, K. W., T. H. Jefferson, T. Suyehiro, and L. Walton (1993), Guide to the slatec common mathematical library.

Fredrich, J. T., K. H. Greaves, and J. W. Martin (1993), Pore geometry and transport-properties of fontainebleau sandstone, *International Journal of Rock Mechanics and Mining Sciences & Geomechanics Abstracts*, *30*, 691–697.

Fredrich, J. T., B. Menendez, and T. F. Wong (1995), Imaging the pore structure of geomaterials, *Science*, *268*, 276–279.

Frette, O. I., K. . J. Måløy, S. J., and A. Hansen (1997), Immiscible displacement of viscosity matched fluids in two-dimensional porous media, *Phys. Rev. E*, *55*, 2969–2975.

Fulcher, R. A., T. Ertekin, and C. D. Stahl (1985), Effect of capillary number and its constituents on two-phase relative permeability curves, *Journal of Petroleum Technology*, *37*, 249–260.

Gielen, T., S. M. Hassanizadeh, M. A. Celia, H. K. Dahle, and A. Leijnse (2004), A pore-scale network approach to investigate dynamic effects in multiphase flow, pp. 83–94, Chapel Hill, NC, USA.

Gielen, T., S. M. Hassanizadeh, A. Leijnse, and H. F. Nordhaug (2005), Dynamic effects in multiphase flow: A pore-scale network approach, in *Upscaling Multiphase Flow in Porous Media*, edited by D. B. Das and H. S. M., pp. 217–236, Springer, The Netherlands, doi: 10.1007/1-4020-3604-3_11.

Gielen, T. W. J. (2007), Upscaling multiphase transport processes in porous media, Ph.D. thesis, Delft University of Technology.

Glantz, R., and M. Hilpert (2007), Dual models of pore spaces, *Advances in Water Resources*, *30*, 227–248.

Glantz, R., and M. Hilpert (2008), Tight dual models of pore spaces, *Advances in Water Resources*, *31*, 787–806.

Hashemi, M., B. Dabir, and M. Sahimi (1999), Dynamics of two-phase flow in porous media: Simultaneous invasion of two fluids, *AIChE Journal*, *45*, 1365–1382.

Hassanizadeh, S., M. Celia, and H. Dahle (2002), Dynamic effects in the capillary pressure-saturation relationship and their impacts on unsaturated flow, *Vadose Zone Journal*, *1*, 38–57.

Hassanizadeh, S. M., and W. G. Gray (1990), Mechanics and thermodynamics of multiphase flow in porous media including interphase boundaries, *Advances in Water Resources*, *13*, 169–186.

Hassanizadeh, S. M., and W. G. Gray (1993a), Thermodynamic basis of capillary pressure in porous media, *Water Resources Research*, *29*, 3389–3405.

Hassanizadeh, S. M., and W. G. Gray (1993b), Toward an improved description of the physics of two-phase ow., *Advances in Water Resources*, *16*, 53–67.

Hassanizadeh, S. M., O. Oung, and S. Manthey (2004), Laboratory experiments and simulations on the significance of non-equilibrium effect in the capillary pressure-saturation relationship, in *Unsaturated Soils: Experimental Studies. Proceedings of the International Conference: From Experimental Evidence towards Numerical Modeling of Unsaturated Soils*, vol. 1, edited by T. Schanz, pp. 3–14, Springer Verlag, Berlin.

Held, R. J., and M. A. Celia (2001), Modeling support of functional relationships between capillary pressure, saturation, interfacial area and common lines, *Advances in Water Resources*, *24*, 325–343.

Helland, J. O., and S. M. Skjæveland (2007), Relationship between capillary pressure, saturation, and interfacial area from a model of mixed-wet triangular tubes, *Water Resources Research*, *43*, W12S10, doi:10.1029/2006WR005698.

Hinkley, R. E., M. M. Dias, and A. C. Payatakes (1987), On the motion of oil ganglia in porous media, *Physicochemical Hydrodynamics*, *8*, 185–211.

Horváth, V. K., and H. E. Stanley (1995), Temporal scaling of interfaces propagating in porous media, *Phys. Rev. E*, *52*(5), 5166–5169, doi:10.1103/PhysRevE.52.5166.

Hughes, R. G., and M. J. Blunt (2000), Pore scale modeling of rate effect in imbibition, *Transport in Porous Media*, *40*, 295–322.

Hui, M. H., and M. J. Blunt (2000), Pore-scale modeling of three-phase ow and the effects of wettability, 2000SPE/DOE improved oil recovery symposium, Tulsa, Oklahoma.

Ioannidis, M. A., I. Chatzis, and A. C. Payatakes (1991), A mercury porosimeter for investigating capillary phenomena and microdisplacement mechanisms in capillary networks, *Journal of Colloid and Interface Science*, *143*, 22–36.

Jensen, S. K., and J. O. Domingue (1988), Extracting topographic structure from digital elevation data for geographic information system analysis, *Photogrammetric Engineering and Remote Sensing*, *54*, 1593–1600, doi:10.1007/s11242-007-9191-7.

Joekar-Niasar, V., and S. M. Hassanizadeh (2010), Effect of fluids properties on non-equilibrium capillarity effects; dynamic pore-network modelling, *International Journal of Multiphase Flow*, p. submitted.

Joekar-Niasar, V., S. Hassanizadeh, and A. Leijnse (2008), Insights into the relationships among capillary pressure, saturation, interfacial area and relative permeability using pore-network modeling, *Transport in Porous Media*, *74*(2), 201–219.

Joekar-Niasar, V., S. M. Hassanizadeh, L. J. Pyrak-Nolte, and C. Berentsen (2009), Simulating drainage and imbibition experiments in a high-porosity micromodel using an unstructured pore network model, *Water Resources Research*, *45*, W02,430, doi:10.1029/2007WR006641.

Joekar-Niasar, V., S. M. Hassanizadeh, and H. K. Dahle (2010a), Non-equilibrium effects in capillarity and interfacial area in two-phase flow: Dynamic pore-network modelling, *Journal of Fluid Mechanics*, doi:10.1017/S0022112010000704.

Joekar-Niasar, V., M. Prodanović, D. Wildenschild, and S. M. Hassanizadeh (2010b), Network model investigation of interfacial area, capillary pressure and saturation relationships in granular porous media, *Water Resources Research*, p. in press, doi:10.1029/2009WR008585.

Kaestner, A., E. Lehmann, and M. Stampanoni (2008), Imaging and image processing in porous media research, *Advances in Water Resources*, *31*(9), 1174–1187, doi:DOI: 10.1016/j.advwatres.2008.01.022.

Kalaydjian, F., and C. M. Marle (1987), Thermodynamic aspects of multiphase flow in porous media, *Collection colloques et séminaires - Institut français du pétrole*, *45*, 513–531.

Karkare, M. V., and T. Fort (1996), Determination of the air–water interfacial area in wet unsaturated porous media, *Langmuir*, *12*, 2041–4044.

Kim, H., P. S. C. Rao, and M. D. Annable (1997), Determination of effective air–water interfacial area in partially saturated porous media using surfactant adsorption, *Water Resources Research*, *33*, 2705–2711.

Kim, H., P. S. C. Rao, and M. D. Annable (1999), Gaseous tracer technique for estimating air–water interfacial areas and interface mobility, *Soil Sci. Soc. Am. J.*, *63*, 1554–1560.

King, P. R. (1987), The fractal nature of viscous fingering in porous media, *Journal of Physics.A, Mathematical and General*, *20*, L529–L534.

Knackstedt, M., C. Arns, A. Limaye, A. Sakellariou, T. Senden, A. Sheppard, R. Sok, W. Pinczewski, and G. Bunn (2004), Digital core laboratory: properties of reservoir core derived from 3d images, *Journal of Petroleum Technology*, *56*, 66–68.

Knudsen, H. A., and A. Hansen (2002), Relation between pressure and fractional flow in two-phase flow in porous media, *Physical Review E*, *65*, 056,310_1–056,310_10.

Knudsen, H. A., E. Aker, and A. Hansen (2002), Bulk flow regimes and fractional flow in 2d porous media by numerical simulations, *Transport in Porous Media*, *47*, 99–121.

Knutson, C. E., C. J. Werth, and A. J. Valocchi (2001), Pore-scale modeling of dissolution from variably distributed nonaqueous phase liquid blobs, *Water Resources Research*, *37*, 2951–2963.

Koplik, J., and T. J. Lasseter (1985), Two-phase flow in random network models of porous media, *Society of Petroleum Engineers Journal*, *25*, 89–110, doi:10.2118/11014-PA.

Korteland, S., S. Bottero, S. M. Hassanizadeh, and C. W. J. Berentsen (2009), What is the correct definition of macroscale pressure?, *Transport in Porous Media*, doi:10.1007/s11242-009-9490-2.

Koval, E. J. (1963), A method for predicting the performance of unstable miscible displacments in heterogenous media, *Trans. AIME*, *219*, 145–150.

Lam, C., and V. K. Horváth (2000), Pipe network model for scaling of dynamic interfaces in porous media, *Physical Review Letters*, *85*, 1238–1241.

Lam, L., and S. W. Lee (1992), Thinning methodologies-a comprehensive survey, *IEEE Transactions on pattern analysis machine intelligence*, *14*, 869–885.

Lee, D. T. (1982), Medial axis transformation of a planar shape, *IEEE Trans. Pattern Anal. Mach. Intell. PAMI*, *4*, 363–369.

Lefebvre du Prey, E. J. (1973), Factors affecting liquid-liquid relative permeabilities of a consolidated porous medium, *Soc. Pet. Eng. Journal*, pp. 39–47.

Lenormand, R. (1990), Liquids in porous media, *Journal of Physics: Condensed Matter*, *2*(S), SA79–SA88.

Lenormand, R., and C. Zarcone (1983), Mechanism of the displacement of one fluid by another in a network of capillary ducts, *J. Fluid Mech.*, *135*, 337–353.

Lenormand, R., and C. Zarcone (1984), Role of roughness and edges during imbibition in square capillaries, 59th Annual Technical Conference of the SPE, p. No 13264, Houston, Richardson, TX.

Lenormand, R., E. Touboul, and C. Zarcone (1988), Numerical models and experiments on immiscible displacements in porous media, *Journal of Fluid Mechanics*, *189*, 165–187.

Lerdahl, T. R., P. E. Øren, and S. Bakke (2000), A predictive network model for three-phase ow in porous media, SPE Symposium on Improved Oil Recovery, pp. 2–5, Tulsa, OK.

Lindquist, W. B. (2002), Network flow model studies and 3d pore structure, *Contemporary Mathematics*, *295*, 355–366.

Lindquist, W. B. (2009), 3dma-rock, a software package for automated analysis of pore rock structure in 3d computed microtomography images.

Lindquist, W. B., A. Venkatarangan, J. Dunsmuir, and T. F. Wong (2000), Pore and throat size distributions measured from sychrotron x-ray tomographic images of fontainebleau sandstones, *J. Geophys. Research*, *105B*, 21,508–21,528.

Liu, M., P. Meakin, and H. Huang (2006), Dissipative particle dynamics with attractive and repulsive particle-particle interactions, *Physics of Fluids*, *18*, 017,101.

Løvoll, G., Y. Méheust, K. J. Maløøy, E. Aker, and J. Schmittbuhl (2005), Competition of gravity, capillary and viscous forces during drainage in a two-dimensional porous medium, a pore scale study, *Energy*, *30*, 861–872.

Lu, T., D. Nielsen, and J. Biggar (1995), Water movement in glass bead porous media. 3. theoretical analysis of capillary rise into initially dry media, *Water Resources Research*, *31*(1), 11–18.

Ma, S., G. Mason, and N. R. Morrow (1996), Effect of contact angle on drainage and imbibition in regular polygonal tubes, *Colloids and Surfaces A.*, *117*, 273–291.

Mahmud, W. M., and V. H. Nguyen (2006), Effects of snap-off in imbibition in porous media with different spatial correlations, *Transport in Porous Media*, *64*, 279–300.

Man, H. N., and X. D. Jing (2000), Pore network modelling of electrical resistivity and capillary pressure characteristics, *Transport in Porous Media*, *41*(3), 263–285, doi: 10.1023/A:1006612100346.

Manthey, S., S. M. Hassanizadeh, O. Oung, and R. Helmig (2004), Dynamic capillary pressure effects in two-phase flow through heterogeneous porous media, 15th International Conference on Computational Methods in Water Resources.

Manthey, S., S. M. Hassanizadeh, and R. Helmig (2005), Macro-scale dynamic effects in homogeneous and heterogeneous porous media, *Transport in Porous Media*, *58*, 121–145, doi: 121-14510.1007/s11242-004-5472-6.

Manthey, S., S. M. Hassanizadeh, R. Helmig, and R. Hilfer (2008), Dimensional analysis of two-phase flow including a rate-dependent capillary pressure–saturation relationship, *Advances in Water Resources*, *31*, 1137–1150, doi:10.1016/j.advwatres.2008.01.021.

Martys, N. S., and J. G. Hagedorn (2002), Multiscale modeling of fluid transport in heterogenous material using discrete bolzmann methods, *Materials and Structures*, *35*, 650–659.

Mason, G., and N. R. Morrow (1987), Meniscus configurations and curvatures in non-axisymmetric pores of open and closed uniform cross section, *Proceedings of the Royal Society of London. Series A, Mathematical and Physical Sciences*, *414*(1846), 111–133.

Mason, G., and N. R. Morrow (1991), Capillary behavior of a perfectly wetting liquid in irregular triangular tubes, *J. Colloid Interface Sci.*, *141*, 262–274.

Matsuyama, T., and T. Y. Phillips (1984), Digital realization of the labeled voronoi diagram and its application to closed boundary detection, 7th International Conference on Pattern Recognition, pp. 478–480.

Mayer, R. P., and R. A. Stowe (1965), Mercury porosimetry-breakthrough pressure for penetration between packed spheres, *J. Colloid Sci.*, *20*, 891–911.

Mirzaei, M., and D. B. Das (2007), Dynamic effects in capillary pressure-saturations relationships for two-phase flow in 3d porous media: Implications of micro-heterogeneities, *Chemical Engineering Science*, *62*(7), 1927 – 1947, doi:DOI: 10.1016/j.ces.2006.12.039.

Mogensen, K., and E. H. Stenby (1998), A dynamic two-phase pore-scale model for imbibition, *Transport in Porous Media*, *32*, 299–327.

Montanari, U. (1969), Continuous skeletons from digitized images, *J. ACM*, *16*, 534–549, doi: http://doi.acm.org/10.1145/321541.321543.

Montemagno, C. D., and L. J. Pyrak-Nolte (1995), Porosity of fracture networks, *Geophysical Research Letters*, *22*, 1397–1401.

Montoto, M., A. Martineznistal, A. Rodriguezrey, N. Fernandezmerayo, and P. Soriano (1995), Microfractography of granitic-rocks under confocal scanning laser microscopy, *Journal of Microscopy-Oxford*, *177*, 138–149.

Ng, K. M., and A. C. Payatakes (1980), Stochastic simulation of the motion, breakup and stranding of oil ganglia in water-wet granular porous media during immiscible displacement, *AIChE Journal*, *26*, 419–429.

Nguyen, V. H., A. P. Sheppard, M. A. Knackstedt, and W. V. Pinczewski (2004), A dynamic network model for imbibition, *SPE Journal*, p. SPE 90365.

Nguyen, V. H., A. P. Sheppard, M. A. Knackstedt, and W. Pinczewski (2006), The effect of displacement rate on imbibition relative permeability and residual saturation, *Journal of petroleum science & engineering*, *52*, 54–70.

Niessner, J., and S. M. Hassanizadeh (2008), A model for two-phase flow in porous media including fluid-fluid interfacial area, *Water Resources Research*, *44*, W08,439, doi: 10.1029/2007WR006721.

Niessner, J., and S. M. Hassanizadeh (2009), Modeling kinetic interphase mass transfer for two-phase flow in porous media including fluid–fluid interfacial area, *Transport in Porous Media*, *80*(2), 329–344, doi:10.1007/s11242-009-9358-5.

Nordbotten, J., M. Celia, H. Dahle, and S. Hassanizadeh (2007), Interpretation of macroscale variables in darcy's law, *Water Resources Research*, *43*(8), W08,430.

Nordbotten, J., M. Celia, H. Dahle, and S. Hassanizadeh (2008), On the definition of macroscale pressure for multiphase flow in porous media, *Water Resources Research*, *44*(6), W06S02.

Nordhaug, H. F., M. Celia, and H. K. Dahle (2003), A pore network model for calculation of interfacial velocities, *Advances in Water Resources*, *26*, 1061–1074.

Nowak, U., and L. Weimann (1991), *A family of Newton codes for systems of highly nonlinear equations*, Konrad-Zuse-Zentrum für Informationstechnik Berlin.

O'Carroll, D. M., T. J. Phelan, and L. M. Abriola (2005), Exploring dynamic effects in capillary pressure in multistep outflow experiments, *Water Resources Research*, *41*, W11,419, doi:10.1029/2005WR004010.

Ogniewicz, R., and M. Ilg (1992), Voronoi skeletons: Theory and applications, Proc. ICPR, pp. 63–69.

Øren, P. E., and S. Bakke (2002), Process based reconstruction of sandstones and prediction of transport properties, *Transport in Porous Media*, *46*(2), 311–343, doi: 10.1023/A:1015031122338.

Øren, P. E., S. Bakke, and O. J. Arntzen (1998), Extending predictive capabilities to network models, *SPE Journal*, *3*, 324–336.

Oung, O., S. M. Hassanizadeh, and A. Bezuijen (2005), Two-phase flow experiments in a geocentrifuge and the significance of dynamic capillary pressure effect, *Journal of Porous Media*, *8*, 247–257.

Pan, C., M. Hilpert, and C. T. Miller (2004), Lattice-boltzmann simulation of two-phase flow in porous media, *Water Resources Research*, *40*, W01,501, doi:10.1029/2003WR002120.

Patzek, T. W. (2001), Verification of a complete pore network simulator of drainage and imbibition, *SPE Journal*, *6*, 144–156.

Patzek, T. W., and D. B. Silin (2001), Shape factor and hydraulic conductance in noncircular capillaries: I. one-phase creeping flow, *Journal of Colloid and Interface Science*, *236*(2), 295 – 304, doi:10.1006/jcis.2000.7413.

Payatakes, A. C. (1982), Dynamics of oil ganglia during immiscible displacement in water-wet porous media, *Ann. Review Fluid Mechanics*, *14*, 365–393.

Payatakes, A. C., K. M. Ng, and R. W. Flumerfelt (1980), Oil ganglion dynamics during immiscible displacement: model formulation, *AIChE Journal*, *26*, 430–442.

Pereira, G. G., W. V. Pinczewski, D. Y. C. Chan, L. Paterson, and P. E. Øren (1996), Pore-scale network model for drainage-dominated three-phase flow in porous media, *Transport in Porous Media*, *24*, 167–201.

Piri, M., and M. J. Blunt (2005a), Three-dimensional mixed-wet random pore-scale network modeling of two- and three-phase flow in porous media. i. model description, *Phys. Rev. E*, *71*(2), 026,301, doi:10.1103/PhysRevE.71.026302.

Piri, M., and M. J. Blunt (2005b), Three-dimensional mixed-wet random pore-scale network modeling of two- and three-phase flow in porous media. ii. results, *Physical Review E*, *71*(2), 026,302.

Pop, I., C. van Duijn, J. Niessner, and S. Hassanizadeh (2009), Horizontal redistribution of fluids in a porous medium: The role of interfacial area in modeling hysteresis, *Advances in Water Resources*, *32*(3), 383 – 390, doi:DOI: 10.1016/j.advwatres.2008.12.006.

Porter, M. L., M. G. Schaap, and D. Wildenschild (2009), Lattice-boltzmann simulations of the capillary pressure-saturation-interfacial area relationship for porous media, *Advances in Water Resources*, *32*(11), 1632 – 1640, doi:DOI: 10.1016/j.advwatres.2009.08.009.

Prat, M. (2002), Recent advances in pore-scale models for drying of porous media, *Chemical Engineering Journal*, *86*, 153–164, doi:10.1016/S1385-8947(01)00283-2.

Prat, M. (2007), On the influence of pore shape, contact angle and film flows on drying of capillary porous media, *International Journal of Heat and Mass Transfer*, *50*, 1455–1468.

Princen, H. M. J. (1969a), Capillary phenomena in assemblies of parallel cylinders i.capillary rise between two cylinders, *Colloid Interface Sci.*, *30*, 69–75.

Princen, H. M. J. (1969b), Capillary phenomena in assemblies of parallel cylinders ii.capillary rise in systems with more than two cylinders, *Colloid Interface Sci.*, *30*, 359–371.

Princen, H. M. J. (1970), Capillary phenomena in assemblies of parallel cylinders iii.liquid columns between horizontal parallel cylinders, *Colloid Interface Sci.*, *34*, 171–184.

Prodanović, M., and S. L. Bryant (2006), A level set method for determining critical curvatures for drainage and imbibition, *Journal of Colloid and Interface Science*, *304*, 442–458.

Prodanović, M., W. B. Lindquist, and R. S. Seright (2006), Porous structure and fluid partitioning in polyethylene cores from 3d x-ray microtomographic imaging, *Journal of Colloid and Interface Science*, *298*, 282–297.

Prodanović, M., W. B. Lindquist, and R. S. Seright (2007), 3d image-based characterization of fluid displacement in a berea core, *Advances in Water Resources*, *30*, 214–226, doi: 10.1016/j.advwatres.2005.05.015.

Pyrak-Nolte, L. J. (2007), Url of website with original data:http://www.physics.purdue.edu/rockphys/dataimages/.

Pyrak-Nolte, L. J., D. D. Nolte, D. Q. Chen, and N. J. Giordano (2008), Relating capillary pressure to interfacial areas, *Water Resources Research*, *44*, W06,408, doi:10.1029/2007WR006434.

Raeesi, B., and M. Piri (2009), The effects of wettability and trapping on relationships between interfacial area, capillary pressure and saturation in porous media: A pore-scale network modeling approach, *Journal of Hydrology*, doi:10.1016/j.jhydrol.2009.07.060.

Ransohoff, T. C., and C. J. Radke (1988), Laminar flow of a wetting liquid along the corners of a predominantly gas-occupied noncircular pore, *J. Coll. Int. Sci.*, *121*, 392–401.

Raoof, A., and S. Hassanizadeh (2009), A new method for generating pore-network models of porous media, *Transport in Porous Media*, doi:10.1007/s11242-009-9412-3.

Rapin, S. (1980), Behavior of non-wetting oil ganglia displaced by an aqueous phase, Master's thesis, Univ Houston, Houston, Tex.

Reeves, P. C. (1997), Development of porescale network model for the simulation of capillary pressure, saturation, interfacial area, relative permeability in multi-uid porous media, Ph.D. thesis, Princeton University.

Reeves, P. C., and M. A. Celia (1996), A functional relationship between capillary pressure, saturation, and interfacial area as revealed by a pore-scale network model, *Water Resources Research*, *32*, 2345–2358.

Reimbrecht, E. G., E. Bazzo, L. H. S. Almeida, H. C. Silva, C. Binder, and J. L. R. Muzart (2003), Manufacturing of metallic porous structures to be used in capillary pumping systems, *Mat. Res.*, *6*, 481–486.

Roof, J. G. (1970), Snap-off of oil droplets in water-wet pores, *SPE J.*, *10*, 85–90.

Rosenfeld, A., and J. L. Pfalz (1968), Distance function on digital pictures, *Pattern Recognition*, *1*, 33–61.

Ryazanov, A. V., M. I. J. van Dijke, and K. S. Sorbie (2009), Two-phase pore-network modelling: Existence of oil layers during water invasion, *Transport in Porous Media*, *80*(1), 79–99.

Saint-Marc, P., H. Rom, and G. Medioni (1993), B-spline contour representation and symmetry detection, *IEEE Trans. Pattern Anal. Mach. Intell.*, *15*, 1191–1197.

Saripalli, K. P., P. S. C. Rao, and M. D. Annable (1998), Determination of specic naplwater interfacial areas of residual napls in porous media using the interfacial tracers technique, *J. Contam. Hydrogeol*, *30*, 375–391.

Schaap, M. G., M. L. Porter, B. S. B. Christensen, and D. Wildenschild (2007), Comparison of pressure-saturation characteristics derived from computed tomography and lattice boltzmann simulations, *Water Resources Research*, *43*, W12S06, doi:10.1029/2006WR005730.

Schaefer, C. E., D. A. Dicarlo, and M. J. Blunt (2000), Experimental measurement of air–water interfacial area during gravity drainage and secondary imbibition in porous media, *Water Resources Research*, *36*, 885–890.

Schnaar, G., and M. L. Brusseau (2005), Pore-scale characterization of organic immiscible-liquid morphology in natural porous media using synchrotron x-ray microtomography, *Environ. Sci. Technol.*, *39*, 8403–8410.

Schnaar, G., and M. L. Brusseau (2006), Characterizing pore-scale conguration of organic immiscible liquid in multi-phase systems with synchrotron x-ray microtomography, *Vadose Zone J.*, *5*, 641–648.

Shan, X., and H. Chen (1994), Simulation of nonideal gases and liquid-gas phase transitions by the lattice boltzmann equation, *Phys. Rev. E*, *49*(4), 2941–2948, doi: 10.1103/PhysRevE.49.2941.

Sheludko, A. (1967), Thin liquid films, *Advances in Colloid Interface Science*, *1*, 391–464.

Sholokhova, Y., D. Kim, and W. B. Lindquist (2009), Network flow modeling via lattice-boltzmann based channel conductance, *Advances in Water Resources*, *32*(2), 205–212, doi: 10.1016/j.advwatres.2008.10.016.

Sibson, R. (1981), A brief description of natural neighbor interpolation, in *Interpolating multivariate data*, chap. 2, pp. 21–36, John Wiley & Sons, New York.

Singh, M., and K. K. Mohanty (2003), Dynamic modelling of drainage through three-dimensional porous materials, *Chem Eng Sci*, *58*, 1–18.

Sinha, P. K., and C. Wang (2007), Pore-network modeling of liquid water transport in gas diffusion layer of a polymer electrolyte fuel cell, *Electrochimica Acta*, *52*(28), 7936 – 7945, doi:DOI: 10.1016/j.electacta.2007.06.061.

Smith, R. W. (1987), Computer processing of line images: a survey, *Pattern Recognition*, *20*, 7–15.

Stauffer, F. (1978), Time dependence of the relations between capillary pressure, water content and conductivity during drainage of porous media, IAHR, pp. 3.35–3.52, Thessaloniki.

Tartakovsky, A., and P. Meakin (2005), Simulation of unsaturated flow in complex fractures using smoothed particle hydrodynamics, *Vadose Zone Journal*, *4*, 848–855.

Thompson, K. E. (2002), Pore-scale modeling of fluid transport in disordered fibrous materials, *AIChE Journal*, *48*, 1369–1389, doi:10.1002/aic.690480703.

Touboul, E., R. Lenormand, and C. Zarcone (1987), Immiscible displacements in porous media: testing network simulators by micromodel experiments, in *SPE Annual Technical Conference and Exhibition*, 27-30, Society of Petroleum Engineers.

Tsakiroglou, C. D., M. A. Theodoropoulou, and V. Karoutsos (2003), Nonequilibrium capillary pressure and relative permeability curves of porous media, *AIChE Journal*, *49*(10), 2472–2486.

Valvanides, M. S., and A. C. Payatakes (2001), True-to-mechanism model of steady-state two-phase flow in porous media, using decomposition into prototype flows, *Advances in Water Resources*, *24*, 385–407.

Valvanides, M. S., G. N. Constantinides, and A. C. Payatakes (1998), Mechanistic model of steady-state two-phase flow in porous media based on ganglion dynamics, *Transport in Porous Media*, *30*, 267–299.

Valvatne, P. H., and M. J. Blunt (2004), Predictive pore-scale modeling of two-phase flow in mixed wet media, *Water Resources Research*, *40*, W07,406, doi:10.1029/ 2003WR002627.

Van der Marck, S. C., T. Matsuura, and J. Glas (1997), Viscous and capillary pressures during drainage: Network simulations and experiments, *Physical Review E*, *56*, 5675–5687.

van Dijke, M. I. J., and K. S. Sorbie (2006), Existence of fluid layers in the corners of a capillary with non-uniform wettability, *Journal of Colloid and Interface Science*, *293*, 455–463.

Vidales, A. M., J. L. Riccardo, and G. Zgrabli (1998), Pore-level modelling of wetting on correlated porous media, *J. Phys. D, Appl. Phys.*, *31*, 2861–2868.

Vizika, O., D. G. Avraam, and A. C. Payatakes (1994), On the role of viscosity ratio during low-capillary-number forced imbibition in porous media, *Journal of Colloid and Interface Science*, *165*, 386–401.

Vogel, H. J. (1997), Morphological determination of pore connectivity as a function of pore size using serial sections, *European journal of soil sciences*, *48*, 365–377.

Vogel, H. J. (2000), A numerical experiment on pore size, pore connectivity, water retention, permeability, and solute transport using network models, *European journal of soil sciences*, *51*, 99–105.

Vogel, H. J., and K. Roth (1998), A new approach for determining effective soil hydraulic functions, *European journal of soil sciences*, *49*, 547–556.

Wardlaw, N. C., and L. Yu (1988), Fluid topology, pore size and aspect ratio during imbibition, *Transport in Porous Media*, *3*, 17–34.

Washburn, E. W. (1921), The dynamics of capillary flow, *Physical Review*, *17*, 273 – 283.

Whitaker, S. (1977), Simultaneous heat, mass, and momentum transfer in porous media: a theory of drying, *Adv. Heat Transfer*, *13*, 119–200.

Wildenschild, D., J. W. Hopmans, C. M. P. Vaz, M. L. Rivers, and D. Rikard (2002), Using x-ray computed tomography in hydrology: Systems, resolutions, and limitations, *J. Hydrology*, *267*, 285–297.

Wilkinson, D. (1984), Percolation model of immiscible displacement in the presence of the buoyancy forces, *Physical Review A*, *30*, 520–531.

Wu, A. Y., S. K. Bhaskar, and A. Rosenfeld (1986), Computation of geometric properties from the medial axis transform in time, *Computer Vision, Graphics, and Image Processing*, *34*, 76–92.

Wu, A. Y., S. K. Bhaskar, and A. Rosenfeld (1988), Parallel computation of geometric properties from the medial axis transform, *Computer Vision, Graphics, and Image Processing*, *41*, 323–332.

Yang, D., R. P. Currier, and D. Z. Zhang (2009), Ensemble phase averaged equations for multiphase flows in porous media. part 1: The bundle-of-tubes model, *International Journal of Multiphase Flow*, *35*(7), 628 – 639, doi:DOI: 10.1016/j.ijmultiphaseflow.2009.03.002.

Ye, Q. Z. (1988), The signed euclidean distance transform and its applications, 9th International Conference on Pattern Recognition, pp. 495–499.

Zhou, D., M. J. Blunt, and F. M. Orr (1997), Hydrocarbon drainage along corners of noncircular capillaries, *J. Coll. Int. Sci.*, *187*, 11–21.

Samenvatting

De gangbare theorieën voor tweefasen stroming in poreuze media zijn gebaseerd op uitbreidingen van de klassieke vergelijking die de stroming van grondwater beschrijft: de Wet van Darcy. Deze vergelijking veronderstelt een algebrasche relatie tussen de capillaire druk en de verzadiging van de bevochtigende fase in het poreuze medium. Reeds in de jaren 60 zijn er tweefasen experimenten uitgevoerd die dynamische effecten aantoonden die niet met de gangbare theorieën verklaard en gemodelleerd konden worden. Dit heeft geleid tot een herformulering van de wiskundige vergelijkingen voor tweefasen stroming, welke in het bijzonder gebaseerd zijn op thermodynamische principes en wetmatigheden.

In dit proefschrift worden deze nieuwe vergelijkingen voor meerfasen stroming in poreuze media bestudeerd. Om een grondig inzicht te verkrijgen in de meerfasen processen en om het meerfasen (dynamisch) stromingsgedrag te kunnen modelleren (voorspellen) wordt gebruik gemaakt van numerieke porienetwerk modellen. Dit, om zowel gemiddelde quasistatische als gemiddelde dynamische relaties tussen de capillaire druk en de verzadiging, als mede het specifiek grensvlakoppervlak (interfacial area) tussen de verschillende fasen in het poreuze medium, te kunnen bepalen. Zowel voor drainage als invasie van de vloeistoffen. Andere verschijnselen die met de porienetwerk modellen bestudeerd zijn: immobilisatie (trapping), verzadigings profielen, niet-evenwichts processen m.b.t. de vloeistofdrukken en het specifiek grensvlak oppervlak tussen de vloeistoffasen.

Naast de genoemde studie van de fysica van meerfasen stroming zijn er enige technieken ontwikkeld om poreuze media meer realistisch te presenteren in porienetwerk modellen. Met name gaat het hier om het definiëren van de topologie en de geometrie van poreuze media. Quasistatische simulaties zijn uitgevoerd in drie typen poreuze media: een hypothetisch poreus medium, een tweedimensionaal micromodel en een driedimensionale glasparelkolom. De porienetwerk modellen zijn gevalideerd d.m.v. vergelijking met experimentele gegevens van meer-fasen experimenten. Bovendien is een realistisch dynamisch porienetwerk ontwikkeld met verbeterde numerieke en geometrische eigenschappen. De in dit proefschrift gepresenteerde dynamische porienetwerk modellen maken het mogelijk realistische meerfasen stroming in poreuze media te simuleren voor een range van capillaire getallen en viscositeitsverhoudingen, voor zowel drainage als invasie van niet-mengende vloeistoffen in een poreus medium.

List of Publications (in Chronological Order)

[1] Joekar-Niasar, V., Hassanizadeh, S.M., Leijnse A. (2008) "*Insights into the relationships among capillary pressure, saturation, interfacial area and relative permeability using pore-network modelling,*" Transport in Porous Media, 74, 201–219.

[2] Joekar-Niasar, V., Hassanizadeh, S.M., Pyrak-Nolte, L., Berentsen, C. (2009) "*Simulating drainage and imbibition experiments in a high-porosity micro-model using an unstructured pore-network model,*" Water Resources Research, 45, W02430, doi:10.1029/2007WR006641.

[3] Joekar-Niasar, V., Prodanović, M., Wildenschild, D., Hassanizadeh, S.M. (2010) "*Network model investigation of interfacial area, capillary pressure and saturation relationships in granular porous media,*" Water Resources Research, doi:10.1029/2009WR008585.

[4] Joekar-Niasar, V., Hassanizadeh, S. M., Dahle, H. K. (2010) "*Non-equilibrium effects in capillarity and interfacial area in two-phase flow: dynamic pore-network modeling,*" Journal of Fluid Mechanics, doi:10.1017/S0022112010000704.

[5] Joekar-Niasar, V., Hassanizadeh, S. M. (2010) "*Effect of fluids properties on non-equilibrium capillarity effects; dynamic pore-network modelling,*" International Journal of Multiphase Flow, under review.

[6] Joekar-Niasar, V., Hassanizadeh, S. M. (2010) "*Dynamics of two-phase flow in porous media; from pore scale to Darcy scale,*" journal of Critical Reviews in Environmental Science and Technology, under review.

[7] Joekar-Niasar, V., Hassanizadeh, S. M. (2010) "*Fluid-fluid interfacial area under nonequilibrium conditions,*" XVIII International Conference on Computational Methods in Water Resources, under review.

[8] Joekar-Niasar, V., Hassanizadeh, S. M. (2010) "*Specific interfacial area; the missing state variable in two-phase Flow*" Water Resources Research, under review.